Wrocław University
of Science and Technology

DTU

Doctoral Dissertation

InAs/InP quantum dots for telecom quantum photonics

Paweł Holewa

Supervisors: Marcin Syperek
Elizaveta Semenova

Field of science: Natural sciences
Discipline of science: Physical sciences
Keywords: semiconductor quantum dots, InAs/InP, telecom spectral range, single-photon sources

Wrocław 2023

Nonlinear Quantum Photonics Group
Laboratory for Optical Spectroscopy of Nanostructures
Department of Experimental Physics
Faculty of Fundamental Problems of Technology
Wrocław University of Science and Technology

Wybrzeże Wyspiańskiego 27
50-370 Wrocław, Poland
www.wppt.pwr.edu.pl

Nanophotonic Devices Group
Department of Electrical and Photonics Engineering
DTU Electro
Technical University of Denmark

Ørsteds Plads
Building 345A
2800 Kgs. Lyngby, Denmark
www.electro.dtu.dk

The doctoral thesis was co-financed by the European Union under the European Social Fund, project no. POWR.03.02.00-00-I003/16.

Abstract

Semiconductor nanotechnology is a rapidly growing branch of science and industry, benefiting from the unique properties of structures with reduced dimensionality, like quantum dots (QDs). These have a discrete energy spectrum and properties similar to atoms, which are essential for creating non-classical light sources, emitting nearly on-demand single photons or entangled photon pairs. Such light sources are crucial for photon-based quantum information processing (QIP), specifically for quantum communication protocols that rely on quantum mechanics principles, providing highly secure optical data transfer, meeting the demands of the modern information society.

In the telecom industry, silica fiber networks are crucial for providing a transfer medium for optical signals distributed between network nodes. To operate at a single photon level, it is necessary to overcome optical losses in fiber so that photon-encoded quantum information can be transmitted over long distances with minimal data transfer errors. Since silica fibers have the lowest transmission losses at 3rd telecommunication window (∼1.46-1.62 µm), it is beneficial to provide QD-based non-classical light sources operating at this spectral window.

Self-assembled InAs QDs epitaxially grown on InP substrates are among the most promising candidates for such quantum emitters. However, a significant drawback of the currently available nanostructures operating at 3rd telecom window is the absence of high-performance photonic devices that could be fabricated deterministically. First, the low photon extraction efficiency, typically <1 %, limits the QD-based device performance. Secondly, the self-assembly process seriously deteriorates the device fabrication yield since the QD nucleation site is probabilistic. The thesis aims to address these problems and proposes solutions that pave the way for fabricating bright and scalable photonic devices with InAs/InP QDs that can potentially meet industry standards.

The thesis first elaborates on various fabricated and optically examined InAs/InP QD systems, focusing on their potential for QIP schemes. Second, novel hybrid heterostructures with InAs/InP QDs on the silicon platform are developed and presented. These structures are fabricated within the flip-chip technique and provide an enhanced photon extraction efficiency due to the presence of a metallic mirror. The QD brightness is sufficient for imaging their emission, thus providing information on their spatial position. The final part focuses on the establishment of a deterministic approach by employing photoluminescence imaging, exemplified by the fabrication of circular Bragg grating cavities at the QD nucleation sites. The state-of-the-art quantum emission properties in the 3rd telecommunication window are reached, facilitating the light-matter interaction. The reported research has enabled:

1. obtaining InAs/InP QDs with good optical quality and low surface density,
2. maximizing the efficiency of emission extraction,
3. introducing determinism into the QD-based technologies at 3rd telecom window.

The scientific findings were published in international peer-reviewed journals, with a focus on:

- Low density quantum dot ensembles as candidates for single-photon sources at 3rd telecom window: P. Holewa *et al.*, **Physical Review B**, 101, 19 (2020), P. Holewa *et al.*, **Physical Review Applied**, 14, 6 (2020), P. Holewa *et al.*, **Nanophotonics**, 11, 8 (2022),
- Quantum dot-based heterostructure with bright single-photon sources: P. Holewa *et al.*, **ACS Photonics**, 9, 7 (2022).

Additionally, one preprint complements the thesis:

- Optical localization of quantum dots, deterministic fabrication of nanocavities, and QD-cavity coupling: P. Holewa *et al.*, *Scalable quantum photonic devices emitting indistinguishable photons in the telecom C-band*, arXiv:2304.02515 (2023).

All articles are summarized in the introduction to the thesis, and full texts are included. Supplemental material is provided if relevant.

Streszczenie

Nanotechnologia półprzewodnikowa jest szybko rozwijającą się gałęzią nauki i przemysłu, korzystającą z unikalnych właściwości struktur o zmniejszonej wymiarowości, takich jak kropki kwantowe. Mają one dyskretne widmo energetyczne i właściwości podobne do atomów, co jest niezbędne do stworzenia nieklasycznych źródeł światła, emitujących pojedyncze fotony na żądanie lub pary splątanych fotonów. Takie źródła światła są kluczowe dla kwantowego przetwarzania informacji opartego na fotonach, a konkretnie dla protokołów komunikacji kwantowej, które bazując na zasadach mechaniki kwantowej, zapewniają wysoce bezpieczny optyczny transfer danych, spełniający wymagania nowoczesnego społeczeństwa informacyjnego.

Sieci światłowodowe z krzemionki są kluczowe dla zapewnienia medium transmisyjnego dla sygnałów optycznych dystrybuowanych pomiędzy węzłami sieci w przemyśle telekomunikacyjnym. Pokonanie strat optycznych w światłowodzie jest konieczne do działania na poziomie pojedynczego fotonu, tak aby informacja kwantowa zakodowana w fotonie mogła być przesyłana na duże odległości przy minimalnych błędach transferu danych. Ponieważ światłowody krzemionkowe mają najniższe straty transmisyjne w zakresie trzeciego okna telekomunikacyjnego ($\sim$1.46-1.62 µm), korzystne jest dostarczenie nieklasycznych źródeł światła bazujących na kropkach kwantowych, działających w tym zakresie spektralnym.

Samorosnące kropki z InAs wzrastane epitaksjalnie na podłożu InP są jednymi z najbardziej obiecujących kandydatów na takie emitery kwantowe. Jednakże istotną wadą obecnie dostępnych nanostruktur działających w zakresie trzeciego okna telekomunikacyjnego jest brak wysokowydajnych urządzeń fotonicznych, które mogłyby być wytwarzane w sposób deterministyczny. Po pierwsze, niska wydajność ekstrakcji fotonów, typowo <1 %, ogranicza wydajność takich urządzeń. Po drugie, proces samoorganizacji kropek poważnie pogarsza wydajność fabrykacji, skoro miejsce nukleacji kropki jest probabilistyczne. Niniejsza praca doktorska ma na celu rozwiązanie tych problemów i zaproponowanie rozwiązań, które wyznaczą drogę do produkcji jasnych i skalowalnych urządzeń fotonicznych opartych o kropki InAs/InP, które mogą spełniać standardy przemysłowe.

W pierwszej kolejności opisane zostały różne wytworzone i zbadane optycznie struktury z kropkami InAs/InP, ze szczególnym uwzględnieniem ich potencjału dla schematów kwantowego przetwarzania informacji. Następnie, opracowano i wykonano nowe hybrydowe heterostruktury z kropkami InAs/InP na platformie krzemowej. Struktury te są wytwarzane w technice *flip-chip* i zapewniają zwiększoną wydajność ekstrakcji fotonów dzięki obecności metalicznego lustra. Jasność kropek jest wystarczająca do obrazowania ich emisji, dostarczając informacji o ich położeniu przestrzennym. W ostatniej części skupiono się na zaprezentowaniu deterministycznego wytwarzania nanostruktur dzięki wykorzystaniu obrazowania fotoluminescencji. Za przykład posłużyły kołowe siatki Bragga, wytworzone w miejscach nukleacji kropek. Osiągnięto rekordowe właściwości emisji kwantowej z kropek w trzecim oknie telekomunikacyjnym, a także pokazano oddziaływanie światło-materia. Zaprezentowane badania umożliwiły w szczególności:

1. otrzymanie kropek InAs/InP o dobrej jakości optycznej i niskiej gęstości powierzchniowej,
2. maksymalizację wydajności ekstrakcji emisji,
3. wprowadzenie determinizmu do technologii opartych o kropki kwantowe w trzecim oknie telekomunikacyjnym.

Wyniki badań naukowych zostały opublikowane w międzynarodowych recenzowanych czasopismach naukowych, ze szczególnym uwzględnieniem następujących zagadnień:

- Zbiory kropek o niskiej gęstości jako potencjalne źródła pojedynczych fotonów w zakresie trzeciego okna telekomunikacyjnego: P. Holewa *et al.*, **Physical Review B**, 101, 19 (2020), P. Holewa *et al.*, **Physical Review Applied**, 14, 6 (2020), P. Holewa *et al.*, **Nanophotonics**,

11, 8 (2022),

- Heterostruktura oparta o kropki kwantowe, z jasnymi źródłami pojedynczych fotonów: P. Holewa *et al.*, **ACS Photonics**, 9, 7 (2022).

Dodatkowo, jeden preprint stanowi uzupełnienie pracy doktorskiej:

- Lokalizacja optyczna kropek, deterministyczna produkcja nano-wnęk i sprzężenie kropki z wnęką: P. Holewa *et al.*, *Scalable quantum photonic devices emitting indistinguishable photons in the telecom C-band*, arXiv:2304.02515 (2023).

Wszystkie artykuły są podsumowane we wstępie do rozprawy, a pełne teksty artykułów są przedrukowane. Materiały uzupełniające artykuły są załączone w zależności od wkładu autora rozprawy.

Preface

This thesis is submitted in partial fulfillment of the requirements for the Ph.D. degree from the Wrocław University of Science and Technology (WUST). The research has been carried out in collaboration between the Nonlinear Quantum Photonics Group, at the Laboratory for Optical Spectroscopy of Nanostructures (WUST), where the optical part of research has been done, and the Nanophotonic Devices Group at the Department of Electrical and Photonics Engineering, Technical University of Denmark (DTU), where the epitaxial growth of quantum dots and the fabrication of the quantum dot-based heterostructures has been performed. The project was jointly supervised at WUST by Associate Professor Marcin Syperek and at DTU by Senior Researcher Elizaveta Semenova.

The author of the thesis was supported by the Etiuda doctoral scholarship, financed by the Polish National Science Center, Grant no. 2020/36/T/ST5/00511, and by the project *InterDok – Interdisciplinary Doctoral Studies Projects at Wroclaw University of Science and Technology*, financed by the European Union under the European Social Fund, project no. POWR.03.02.00-00-I003/16.

Wrocław
June 6, 2023

Paweł Holewa

Acknowledgements

First and foremost, I would like to thank deeply my both supervisors, Marcin Syperek and Elizaveta Semenova, for all their guidance, support, and belief in me from the beginning. They are endless sources of professional expertise, wisdom, and fresh ideas, giving our project strong prospects to thrive. Being inspired by their example and passion for science allowed me to advance and become a better researcher.

The success of this project would not be possible without the collective work of many people to whom I am deeply grateful. First, I am thankful to Aurimas Sakanas, my first fabrication teacher, whose expertise and curiosity inspired and enabled the fabrication of numerous InP-based structures, including those described in this thesis. I enjoyed working in the optical lab with Paweł Wyborski, who was always ready to discuss the arising challenges and to look together for the best solution, and with whom we used to challenge the definition of reasonable working hours. I am also grateful to Michał Gawełczyk whose reliable theoretical support and attention to detail were vital to data interpretation and always provided us with the complete picture of exciton physics.

I greatly appreciate the opportunity to work together with my fellow friends and peers that I met both at WUST at the Laboratory for Optical Spectroscopy of Nanostructures, led by Grzegorz Sęk, and at DTU, including members of the NanoPhoton Center of Excellence, Quantum Nanophotonics section, and Nanodevices group with the leaders Kresten Yvind and Jesper Mørk. The positive work atmosphere made my research work and my stays at DTU so memorable.

Last but not least, I would like to express my deepest gratitude to my beloved fiancée Marta for all the love, understanding, patience, and support that I have received in this challenging time, and to my parents, who always believed in my capabilities, for their love and encouragement since the very beginning.

List of thesis papers

Published articles

1. P. Holewa, M. Gawełczyk, C. Ciostek, P. Wyborski, S. Kadkhodazadeh, E. Semenova, M. Syperek, *Optical and electronic properties of low-density InAs/InP quantum dot-like structures devoted to single-photon emitters at telecom wavelengths*, **Physical Review B**, 101, 19 (2020).

– included in this thesis, p. 95.

2. P. Holewa, M. Gawełczyk, A. Maryński, P. Wyborski, J. P. Reithmaier, G. Sęk, M. Benyoucef, M. Syperek, *Optical and Electronic Properties of Symmetric InAs/(In,Al,Ga)As/InP Quantum Dots Formed by Ripening in Molecular Beam Epitaxy: A Potential System for Broad-Range Single-Photon Telecom Emitters*, **Physical Review Applied**, 14, 6 (2020).

– included in this thesis, p. 111.

3. P. Holewa, S. Kadkhodazadeh, M. Gawełczyk, P. Baluta, A. Musiał, V. G. Dubrovskii, M. Syperek, E. Semenova, *Droplet epitaxy symmetric InAs/InP quantum dots for quantum emission in the third telecom window: morphology, optical and electronic properties*, **Nanophotonics**, 11, 8 (2022).

– included in this thesis, p. 127.

4. P. Holewa, A. Sakanas, U. M. Gür, P. Mrowiński, A. Huck, B. Wang, A. Musiał, K. Yvind, N. Gregersen, M. Syperek, E. Semenova, *Bright Quantum Dot Single-Photon Emitters at Telecom Bands Heterogeneously Integrated with Si*, **ACS Photonics**, 9, 7 (2022).

– included in this thesis, p. 143.

Preprint

5. P. Holewa, E. Zięba-Ostój, D. Vajner, M. Wasiluk, B. Gaál, A. Sakanas, M. Burakowski, P. Mrowiński, B. Krajnik, M. Xiong, A. Huck, K. Yvind, N. Gregersen, A. Musiał, T. Heindel, M. Syperek, E. Semenova, *Scalable quantum photonic devices emitting indistinguishable photons in the telecom C-band*, arXiv:2304.02515 (2023).

– included in this thesis, p. 153.

×

Contents

Part I

Introduction

CHAPTER 1

Motivation

1.1 Quantum information processing

Emerging platforms known as quantum technologies are based on the unique qualities provided by quantum physics, such as quantum interference, superposition, entanglement, etc. These qualities can significantly improve measurement sensitivity, communication security, and computational power compared to conventional or classical techniques. One of the most popular methods to encrypt, transport, and process quantum information is to use a single photon as a "qubit" – the quantum mechanical counterpart of a classical bit [1]. This is well-justified as photons can travel quickly over large distances without losing their coherence and are compatible with widely-used photonic technologies. Therefore, the quantum information encoded and carried by photons can be readily utilized in the schemes of quantum information processing (QIP), especially quantum communication [2–4], benefiting from the low photon decoherence. Extremely efficient sources of single and indistinguishable photons compatible with low-loss photonic technologies are a foundation for optical QIP.

Single photons are also an enabling resource to fuel photonic quantum computers. This term was proposed in 1982 by Richard Feynman, and ever since then, it has captured the enormous interest of researchers and IT companies, becoming a "holy grail" of physics. An optical version of a quantum computer was initially shown in 2001 [3] by Knill et al. using single-photon generators, detectors, and optical components, such as mirrors and beam splitters. In this design, a single-photon source (SPS) is needed to produce photons that are used to encode the quantum computer qubits. Various ideas [1] for improving the initial protocol were implemented in the following years.

Why single-photon sources at telecom?

Quantum networks play a significant role in a broader framework of QIP, both for the formal analysis and the practical implementation of quantum communication, computing, and metrology [5]. A quantum network [6, 7] consisting of remote nodes capable of transmitting photon-encoded quantum information provides opportunities to implement ultra-secure data exchange protocols [8] and distributed quantum computing schemes [7, 9]. The ultimate security of the data transfer based on single photons originates from the "no-cloning theorem" that prevents the quantum information from being copied.

An example of such a network is shown in Fig. 1.1a [6, 7]. There, quantum nodes produce, process, and store quantum information locally. They are interconnected by quantum channels that distribute quantum entanglement and transmit quantum states from site to site with high fidelity. Such a network could carry out activities that in the context of conventional physics seem impractical, and do so with very little processing power, e. g., distribution of the "quantum software" [6].

Depending on the communication protocol, there are specific requirements for the properties of single photons (on top of their purity P), such as concerning their indistinguishability or creation of entanglement between them [10]. Therefore, the requirements for using quantum emitters as quantum light sources for QIP typically include on-demand photon generation, narrow transition linewidth, fast decay rate, and long coherence time, reflected by high indistinguishability of emitted photons.

Currently, two major non-classical optical communication channels are under development. The first one is free-space satellite-mediated communication over very long distances (thousands

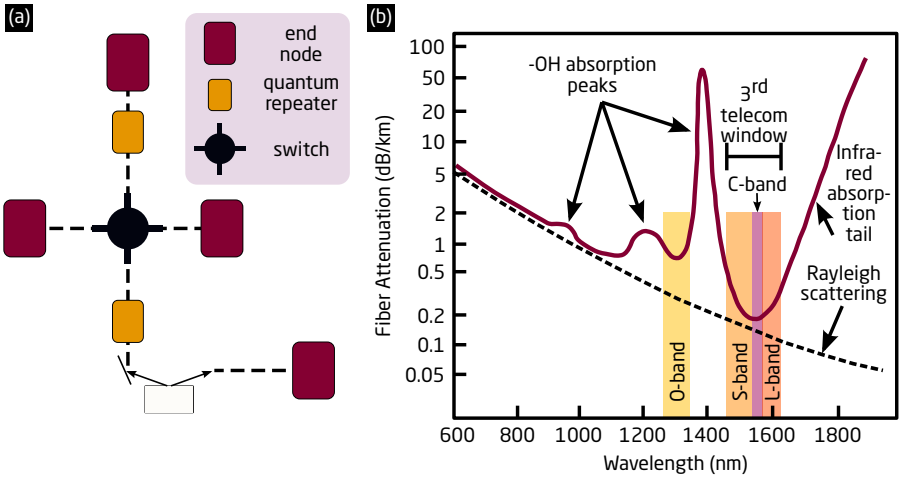

Figure 1.1: **a**, Scheme of a quantum network with a source of entangled photon pairs, quantum channels for distributing the information, and quantum nodes for processing and storing the states, **b**, attenuation in silica optical fibers.

of km) with single photons typically originating from nonlinear processes in crystals (parametric down-conversion) [11]. The choice of wavelength is determined by the transmission windows of the Earth's atmosphere, and the InAs/GaAs quantum dots (QDs) can be used here. The second approach, constituting the motivation for the thesis, is the use of silica fiber networks conveniently employed in the telecom infrastructure worldwide. In this case, optimal wavelengths for transmitted photons are different than for the atmospheric links, as defined by transmission windows of silica fibers, and suitable quantum light sources are covered in the following section. The optical signal attenuation in the silica fiber is presented in Fig. 1.1b. It reaches the minimal value for the 1550 nm photon wavelength and is spectrally limited by the elastic Rayleigh scattering with strong wavelength dependence ($I \approx \lambda^{-4}$) from the short-wavelength part of the spectrum and the infrared (IR) absorption at the long-wavelength part. Additionally, the absorption of light by hydroxyl groups, especially around 1400 nm, separates the short wavelength "original" O-band (2$^{\text{nd}}$ telecom window) at 1260-1360 nm from the 3$^{\text{rd}}$ telecom band, covering the S- (1460-1530 nm), C- (1530-1565 nm), and L- (1565-1625 nm) bands.

Therefore, deterministic SPSs with high photon emission rates at 3$^{\text{rd}}$ telecom window (centered at 1.55 µm) for low-loss fiber transmission are crucial building blocks for QIP schemes [2, 7], and quantum computing networks [7], due to their compatibility with the existing silica-fiber-based telecom networks, allowing for optical signal transfer at long distances [12, 13]. As the network can rely on the silica-fiber-based infrastructure, the photon transfer channel is characterized by ultimately low losses, $\leq 0.2\,\text{dB/km}$[1] in the telecom C-band. Furthermore, the quantum network can benefit from existing devices and classical signal management protocols, making quantum state transfer feasible across large distances and accessible for many users simultaneously. Yet, all these require bright and efficient non-classical photon state generators with high emission rates and an on-demand/triggered generation in the nearly-optimal case.

The following section describes how C-band-emitting SPSs have been realized so far, focusing on the applications of QDs in this respect.

Development of single-photon sources at telecom

The early reports on the SPSs from the 1990s and the beginning of the 2000s have focused on a variety of solutions for a SPS, such as molecules [14–16], color centers [17, 18], trapped ions [19], nanocrystals [20], and semiconductor QDs [21–23]. The wavelength range of the source was out of concern in these proof-of-principle demonstrations hence the application potential for the QIP

[1]Value for the Corning® SMF-28® Ultra Optical Fiber available in the Product Information.

was not directly addressed. However, as the field was under development, the research activities started to focus also on C-band emission. Before discussing the QDs, other material systems are briefly mentioned here, as the SPSs at C-band have been realized in many ways, including, i. a., non-linear energy conversion processes, atoms, or defects in carbon nanotubes.

In the first approach, non-linear energy conversion, the heralded photon pairs are generated in non-linear optical media, including spontaneous parametric down-conversion in $\chi^{(2)}$ materials [24–28] (also using QD transition as a pump photon [26]), or spontaneous four-wave mixing in $\chi^{(3)}$ materials [29–31]. However, as stochastic processes, these schemes provide multi-pair events according to the Poisson statistics, and their suppression requires a substantial lowering of the pump power, hence compromising the energy conversion efficiency. Therefore, reaching high generation frequencies is difficult, with multiplexing of photons offering a somewhat complex workaround. Although the heralded SPSs can operate at room temperature and may have high photon emission rates [32] with tailored spectral properties [33] and near-perfect spatial modes [34], the inherently probabilistic nature of the nonlinear generation process worsens the source brightness, affects the single-photon purity P [35], and is far from the on-demand operation conditions. Moreover, many systems are bulk-like [24, 25, 29], preventing their scalability, a severe constraint for many applications.

Except for SPSs employing nonlinear photon conversion processes in a solid state, other candidates for non-classical photon emitters have also been presented. A very interesting one is an erbium ion (Er^{3+}) [36], which generates single photons at 1.5 µm [37]. However, a millisecond-long emitter's lifetime confronts the demand for a high photon generation rate. Also, the considerable optical spectral diffusion challenges the long coherence of photons. Consequently, indistinguishable single photons from Er^{3+} hosted in $CaWO_4$ were demonstrated only in 2023 [38]. Therefore, fabricating a high-quality cavity-confined Er-based device remains a troublesome task.

In 2017, an emitter based on the aryl sp^3 defect in carbon nanotubes was presented [39] with operation at room temperature, broad emission spectrum, and limited brightness. However, for now, the realization of an active part of a device based on carbon nanotubes is challenging, limiting the application potential of this approach.

There is also an intensive search for a single photon emitter at C-band hosted by a two-dimensional (2D) material. In 2021, an induced defect state was shown in bulk-like $MoTe_2$, a candidate for optoelectronics at telecom made of transition metal dichalcogenides, offering non-classical photon emission capabilities in the C-band [40].

Although attracting the great interest of the research community, all of these approaches often constitute less mature solutions in at least some aspects compared with QDs. Each route has its material-specific challenges, while their future and feasible applications remain to be revealed.

1.2 Quantum dots

Semiconductor quantum dots — a historical perspective

The idea of utilizing the fundamental quantum mechanical effects present in systems of reduced dimensionality to control macroscopic material properties relevant for the device applications was first realized at the beginning of the 1970s by introducing quantum wells (QWs) in semiconductor lasers to control the band gap by the quantum size effect and to improve carrier confinement along the growth direction.

Further dimensionality reduction by restricting the carrier movement in three dimensions in QD-like structures appeared already in the 1980s [41, 42], still before QW lasers reached a final development stage. It took quite a long time to demonstrate the real advantages of the QD laser materials, among them lower threshold current density [43], and improved temperature stability of the threshold current density [44, 45] by 2000.

The first experimental demonstration by Reed et al. of an electron confined in a three-dimensional (3D) potential in a solid state appeared in 1988, using a lithographically-defined QD with a QW as an active material [46]. Transport experiments revealed the discrete density of states characteristic for quasi-zero-dimensional (0D) structures (cf. Section 2.3 for details on the density of states function). Owing to the development in semiconductor technology over the past three

decades, it has become possible to fabricate nanostructures of much smaller sizes than the first implementation by Reed et al. using self-organization techniques.

Since the beginning of the 2000s, a new research field has emerged. The regime of low QD density, such that QDs are separated in-plane at least by 1 µm, started to be investigated alongside the laser (or amplifier) applications, where the high surface density of QDs is beneficial. In the low-density regime, the QDs can be individually addressed, and the applications utilizing *single* QDs can be developed. A significant milestone in this research direction was the demonstration of single-photon emission from a single InAs/GaAs Stranski-Krastanow (S-K) QD by Michler et al. in 2000 [21], quickly followed by the demonstration of indistinguishable photons emission from a QD in the same material system by Santori et al. in 2002 [47]. This area of semiconductor technology has been under considerable development in recent years, and the most significant achievements, approaches, and application potential are outlined in the following sections.

Quantum dots for quantum information processing

Before delving into the state-of-the-art of semiconductor QDs at telecom wavelengths, a broader picture of the self-assembled QDs is given to establish a reference.

The epitaxial QDs seem to be one of the most perspective solutions as near-perfect single-photon emitters for QIP purposes [2, 48–53], with recent years witnessing a rapid development of QD-based technologies where a single QD is used as a source of photonic qubits – single and indistinguishable photons [49–51, 54, 55], entangled photon pairs [54, 56–61], also employing entanglement swapping [53], or multi-photon cluster states [62], depending on the quantum technology-related application. Photonic-based computations [4, 63], including boson sampling [64–67], also employ single QDs. A QD has been demonstrated to be a SPS of highest single-photon emission purity P [52], measured by the second-order correlation function $P = 1-g^{(2)}(0) = (7.5\pm1.6)\times10^{-5}$ (see Section 2.4 for the definition of $g^{(2)}(\tau)$ function), and highest emission rates [68]. New milestones are regularly reported, for example, the quantum interference of identical photons from remote GaAs QDs was shown in 2022 [69], or a photonic cluster state composed of indistinguishable photons in 2023 [70].

Only atom-based SPSs can compete with QDs in terms of emission purity, however, they are much less practical concerning their integrability and scalability of the solutions based upon them. Importantly, embedding a SPS in a III-V platform offers enormous engineering flexibility for device fabrication, including bandgap tuning, modification of their photonic environment, and formation of *p-i-n* structures with electrical contacts.

Material systems for quantum dot emission at third telecom window

Despite many reported QD-based demonstrations in the field of QIP, the majority of them focus on the short wavelength spectral range ($\lambda < 1\,\mu$m) [2, 13, 71–73] what separates them from applications where photonic qubits are transmitted using fiber networks. At the 3$^{\text{rd}}$ telecom window, there are two material systems for QDs that have been developed in parallel over the years: InAs/-GaAs [74, 75] and InAs/InP [12, 76].

InAs/GaAs quantum dots

The GaAs-based QDs benefit from the well-developed GaAs technology, including a relatively straightforward growth of Al(Ga)As/GaAs distributed Bragg reflectors (DBRs). However, reaching the emission at 1.55 µm is challenging due to the high lattice mismatch ϵ_0 between InAs and GaAs. The growth requires careful lowering of built-in strain to redshift the emission. Different approaches have been investigated, but the only results with QD emission at 3$^{\text{rd}}$ telecom window concern the metamorphic approach [13, 74, 77–81] (i. e., the introduction of InGaAs metamorphic buffer layer (MBL), where an indium content is increased between the substrate and the QD layer). This can be done linearly [77, 78, 81, 82], or using a more complex, non-linear In profile in the MBL design [74, 80]. There are also other approaches allowing redshifting the emission of GaAs-based QDs (for a review, see an introduction in Ref. [83]), with the application of the

strain-reducing layer [84–88] particularly worth mentioning. Within this approach, the redshift to the 2nd telecom window can be obtained [83, 89], but the emission at 3rd window remains elusive. Although the MBL approach often complicates the epitaxial process by the introduction of structural defects deteriorating the optical quality of QDs [77, 90], single-photon emission at 1.55 µm has been demonstrated [74, 78, 82, 91], followed by the photon entanglement [61, 92], narrowband piezoelectric wavelength tuning [79], coherent control of the QD state [61, 93], and the generation of indistinguishable single photons [91, 93, 94].

InAs/InP quantum dots

Compared with InAs/GaAs, the great advantage of InAs/InP QDs is their natural coverage of the 3rd telecom window due to lower lattice mismatch ϵ_0 (no strain engineering is needed) with simultaneous single-photon emission of high purity [59, 95–98], also under non-resonant excitation [96], what makes them interesting for multiple applications in quantum technologies. These QDs can be placed in ternaries, e. g. (In,Al)As, or quaternaries, e. g. (In,Al,Ga)As, lattice-matched to InP, which provide an additional degree of freedom in strain engineering and shaping the barrier potential (carrier confinement regime) [76, 99, 100].

Lowering the InAs/InP QD density can be achieved in a few ways in the S-K growth mode, where QDs nucleate on top of a 2D wetting layer (WL) (see Section 2.2 for a thorough description of the S-K growth mode). Among them is the QD "ripening" [101–103], leading to high-quality single-photon emission [103], also for QDs of high in-plane symmetry [96]. It is as well possible to apply "double capping" technique [104], resulting primarily in lowering the QD height but also in surface density reduction, with high-quality single-photon emission obtained under non-resonant [105] and quasi-resonant excitation [95, 106].

An alternative growth mode is droplet epitaxy (DE) [76, 107–110], where group III metal droplet (In or Ga) is deposited on the substrate and annealed in the As flow (group V). In DE applied to InAs/InP QDs, the indium flux is supplied to the InP surface first, forming metal droplets in random positions which are annealed under arsine flux, leading to QD crystallization. Here, the emission wavelength in the telecom C-band can also be naturally achieved [59, 76, 97, 111] with the density of QDs on the level of $10^8/\mathrm{cm}^2$ achievable [111].

As opposed to S-K growth, which is a strain-driven process resulting in random positions of QDs, in the DE approach the QD nucleation does not rely on lattice mismatch ϵ_0 between the QD and the host material, making the DE a powerful method for tailoring the QD shape. This can lead to high in-plane QD symmetry yielding a much lower exciton fine structure splitting (FSS) than for S-K QDs [76]. This provides the possibility to separate processes responsible for surface density and QD size or geometry, allowing tailoring the QD properties [107].

DE QDs are typically in-plane symmetric when deposited on high Miller index substrate, such as InP(111) [108, 109] but also on standard InP(001), as demonstrated, i. a., in P. Holewa *et al.*, *Droplet epitaxy symmetric InAs/InP quantum dots for quantum emission in the third telecom window: morphology, optical and electronic properties*, **Nanophotonics**, 11, 8 (2022)[2] or in Ref. [76]. For the latter structures, the high symmetry enabled demonstrations of quantum entanglement under electric excitation [59] and quantum state teleportation [97]. For details on the DE and related QD symmetrization, see Section 2.2.

1.3 Enhancing brightness of quantum dot-based single-photon sources

As explained in the previous section, semiconductor QDs are very promising and interesting sources of single photons for use in QIP. However, a remaining challenge for their application is achieving high photon extraction efficiency η, defined as the fraction of emitted photons collected by the first lens of the optical system. A typical level for an as-grown structure in both described material systems is $\eta < 1\,\%$ due to the total internal reflection at the air-semiconductor interface. The

[2]This article is included in this thesis, p. 127.

problem of low η is addressed by shaping the QD photonic environment, ideally using a bottom mirror or a full nanostructure (also including a cavity) with an embedded single QD.

The well-developed GaAs technology enables the straightforward application of both the DBR and metallic layers. However, due to the low difference in refractive indices n for dielectric layers offered by the InP material system, the DBR in this system has to include a higher number of mirror pairs compared to GaAs to obtain a high-reflectivity DBR. A thicker DBR based on quaternary compounds requires a laborious, time-consuming, and typically expensive growth calibration [75], additionally significantly increasing the device size and reducing the perspectives for its successful on-chip integration. Due to these reasons, just a few reports up to date feature QDs integrated with an InP-based DBR [59, 96, 112, 113].

The low η levels for semiconductor SPSs can be increased either using a broadband enhancement by the engineering of the far-field directionality without application of a cavity, such as microlenses [114], microobjectives [115], mesas [83, 116], solid immersion lenses [117], or photonic nanowires [118, 119]. Another approach is the narrowband enhancement by placing an emitter in the cavity and benefiting from the weak coupling regime, where the photon emission rate is increased by the Purcell effect [120] with the emission directionality being enhanced simultaneously (see Section 2.5 for details on weak coupling and the Purcell effect). The major realizations exploiting the Purcell enhancement concern micropillars [49, 50, 121–127], circular Bragg gratings (CBGs), or some novel devices based on the open cavity design [55], or tapered nanowire geometry, such as trumpet [128, 129], hourglass [130, 131] or "Bier-Glas" [132] cavities. These approaches can be implemented without prior emitter selection or in a deterministic manner that provides much better process yield and brings the solution closer to the application. For details on the deterministic approach, see Section 1.3.

Moderately-broad cavities and circular Bragg gratings

Placing an emitter in a cavity has three main objectives, important for the applications:

1. increasing the photon emission rate,
2. increasing the coherence of source and emitted photons,
3. imposing the directionality of emission.

The first two points are realized due to the Purcell effect, see Section 2.5 and Eq. (2.111), and the third one – due to the engineering of the mode profile.

The above-mentioned objectives are important for any single-photon source. However, for the source of entangled photon pairs, an additional point should be realized:

4. control over the biexciton (XX)-exciton (X) cascade decay rates.

Among different cavity designs, most solutions feature a cavity characterized by high quality (Q) factors to benefit from the acceleration of emission rate. According to definition of the Q factor, Eq. (2.88), $Q = \omega/\Delta\omega$, where ω is the cavity frequency and $\Delta\omega$ – cavity mode full width at half maximum (FWHM). Therefore, the high-Q cavities are characterized by a very narrow mode width (e. g., $\Delta\omega = 0.15\,\mathrm{nm}$ in a micropillar characterized by $Q = 6124$ [50]), posing a challenge for spectral overlap between the cavity and the emitter to be coupled.

Additionally, the control over the XX-X cascade decay rates is impossible in a high-Q cavity. Typically, such cavities feature Q factors > 5000, which corresponds to a bandwidth that is too narrow to impose the Purcell enhancement over both the X and XX lines, as the typical XX binding energy $\Delta(XX)$ in a III-V QD is a few meV, corresponding to a few nm of the X and XX line separation. However, simultaneous coupling of both transitions is required to boost the generation of entangled photon pairs from the XX-X cascade. Hence, the optimal approach for their generation is to employ a cavity that is a trade-off between the efficient QD-cavity coupling (featuring high F_p), high photon extraction efficiency η, and a considerably broad mode width (moderate Q).

Besides the cavity-based approach, a solution worth mentioning is a "needle"-shaped (tapered) photonic nanowire [118, 133]. Within this approach, an entangled photon pair source characterized by entanglement fidelity of (0.86 ± 0.01) and $\eta = (16 \pm 3)\%$ was shown [134].[3] However, a weakness of this design is the lack of Purcell enhancement and the limited indistinguishability of emitted photons, most probably due to the charge noise in the QD environment. Therefore, a recently-explored alternative is a low-Q micropillar forming a broadband cavity, with Q in the range of 200-300 [136] and the working principle being the suppression of non-cavity modes, predicted theoretically in Ref. [137]. This approach enables $\eta \sim 0.7$ and Bell state fidelity[4] ~ 0.7 but requires a DBR to form a microcavity, which is easily applicable only in the GaAs-based devices.

Another solution should be found for the InP system. An interesting approach is a CBG. This "alternative" cavity can Purcell-enhance the QD emission in the spectral range that spans over the XX binding energy and provides a highly directional far-field pattern allowing for efficient photon collection (high η). Therefore, the benefits of using a cavity are not compromised here by a narrow mode width. For the entangled photon pairs emission, two devices based on a CBG cavity have shown a high degree of entanglement (fidelity > 0.8) and $\eta \sim 0.8$ in GaAs system [54, 60]. CBGs can be etched in the substrate [91, 138], membranized [72, 139] or hybridized (bonded to a metallic mirror separated by a dielectric layer) [54, 60, 140–143]. Further results obtained using CBGs are given in the following section.

In summary, the CBG cavity design is often preferred over micropillars as the cavity mode is spectrally broader, enabling simultaneous coupling of a few QD transition lines while providing decent calculated F_p of 10-20, needed to enhance the emission of polarization-entangled photon pairs [54, 60]. Additionally, it is more stable mechanically than micropillars due to the high aspect ratio of the latter. Figure 1.2 visualizes a hybrid CBG structure, in a configuration employed in this thesis.

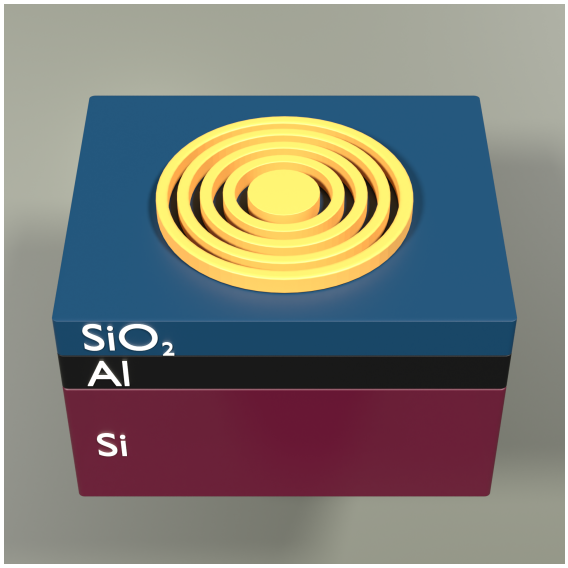

Figure 1.2: A hybrid InP CBG on top of the planar metallic (aluminum) mirror, bonded to the Si carrier wafer.

Brightness at telecom

Despite common claims about the universality of a given solution to boost the QD brightness in the broad spectral range and for various material systems, just a few solutions have been implemented

[3] Very similar parameters have been reported in Ref. [135]: entanglement fidelity of (0.76 ± 0.02) and $\eta = (15 \pm 3)\%$.

[4] *Fidelity* is defined as a probability that a measured state will pass a test to be identified as a reference state. The maximally-entangled Bell states are often used as reference states.

at telecom. Still, the telecom-optimized cavities and CBGs are of utmost performance for long-haul QIP applications. The broadband solutions have been realized in the 2nd telecom window centered at 1.3 µm [125, 127, 144]. Regarding CBGs, the numerical studies promise $\eta > 95\%$ for numerical aperture (NA) of 0.65 and F_P close to 30 [145], or $\eta \approx 79\%$ for NA = 0.7 and $F_P \sim 5$ [146], depending on the specific design. Realized CBGs at 1.3 µm have reached $\eta \approx 23\%$ and F_P of 4 [147] or even 5 [148]. The deterministic fabrication in photoluminescence (PL) imaging was reported only very recently, with $\eta \sim (11.2 \pm 1.0)\%$ and F_P of 4.2 [143].

For 1.55 µm, investigated solutions are proof-of-principle demonstrations of an optical "horn" structures with reported $\eta = 10.9\%$ [106] (no cavity), mesas on DBR with $\eta = 13.3\%$ into NA = 0.4 [113], or $\eta \approx 10\%$ in the broad spectral range of 3rd window for QDs heterogeneously integrated with a metallic mirror, as shown in P. Holewa *et al.*, *Bright Quantum Dot Single-Photon Emitters at Telecom Bands Heterogeneously Integrated with Si*, **ACS Photonics**, 9, 7 (2022)[5]. Regarding the nanocavities, a first QD in a CBG was also reported only in 2022 [91] with $\eta \approx 17\%$ for NA = 0.6 and F_P of 3, while the predicted η values are up to 90% for NA = 0.65 [149, 150]. The CBGs together with photonic crystals [151, 152] are the only cavities realized for enhancing the QD emission in 3rd telecom window.

Importantly, for the deterministic fabrication based on the PL imaging, a planar η enhancement is needed, as the signal from QDs has to be easily detectable during the imaging step. Therefore, an appropriate solution is either a DBR or a metallic mirror underneath the QDs layer. However, the DBR considerably increases the device footprint, which has a negative impact on future on-chip integration. On the other hand, the gold or silver mirrors in photonic nanowires [118], CBGs [54, 141, 142], mesas [153], and optical antennas [154, 155] were successfully employed with InAs/GaAs QDs for the enhancement of <1 µm photon emission off a chip. In contrast, the application of gold mirror in the InP system was reported only for tapered InP nanowires [156, 157] with emission outside telecom windows. Therefore, the easiest solution for the InP system seems to be a metallic mirror, enabling the broadband PL enhancement, as reported in P. Holewa *et al.*, *Bright Quantum Dot Single-Photon Emitters at Telecom Bands Heterogeneously Integrated with Si*, **ACS Photonics**, 9, 7 (2022)[6].

Deterministic fabrication of quantum dot-based devices

All demonstrations of high-quality QD-based quantum light sources mentioned in the previous sections employ well-developed QD epitaxy methods, where the nucleation of a QD is either strain-driven as in the S-K growth mode or begins with the deposition of a metal droplet (DE and/or local droplet etching [107]). Both growth modes provide quantum light emitters of superior quality in terms of single-photon purity P [52], indistinguishability [49, 50] and coherence [158], however, this comes at a price of random QD positions, as the nucleation process is probabilistic.

At the same time, placing a QD in a cavity is highly beneficial for the reasons outlined in Section 1.3. However, due to the random QD positions, proof-of-principle photonic devices incorporating single QDs are typically fabricated on the semiconductor surface in an array pattern that is effectively randomly placed with respect to the QD positions. Examples include otherwise impressive reports such as micropillars [50, 121, 123, 159], photonic cavities [125, 160], or CBGs [60, 91, 139, 142, 147, 148]. This severely reduces the processing yield and technology scalability, as well as the efficiency of light-matter interactions [161], as an effective optical interface between a QD and a photonic device requires high precision of the QD alignment to maximize coupling to specific spatial photonic cavity modes (cf. Box 6). Additionally, the maximization of the QD photon coherence time requires separation of the emitter from the etched surfaces of the device to decouple it from the fluctuating charge environment [162].

Therefore, once the properties of QDs and QD-based devices have been demonstrated in a non-deterministic approach, a subsequently required milestone is shifting the fabrication paradigm to the deterministic workflow. In this way, the random QD placement and extremely low process yield can be overcome by localization of the fabricated QDs on the semiconductor surface *prior* to the fabrication of devices [163].

[5]This article is included in this thesis, p. 143.
[6]This article is included in this thesis, p. 143.

Localization approaches

This section reviews the localization techniques that have been applied to QDs.

Scanning *in-situ* In the scanning *in-situ* methods, a structure with a QD layer, with a resist spin-coated is scanned using a focused electron or laser beam, and cavities are fabricated one by one. The reported realizations include:

1. cathodoluminescence (CL) spectroscopy followed by electron-beam lithography (EBL) [164, 165] that has been applied to fabrication of microlenses [114], microobjectives [115], mesas [116, 164, 166], nanoantennas [167], and CBGs [138],

2. low-temperature laser photolithography [168] with the demonstrations including micropillars [49, 122, 124, 126, 169, 170], CBGs [140], and solid immersion lenses [117], and

3. topography scanning using atomic force microscopy (AFM) [171] or scanning electron microscopy (SEM) [172, 173].

The optical localization of an emitter (points 1. and 2.) is a more advanced and developed approach compared with the topography localization [173], additionally allowing for identification of optically active QDs, the determination of QD emission energy, and in consequence, fine-tuning of the cavity mode energy to match the target QD transition. Therefore, reaching high η values is possible, up to 66-79 % reported experimentally [124, 126]. Besides, the topography-based localization is hard to implement for practical reasons as a QD must provide a strain-induced track on the sample surface. This is not easily achievable for cavity-based applications with out-of-plane emission since QDs are deeply buried in a semiconductor material (typically a few hundred nm beneath the surface of the structure). Additionally, for the hybrid approach where the III-V material is bonded to a metallic mirror separated by a dielectric layer, the flip-chip is required, so neither SEM nor AFM scanning can be applied once the wafers are bonded.

The scanning techniques provide accuracy of 34 nm for *in-situ* EBL [114] or 50 nm for *in-situ* photolithography [169]. Among the disadvantages of the scanning techniques is their limited speed. Additionally, the QDs in *in-situ* EBL are localized using the CL signal, so the e-beam intensity has to be low not to expose the resist, which limits the achievable QD signal intensity. On the other hand, *in-situ* photolithography cannot reliably define designs with sub-micron-size features due to inherent resolution limitations.

Photoluminescence imaging An approach with a more evident prospect for scalable deterministic fabrication is the PL imaging, employed so far predominantly for the near-infrared, 0.75 – 1.4 µm (NIR) spectral range [54, 72, 141, 174, 175], including the 2nd telecom window [143]. In this technique, an image of the $\sim 10^3$ µm^2-large surface is taken (area limited by the objective's field of view (FOV)). The QDs are localized with respect to alignment marks (AMs) with an excellent resolution (a few tens of nm [169] down to a few nm [176]), acting as reference points during the subsequent EBL step. The PL imaging workflow has been applied for the deterministic fabrication of nanocavities, mainly CBGs – either membranized [72] or hybrid [54, 141, 143].

The advantage of PL imaging is the rapid data collection compared to scanning techniques and the separation of QD detection and device fabrication steps so that thousands of devices can be fabricated in a single process run. This provides a high-fidelity route to the fabrication of an ensemble of bright quantum light sources with desired properties on a single semiconductor wafer which can afterward be cleaved into many chips, in analogy to the established microchip fabrication. Such a process up-scaling is challenging for any of the *in-situ* scanning techniques, which are more of a one-by-one fabrication approach than batch processing of a whole wafer.

Challenges of the photoluminescence imaging at telecom

A major obstacle to the use of PL imaging at telecom is the technological limitation of InGaAs-based detector matrices that have to be used at wavelengths longer than 1 µm. The underlying problem is the lack of high-quality InGaAs detectors operating at telecom that would have comparable

properties as their Si-based counterparts operating in the short-wavelength ultraviolet (UV) to NIR spectral range. The central figures of merit for the detectors are dark current, availability of the electron multiplication (EM) technology, pixel size, detection (quantum) efficiency, and chip area. Unfortunately, the EM technology is unavailable in the InGaAs-based cameras. For Si-based, it increases the detection sensitivity nearly down to a single photon level, offering high-quality images extremely important for QD positioning accuracy. The cameras with EM have led to fantastic demonstrations in the 800-950 nm range [54, 72, 176, 177].

Table 1.1 compares these figures of merit for Si- and InGaAs-based 2D detectors. It is evident that the Si-based devices significantly surpass the InGaAs counterparts. So far, there is no alternative when recording the PL signal at 2nd or 3rd telecom window – the InGaAs detectors must be used. In this sense, the comparison with Si given in Tab. 1.1 can serve only as a reference. The main limiting factor is the dark current, a few orders of magnitude higher for the InGaAs. Despite that, as it has been shown in Ref. [143] and in P. Holewa *et al.*, *Scalable quantum photonic devices emitting indistinguishable photons in the telecom C-band*, arXiv:2304.02515 (2023)[7], the imaging process in the telecom spectral range with commercially-available InGaAs-based cameras is possible, giving satisfactory results with spatial positioning accuracy of a few tens of nanometers.

Parameter	Material system for the detector	
	Si	InGaAs
Spectral range	220-1100 nm (UV–NIR)	900-1700 nm (NIR)
Dark current	2×10^{-3} e/px/s	40-4000 e/px/s
EM technology	available	not available
Pixel size	3-16 µm	10-20 µm
Quantum efficiency	>95 %	80-90 %
Chip area	Up to 4096×4096 px^2	640×512 px^2

Table 1.1: Comparison of 2D detectors for PL imaging of QD emission.

1.4 Objectives of the thesis

As outlined so far, QDs have been considered near-perfect sources of non-classical light states for years, including the application potential for long-haul silicon fiber networks. Their natural placement within the host semiconductor crystal lattice allows for vast modifications of their photonic environment while preserving the chemical stability of a QD. However, there are a few important challenges that hinder the progress of quantum technology compatible with the telecom C-band. Among them, the random nucleation site of QDs is the most serious.

The objectives of the thesis are formulated in agreement with the most important challenges in the field. This thesis aims to solve them, and the objectives can be formulated as in Box 1.

The papers described in the thesis and listed on p. ix address these challenges. Objective **1.**, focusing on the morphology of the S-K and DE QDs and their optical properties, is tackled in Articles 1–3. Objective **2.** is realized with the nanofabrication of a QD-based structure and establishing a new platform for the subsequent research and is described in Article 4. Finally, the Objective **3.**, which can be defined as central for this thesis and its principal achievement, is reported in preprint 5.

[7] This article is included in this thesis, p. 153. See also the corresponding Supplemental Material (SM) at p. 180 and Section 3.2 for setup description.

Box 1: Objectives of the thesis.

Objective **1.** **Establishing an optimal QD growth strategy for low-density InAs/InP QDs emitting at C-band, understanding their optical properties, enhancing their in-plane symmetry.**

Objective **2.** **Development of a semiconductor platform for a broadband enhancement of the photon extraction efficiency.**

Objective **3.** **Localization of QDs and deterministic fabrication of optimized nanocavities at the QD nucleation site, investigating the cavity-coupled QDs.**

CHAPTER 2

Theory

This chapter covers the fundamental phenomena important for interpreting the thesis results. They are divided into five sections, with two first focusing on epitaxial growth. The latter three focus on the optical properties of QDs and cavity physics.

Specifically, the first section describes the theory of the metalorganic vapour-phase epitaxy (MOVPE) growth, and the second describes the epitaxy of QDs. The third section describes the physics of charge carriers and Coulomb-correlated excitations in QDs, the fourth introduces the theoretical foundations of the Hanbury Brown and Twiss (HBT) interferometry, and finally, the fifth focuses on the physics of cavities and emitter-cavity coupling.

2.1 Metalorganic vapour-phase epitaxy

A few techniques for the epitaxial growth of high-quality semiconductor layers have been developed over the years. Among the most important are liquid-phase epitaxy (LPE), hydride vapor-phase epitaxy (HVPE), molecular beam epitaxy (MBE), and MOVPE. Only the latter two have proven relevant for the growth of III-V QDs emitting at telecom.

A historical perspective

The MOVPE emerged as a powerful technique of semiconductor epitaxial growth in the late 1960s with the pioneering work of H. M. Manasevit [178].[1] The rapid increase in MOVPE activities in the 1970s and 1980s enabled the early demonstration of ultra-high purity GaAs [179] and high-performance minority carrier devices (e. g., Ref. [180]) which in turn proved the considerable commercial potential of the new technique for large-scale production of a broad spectrum of semiconductor devices, such as lasers, solar cells, light emitting diodes (LEDs), or photocathodes – for virtually all II-VI and III-V compounds and alloys, operating in a broad spectral range from UV to IR.

One of the significant obstacles in the development of MOVPE was its relative complexity. The initial problems with purity and abrupt interfaces of layers grown in MOVPE were, however, overcome long ago. Nowadays, MOVPE can produce very high-purity layers, and the atomically-abrupt interfaces are also not an issue. The advantages and disadvantages of MOVPE and MBE are compared in Tab. 2.1.

Processes during the metalorganic vapour-phase epitaxy

The MOVPE is one of the most complicated growth techniques due to the number of parameters that can be tuned and the variety of chemical and physical processes coinciding in a growth chamber, specifically at a substrate. At the beginning of its development, the MOVPE growth was treated as a “black box” with many “tuning knobs”. A knowledgeable user realized the process optimization by systematically turning these knobs. This approach has been inevitable due to the multi-component, multi-phase system and dynamic processes occurring in the inhomogeneous medium. However, developing simple but accurate and practical models and quite complex

[1] This marks the first publication about MOVPE and honors the contributions by Manasevit to the rapid development of MOVPE in early 1970s. However, the patents concerning the early forms of MOVPE were filed in 1954 by T. Scott et al. in the United Kingdom, and by W. Miederer in 1962 in Germany and a year later in USA.

Technique	Strengths	Weaknesses
MBE	• Process simple to describe and understand • High uniformity • Abrupt interfaces • *In situ* monitoring	• Expensive • As/P alloys are difficult to grow • Low throughput
MOVPE	• Very flexible, reproducible, and robust process • Simple reactor • High uniformity, purity, abrupt interfaces • Suitable for large-scale production, high GR • *In situ* monitoring is limited	• Many parameters that need to be controlled accurately • Complex modeling of the growth • Expensive and hazardous precursors

Table 2.1: Comparison of MBE and MOVPE techniques.

modeling and calculations of the processes has enabled a deeper understanding of MOVPE details. Still, not everything is clear.

Box 2 summarizes the fundamental processes essential for MOVPE growth.

Box 2: The key processes in MOVPE growth.

1. **Thermodynamics** – is the foundation for all processes: it determines the growth driving force.
2. **Kinetics: mass and heat transport** – including hydrodynamics, reactor wall effects, and introducing the boundary layer model [181, 182]. Kinetics defines the rates at which various steps proceed.
3. **Physical surface processes** – including surface reconstruction and diffusion processes, formation of steps, kinks and their evolution, 2D and 3D nucleation, etc.
4. **Chemical reactions** – including homogeneous reactions in the gas phase (adduct formation and pyrolysis of precursors and adducts, etc.), and heterogeneous at the substrate interface (adsorption, desorption, pyrolysis, surface reconstruction, all influencing the density and nature of steps, kinks, and other structures, etc.)

Figure 2.1 presents an artistic vision of the epitaxial growth of InAs on InP to establish an initial understanding of the process described in the following sections. The metalorganic, here trimethylindium, $In(CH_3)_3$ (TMIn), and arsine, AsH_3, molecules arrive at the surface where they decompose so that In and As atoms can build the InAs crystal lattice. The organization of atoms according to the expected zinc blend crystal lattice and WL are not preserved in the image for simplicity.

Growth regimes. The fundamental growth regimes limiting the GR can generally be divided based on the temperature dependence of the GR into [183]:

1. **thermodynamics**, when the GR decreases with the increasing temperature. It is important both for the bulk crystal and for the growing surface.

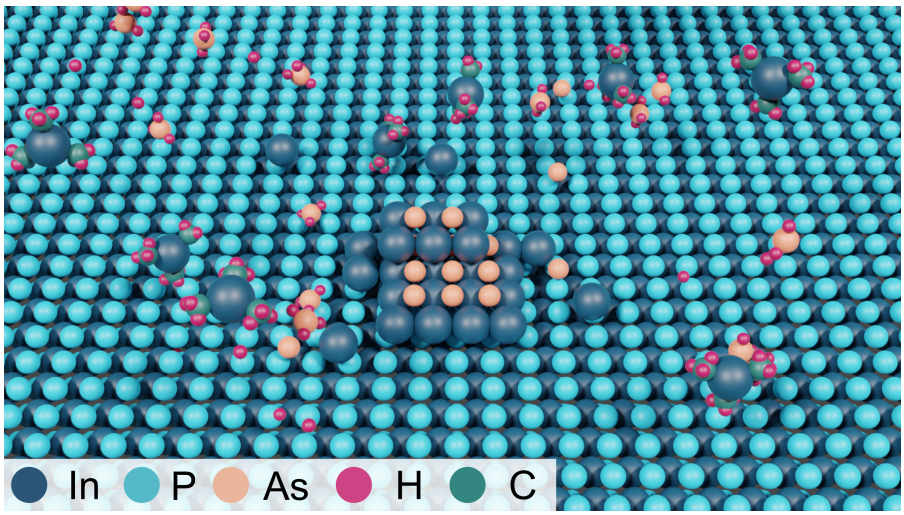

Figure 2.1: MOVPE growth of InAs on InP – an artistic vision.

2. **mass transport**, when the GR rate is nearly independent of substrate temperature, as the gas phase diffusion is a nearly temperature-independent process, or when it depends on the total flow rate.

3. **surface (reaction) kinetics**, when the GR increases with increasing temperature, or when it depends on the substrate orientation.

In the following part of this section, the fundamental processes involved in epitaxial growth will be shortly discussed. Regrettably, the simple introduced models are insufficient to fully describe or understand the growth. With every increase in the sophistication of the tools used to study the process, new complexities are revealed. For this reason, the research community has long ago virtually abandoned the hope of finding simple models to explain the growth process adequately.

Thermodynamics

The description of growth models starts with thermodynamics as it forms the frame for other processes and the entire epitaxial growth. In all techniques, the latter can be seen as a highly controlled phase transition. This formulation underlines the crucial role of thermodynamics for the processes, as it ultimately establishes the driving force of the transition and the maximum GR. Additionally, it allows for the determination of the alloy composition (mutual solubility of its components) and the solid stoichiometry (ratio between cations and anions). The latter controls the concentrations of native defects such as interstitials, vacancies, and antisite defects, and this, in turn, determines the concentration of impurities (both intentional dopants and unintentional contaminants).

Phase equilibrium condition A *phase* can be defined as a homogeneous region that is physically distinguishable and distinct from other phases. During the growth, a particular focus is put on the transition between the vapor and solid phases. The main goal of the thermodynamic considerations is to investigate the relationship between compositions of various phases in a reactor at equilibrium and constant temperature T and pressure P of the system. Here, *equilibrium* is defined as the state where the Gibbs free energy per mole, G:

$$G = H - TS, \tag{2.1}$$

is minimal, where S is entropy and H – enthalpy defined in terms of internal energy E, and volume V:

$$H = E + PV. \tag{2.2}$$

For a two-phase (α, β) system, the total free energy is $G' = G'_\alpha + G'_\beta$, where prime stands for the total free energy as opposed to the free energy per mole G. Because in equilibrium G' is minimal, its partial derivative must be zero. Therefore, if $\mathrm{d}n_i$ is an infinitesimally small number of moles of component i, then moving it between the two phases causes no change in G':

$$\left(\frac{\partial G'}{\partial n_i}\right)^{\alpha}_{T,P,n_j} - \left(\frac{\partial G'}{\partial n_i}\right)^{\beta}_{T,P,n_j} = 0. \tag{2.3}$$

This equation defines the chemical potential μ:

$$\mu_i \equiv \left(\frac{\partial G'}{\partial n_i}\right)_{T,P,n_j}, \tag{2.4}$$

and the equilibrium condition can be expressed in terms of chemical potential as

$$\mu_i^\alpha = \mu_i^\beta. \tag{2.5}$$

The thermodynamic approach to the MOVPE process modeling investigates the conditions at which this equation is fulfilled. It can be shown that for an ideal gas mixture,

$$\mu_i = \mu_i^0 + RT \ln\left(\frac{p_i}{p_i^0}\right), \tag{2.6}$$

where R is the ideal gas constant, "0" is a superscript denoting the value for the standard state (usually pure component i), and $p_i \equiv x_i P$ is the partial pressure with x_i being the mole fraction. For an ideal liquid or solid solution $p_i/{p_i}^0$ can be replaced in Eq. (2.6) by $x_i/{x_i}^0$. The standard state is pure, ${x_i}^0 = 1$, and for a non-ideal solution, x_i is replaced by the activity $a_i \equiv x_i \gamma_i$, where γ_i is the non-ideality factor. Finally, we can write Eq. (2.6) for a non-ideal solution as

$$\mu_i = \mu_i^0 + RT \ln a_i = \mu_i^0 + RT \ln(x_i \gamma_i). \tag{2.7}$$

Driving force for epitaxy The thermodynamic driving force of the growth is to restore the equilibrium between phases α and β, accordingly to Eq. (2.5). When the system is not at equilibrium, this restoring force can be expressed using Eq. (2.7) as

$$\Delta\mu = \mu^\beta - \mu^\alpha = \mu^{\beta,0} + RT \ln a_e^\beta - \mu^{\alpha,0} - RT \ln a_e^\alpha = RT \ln\left(\frac{a_e^\alpha a^\beta}{a^\alpha a_e^\beta}\right). \tag{2.8}$$

The epitaxial growth can be seen as an intentional preparation of the system in non-equilibrium conditions so that it would be forced to produce the solid desired.

Equilibrium at the solid-vapor interface In practice, the GRs are much slower than determined from thermodynamical considerations. Kinetics (surface reaction rates) and mass transport through the gas phase are too slow to allow for arriving at equilibrium throughout the system at all times.

Figure 2.2 schematically shows changes in the chemical potential $\Delta\mu$ during the epitaxial growth, acting as its thermodynamic driving force. The general case shown in Figure 2.2a outlines that the drop in $\Delta\mu$ in each step of the sequence is required to keep all mass fluxes equal (for the mass conservation). $\Delta\mu_D$ represents the drop in chemical potential during diffusion and $\Delta\mu_S$ – during surface reactions. To overcome the near-equilibrium conditions at the growing solid surface, making the interface kinetics much more rapid than the diffusion kinetics is often beneficial. When both processes should proceed at the same rate with $\Delta\mu_S \ll \Delta\mu_D$, the GR is determined by the products diffusion rate, and so is called mass-transport-limited, or, equivalently, diffusion-limited growth. The diffusion-limited growth conditions are often desired for the growth of high-quality epitaxial layers, and the changes in $\Delta\mu$ are compared in Figure 2.2b with the general case. In this case, the *boundary layer* is seen as the region over which the velocity components and temperature change rapidly.

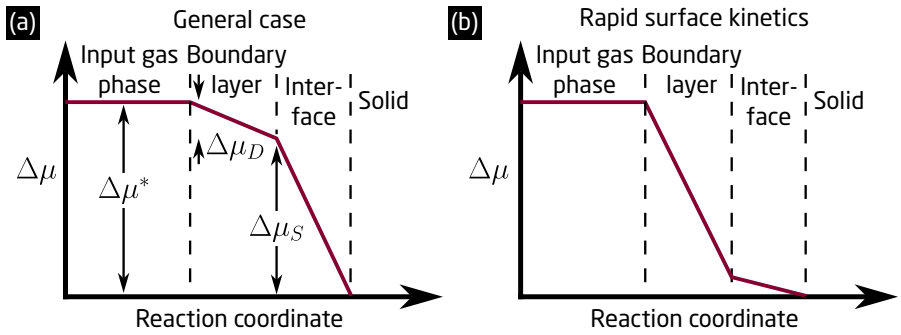

Figure 2.2: Change in the chemical potential $\Delta\mu$ of the input gas phase as a function of the reaction coordinate, **a**, the general case, **b**, for the mass-transport-limited, or, equivalently, diffusion-limited growth (when surface kinetics is rapid). $\Delta\mu_D$ – drop in chemical potential during diffusion, $\Delta\mu_S$ – during surface reactions.

Physical processes at the surface

Thermodynamics reviewed in the previous section describes what happens during growth. It drives all processes outlined in Box 2. However, this approach to understanding MOVPE is certainly insufficient without the knowledge of the *rates* of various processes and it is the kinetics that handles this. It describes the processes that transform the molecules from the vapor phase into the growing crystal which can be highly complex. The growth modeling includes the appearance and evolution of atomic terraces, kinks, adatoms, islands, and advacancy clusters at the growing semiconductor surface. They are schematically shown in Fig. 2.3

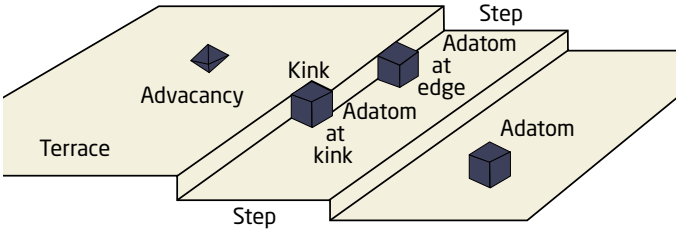

Figure 2.3: Scheme of the physical processes occurring on the crystal surface during epitaxial growth.

Modeling of these processes is supported by data acquired experimentally, for example with AFM, or by the advanced *in-situ* observations with employed techniques such as grazing incidence X-ray scattering (GIXS)[2] or scanning tunneling microscope (STM), which both allow recording the surface reconstruction. This is important as it has the first-order effect on all physical phenomena occurring during the growth, including adatom adsorption and desorption, surface diffusion, and incorporation of adatoms into the solid. Additionally, the STM was used to observe the pyrolysis of precursors or even the motion of adatoms at elevated temperatures.

The most important atomic-level growth processes are:

- adsorption and desorption,
- adatom motion,
- step motion,
- surfactant effects[3].

[2]Requires synchrotron-based X-ray source.

[3]The collection of impurities at the surface due to the low solubility of an element (of relatively low volatility) in the growing lattice, resulting in its rejection.

Kinetics

Kinetics is very useful in providing information on the time required to reach equilibrium, the actual steps involved in minimizing the energy, or the rates of the consecutive processes occurring during the transition from the vapor to the solid phase. It is not possible to resolve these issues with thermodynamics, which is concerned with the changes in the system energy but does not inform about how it is minimized. Therefore, it limits the growth process. Using thermodynamics, one can learn more about the growth driving force, maximum GR, and the number and compositions of the equilibrium phases (including ordered phases) in bulk or on the surface, but the rates of phase transitions are covered by the kinetics.

Theory of absolute reaction rates The theory of absolute reaction rates sufficiently describes the rates of chemical reactions k. The assumption here is that the reaction proceeds with creating an intermediary *activated complex*. As MOVPE is an exothermic reaction, reactants lower their energy. However, the creation of activated (excited) complexes requires additional energy. This is shown schematically in Fig. 2.4, where E_A and $E_A{}^*$ are activation energies for forward and reverse reactions. Their reaction rate constant k can be expressed in the form of the Arrhenius equation,

$$k = A \exp\left(\frac{-E_A}{RT}\right), \tag{2.9}$$

where A is the pre-exponential factor. Figure 2.4 indicates that $E_A \neq E_A{}^*$: they differ by the thermodynamic enthalpy difference from initial to final states,

$$\Delta H = E_A - E_A^*. \tag{2.10}$$

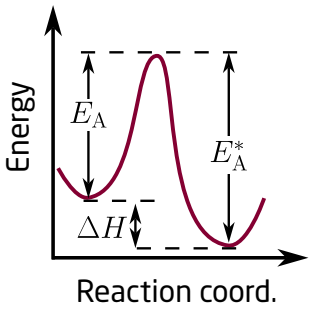

Figure 2.4: Scheme of a reaction with intermediary activated complex.

Then, the equilibrium condition Eq. (2.5) can be re-defined, taking into account that at equilibrium, the rates of the forward and reverse reactions are equal, so that

$$n_i k = n_f k^*, \tag{2.11}$$

as the reaction rate is the product of concentration n_i, n_f and rate constant k, k^*, for initial and final states, respectively.

Different reactions possible Reactions considered here that occur during the MOVPE growth can be divided with respect to the place where they occur into

- **homogeneous**, occurring entirely in the gas phase,
- **heterogeneous**, occurring at a solid surface,

and with respect to the number of species that take part in the reaction into

- **uni-molecular**, a process undergone by an energetically activated species without interaction with other ones,
- **bi-molecular**, a process requiring the collision of two species, producing an activated complex that may undergo a uni-molecular reaction.

Homogeneous reactions The most common type of homogeneous, uni-molecular reaction involved in the pyrolysis of $M(CH_3)_n$ precursors, where M stands for a metal atom, is homolysis, producing methyl radicals. Other possible uni-molecular reactions are β-elimination-type, such as a β-alkyl elimination reaction – for example, $MR_nC_4H_9 = MR_nCH_3 + C_3H_6$, occurring typically on the surface.

Bi-molecular reactions are also crucial for the MOVPE growth. For example, the amount of carbon unintentionally incorporated into the solid is determined mainly by the bi-molecular reactions involving the CH_3 radicals produced during homolysis of the $M(CH_3)_3$ precursors.

Heterogeneous reactions They play a dominant role during growth and are initiated by the adsorption of a molecule onto a surface. Hence, the rate of a uni-molecular heterogeneous reaction is directly proportional to the concentration of a reacting species i, which in turn depends linearly on its partial pressure p_i.

The reaction rates are higher for heterogeneous reactions due to the presence of a surface that weakens the molecular bonds. Therefore, the pre-exponential factors A and E_A in Eq. (2.9) are lower.

Scheme of the growth reactions The above considerations can be summarized by a diagram illustrating subsequent reactions and processes involved in incorporating molecule A into the solid, shown in Fig. 2.5 for only one source molecule, AR_n.

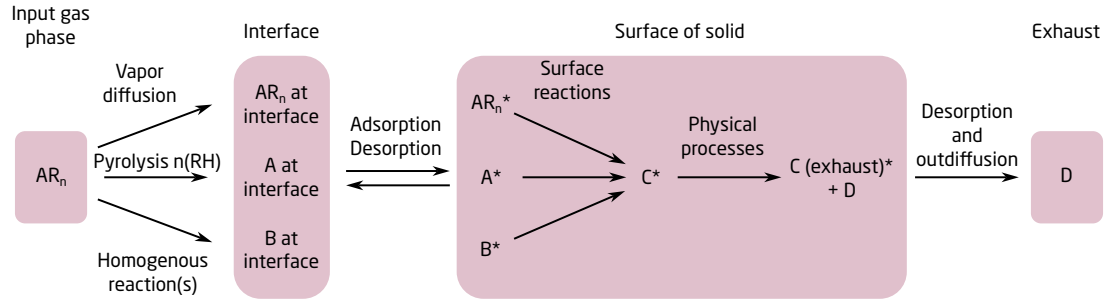

Figure 2.5: Steps involved in the reaction of the organometallic molecule AR_n, resulting in the incorporation of molecule A into the solid. The physical surface processes are, e. g., surface diffusion, attachment at steps and kinks, and incorporation into bulk. An asterisk '*' marks the species adsorbed at the surface.

The reactions involved are homogeneous and heterogeneous, and the most important reaction for both III and V groups is the pyrolysis of molecules. The fundamental pyrolysis reactions for cation source molecules (of the type MR_n, where R = CH_3) are

1. homolytic fission: $M(CH_3)_n = M(CH_3)_{n-1} + CH_3$,
2. hydrogenolysis: $H_2 + M(CH_3)_n = CH_4 + HM(CH_3)_{n-1}$,
3. radical reactions[4], such as: $CH_3 + M(CH_3)_n = CH_4 + CH_2M(CH_3)_{n-1}$, and $H + M(CH_3)_n = CH_4 + M(CH_3)_{n-1}$.

The predominant type of reaction in the case where R is ethyl, propyl, or butyl, is:

4. β-elimination: $MR_n = HMR_{n-1}$ + alkene.

In reality, the situation and reactions involved are far more complex, and many essential pyrolysis reactions are still poorly understood. Additionally, there is a lot of species present simultaneously in the reactor, and their mutual interaction is the source of the following complications:

- Cation and anion precursors can interact in the vapor phase, forming adduct compounds prior to pyrolysis.
- Radicals produced by the pyrolysis of one precursor may attack molecules of another precursor.
- The extrapolation of pyrolysis data for individual precursors to the actual growth reactions when many cations are present simultaneously is non-trivial[5].

[4] As bi-molecular, the radical reactions are more likely to be important for high input cation alkyl concentrations.

[5] For example, the cation alkyls can exchange ligands in the vapor phase. This introduces some novel precursor molecules taking part in the growth.

Apart from these effects that emerge from the multitude of reactants, there are also effects connected with the departure from the ideal growth reactor and homogeneous environment:

- The actual geometry of the reactor and the flow conditions change the residence time of precursors in hot regions of the reactor, affecting the pyrolysis. As a significant temperature gradient is inherently present in the reactors, determining rate constants correctly is impossible.
- Change of the system pressure has two crucial consequences. Generally, it affects all the reaction rates, and specifically for the homogeneous reactions, it changes the number of available species in the vapor phase and hence influences the rates.

As a result, the assumption that the growth can be understood as a superposition of individual pyrolysis reactions, which was an initial approach to the MOVPE growth, is no longer expected to be relevant for the actual growth reactions.

As an example, the pyrolysis of TMIn proceeds by the homolytic fission:

$$\begin{aligned} \mathrm{In(CH_3)_3} &\rightarrow \mathrm{In(CH_3)_2 + CH_3} \\ \mathrm{In(CH_3)_2} &\rightarrow \mathrm{In(CH_3) + CH_3} \\ n - \mathrm{In(CH_3)} &\rightarrow \mathrm{[In(CH_3)]_n(s)} \\ \mathrm{In(CH_3)} &\rightarrow \mathrm{In + CH_3} \end{aligned} \tag{2.12}$$

However, this reaction proceeds differently depending on the carrier gas, with existing reports for toluene, H_2, He_2, and deuterium (D_2).

2.2 Epitaxial growth of quantum dots

After establishing the fundamentals of the MOVPE growth in the previous section, the focus is now changed to the physical phenomena governing the nucleation and growth of QDs in the self-assembled mode. As the self-organized QDs are known to have superior optical properties and allow fulfilling the QIP requirements for a source of the non-classical states of light, the progress in the area of semiconductor-based QIP requires the understanding of the physics governing the spontaneous formation of nanostructures. The discussion is general and based on the considerations of energy and the thermodynamic force of the system [184, 185].

Thermodynamics and kinetics of quantum dot growth

The strain-driven formation of QDs, especially in the S-K growth mode, is at the center of attention in this section. As explained in the previous paragraphs, surface thermodynamics during the growth plays a pivotal role in determining equilibrium conditions and hence QD size and shape in the MOVPE growth. The growth of QDs can be modeled using various theoretical techniques, such as first-principles calculations – density functional theory (DFT), molecular dynamics, or Monte Carlo (MC), but also the continuum description.

The free energies and surface stress conditions of the surfaces and interfaces that are being formed can be calculated in DFT approach using realistic atomic models. This is crucial due to the surface reconstruction happening during growth. This combination of the DFT and detailed thermodynamics of the surface atomic structure is known as *ab initio* thermodynamics. Here, the potential-energy surfaces are considered for the relevant molecular processes with interfaces including a WL, QD side facets, and a QD-cap. This allows for calculating the energy maxima that define the preferred adsorption sites for atoms (both III and V groups) and the energy barriers that determine rates of diffusion, desorption, and nucleation of islands.

However, a *hybrid approach* has been introduced to calculate the factors that govern the size and shapes of QDs. On the one hand, the continuum elasticity theory considers the energy change induced by the long-range strain fields. On the other hand, strain relaxation, for example, is modeled in the finite-element method. The continuum theories can be applied as the structural

and elastic properties of QDs are unaffected by quantum size effects. On the contrary, an average QD is composed of 10^4-10^5 atoms, and the classical elasticity theory can be used to describe the pseudomorphic growth of InAs QDs on lattice-mismatched substrates, basing on the elastic energy both in the QD and in the substrate. The equilibrium QD shape has been determined using the hybrid approach for, e. g., InAs islands on GaAs(001) [186, 187], and for InP/GaP(001) [188].

Equilibrium theory of heteroepitaxy

The assumption that the heteroepitaxial system evolves toward a *surface equilibrium* is fundamental for the equilibrium theory of heteroepitaxy. Experimentally, this assumption is obtained by introducing the growth interruption or annealing to allow the system to approach equilibrium.[6] Traditionally, three *growth modes* are distinguished using the equilibrium theory [189]:

- Frank-van der Merwe (F-M), or layer-by-layer,
- Volmer-Weber (V-W), or 3D island growth,
- Stranski-Krastanow, where a flat WL is formed first and 3D islands are formed when the WL reaches a critical thickness, h_c [190].

The growth mode can be determined by considering changes in chemical potentials of the first few deposited layers or can be defined by the interplay between the interface energy γ_{12} and surface energies for the substrate, γ_1, and for the epilayer material, γ_2 [185]. If $\gamma_2+\gamma_{12} \leq \gamma_1$, the reduction of the substrate's surface is preferential, and the epilayer wets the substrate (F-M). The transition to the V-W mode can be driven by the change in $\gamma_2+\gamma_{12}$ and is realized if $\gamma_2+\gamma_{12} > \gamma_1$. Finally, if the initial layer-by-layer growth results in the accumulation of strain energy W_{2D} as the layer gets thicker, the energy can be lowered by the formation of isolated islands that help in the strain relaxation (S-K mode), which is described in the following section. The energy condition is again $\gamma_2+\gamma_{12} < \gamma_1$, as for F-M mode. Still, additional conditions require preferential strain relations between the epilayer and the substrate. The growth modes are summarized in Fig. 2.6a.

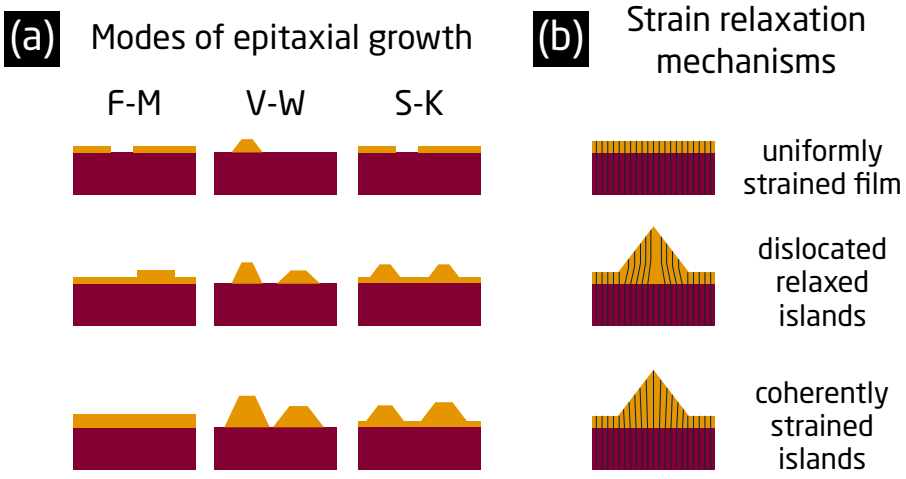

Figure 2.6: **a**, Diagrams of the three growth modes for heteroepitaxial systems: Frank-van der Merwe (F-M), Volmer-Weber (V-W), and Stranski-Krastanow (S-K). **b**, Elastic strain relaxation during S-K growth, with lines symbolizing the lattice planes. Based on Ref. [186].

The strain considerations are crucial for the description of the system, as all heteroepitaxial processes induce the misfit strain at the interface between the substrate and epilayer, given by the

[6] This is possible provided that the evaporation of atoms and their intermixing/segregation is negligible.

mismatch ϵ_0 between the lattice parameters for the substrate, a_1, and the epilayer, a_2:

$$\epsilon_0 = \frac{a_2 - a_1}{a_1}. \tag{2.13}$$

Stranski-Krastanow growth mode

The S-K growth mode can be considered the most popular for obtaining QDs in semiconductor systems of major interest, including Ge/Si, InAs/GaAs, and InAs/InP. When the amount of deposited material is below 1 ML (monolayer), the WL is formed as an array of 1 ML-high 2D islands that coalesce and wet the substrate. The associated strain energy increases rapidly as the WL height increases. In short, if the amount of material exceeds the critical thickness h_c, strongly dependent on the lattice mismatch ϵ_0, the strain relaxation can preferentially occur via the formation of 3D islands. This section describes this step in more detail.

The island formation can occur in either a *coherent* or *dislocated* fashion which is crucial for the structural and optical quality of the island. In the dislocated islands, the strain is relieved by the formation of interfacial misfit dislocations. It was initially believed that the islands indeed relax the elastic strain solely in this manner (see Fig. 2.6b for the comparison of possible strain relaxation schemes), however, early experiments on InAs/GaAs [191] and Ge/Si(100) QDs [192] have evidenced the formation of coherently-strained (dislocation-free) islands, of great importance for the minimization of nonradiative recombination centers and hence maximization of the quantum internal efficiency of QDs. This indicates the presence of an effective, coherent strain relaxation mechanism in QDs, which can be explained based on the Asaro-Tiller-Grinfel'd (ATG) instability[7] of a strained layer against a long-wavelength corrugation of the surface.

Elastic strain considerations

The central mechanism for the growth transition and QDs formation from the WL in the S-K mode is the elastic strain relaxation. Understanding this process is crucial for effectively tuning the QD properties.

First, the elastic strain energy W_{2D} of a 2D layer of thickness h and surface area S can be defined as [195]:

$$W_{2D} = \frac{E_Y}{1-\nu}\epsilon_0^2 Sh, \tag{2.14}$$

where E_Y is Young's modulus and ν is the Poisson's ratio of the deposited material. Notably, the elastic energy scales linearly with h. For small h, the layer is pseudomorphic, i. e., it is uniformly strained, and conforms to the substrate crystal lattice. It is therefore called a *wetting layer*. If the transition to the 3D growth is not possible, the only way to relax the elastic energy $W_{2D} \propto h$ is by introducing misfit dislocations (see Fig. 2.6b) as the substrate lattice constant can be matched by the growing layer only by plastic deformations.

However, suppose the deposited material can change its organization and form 3D islands. In that case, the energy cost of new free lateral surfaces can be a way to minimize the accumulated elastic energy and so the system's total energy. Yet, creating the lateral facets and some work against the wetting force in a 2D layer is necessary for the stress-driven nucleation of 3D islands. Therefore, the emergence of islands has some analogy to the reaction with activation energy (cf. Fig. 2.4), where the reaction or phase transition is possible only with additional energy to drive the system from the metastable state.

As a result, it is expected that the S-K islands are not energetically favored until the 2D WL thickness surpasses a certain quasi-equilibrium value, h_{eq}. Indeed, the island nucleation should have a barrier character as the process includes a competition between an energetically beneficial process of elastic stress relaxation and an energetically unfavorable faceting in the presence of a wetting force. Each heteroepitaxial system with a sufficient lattice mismatch (typically, at $\epsilon_0 \geq 2\,\%$) theoretically tends to form islands which, as long as they are small enough, remain dislocation-free.

[7] The description of the ATG instability was derived originally for stress-corrosion cracking [193, 194].

In other words, nucleation of QDs is possible when a particular level of metastability is acquired by the WL by increasing its thickness so that $h > h_{eq}$, and finally, at the critical thickness $h_c > h_{eq}$, the accumulated stress is large enough to cause an abrupt 2D-3D transition, what reflects the barrier character of the island formation.

Quantum dot formation energy

This subsection builds upon the elastic strain considerations and gives a more detailed treatment of the energy conditions crucial for forming strained self-assembled 3D islands. Their total formation energy can be separated into the energy cost of forming side facets and edges E_{surf}, and the energy gain from partial strain relief. To minimize the formation energy, defined in Eq. (2.15), it is crucial to determine the shape of an island for a given amount of material (N atoms), assuming the thermal equilibrium [196]:

$$E(N) = -\Delta E_{\text{elast}} N + \Delta E_{\text{surf}} N^{2/3} + \Delta E_{\text{edges}} N^{1/3} - \Delta E_{\text{elast}}^{\text{edges}} N^{1/3} \ln N^{1/3}, \tag{2.15}$$

where:

- $-\Delta E_{\text{elast}} N$ is the energy of the volume elastic relaxation due to the transition of the material from a highly strained flat WL to a partially relaxed 3D strained island. This term is always **negative**.
- $\Delta E_{\text{surf}} N^{2/3}$ is the change of the total surface energy of the system due to the formation of tilted facets of the island and the disappearance of the WL surface beneath the island. This term can be either **positive or negative**. It is calculated applying DFT.
- $\Delta E_{\text{edges}} N^{1/3}$ is the short-range contribution to the energy of the edges. This term is always **positive**.
- $-\Delta E_{\text{elast}}^{\text{edges}} N^{1/3} \ln N^{1/3}$ is the energy of the elastic relaxation due to surface stress tensor discontinuity at the edges. This term is always **negative**.

As the sign of the total surface energy ΔE_{surf} can change during growth, the parameter α defined as $\alpha = \sqrt{e}\Delta E_{\text{surf}}/\Delta E_{\text{elast}}^{\text{edges}}$ [196] is crucial for the determination of optimal island size, N^3, by minimization of the energy per atom, $E(N)/N$. It can be shown [197] that as long as $\alpha < 1$, the finite size of the islands N_0^3 can be determined (i. e., $E(N)/N$ has a minimum at N_0). However, if $\alpha > 1$, the $E(N)/N$ function does not have a minimum, and the system is unstable: there is a thermodynamic driving force toward Ostwald ripening – indefinite growth of islands, prone to structural defects, resulting ultimately in the accumulation of material in a single and large island in theory, and a few large islands in reality. The underlying mechanism is the elastic interaction between islands mediated by the substrate, which becomes an essential contribution to $E(N)/N$ if the density of islands increases.

Super- and subcritical Stranski-Krastanow quantum dots

As explained in the previous subsection, the elastic stress accumulated in the WL is the driving factor for the 2D-3D transition, and the thickness at which the layer enters into the metastable region is h_{eq}. As a result, it is reasonable to suppose that the measure of WL metastability of thickness h is given by the superstress ζ, an analog of supersaturation:

$$\zeta = h/h_{eq} - 1. \tag{2.16}$$

Formation of islands can happen only when $\zeta > 1$. Figure 2.7 presents a more detailed scheme of consecutive stages of the S-K nucleation, presenting the routes for the super- and subcritical QDs. The creation of a 2D WL of equilibrium thickness h_{eq} is the first stage. Continued layer growth in the range $h_{eq} < h < h_c$ creates metastability with $\zeta > 1$, which however cannot initiate island nucleation under the deposition flux. Only reaching the critical thickness h_c can trigger the rapid

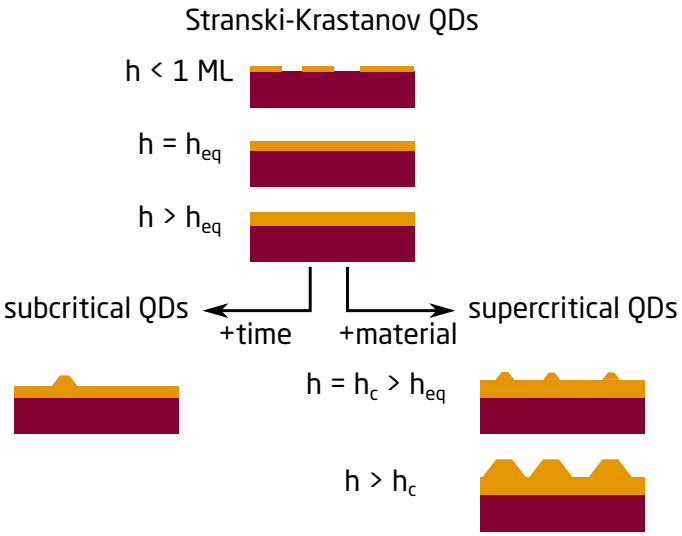

Figure 2.7: Qualitative representation of the QD formation stages in the S-K mode. Initially deposited atoms form 1 ML-high 2D islands that merge into the equilibrium WL. The layer height h increases until it reaches the equilibrium value h_{eq}, followed by the 2D growth between h_{eq} and h_c where the WL is metastable. The metastability provides different routes for the QD nucleation. Left: After sufficient exposition time (growth interruption), the layer can reorganize itself into the ensemble of low-density *subcritical* QDs by consuming the WL material. Right: Rapid nucleation stage occurs after passing the h_c (*supercritical* QDs), followed by the regular growth of islands. Based on Ref. [195].

nucleation of QDs in the supercritical case. The stress-driven diffusion from the WL to islands is the primary kinetic channel influencing the island development rate.

However, in the subcritical regime, the deposition flux is not constant, and a growth interruption (GI) is introduced. Generally, nothing prevents the formation of QDs before reaching h_c, as the WL is metastable already after reaching h_{eq}. For example, in the III-V systems exposing the surface to arsenic flux and waiting long enough can be sufficient for forming QDs. It is only the initial level of metastability that is insufficient for immediate nucleation. As the nucleation happens before reaching h_c, the QDs are called *subcritical*. Notably, the density of subcritical QDs is much lower and growth rate much slower compared to supercritical QDs, which is a very appealing route for growing QDs for SPS applications.

It is important to reiterate the difference between the equilibrium thickness h_{eq} and the critical thickness h_c:

- As long as the deposited material thickness $h < h_{eq}$, the surface and wetting energy dominate over the elastic stress energy; hence the stress-driven nucleation is impossible.
- When $h_{eq} < h < h_c$, the elastic energy relaxation exceeds the surface energy, and the WL becomes metastable. However, the island formation cannot be initiated immediately as metastability is insufficient, requiring a specific exposure time to observe it. Subcritical QDs can be obtained.
- The intense islanding can be initiated only for $h \approx h_c$ (supercritical QDs), having a kinetic origin.

Control of the strain-driven QD growth by external parameters

The crystallographic conditions of a given system determine the geometrical shape of islands, however, it can be influenced by the deposition conditions. It is assumed that in III-V material systems,

there are five external growth parameters of major importance for controlling the QDs properties [195]:

- temperature T,
- flow rate F,
- thickness of deposited material H_0,
- the ratio of fluxes (V/III ratio).
- GI conditions, mostly time (for subcritical QDs),

The V/III ratio changes the energy conditions on the surface, as well as the kinetics of growth.

Theoretical modeling of the QD nucleation summarized in Ref. [195] leads to the conclusion that in the supercritical regime, temperature T and flow rate F crucially influence the island density ρ,

$$\rho \propto F^{3/2} T^{5/2} \exp\left(\frac{3E_D}{2k_B T}\right), \tag{2.17}$$

where E_D is the characteristic activation energy for the stress-driven diffusion (the characteristic diffusion temperature $T_D = E_D/k_B$ is always much larger than T). This relationship holds if the island shape remains temperature-independent during growth, which is not always true. Eq. (2.17) shows the general tendency that ρ increases with the flow rate F and decreases with the temperature in the supercritical deposition regime. This can be explained by observing that more nucleation centers are created on the surface by an increased deposition rate (dependent on F) at a given temperature, which increases the ρ. Secondly, at a given F and deposition thickness, the solid diffusion in the WL is faster at elevated temperatures so that QDs grow larger while ρ must decrease as the thickness of deposited material fixes their total volume. Importantly, the dependence given by Eq. (2.17) is much less dependent on the system thermodynamics and has an essentially **kinetic** origin.

For the subcritical QDs, their nucleation takes more time compared to supercritical QDs, which induces easier access to process control during the GI by altering the conditions. The density after an infinite nucleation time can be expressed as

$$\rho \propto \exp\left(-\frac{3}{5}\frac{T_e}{T(H_0/h_{eq}-1)^2}\right), \tag{2.18}$$

where T_e is a quasi-equilibrium temperature characterizing the energetics of a given heteroepitaxial system. The maximum lateral size of islands R_g can be calculated as

$$R_g \propto (H_0 - h_{eq})^{1/3} \rho^{1/3}. \tag{2.19}$$

Therefore, the density ρ of subcritical QDs exponentially increases with deposition thickness H_0 and the substrate temperature T, as opposed to the supercritical QDs, while R_g increases with the deposition thickness H_0. These dependencies are typical for the **thermodynamically**-controlled nucleation process. Importantly, stopping the nucleation faster than after the characteristic QD nucleation time (setting a shorter GI time) lowers the density ρ and the mean size of QDs, as compared to R_g. On the other hand, as the nucleation has a continuous character, the QD-to-QD difference in growth duration is considerable: allowing the nucleation process to complete results in a large size dispersion of the QD ensemble.

Droplet epitaxy

Although the coherent strain relaxation and small size distribution of S-K QDs together with the simplicity and robustness of the growth have led to their large dominance (see discussion in Section 1.2 and Refs. [2, 60, 198]), a few drawbacks of S-K growth must be mentioned here. The most important include [107]:

- the QDs are typically elongated in InAs/GaAs and InAs/InP material systems,
- the QD geometry and surface density are difficult to be controlled separately,

- the range of emission frequencies accessible with S-K QDs is limited due to only a few possible combinations of material composition,
- island shapes have a limited range, which is mostly determined by the energetically favored facets and QD size.

Additionally, the presence of the WL results in a more effective escape of carriers from QDs by lowering their confining potential and acting against the emission at elevated temperatures[8].

The first drawback, the in-plane elongation of QDs, severely limits their usability as entangled photon pair sources. The elongation roots in an anisotropic surface diffusion of ad-atoms along different crystallographic directions during growth. This in-plane asymmetry of QDs induces the FSS of X states, a fundamental obstacle towards reaching polarization entanglement by employing the XX-X cascade emission. Hence, to develop a QD-based source that generates polarization-entangled photon pairs, the FSS must be minimized, either during growth [199], by the post-growth tuning using external fields (magnetic [57], electric [200], or strain [201]), using the optical Stark effect [202], or by shifting to another growth paradigm.

Therefore, already in 1991, an alternative growth mode was proposed [203] – *droplet epitaxy*, which exploits the controlled crystallization of group-III metal nanodroplets into III-V QDs. The growth procedure can be described as follows:

1. **Deposition and assembly of metallic droplets.** The deposition of group-III metal adatoms leads to the spontaneous formation of nanometer-scale droplets, which follow the V-W growth mode. The temperature and material coverage were identified as the tuning knobs to change fairly independently the density of droplets and their size [76].
2. **Crystallization of droplets into QDs.** It results from annealing the group-III droplets in group-V ambient. At this step, the QD shape and topology can be controlled [204].

The resulting QD growth is more controllable as it is not strain-driven. Importantly, it is compatible with the site-selective QD nucleation approach, as explored for example in P. Holewa *et al.*, *Optical Properties of Site-Selectively Grown InAs/InP Quantum Dots with Predefined Positioning by Block Copolymer Lithography*, **Materials**, 14, 391 (2021)[9], where the emphasis was placed on the fabrication and investigation of a high-density uniform array of InAs/InP QDs, grown in the openings etched in InP using a block-copolymer mask. The site-selective approach is particularly interesting as an alternative for the post-growth QD positioning approaches described in Section 1.3.

Symmetrization of droplet epitaxy quantum dots

Different nucleation and growth mechanisms of S-K and DE QDs result in higher symmetry of the latter, especially in the InAs/InP case [76], where almost unavoidable elongation of S-K QDs, resulting in the formation of quantum dashes (QDashes), was an issue for a long time. For a comprehensive review, see the introduction in P. Holewa *et al.*, *Inter-dash coupling within dense ensembles of quantum dashes: comparison of InAs/(In,Al,Ga)As/InP and InAs/(In,Al)As/InP systems*, **Physical Review Applied**, 17, 5 (2022)[10]. Indeed, the demonstration of entangled photon pairs emission for InAs/InP QDs at C-band was demonstrated for the first time for DE QDs [59].

The QD symmetry is, however, often inherited from the substrate. Employing high-Miller index substrates, such as (111)A- [205] and (111)B-oriented GaAs [199], or InP(111)A with C_{3v} symmetry [109, 206] is an impractical solution: although the (111) substrate orientation is appealing for its high in-plane symmetry, the relaxation of a strained III-V semiconductor epilayer deposited on the (111)-oriented substrate does not result in the formation of coherent 3D islands. Instead, the relaxation immediately proceeds through the generation of misfit dislocations at the substrate-QD interface [207] which is very problematic for the S-K growth. High-symmetry substrates are also much more expensive than the standard (001) ones.

[8] See also the discussion in Section 2.3 for the comments on temperature-induced effects.
[9] This article is not included in this thesis.
[10] This article is not included in this thesis.

Although the FSS of DE InAs/InP QDs is statistically lower than for S-K QDs [76], it is still at a moderate level. Recent studies reported the average FSS of (60 ± 38) µeV even for GaAs/AlGaAs QDs [208]. That fact poses challenges for this QD epitaxy route, otherwise very promising as resulting in *ideal sources of entangled photon pairs*, according to Ref. [209].

Annealing of droplet epitaxy QDs, or local droplet etching

A modification of the DE scheme has been proposed for the GaAs-based QDs, known as the local droplet etching (LDE) [210, 211]. In this approach, the QD nucleation sites are prepared in the form of openings in the substrate due to the surface etching by symmetric metallic droplets. In the GaAs system, the substrate etching proceeds due to the instability of the Ga-rich interface between the substrate and the Ga droplet, the so-called *nanohole drilling* mechanism [210]. The fabricated nanoholes have high in-plane symmetry and are ready to be filled with the QD material. The QDs fabricated in this way have the symmetry imposed by the nanohole and hence have very low FSS values, including structures grown on industry-compatible (001) substrates [212, 213]. The recent applications of this scheme include the demonstration of the quantum communication schemes based on the entangled photon pairs [53, 214].

The nanohole drilling mechanism explains well what happens in GaAs- or AlGaAs-based QD systems but fails for the InP one. As recently shown by Sala et al. [111] and in P. Holewa *et al.*, *Droplet epitaxy symmetric InAs/InP quantum dots for quantum emission in the third telecom window: morphology, optical and electronic properties*, **Nanophotonics**, 11, 8 (2022)[11], the application of conditions that are expected to result in the droplet etching in the InP system causes *annealing* of QDs instead. Additionally, the local etching of asymmetric pits around the QDs is observed rather than metallic droplet removal. However, as reported in P. Holewa *et al.*, *Droplet epitaxy symmetric InAs/InP quantum dots for quantum emission in the third telecom window: morphology, optical and electronic properties*, **Nanophotonics**, 11, 8 (2022), the QDs annealing results in their significant symmetrization while preserving the emission at the C-band and low surface density.

2.3 Physics of Coulomb-correlated excitations in quantum dots

This section covers theoretical considerations of excitons confined in QD potential and explains how this fact modifies the properties of the excitation. After short remarks regarding characteristics of the QD spatial confinement, the description of charge carriers' wavefunction properties is given, illustrated by single particle calculation methods. As this thesis focuses on experimental investigations, the continuum and atomistic pseudopotential methods are briefly introduced, and their most important properties and results are outlined. After the information on the charge wavefunctions calculations is presented, the wavefunctions of an exciton and other Coulomb-correlated excitations can be constructed. The relevant concepts are introduced, followed by a more subtle effect of the exchange interaction (EI). Finally, the interaction with light is covered by considerations of the radiative recombination and the selection rules.

Spatial confinement

The precondition to the following considerations is the quantization of energy levels for a carrier confined to the QD potential. It occurs when the QD size is comparable with de Broglie wavelength of the carrier, $\lambda_B = h/\sqrt{2m_e k_B T}$, where m_e is an effective mass of the confined particle. At low temperatures, $\lambda_B = 10\text{-}100\,\text{nm}$, and the energy levels in a QD are quantized.

In a QD, an electron and a hole are confined to the same spatial area. Therefore, except for spatial quantization, the Coulomb correlations between the charged particles become very important. The strong electrostatic interaction correlates electrons and holes that form Coulomb-correlated excitations, or *excitonic complexes*: exciton (Coulomb-correlated electron-hole pair),

[11] This article is included in this thesis, p. 127.

biexciton (two excitons), charged exciton, or trion (an exciton with a Coulomb-bound additional carrier, either a hole or an electron). Alternative names for a charged exciton, or trion (CX) are positively-charged exciton (X^+) and negatively-charged exciton (X^-), dependent on the sign of an additional carrier. All excitonic complexes have well-defined energy levels, so their radiative recombination can be observed as isolated and narrow emission lines in the optical spectrum.

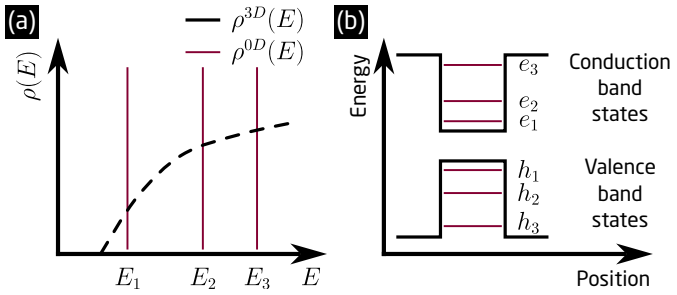

Figure 2.8: **a**, Density of states for a QD, $\rho^{0D}(E)$ (lines), and for bulk material, $\rho^{3D}(E)$ (dashed line). **b**, Scheme of the conduction and valence states for a model QD with marked electron (e_1, e_2, e_3) and hole (h_1, h_2, h_3) energy levels.

The density of states function $\rho(E)$ is defined as the number N of energy states per unit energy E,

$$\rho(E) = \frac{\mathrm{d}N}{\mathrm{d}E}. \tag{2.20}$$

The schemes of the $\rho(E)$ function for a QD, $\rho^{0D}(E)$, and for a bulk structure, $\rho^{3D}(E)$, are shown in Fig. 2.8a. For the bulk structure the $\rho^{3D}(E)$ is continuous,

$$\rho^{3D}(E) = \frac{1}{2\pi^2}\left(\frac{2m_e}{\hbar^2}\right)^{3/2}\sqrt{E}, \tag{2.21}$$

where $\hbar$ is the reduced Planck constant, so that $\rho^{3D}(E) \propto \sqrt{E}$. The spatial quantization in a QD leads to the discrete density of states, which can be described by a series of Dirac δ functions:

$$\rho^{0D}(E) = \sum_{i=1}^{n} \delta(E - E_i). \tag{2.22}$$

The QD confining potential is presented schematically in Fig. 2.8b in the two-particle picture (electrons and holes are treated separately). In this model picture, the QD potential can be seen as a finite potential well both for electrons and holes. It is overly simplified as one-dimensional (1D) (valid for an arbitrary direction) and as not including modifications to the potential, e. g., due to the strain or piezoelectric effects.

The 0D confinement in semiconductor self-assembled QDs can be achieved, for example, by methods described in Section 2.2, where the QD material has a lower energy gap than the surrounding material. Structures obtained in the epitaxy are characterized by long-term stability. The physical parameters controlling the electronic structure of QDs are established during growth: QDs size, shape, strain, material composition and distribution, and built-in electric fields.

Although the confinement is created along all three perpendicular directions, commonly, the height of a QD (dimension along the growth direction of a few nm) is much smaller than its in-plane size, hence this direction plays the decisive role in the determination of the QD energy structure. Therefore, the energy levels can be approximated by the following equation in analogy to the QW with finite potential barriers, and with energy levels E_i (see Fig. 2.8b):

$$E_i = \frac{\hbar^2\pi^2}{2m_e}\frac{i^2}{H^2}, \tag{2.23}$$

where i iterates over the states, m_e is the carrier effective mass, and H is the QD size (height). As $E_i \propto H^{-2}$, increasing the size of a QD lowers the energy structure and reduces the energy level separation.

Single particle calculations

To obtain the energetic structure of a QD, single-particle states (eigenfunctions ψ_i and eigenenergies ϵ_i) are first computed in the absence of other confined particles. This section introduces three methods for single-particle state calculations. These are the continuum models, effective mass approximation (EMA) and the $k{\cdot}p$ approach, and the atomistic pseudopotential method. The pseudopotential method also defines the relevant physical quantities used in the following sections.

Effective mass and adiabatic approximations

The most straightforward approach to calculate the electronic structure of an epitaxial QD is the EMA, developed by Luttinger and Kohn for the bulk semiconductors [215]. Applied together with the adiabatic approximation, it was used to reproduce the lowest electron energies for a lens-shaped QD [216, 217].

The effective mass of an electron m_e enters the effective Rydberg constant $R^* = m_e e^4/2\varepsilon^2\hbar^2$ and the effective Bohr radius $a_B^* = \varepsilon\hbar^2/m_e e^2$, both set to one, $R^* = a_B^* \equiv 1$, with ε being the dielectric constant. All effects related to strain, dielectric constants, or the discontinuity of m_e are included only using these parameters. Additionally, the potential V_e is set to zero inside the QD and WL regions, and to the difference in conduction band energies in the barrier. The considerable advantage of the adiabatic approximation is the separation of the spatial variables and, consequently, the possibility to analytically solve the Schrödinger equation.

In this method, the Schrödinger equation in cylindrical coordinates (r, θ) for electrons reads:

$$\mathscr{H}\psi(r,\theta,z) = \left[-\frac{1}{r^2}\left(r\frac{\partial}{\partial r}r\frac{\partial}{\partial r} + \frac{\partial^2}{\partial\theta^2}\right) - \frac{\partial^2}{\partial z^2} + V_e(r,z)\right]\psi(r,\theta,z) = E\psi(r,\theta,z), \tag{2.24}$$

where $\mathscr{H}$ is the Hamiltonian, z is the growth direction, and r is the radial coordinate. The adiabatic approximation allows separating r and z and writing the solutions to the Schrödinger equation in the form:

$$\psi(r,\theta,z) = \frac{1}{\sqrt{2\pi}}\exp(im\theta)g_r(z)f_m(r), \tag{2.25}$$

where $i^2 = \sqrt{-1}$, m is the angular momentum channel, and $g_r(z)$ is a slowly varying function of r. The exact eigenenergies for the first three electron levels were shown to be well approximated by the states of a 2D, infinite parabolic potential [216].

Pseudopotential

The EMA is not satisfactory for the quantitative calculations of the QD electronic structure, especially for the electron-hole Coulomb energy [218]. The pseudopotential approach was shown to successfully account for the many-body effects (the electron-hole interaction) in QDs [218], and then used to calculate the electronic structure for InAs/GaAs [219–222] and InAs/InP [223, 224] QDs. In this subsection, an outline for calculating single-particle wavefunctions and energies is presented. They neglect the strain and piezoelectric effects for the sake of simplicity, although they have to be included in the calculations of the realistic strain-driven QDs [219].

Single-particle pseudopotential First, the single-particle pseudopotential Schrödinger equation is set up at relaxed atomic positions, $\left\{\mathbf{R}_{n,\alpha}\right\}$[12] [220]:

$$\mathscr{H}\psi_i(\mathbf{r},\sigma) = \left[-\frac{\hbar^2}{2m_0}\nabla^2 + \sum_{n,\alpha}\mathbf{v}_\alpha(\mathbf{r}-\mathbf{R}_{n,\alpha})\right]\psi_i(\mathbf{r},\sigma) = \epsilon_i\psi_i(\mathbf{r},\sigma), \tag{2.26}$$

where i iterates over the particles, n over the atoms, α over the atom types, m_0 is the mass of an electron, $\mathbf{r}$ is the position function, and σ is the single-particle spin. The potential of the system

[12] Vectors in 3D are written using the bold face.

$\mathbf{V}_{\mathrm{ps}}(\mathbf{r}) = \sum_{n,\alpha} \mathbf{v}_{\alpha}(\mathbf{r} - \mathbf{R}_{n,\alpha})$ is written as a superposition of screened atomic pseudopotentials, as $\mathbf{v}_{\alpha}(\mathbf{r} - \mathbf{R}_{n,\alpha})$ is the screened empirical atomic potential for n-th atom of type α located at the position $\mathbf{R}_{n,\alpha}$. These potentials are derived by first-principle calculations (by obtaining the bulk screened pseudopotential) and extracted from experiments by fitting to the data to obtain the measured bulk transition energies, effective masses, and deformation potentials [224].

Eq. (2.26) can be solved by expanding ψ_i in the basis of bulk states ϕ_{nk}, $\{\phi_{nk}\}$. These states are bulk Bloch orbitals [220]:

$$\phi_{nk}(\mathbf{r}) = u_{n,k}(\mathbf{r}) \exp(i\mathbf{kr}), \tag{2.27}$$

where $u_{n,k}(\mathbf{r})$ is the cell periodic part of the bulk Bloch wavefunction at the n-th band and the k-th k-point (usually considered are only k-points around the Γ point). Therefore, the $\psi_i(\mathbf{r})$ can be written as a linear combination of orbitals $\phi_{nk}(\mathbf{r})$:

$$\psi_i(\mathbf{r}) = \sum_{n,k} c_{n,k}^{(i)} \phi_{nk}(\mathbf{r}). \tag{2.28}$$

Eight-band $k{\cdot}p$ theory

The $k{\cdot}p$ theory has been useful since the very beginning of the semiconductor research as the works of E. Kane helped to understand the semiconductor band structure for group IV (germanium and silicon) [225] and III-V materials (e. g., InSb [226]). Then, the model was extended by coupling between conduction and valence bands, and the 8-band $k{\cdot}p$ model was introduced in 1979 [227]. It was later extended to include the uniform strain using the Pikus-Bir deformation potential approach [228].

As initially developed for bulk materials, the applicability of this continuum model to low-dimensional structures was not evident at the beginning. The development of the new envelope-function method by Burt [229] (elaborated for valence bands in [230]) has proven the applicability of EMA to microstructures and, in consequence, opened the way for applications of the $k{\cdot}p$ model for low-dimensional structures. The 8-band $k{\cdot}p$ was used to model the multi-QW quaternary lasers [231], strained quantum wires [232], and finally pyramidal shaped InAs/GaAs QDs [233–235].

The $k{\cdot}p$ model is widely used to calculate the QD band structure, considering various QD geometries and chemical compositions. This approach has been especially important for the research reported in this thesis. This is because the 8-band $k{\cdot}p$ modeling allowed for a reliable explanation of the optical properties of investigated QDs, providing information on the origin of 0D and 2D confined states and excitonic complexes, giving an explanation of polarization properties of emitted states (FSS, degree of linear polarization (DOLP)), radiative recombination times, etc.[13] Also, the 8-band $k{\cdot}p$ framework is implemented in the NEXTNANO software that was employed to model the QDs and WL states[14].

The general outline of the $k{\cdot}p$ calculations for exciton states in QDs is given in Box 3:

Box 3: 8-band $k{\cdot}p$ calculations steps

1. Set up the QD geometry and composition.
2. Calculate the strain distribution profile (using the continuum elastic model [235, 236]).
3. Calculate the piezoelectric potential (first and second order) [237, 238]
4. Perform the strain-dependent 8-band $k{\cdot}p$ calculations to obtain the single-particle states.
5. Construct the excitonic states by configuration interaction (CI) and EI.
6. Calculate the optical properties.

[13] The calculations and their analysis have been performed by Michał Gawełczyk.
[14] Performed by the author of this thesis.

The parameters needed for the calculations are typically obtained experimentally for bulk materials. This direct availability is one of the most appealing features of the 8-band $k{\cdot}p$ method, providing transparency and relatively small computational expense.

NEXTNANO software The NEXTNANO software follows the steps outlined in Box 3 to solve the Schrödinger equation for a given quantum confinement geometry (e. g., for QDs). The exception is point 5., as the CI is not implemented in NEXTNANO, so only single-particle states can be calculated. Therefore, NEXTNANO calculates strain in a semiconductor structure and determines single-particle energy states and eigenfunctions.

The software uses the stress field continuity model to calculate the strain field. It solves the Poisson equation to find the piezoelectric charge distribution, which is then considered for calculating single-particle states. Although the calculation of optical properties is possible, it is not useful for QDs when the CI is omitted. The details on the NEXTNANO can be found in Ref. [239], and the description of how it was employed in the research reported in this thesis can be found in Summary of the results.

Energy calculations for the excitonic complexes

The Coulomb interaction and purely quantum CI have critical importance for excitonic effects in QDs. This section gives an overview of the methodology employed for the construction of the excitonic states, covering both mentioned contributions.

Interparticle many-body interactions

In general, the direct (D) and exchange (C) Coulomb integrals for i-th and j-th electronic states, $D_{i,j}$ and $C_{i,j}$, can be calculated using the microscopic pseudopotential wavefunctions (rather than envelope functions or tight-binding orbitals) as [220, 223]:

$$D_{i,j} = \iint \frac{|\psi_i(\mathbf{r}_1)|^2 |\psi_j(\mathbf{r}_2)|^2}{\bar{\varepsilon}(\mathbf{r}_1-\mathbf{r}_2)\,|\mathbf{r}_1-\mathbf{r}_2|}\,\mathrm{d}\mathbf{r_1}\,\mathrm{d}\mathbf{r_2}, \tag{2.29}$$

$$C_{i,j} = \iint \frac{\psi_i^*(\mathbf{r}_1)\psi_i(\mathbf{r}_2)\psi_j^*(\mathbf{r}_2)\psi_j(\mathbf{r}_1)}{\bar{\varepsilon}(\mathbf{r}_1-\mathbf{r}_2)\,|\mathbf{r}_1-\mathbf{r}_2|}\,\mathrm{d}\mathbf{r_1}\,\mathrm{d}\mathbf{r_2}, \tag{2.30}$$

where $\bar{\varepsilon}$ is the phenomenological, screened dielectric function [220]. The exchange integral $C_{i,j}$ includes both short- and long-range components.

The direct and exchange Coulomb integrals result in the Coulomb correlation energy E_{Coul} and EI energy E_{exch}, respectively, for the electron e and hole h. They can be expressed as [218]:

$$E_{\mathrm{Coul}} = \frac{e^2}{\varepsilon}\sum_{\sigma_h,\sigma_e}\int \frac{|\psi_h(\mathbf{r}_h,\sigma_h)|^2 |\psi_e(\mathbf{r}_e,\sigma_e)|^2}{|\mathbf{r}_h-\mathbf{r}_e|}\,\mathrm{d}^3\mathbf{r_h}\,\mathrm{d}^3\mathbf{r_e}, \tag{2.31}$$

$$E_{\mathrm{exch}} = e^2\sum_{\sigma_h,\sigma_e}\mathrm{Re}\int \frac{\psi_h^*(\mathbf{r}_h,\sigma_h)\psi_e^*(\mathbf{r}_e,\sigma_e)\psi_h(\mathbf{r}_e,\sigma_e)\psi_e(\mathbf{r}_h,\sigma_h)}{|\mathbf{r}_h-\mathbf{r}_e|}\,\mathrm{d}^3\mathbf{r_h}\,\mathrm{d}^3\mathbf{r_e}, \tag{2.32}$$

where ψ_e, ψ_h are the electron and hole single-particle wavefunctions of spin σ.

So far, the energy of an excitonic complex is independent of the number of constituent carriers as the calculations of a single-particle state do not include the information about other carriers trapped in a QD. However, the direct Coulomb interaction between carriers lifts this degeneracy, and the energies of X, XX, X^+, and X^- differ. The direct Coulomb interactions D are schematically shown for the complexes in Fig. 2.9. The most important is the attractive electron-hole interaction $D^{e,h}$ labeled by bold arrows. The other interactions ($D^{e,e}$, $D^{h,h}$, and $D^{e,h}$ which includes the second carrier in a CX state) can be considered as additional, and their relative strength is responsible for ordering the energies of the complexes. It is translated onto different spectral positions of emitting lines originating from the complexes. For example, X^+ has higher energy than X if $D^{h,h} > |D^{e,h}|$

(an additional hole introduces both interactions). The same applies to X^- and XX but for the latter, always $D^{h,h} + D^{e,e} > 2|D^{e,h}|$ what results in XX emission energy always being higher than X (an antibinding XX state is formed, i. e., $\Delta(XX)$ is negative).

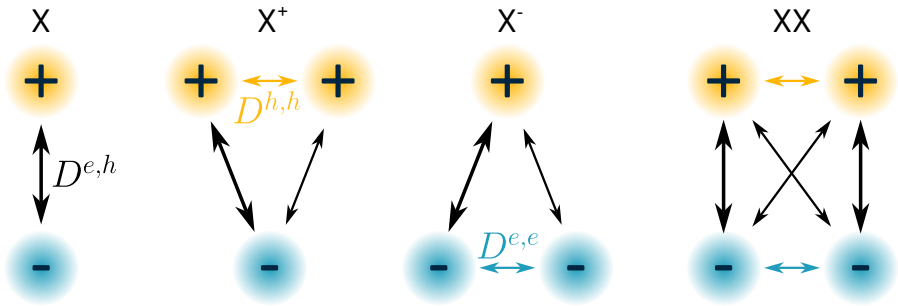

Figure 2.9: Direct Coulomb interaction D shown schematically for four excitonic complexes, exciton (X), positively-charged exciton (X^+), negatively-charged exciton (X^-), and biexciton (XX). The bold arrow marks the electron-hole Coulomb interaction $D^{e,h}$ that is a reference interaction for the determination of the binding or antibinding character of X^+, X^-, and XX states, depending on the relation between $D^{e,h}$, $D^{h,h}$, and $D^{e,e}$.

Hartree-Fock approach

Once the single-particle energies $\psi_i(\mathbf{r})$ and direct and exchange Coulomb integrals, $D_{i,j}$ and $C_{i,j}$, are calculated, the energy of a single exciton $E^{\text{exc}}_{a,b}$ created by the promotion of an electron from a hole state a of energy ϵ_{h_a} to an electron state b of energy ϵ_{e_b} can be calculated employing the screened Hartree-Fock theory. For that, first, we consider the energy needed to load N electrons into a QD [220]:

$$E_N = \sum_i \epsilon_i n_i + \sum_{i<j} \left(D^{e,e}_{i,j} - C^{e,e}_{i,j} \right) n_i n_j, \tag{2.33}$$

where n_i, n_j are the occupation numbers ($\sum_i n_i = N$). Here, the polarization self-energies of the electron states, originating in the difference between the dielectric constants ε inside and outside of the QD, are neglected due to the similarity of ε values [220].

Then, taking into account the D and C integrals for electron-electron $\left(D^{e,e}_{i,j}, C^{e,e}_{i,j}\right)$, hole-hole $\left(D^{h,h}_{i,j}, C^{h,h}_{i,j}\right)$, and electron-hole $\left(D^{e,h}_{i,j}, C^{e,h}_{i,j}\right)$ interactions, the total energy of a complex formed by N electrons and M holes is

$$E_{MN} = \sum_i -\epsilon_{h_i} m_i + \sum_{i<j} \left(D^{h,h}_{i,j} - C^{h,h}_{i,j} \right) m_i m_j + \sum_i \epsilon_{e_i} n_i + \sum_{i<j} \left(D^{e,e}_{i,j} - C^{e,e}_{i,j} \right) n_i n_j - \sum_{i,j} \left(D^{e,h}_{i,j} - C^{e,h}_{i,j} \right) n_i m_j, \tag{2.34}$$

where again n_i, m_i are the electron and hole occupation numbers, $\sum_i n_i = N$, $\sum_i m_i = M$. If the carriers are in the strong QD confinement regime, where exchange and correlation effects are dominated by the kinetic energy effects, the $E^{\text{exc}}_{a,b}$ can be calculated employing Eq. (2.34) as [220]

$$E^{\text{exc}}_{a,b} = \left(\epsilon_{e_b} - \epsilon_{h_a} \right) - D^{e,h}_{b,a} + C^{e,h}_{b,a} \delta_{S0}, \tag{2.35}$$

where $\delta_{S0} = 1$ for triplet states and 0 for singlet states.

Configuration interaction

The calculation of exciton states so far includes the direct Coulomb interaction D but only for fixed single-particle states. This, however, is insufficient as the single-particle orbitals change their shape and location due to Coulomb interaction. Therefore, the self-consistent calculations of the single-particle states are performed by coupling the carriers' positions in a QD.

To gain access to the Coulomb correlations, the self-consistent calculations have to be performed in the CI approach, where the exciton wavefunction Ψ_{exc} is calculated as a linear combination of the Slater determinants Φ, constructed from the single-particle wavefunctions $\psi_i(\mathbf{r}_i,\sigma_i)$. This allows for expanding an excitonic Hamiltonian $\mathscr{H}$ into the Slater determinants basis. The term *configuration* refers to the mathematical procedure of constructing a linear combination of Φ, and *interaction* – to the mixing of different electronic states.

The CI was applied first in the single-band EMA approach [240], and later in the tight-binding approximation [241]. The Hamiltonian matrix is expressed in the basis of Slater determinants and diagonalized. The number of basis states can be greatly reduced by considering the determinants corresponding to a single electron-hole excitation [241]. In this approach, the one-electron conduction and valence states, $\left|\psi_c\right\rangle$ and $\left|\psi_v\right\rangle$, respectively, are used to construct the Slater determinants $\Phi_{v,c} \equiv \left|\psi_v \rightarrow \psi_c\right\rangle$ as a promotion of an electron from the occupied valence state $\left|\psi_v\right\rangle$ to an unoccupied conduction state $\left|\psi_c\right\rangle$ from the ground state determinant Φ_0 [223]:

$$\Phi_0(\mathbf{r}_1,\sigma_1,\cdots,\mathbf{r}_N,\sigma_N) = \mathscr{A}\left[\psi_1(\mathbf{r}_1,\sigma_1)\cdots\psi_v(\mathbf{r}_v,\sigma_v)\cdots\psi_N(\mathbf{r}_N,\sigma_N)\right], \tag{2.36}$$

$$\Phi_{v,c}(\mathbf{r}_1,\sigma_1,\cdots,\mathbf{r}_N,\sigma_N) = \mathscr{A}\left[\psi_1(\mathbf{r}_1,\sigma_1)\cdots\psi^c(\mathbf{r}_v,\sigma_v)\cdots\psi_N(\mathbf{r}_N,\sigma_N)\right], \tag{2.37}$$

where N is the total number of electrons in the system, σ is the spin variable, and $\mathscr{A}$ is the antisymmetrizing operator. Then, the exciton wavefunctions $\Psi_{\text{exc}}{}^{(\beta)}$, with β denoting the exciton quantum numbers, are

$$\Psi_{\text{exc}}^{(\beta)} = \sum_{v=1}^{N_v}\sum_{c=1}^{N_c} a_{v,c}^{(\beta)}\Phi_{v,c}, \tag{2.38}$$

where $a_{v,c}^{(\beta)}$ are the variational parameters. The Hamiltonian can be expressed in the Slater determinants basis $\{\Phi_{v,c}\}$ and the matrix elements $\mathscr{H}_{vc,v'c'}$ of the many-particle Hamiltonian $\mathscr{H}$ are:

$$\mathscr{H}_{vc,v'c'} \equiv \left\langle \Phi_{v,c}\right| \mathscr{H} \left|\Phi_{v',c'}\right\rangle = \left(\epsilon_c - \epsilon_v\right)\delta_{v,v'}\delta_{c,c'} - D_{vc,v'c'} + C_{vc,v'c'}. \tag{2.39}$$

Then, the excitonic states are obtained by solving the secular equation:

$$\sum_{v'=1}^{N_v}\sum_{c'=1}^{N_c} \mathscr{H}_{vc,v'c'}c_{v',c'}^{(\beta)} = E^{(\beta)}a_{v,c}^{(\beta)}, \tag{2.40}$$

and the transition matrix elements $M^{(\beta)}$ can be calculated as:

$$M^{(\beta)} = \sum_{vc} a_{v,c}^{(\beta)}\left\langle\psi_v\right|\mathbf{r}\left|\psi_c\right\rangle = \sum_{vc} a_{v,c}^{(\beta)}\int \psi_v^*(\mathbf{r})\,\mathbf{r}\,\psi_c(\mathbf{r})\,\mathrm{d}^3\mathbf{r}. \tag{2.41}$$

The CI step can be seen as the energy minimization for the excitonic complex energy so that the energy decrease of δ_Φ can be associated with this procedure. The exciton energy is maximized by the large separation of electron and hole wavefunctions and by their dissimilarity.

Importantly, binding XX states become allowed after performing the CI ($\Delta(XX)$ can be positive). Therefore, the remark given at p. 34 regarding the formation of the antibinding XX state as the only option is no longer true once the CI is taken into account. The correlation energy δ_Φ can be very different for electrons and holes, possibly resulting in a complete re-ordering of the excitonic complexes' energy, even though the present discussion is limited to the ground states of the four simplest complexes.

Summary of excitonic energies

At this point of the discussion, it is possible to determine the energies for the excitonic complexes (E_X, E_{X^-}, E_{X^+}, E_{XX}), the optical transition energies ($\hbar\omega_X$, $\hbar\omega_{X^-}$, $\hbar\omega_{X^+}$, $\hbar\omega_{XX}$), and binding energies ($\Delta(X)$, $\Delta(X^-)$, $\Delta(X^+)$, $\Delta(XX)$). Table 2.2 summarizes their construction and presents their explicit forms. The rules for the construction of energies are as follows:

	Energy		
Name	Complex	Optical transition	Binding
X	$E_X = (\epsilon_e - \epsilon_h) + D^{e,h} + \delta_\Phi(X)$	$\hbar\omega_X = E_X$	$\Delta(X) = \epsilon_e - \epsilon_h - \hbar\omega_X$
X^-	$E_{X^-} = E_X + \epsilon_e + D^{e,h} + D^{e,e}$	$\hbar\omega_{X^-} = E_{X^-} - \epsilon_e$	$\Delta(X^-) = \hbar\omega_{X^-} - \hbar\omega_X$
X^+	$E_{X^+} = E_X + \epsilon_h + D^{e,h} + D^{h,h}$	$\hbar\omega_{X^+} = E_{X^+} - \epsilon_h$	$\Delta(X^+) = \hbar\omega_{X^+} - \hbar\omega_X$
XX	$E_{XX} = 2E_X + 2D^{e,h} + D^{e,e} + D^{h,h}$	$\hbar\omega_{XX} = E_{XX} - E_X$	$\Delta(XX) = \hbar\omega_{XX} - \hbar\omega_X$

Table 2.2: Excitonic energies: energy of the complex, energy of the optical transition, binding energy.

- The **exciton energy** E_X is constructed as a sum of single-particle ground electron and hole state energies ϵ_e and ϵ_h, the direct Coulomb interaction $D^{e,h}$, as well as the decrease in energy by $\delta_\Phi(X)$ due to the CI approach. The energies of three- and four-particle complexes are constructed as a sum of E_X, single-particle energies (ϵ_e, ϵ_h), and D terms.
- Energy of an **optical transition** is the difference between an initial state (energy of a given excitonic complex) and a final state (empty QD for X, single-particle states for X^- and X^+, exciton for XX).
- **Binding energy** of an exciton $\Delta(X)$ is the energy required for its dissociation and can be expressed as a difference between the single-particle states and the X emission energy. It is not trivial to access it experimentally as it requires the measurement of the ϵ_e and ϵ_h energies. For other complexes, the binding energy is the amount of energy needed to correlate additional carrier(s) to an exciton state. Hence, it can be expressed as a difference between the optical transition energy for the given complex and the exciton transition energy, $\hbar\omega_X$.

Binding energies are considerably larger in QDs than in structures of higher dimensionality due to better electron and hole wavefunction overlap. Therefore, the QD geometry and the shape of confining potential are the most important to determine the binding energies, which are typically in a few meV range for III-V QDs.

Exchange interaction

So far, the carrier spin state was included in the equations but largely omitted in the discussion. However, each of the optical transitions is, in fact, formed by a multiplet of spin states, resulting from all allowed spin configurations. For neutral excitons, the spin degeneracy of the multiplet is lifted by the EI and the Zeeman interaction with the magnetic field. The latter will not be discussed here as the magnetic field was not used in the research presented in this thesis. However, magneto-photoluminescence is an important tool to investigate the interaction between the magnetic field and the exciton wavefunction and to determine, i. a., the electron and hole g factors. The following discussion focuses on the electron-hole EI and how it imprints the exciton state, especially, the introduction of the neutral exciton FSS.

Before delving into the discussion, it should be noted that if the heavy-hole–light-hole states (HH-LH) splitting is large (as it is in III-V materials), the exciton wavefunction has a predominant contribution from the heavy hole states with spin $J_h = 3/2$, and spin projection $J_{h,z} = \pm 3/2$. In contrast, the contribution from the light holes with $J_h = 1/2$ can be neglected. This is true both in QWs and QDs: symmetry breaking and strain introduce the HH-LH splitting of at least several tens of meV, what is much more than the EI. The spin of an electron is $S_e = 1/2$ and spin projection $S_{e,z} = \pm 1/2$. The projection of the angular momentum of the exciton is $M = J_{h,z} + S_{e,z}$ so that four X states can be formed, characterized by $|M| = 1$ or $|M| = 2$. As the total angular momentum of a photon is 1, excitons with $|M| = 1$ can couple to the light field and thus recombine radiatively, hence are called *bright excitons*. For excitons with $|M| = 2$, the exciton-light field coupling is forbidden. Such excitons are therefore *dark*.

The EI has two parts, short- and long-range. The first splits the dark and bright excitons (for all QD geometries), while the latter contributes to this splitting but, importantly, introduces the splitting of bright states in in-plane asymmetric QDs. In real space, the differentiation between these parts is based on the probability of finding both carriers either in the same Wigner-Seitz unit cell (short-range) or in different cells (long-range). At zero magnetic field, the EI couples spins of an electron and a hole. Its magnitude is proportional to the $C^{e,h}$ integral, defined in Eq. (2.30).

Exchange interaction Hamiltonian and energy splitting

The fine structure of excitons due to the EI is present already in bulk. However, its magnitude is sensitive to the electron-hole overlap so it is increased in QWs. The theory of the EI has been established for AlGaAs/GaAs heterostructures (QWs) [242–245], and afterwards extended to QDs [246, 247] with the first observation reported for the AlGaAs/GaAs QW interface fluctuations in Ref. [248].

If the HH-LH splitting is large, QW excitons in their ground states have the predominant contribution from the heavy hole states, so the spin of a hole is $J_h = 3/2$ and the spin of an electron is $S_e = 1/2$. The Hamiltonian for such an exciton can be deduced from the group theory considerations which describe the electron-hole spin-spin coupling in the absence of magnetic field ($\mathbf{B} = 0$), and can be written as [243, 247]:

$$\mathscr{H}_{ex} = -\sum_{i=x,y,z} (a_i J_{h,i} S_{e,i} + b_i J_{h,i}^3 S_{e,i}), \tag{2.42}$$

where $\mathscr{H}_{ex}$ is the exchange Hamiltonian, a_i, b_i are the spin-spin coupling constants, and $J_{h,i}$, $S_{e,i}$ are spin projections on the i-th axis.[15]

Using the eigenstates of the projection of the exciton angular momentum M, $|+1\rangle$, $|-1\rangle$, $|+2\rangle$, $|-2\rangle$ as the basis, the matrix representation of the exchange Hamiltonian $\mathscr{H}_{ex}$ can be written as

$$\mathscr{H}_{ex} = \frac{1}{2}\begin{pmatrix} +\delta_0 & +\delta_1 & 0 & 0 \\ +\delta_1 & +\delta_0 & 0 & 0 \\ 0 & 0 & -\delta_0 & +\delta_2 \\ 0 & 0 & +\delta_2 & -\delta_0 \end{pmatrix}, \tag{2.44}$$

where $\delta_0 = 3/2 \times (a_z + 9/4 \times b_z)$, $\delta_1 = 3/4 \times (b_x - b_y)$, and $\delta_2 = 3/4 \times (b_x + b_y)$. As the matrix has a block diagonal form, the bright states $|\pm 1\rangle$ do not mix with dark ones $|\pm 2\rangle$, and the bright-dark splitting is electron-hole exchange energy δ_0. Conversely, the δ_1, δ_2 off-diagonal terms in the bright and dark sub-blocks result in the hybridization of the bright and dark states, respectively. For the latter, mixing of $M = |\pm 2\rangle$ states is inevitable, and the dark states splitting is δ_2. Eigenstates are symmetric and antisymmetric linear combinations of $|\pm 2\rangle$ states, $\left|X_D, Y_D\right\rangle = \left(|+2\rangle \pm |-2\rangle\right)/\sqrt{2}$.

However, as $\delta_1 \propto (b_x - b_y)$, if a potential is characterized by the rotational D_{2d} symmetry, bright states are degenerate ($\delta_1 = 0$) and $|\pm 1\rangle$ are eigenstates of the exchange Hamiltonian, Eq. (2.44). This is no longer true if $b_x \neq b_y$ as in structures of lower symmetry ($< D_{2d}$, for example C_{2v}) what leads to the mixing of $M = |+1\rangle$ and $|-1\rangle$ states which are now split by the bright states splitting, or the FSS energy, δ_1. In this case, the eigenstates are $\left|X_B, Y_B\right\rangle = \left(|+1\rangle \pm |-1\rangle\right)/\sqrt{2}$. The relation between the splittings is $\delta_1 < \delta_2 \ll \delta_0$, where the dominance of the δ_0 term stems from the fact that it is proportional to the term in Eq. (2.42) which is linear in $J_{h,i}$, while δ_1, δ_2 come from the second term in Eq. (2.42), which is proportional to $J_{h,i}^3$. The polarization of emitted photons changes from circularly-polarized $\sigma^{\pm}$ for excitons in the angular momentum eigenstates $M = |\pm 1\rangle$ to linearly-polarized $\pi_{x,y}$ for hybridized $\left|X_B\right\rangle$ and $\left|Y_B\right\rangle$ states.

[15] The interaction with an external magnetic field $\mathbf{B}$ introduces an additional Zeeman term [243–245],

$$\mathscr{H}_{\text{Zeeman}}(B) = -\mu_B \sum_i \left(g_{e,i} S_{e,i} - 2\kappa_i J_{h,i} - 2q_i J_{h,i}^3\right) B_i, \tag{2.43}$$

where μ_B – Bohr magneton, $g_{e,i}$ – electron g factor, and κ_i, q_i are Luttinger-Kohn valence band parameters which can be used to extract the effective hole g factor, $g_{h,z}$ [246].

The (001)-grown QWs have the D_{2d} symmetry (in-plane rotational invariance), and the same results apply to the QDs with in-plane symmetric potential. Realistic self-assembled QDs are typically at least slightly elongated and hence are characterized by C_{2v} symmetry.

The discussion on the influence of Coulomb interactions on the energy of excitonic complexes and the EI anisotropy on the fine structure of the exciton state can be summarized in a scheme shown in Fig. 2.10. It is valid for III-V group semiconductor QDs (e. g., InAs, GaAs, InP).

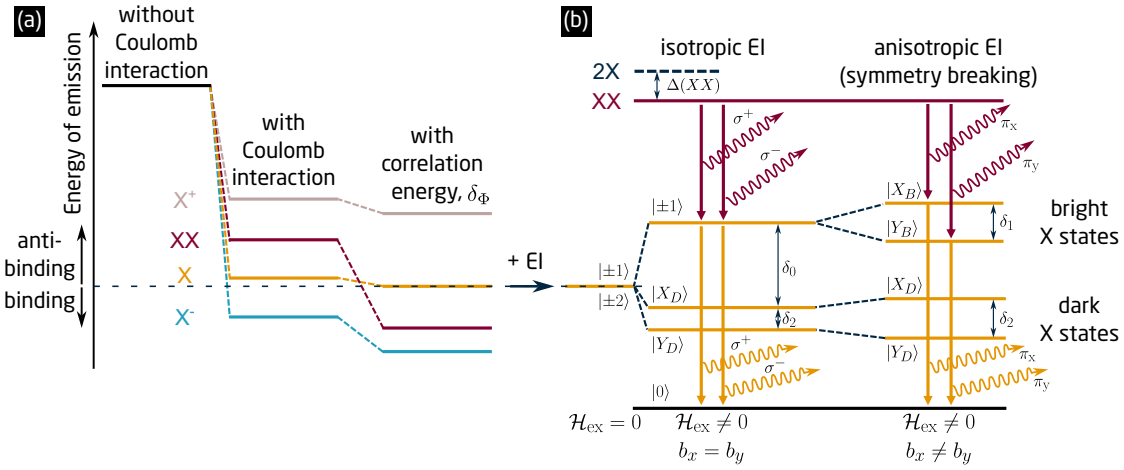

Figure 2.10: **a**, The evolution of energy for four basic QD excitonic complexes with a next level of detail consecutively being added (left to right). First, the Coulomb interaction lifts the degeneracy of the single-particle level. Second, the CI energy δ_Φ can change the energetic ordering of states. See the text for details. **b**, The inclusion of the EI for the neutral exciton energy lifts the spin degeneracy; already in a rotationally-invariant QD potential with an isotropic EI, the dark and bright exciton states are split by δ_0, and dark states are hybridized and split by δ_2. In a QD with an asymmetric confining potential, the electron-hole EI is anisotropic, and an additional bright exciton splitting δ_1 occurs so that the bright states become hybridized as well. $\Delta(XX)$ – biexciton binding energy, δ_0 – bright-dark states splitting, δ_1 – bright states splitting, δ_2 – dark states splitting, $\sigma^\pm$ – circularly-, $\pi_{x,y}$ – linearly-polarized photons, shown with wavy arrows.

Charged excitons Importantly, this discussion is valid only for neutral excitons, X. For charged excitons, CX, an additional carrier in the system changes the total spin of the system from an integer to a half-integer. For a negative trion, X^-, the ground state consists of two electrons with antiparallel spins and one hole, all in the lowest-energy shells. The situation is reversed for a positive trion, X^+, and two holes occupy the lowest-energy state with antiparallel spins. Since the total spin of a pair of electrons (or holes) is now zero, there is effectively no electron-hole EI that could be asymmetric, as the exchange Hamiltonian, Eq. (2.42), is equal to zero. As a result, there is no lifting of spin degeneracy for CX states.

Alternatively, Kramer's theorem can be used to explain spin degeneracy for CX. The theorem states that for every energy eigenstate of a time-reversal symmetric system with half-integer total spin, every energy level is at least double-degenerate. In this case, it implies that the eigenstates of the CX are doublets degenerate without a magnetic field, regardless of the QD symmetry.

This leads to the conclusion that CX has no bright-dark states splitting and no FSS.

Microphotoluminescence spectra Regarding the polarization dependence of the microphotoluminescence (μPL) spectrum of a single QD, in the general case of asymmetric confining potential, the X states are energetically split and, to a first approximation, linearly polarized (H and V polarizations).

The XX state is not split, as there is only one possible carrier spin configuration due to the Pauli exclusion principle. However, due to the two possible final states of the XX transition (H- or V-polarized X), the XX is also linearly polarized. In contrast, the CX state is degenerate, and its emission is circularly polarized. All these conclusions allow for the identification of the QD emission lines based on the polarization-resolved series of μPL spectra.

Radiative recombination

The transition rate $\Gamma_{i\to f}$ between an initial state $|i\rangle$ and a final state $|f\rangle$ can be defined by Fermi's Golden Rule that takes into account the transition matrix element M_{if} and photon density of states $g(\omega)$:

$$\Gamma_{i\to f} = \frac{2\pi}{\hbar^2}|M_{if}|^2 g(\omega), \tag{2.45}$$

where $g(\omega)$ is defined in analogy to $\rho(E)$ in Eq. (2.20) as a number of states per unit energy.

The following discussion adopts a semi-classical approach that treats the atoms quantum-mechanically while the light field is treated classically, as the electromagnetic wave with electric field amplitude $\boldsymbol{E}_0$. In this approach, different types of light-matter interaction are possible (dipole, quadrupole, octupole) for both the electric and magnetic fields, however, the dipole interaction for electric field is stronger by several orders of magnitude compared with other multipolarities, and with the magnetic field, therefore the **dipole approximation** is used in the following discussion.

Within this frame, the light-matter interaction can be seen as a perturbation of the electric dipole $\mathbf{d} = -e\mathbf{r}$ caused by field $\boldsymbol{E}_0$:

$$\mathscr{H}_{\text{dipole}} = -\mathbf{d}\cdot\boldsymbol{E}_0 = e\mathbf{r}\cdot\boldsymbol{E}_0. \tag{2.46}$$

The form of $\mathbf{d}$ is based on the assumption that holes are too heavy to respond to $\boldsymbol{E}_0$ at optical frequencies. The scalar product $\mathbf{r}\cdot\boldsymbol{E}_0$ results in the construction of the **transition matrix element** as:

$$M_{if} \equiv \langle f|\mathscr{H}_{\text{dipole}}|i\rangle = -\boldsymbol{\mu}_{if}\cdot\boldsymbol{E}_0, \tag{2.47}$$

where $\boldsymbol{\mu}$ is the **transition dipole moment**,

$$\boldsymbol{\mu}_{if} = -e\left(\sum_{j=x,y,z}\langle f|j|i\rangle\hat{\jmath}\right), \tag{2.48}$$

and $\hat{\jmath}$ is an axis versor. For linearly polarized light (e. g., along x axis) this formula simplifies to:

$$\mu_{if,x} = -e\langle f|x|i\rangle. \tag{2.49}$$

The dipole moment $\boldsymbol{\mu}$ is a key parameter of the transition, as it defines its **oscillator strength** f_{if}:

$$f_{if} = \frac{2m\omega_{fi}}{3\hbar}|\langle f|\mathbf{r}|i\rangle|^2 \equiv \frac{2m\omega_{fi}}{3\hbar e^2}|\boldsymbol{\mu}_{if}|^2. \tag{2.50}$$

Selection rules

The oscillator strength f, defined in Eq. (2.50) and transition matrix element M, Eq. (2.47), show that the transition dipole moment $\mu_{if,x} = -e\langle f|x|i\rangle$ decides about the transition rate $\Gamma_{i\to f}$ for any given pair of initial and final states $|i\rangle$ and $|f\rangle$. If the transition rate is zero, the transition is *forbidden* (does not couple to light so no radiative recombination can occur). Therefore, the set of rules, known as the **selection rules**, define the quantum numbers of states $|i\rangle$ and $|f\rangle$ so that a transition between them is optically *allowed*. The transitions allowed in the dipole approximation have high probabilities and hence short radiative lifetimes, typically in the range of 1-100 ns.

For the discussion of selection rules applicable to excitonic complexes in QDs, it is convenient to express the wavefunctions of an electron in the conduction band (c) or a hole in the valence band (v) as

$$\left|\psi_{c/v}\right\rangle = \left|F_{c/v}\right\rangle\left|u_{c/v}\right\rangle\left|\sigma_{c/v}\right\rangle, \tag{2.51}$$

where $\left|F_{c/v}\right\rangle$ is the envelope function, $\left|u_{c/v}\right\rangle$ is the Bloch function at Γ point of the Brillouin zone [in analogy to Eq. (2.27)], and the $\left|\sigma_{c/v}\right\rangle$ term describes the spin σ state of the carrier. The envelope function can be found in analogy to Eq. (2.26) by solving the effective-mass Schrödinger equation:

$$-\frac{\hbar^2}{2m_0}\nabla\cdot\left(\frac{1}{m_e(\mathbf{r})}\nabla F_{c/v}(\mathbf{r})\right)+V_{c/v}(\mathbf{r})F_{c/v}(\mathbf{r})=\left(\epsilon-E_{c/v}\right)F_{c/v}(\mathbf{r}), \tag{2.52}$$

where $m_e(\mathbf{r})$ is the effective mass function, $V_{c/v}(\mathbf{r})$ is the confining potential function, ϵ is the electron eigenenergy and $E_{c/v}$ is the band-edge energy. The form of the wavefunctions given by Eq. (2.51) shows that it can be divided into orbital, $\left|F_{c/v}\right\rangle\left|u_{c/v}\right\rangle$ and spin, $\left|\sigma_{c/v}\right\rangle$, parts, so that it depends both on the position $\mathbf{r}$ and spin σ. Additionally, the hole wavefunctions can be introduced to construct the equivalent picture of the electron-hole recombination by transforming the electron state $\left|\psi_v\right\rangle$ into hole state $\left\langle\psi_v\right|$.

Expanding the transition matrix element M_{if} given in Eq. (2.47) by the wavefunction form given in Eq. (2.51), and using $\left|\psi_c\right\rangle$, $\left|\psi_v\right\rangle$ as initial and final states $|i\rangle$, $|f\rangle$, respectively, the matrix element $M_{c,v}$ can be written as

$$M_{c,v}=\left\langle F_v\middle|F_c\right\rangle\left\langle u_v\middle|\mathbf{d}\cdot\boldsymbol{E}_0\middle|u_c\right\rangle\left\langle\sigma_v\middle|\sigma_c\right\rangle. \tag{2.53}$$

The essential conclusions concerning maximizing the transition matrix element $M_{c,v}$ can be made based on its form given in Eq. (2.53). They are outlined in Box 4.

Box 4: Selection rules for optical transitions in QDs

1. **The same parity of the envelope functions** $\left|F_{c/v}\right\rangle$**.**
2. **Different parity of the Bloch functions** $\left|u_{c/v}\right\rangle$, as $\mathbf{r}$ is an odd-parity function, and $\mathbf{d}=-e\mathbf{r}$.
3. **The spin state** σ **of the electron is preserved**, as a photon does not interact with electron spins,
4. $\boldsymbol{E}_0\parallel\mathbf{d}$, as $M_{c,v}$ depends on the $\boldsymbol{E}_0$ polarization via the scalar product $\mathbf{d}\cdot\boldsymbol{E}_0$. Therefore, the $M_{c,v}$ is maximized for the parallel orientation of both vectors.

The additional condition can be added based on the conservation of total angular momentum in the dipole-photon system,

5. **The angular momentum** M **changes by** ±1**.**

In III-V semiconductors, rule 2 is usually automatically fulfilled for the interband transitions, as the valence band is composed of the p-type orbitals (of odd symmetry), while the conduction band – of the s-type (even symmetry) ones so that the electron-hole recombination changes the parity of the electron $\left|u_{c/v}\right\rangle$ function from s-like to p-like.

Recombination time

The recombination time $\tau_{i\to f}$ is inversely proportional to the transition rate $\Gamma_{i\to f}$ and equal to [249]:

$$\Gamma_{\mathrm{i}\to\mathrm{f}}\equiv\frac{1}{\tau_{i\to f}}=\frac{4}{3}\frac{e^2}{\hbar^2m_0^2c^3}n\omega_{i\to f}\sum_{j=x,y,z}|M_{if,j}|^2, \tag{2.54}$$

with c being the speed of light in a vacuum, and n – the refractive index of a QD. It can also be shown [250] that the recombination rate $\Gamma_{i\to f}$ is equivalent to:

$$\Gamma_{\mathrm{i\to f}} = \frac{2\pi}{3(\lambda/n)^2}\frac{e^2 f_{if}}{\epsilon_0 c m_0 n} = n\frac{2\pi}{3\lambda^2}\frac{e^2 f_{if}}{\epsilon_0 c m_0}, \tag{2.55}$$

where ϵ_0 is the vacuum permittivity. This numerically corresponds to [251]:

$$\tau_{i\to f}[\mathrm{ns}] \approx 45\frac{\lambda^2[\mu\mathrm{m}]}{n f_{ij}}. \tag{2.56}$$

This equation was used to calculate the exciton lifetime, which is part of the research presented in this thesis.[16] Provided that the exciton wavefunctions are available, the oscillator strength f can be calculated according to Eq. (2.50).

Thus far, the recombination rate is independent of the temperature and the occupancy of state $|i\rangle$. Therefore, the recombination time $\tau_{i\to f}$ defined using Eq. (2.54) is a characteristic property of the transition $|i\rangle \to |f\rangle$. However, if both temperature and occupancy of states $|i\rangle$ and $|f\rangle$ are taken into account, the recombination time τ_γ of an excitonic complex γ depends on temperature-dependent probabilities $n_i(T)$ of having the initial states $|i\rangle$ occupied and the number of final states $|f\rangle$ available for recombination [252]:

$$\frac{1}{\tau_\gamma} = \sum_f \sum_i n_i \frac{1}{\tau_{i\to f}}, \tag{2.57}$$

and $\sum_i n_i = 1$. If intra-level relaxation of excited exciton states is much faster than considered lifetimes, $n_i(T)$ coefficients follow the Boltzmann distribution. Taking into account Eq. (2.56),

$$\tau_\gamma \propto \frac{1}{E^2}. \tag{2.58}$$

Rate equation model

Let us consider a cascaded emission of excitons with index γ numbering the electron-hole pairs in a QD (multiexcitons), so that n_γ is the probability of finding the γ-th exciton in a QD (only one exciton configuration can exist in a QD in a given moment: $\sum_{i=0}^{\infty} n_\gamma = 1$). Then, for each excitonic configuration and constant exciton photogeneration rate $G(t) \equiv G$ (proportional to the QD excitation power), the rate equation can be written as [253]:

$$\frac{\mathrm{d}n_\gamma}{\mathrm{d}t} = G n_{\gamma-1} - \frac{n_\gamma}{\tau_\gamma} + \frac{n_{\gamma+1}}{\tau_{\gamma+1}} - G n_\gamma, \tag{2.59}$$

for all N considered multiexcitons ($\gamma < N$). The first two terms describe the creation of γ-th from the $(\gamma-1)$-th exciton state and its radiative recombination with rate $1/\tau_\gamma$, while the latter two express its creation by recombination of one electron-hole pair from exciton $(\gamma+1)$, and the disappearance of γ-th exciton by the creation of $(\gamma+1)$-th exciton. The steady-state solutions ($\mathrm{d}n_\gamma/\mathrm{d}t = 0$ for all γ) lead to $n_\gamma(G)$ values of

$$n_\gamma(G) = \frac{G^\gamma \prod_{i=1}^{\gamma}\tau_i}{1+\tau_1 G+\tau_1\tau_2 G^2+\cdots+G^N\prod_{i=1}^{N}\tau_i}. \tag{2.60}$$

This can easily be translated to the emission intensity of the γ-th exciton I_γ with an assumption that the emission intensity is proportional to the level occupation probability and its recombination rate, i. e., $I_\gamma \propto n_\gamma/\tau_\gamma$. This can be done by restricting the multiplication in the nominator to $(\gamma-1)$, i. e., $\prod_{i=1}^{\gamma-1}\tau_i$:

$$I_\gamma(G) \propto \frac{n_\gamma}{\tau_\gamma} = \frac{G^\gamma \prod_{i=1}^{\gamma-1}\tau_i}{1+\tau_1 G+\tau_1\tau_2 G^2+\cdots+G^N\prod_{i=1}^{N}\tau_i}. \tag{2.61}$$

[16] Calculated by Michał Gawełczyk.

Three level system

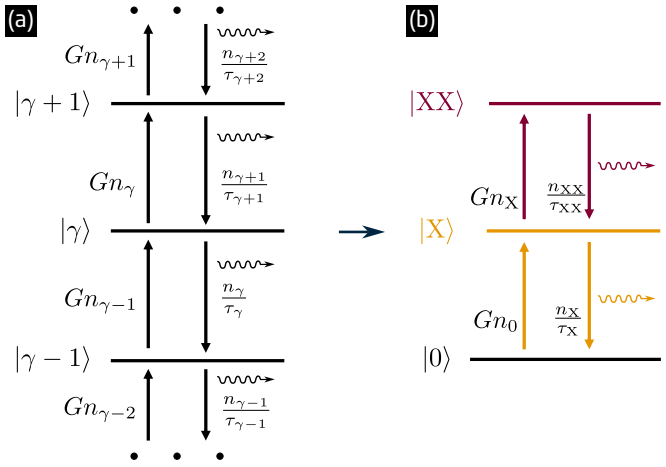

Figure 2.11: **a**, A multi-level scheme with transition rates indicated with arrows and labeled with terms based on Eq. (2.59). **b**, The simplest, three-level scheme that can approximate the XX-X cascade in a QD, based on Eq. (2.62).

It is instructive to apply Eqs. (2.59)–(2.61) to the three-level system, composed of the ground QD state $|0\rangle$ (empty QD, $\gamma = 0$), exciton (X, $\gamma = 1$, a spin-degenerated level), and biexciton (XX, $\gamma = 2$), as it was done in Ref. [254]. In this case, the rate equations Eq. (2.59) for X and XX can explicitly be written as

$$\begin{aligned} \frac{\mathrm{d}n_X}{\mathrm{d}t} &= Gn_0 - \frac{n_X}{\tau_X} + \frac{n_{XX}}{\tau_{XX}} - Gn_X, \\ \frac{\mathrm{d}n_{XX}}{\mathrm{d}t} &= Gn_X - \frac{n_{XX}}{\tau_{XX}}, \end{aligned} \tag{2.62}$$

with τ_X and τ_{XX} being the X and XX radiative recombination lifetimes. The equations reflect the fact that for the exciton, two processes increase its occupancy, optical excitation of an empty QD (Gn_0), or the biexciton recombination (n_{XX}/τ_{XX}). The occupancy can be decreased by exciton recombination ($-n_X/\tau_X$), or the biexciton creation ($-Gn_X$). In this simplified model, the XX is the highest level so that only biexciton generation (Gn_X) and recombination ($-n_{XX}/\tau_{XX}$) should be taken into account. Similarly, the emission intensity expressions, Eq. (2.61), can be written as

$$\begin{aligned} I_X(G) &\propto \frac{n_X}{\tau_X} = \frac{G}{1+\tau_X G+\tau_X\tau_{XX}G^2}, \\ I_{XX}(G) &\propto \frac{n_{XX}}{\tau_{XX}} = \frac{G^2\tau_X}{1+\tau_X G+\tau_X\tau_{XX}G^2}. \end{aligned} \tag{2.63}$$

For a low generation rate G, Eq. (2.63) is reduced to the linear ($I_X(G) \propto G$) and quadratic ($I_{XX}(G) \propto G^2$) power dependences for the exciton and biexciton, respectively. This fact has great importance for the identification of the XX-X cascade in the μPL spectra obtained under low excitation power. Besides the

1. linear vs. quadratic excitation power dependencies for X and XX,

other characteristic features of the XX-X cascade are

2. the appearance of the X line at lower excitation power than the XX one, as more carriers are required for the XX to be created, and
3. at high excitation power, the X emission saturates and the XX emission dominates the spectrum. For even higher excitation, the X emission intensity decreases as the generation rate is

so high that after the XX recombination, the exciton radiative recombination is less probable (slower) than the XX creation (generation of another electron-hole pair in the system).

Figure 2.11 summarizes the rate equations for the general case [panel a, reflecting Eq. (2.59)], and for the simplest, three-level ladder of XX-X cascade [panel b, based on Eq. (2.62)].

Charged excitons The reasoning for the charged excitonic (CX) states ladder can be similar to the one presented so far, depending on the origin of the additional carrier trapped in the QD. In the case of residual structure doping, the resident carrier comes from a donor or acceptor impurity, and the expected power dependence is identical to this of a neutral exciton – a linear one. On the other hand, a superlinear trend is expected if an extra carrier has to be captured by a QD from the photo-created population, for example, $I_{\mathrm{CX}}(G) \propto G^{1.5}$ [255].

Role of the thermal energy

Analyzing the changes in the PL spectrum induced by the supply of thermal energy to the system is a powerful tool for investigating the bandgap evolution of the materials, energy structure of confined states, and charge transfer processes.

Typically, the analysis is performed on the optical response of the system (PL, photoluminescence excitation (PLE)) as a function of the structure's temperature. Three main parameters are monitored: the position of the peak response, the intensity of the optical response, and the peak broadening.

Photoluminescence intensity It enables extracting the activation energies and probabilities (efficiencies) for consecutive quench processes. If N PL quenching mechanisms with activation energies $E_{\mathrm{A},i}$ and efficiencies B_i decrease the PL intensity I, the temperature dependence can be fitted with the function:

$$I(T) = \frac{I(0)}{1 + \sum_{i=1}^{N} B_i \exp\left(-E_{\mathrm{A},i}/k_B T\right)}. \tag{2.64}$$

Activation energies $E_{\mathrm{A},i}$ can be connected with the relevant energy scales of a system and indicate the quenching mechanisms, while the B_i coefficients correspond to their relative importance. In the III-V epitaxial QD systems, the most common mechanism is the carrier escape to another confined QD state, WL states, or a barrier. Alternatively, the dissociation of an excitonic complex can occur after supplying sufficient thermal energy to surpass its binding energy.

The redistribution of carriers among QDs of different sizes is especially relevant for the QD ensembles investigated in this thesis. In this case, at low temperatures, photogenerated carriers are trapped by one of the QDs spatially located in the vicinity of the photogeneration spot. However, at elevated temperatures, carriers can be re-excited from a QD potential and redistributed within the ensemble. Typically, QDs with a shallow confining potential supply the carriers which are subsequently trapped by QDs with a deeper confining potential. This is the *charge transfer* process among the ensemble of QDs and the efficiency of this process is controlled by the thermal energy. The excitation transfer can occur via migration of the carriers in the WL in the case of S-K QDs.

Emission energy The discrepancy between the expected rate of the temperature-induced bandgap change and the related PL energy shift is another parameter important in the analysis. For bulk, the expected situation is the renormalization of the semiconductor bandgap caused by the thermal expansion of the crystal lattice. A few empirical models were developed to describe the anticipated temperature-induced rate of the interband transition energy change, including the Varshni relation [256]:

$$E_g(T) = E_g(0) - \frac{aT^2}{T+b}, \tag{2.65}$$

where a and b are material-dependent fit parameters. Among other developed approaches is the method taking into account the increasing role of the electron-phonon coupling and its influence on chemical bonds through the bosonic distribution of phonons, developed by O'Donnell and Chen

[257], or the model developed by Lautenschlager et al. concerning the electron-lattice interaction [258].

For the ensemble of QDs, the observed PL peak position is determined by the energy of the system and the occupation of QD states. Any discrepancy in the bandgap of the system from the bulk model dependence can provide valuable information on the change of the QD occupation (charge carrier transfer between QDs). The trapping of carriers at low temperatures and their temperature-induced release and capture by the global energy minimum causes the filling of the QDs with deep confining potential, leaving empty QDs with a shallow one.

This can be transformed on the observation of the PL band emission shifting towards the lower energy faster than predicted by the temperature-induced changes in the bandgap of the system. In the case of a single PL emission maximum, the redistribution can be observed as lowering the emission intensity of the high-energy tail and increasing the low-energy one, which effectively results in the increased rate of the PL emission peak redshift. In the case of a multi-peak PL emission pattern, the redistribution is seen as the temperature-induced increase of the emission intensity for the low-energy QD peaks in the low-temperature range.

The understanding of the temperature-induced phenomena in the ensemble of low-density QDs is a vital part of P. Holewa *et al.*, *Optical and electronic properties of low-density InAs/InP quantum dot-like structures devoted to single-photon emitters at telecom wavelengths*, **Physical Review B**, 101, 19 (2020)[17] and P. Holewa *et al.*, *Optical and Electronic Properties of Symmetric InAs/(In,Al,Ga)As/InP Quantum Dots Formed by Ripening in Molecular Beam Epitaxy: A Potential System for Broad-Range Single-Photon Telecom Emitters*, **Physical Review Applied**, 14, 6 (2020)[18], where multi-peak PL was investigated and modeled.[19]

2.4 Single photons in experiments

The most appropriate way to experimentally verify the single-photon character of emission is to measure the statistics of photons in the emitted mode of electromagnetic radiation. This can be achieved in the HBT interferometer configuration covered in this section. The result of this measurement gives access to a part of the photon statistics that is sufficient for evaluating the single-photon purity P, based on the second-order correlation function $g^{(2)}(\tau)$. The definition of the $g^{(2)}(\tau)$, its physical significance, and the interpretation are explained in the rest of this section.

The original Hanbury Brown and Twiss configuration

The first $g^{(2)}(\tau)$ measurement was proposed by Hanbury Brown and Twiss [259] to measure the *spatial* coherence of a source.[20] Their experimental design improved the Michelson stellar light intensity interferometer and is known nowadays as the HBT interferometer. Figure 2.12a shows the original HBT interferometer configuration, where the light was detected by two separated detectors that generated photocurrents i_1 and i_2, proportional to the light intensity I_1 and I_2 incident on the detectors. Both signals were then correlated using an electronic multiplier so that the experiment's output was proportional to the time average of $I_1 I_2$.

This configuration has, however, raised some conceptual problems rooted in the quantum mechanical theory of detection realized by the photodetectors: Can the separated clicks of the detectors be correlated if the photodetection events are, in principle, statistical quantum processes? Or, in other words, is it true that

> *the time of arrival of photons at the two photocathodes should be correlated when the light beams incident upon the two mirrors are coherent? [260].*

[17] This article is included in this thesis, p. 95.
[18] This article is included in this thesis, p. 111.
[19] The author of the thesis acknowledges the role of Michał Gawełczyk and Marcin Syperek in establishing the understanding.
[20] It was constructed to work at radio frequencies and was applied for the starlight. The purpose of the first experiments was the determination of the star diameter by measuring the spread of the angles at which the incoming light is coherent.

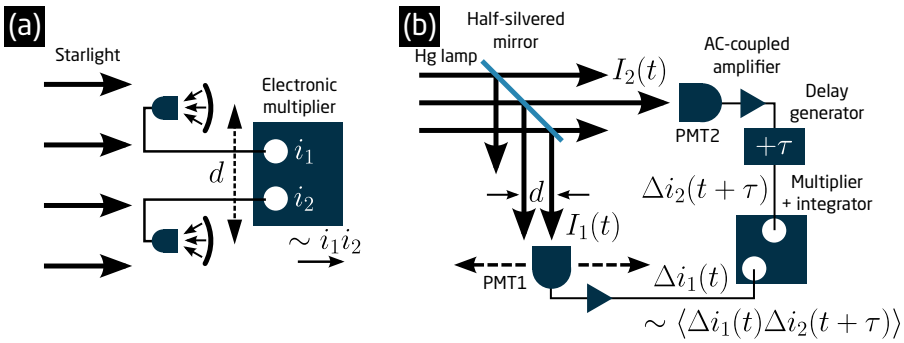

Figure 2.12: **a**, The original HBT stellar intensity interferometer [259], constructed as a corrected Michelson interferometer. The starlight is recorded on two detectors separated by d, and it generates photocurrents i_1 and i_2, which are then correlated using an electronic multiplier. **b**, The configuration of the HBT interferometer with a beam splitter (half-silvered mirror) [260]. PMT – photomultiplier tubes measuring the light intensities $I_1(t)$ and $I_2(t)$. The photocurrent fluctuation signals $\Delta i_1(t)$ and $\Delta i_2(t+\tau)$ produce the output proportional to $\langle \Delta i_1(t) \Delta i_2(t+\tau) \rangle$. The spatial coherence of the source is measured by translating the PMT1 using a stage to investigate the light separated by d.

To answer this question, a new configuration was designed [260], which is shown in a simplified form in Fig. 2.12b. Here, a beam splitter was introduced, the light source was the mercury 435.8 nm emission line, and photomultipliers measured the light intensities $I_1(t)$ and $I_2(t)$. At the same time, one of the detector signals was delayed with an electronic circuit by a time τ. Then, the two photocurrent fluctuation signals $\Delta i_1(t)$ and $\Delta i_2(t+\tau)$ were processed by an electronic multiplier-integrator with the output signal proportional to $\langle \Delta i_1(t) \Delta i_2(t+\tau) \rangle$, where $\langle \ldots \rangle$ stands for time averaging over a long period. This, in turn, is proportional to the time-averaged product of fluctuations ΔI_1, ΔI_2 of signals $I_1(t)$, $I_2(t)$, i. e.,

$$\langle \Delta i_1(t) \Delta i_2(t+\tau) \rangle \propto \langle \Delta I_1(t) \Delta I_2(t+\tau) \rangle . \tag{2.66}$$

Therefore, the result of the HBT experiment is in fact the correlation between the fluctuations ΔI_1 and ΔI_2 of the light intensity impinging on two detectors.

Principle of the Hanbury Brown and Twiss interferometry

The HBT interferometry differs from the classical approaches, such as Michelson or Mach-Zender, in which the light beams that travel via two paths are combined and the result of the signal interference is detected. In this case, the result of the interferometric measurement depends mainly on the *phase* difference between the two interfering signals, placing the coherence of the combined signals as a requirement.

In contrast to those phase-based interferometers, in the HBT experiment the *intensity* fluctuations ΔI_1, ΔI_2 of the light beam can be related to its coherence: the coherence properties of the light can be deduced by measuring the correlations between the ΔI_1 and ΔI_2. This is because the ΔI_1 and ΔI_2 will be mutually correlated only if the light detected by two detectors is coherent. For some applications, this technique is far more powerful than phase-based interferometers.

The second-order correlation function

Coherence time τ_c

One of the results of the HBT interferometric experiment is the coherence time τ_c of the light source. Let us assume that the two beams impinging on the detectors have equal intensities,

$I_1(t) = I_2(t) \equiv I(t)$, then

$$I(t) = \langle I \rangle + \Delta I(t), \tag{2.67}$$

so that $\Delta I(t)$ is the fluctuation from the average intensity of either beam $\langle I \rangle$. The coherence time τ_c can be conveniently and directly measured as the timescale on which the temporal beam coherence decays, two limiting values of the $\langle \Delta I(t) \Delta I(t+\tau) \rangle$ measured in the HBT experiment can be described:

- for $\tau = 0$, when the coherence is maximal, $\langle \Delta I(t) \Delta I(t+\tau) \rangle_{\tau=0} = \left\langle \Delta I(t)^2 \right\rangle$,
- for $\tau \gg \tau_c$, when there is no temporal coherence (lack of correlation), the sign of $\Delta I(t) \Delta I(t+\tau)$ randomly changes with time and averages to zero,

$$\langle \Delta I(t) \Delta I(t+\tau) \rangle_{\tau \gg \tau_c} = 0. \tag{2.68}$$

Note that although $\Delta I(t)$ measured for long times averages to zero by definition,

$$\langle \Delta I(t) \rangle = 0, \tag{2.69}$$

it is not the case for $\left\langle \Delta I(t)^2 \right\rangle$ in general. The coherence time τ_c can be interpreted as a timescale in which the beam intensity fluctuations are observable.

Definition of the $g^{(2)}(\tau)$ function

Based on the considerations from the previous section, the $g^{(2)}(\tau)$ function can be introduced as the result of the HBT experiment [see Eq. (2.66)], normalized to the intensities I of beams being correlated:

$$g^{(2)}(\tau) = \frac{\langle \boldsymbol{E}^*(t) \boldsymbol{E}^*(t+\tau) \boldsymbol{E}(t+\tau) \boldsymbol{E}(t) \rangle}{\langle \boldsymbol{E}^*(t) \boldsymbol{E}(t) \rangle \langle \boldsymbol{E}^*(t+\tau) \boldsymbol{E}(t+\tau) \rangle} = \frac{\langle I(t) I(t+\tau) \rangle}{\langle I(t) \rangle \langle I(t+\tau) \rangle}, \tag{2.70}$$

where $\boldsymbol{E}$ is the electric field amplitude, $I = \boldsymbol{E}^* \boldsymbol{E}$ – beam intensity, t – an arbitrary moment, τ – time delay.

Therefore, the $g^{(2)}(\tau)$ function quantifies the beam intensity fluctuations and is a convenient way to verify the single-photon character of emission. For the sake of the following analysis of Eq. (2.70), let us assume that

- The source has a constant average intensity, $\langle I(t) \rangle = \langle I(t+\tau) \rangle$.
- The tested light is spatially coherent (comes from a small area of the source). This means that the $g^{(2)}(\tau)$ function investigates the *temporal* coherence of the source.

We can expand:

$$\begin{aligned} \langle I(t) I(t+\tau) \rangle_{\tau \gg \tau_c} &= \left\langle \left(\langle I \rangle + \Delta I(t) \right) \left(\langle I \rangle + \Delta I(t+\tau) \right) \right\rangle \\ &= \langle I \rangle^2 + \langle I \rangle \langle \Delta I(t) \rangle + \langle I \rangle \langle \Delta I(t+\tau) \rangle + \langle \Delta I(t) \Delta I(t+\tau) \rangle, \end{aligned} \tag{2.71}$$

where the Eq. (2.67) was applied. Taking into account the lack of correlation for $\tau \gg \tau_c$, Eq. (2.68) and Eq. (2.69), the last three terms are equal to zero, so that

$$\langle I(t) I(t+\tau) \rangle_{\tau \gg \tau_c} = \langle I \rangle^2. \tag{2.72}$$

Applying this result and the constant intensity of the source, $\langle I(t) \rangle = \langle I(t+\tau) \rangle$, it follows that function $g^{(2)}(\tau)$ is normalized with respect to long delays to unity ($g^{(2)}(\tau \to \infty) = 1$):

$$g^{(2)}(\tau \gg \tau_c) = \frac{\langle I(t) I(t+\tau) \rangle}{\langle I(t) \rangle^2} = \frac{\langle I(t) \rangle^2}{\langle I(t) \rangle^2} = 1. \tag{2.73}$$

On the other hand, for $\tau \ll \tau_c$ fluctuations are time-correlated and for $\tau = 0$:

$$g^{(2)}(0) = \frac{\left\langle I(t)^2 \right\rangle}{\langle I(t) \rangle^2}. \tag{2.74}$$

HBT experiment in quantum optics

Let us start with the wave picture of light. Interestingly, if the light is considered classically, it can be shown that for any $I(t)$ dependence,

$$g^{(2)}(0) \geq 1, \tag{2.75}$$

and

$$g^{(2)}(0) \geq g^{(2)}(\tau) \tag{2.76}$$

will hold. This, however, is valid as long as we operate with light intensities I. If we change to the particle image of light, the detectors register the number of photons $n_1(t)$ and $n_2(t)$, and the $g^{(2)}(0)$ can reach values below 1. In the quantum picture, Eq. (2.70) can be rewritten as

$$g^{(2)}(\tau) = \frac{\langle n_1(t) n_2(t+\tau)\rangle}{\langle n_1(t)\rangle \langle n_2(t+\tau)\rangle}, \tag{2.77}$$

as $n_i(t) \sim I_i(t)$. Therefore, the $g^{(2)}(\tau)$ function measures the conditional probability of detecting a second photon at time $t = \tau$, given that the first photon was detected at $t = 0$. This is precisely the expected outcome of the HBT experiment – a histogram proportional to $g^{(2)}(\tau)$ showing the coincidences defined in the previous sentence. This experimental result after the histogram normalization is a direct measure of the $g^{(2)}(\tau)$ function, as defined in Eq. (2.77).

There is a direct consequence of shifting to the photon picture for the understanding of possible experiment outcomes. Now, the signal beam can be imagined as a stream of photons impinging on a beam splitter and being randomly directed toward either of the detectors with equal probability. If the time intervals between photons are long, then the conditional probability of detecting a photon at the starting detector and the stopping detector at the same time is equal to zero. The timer will record no events at $\tau = 0$. Then, the next photon can be directed with a 50 % probability either toward the starting detector (which triggers no new coincidences) or toward the stopping detector – the stop pulse triggers the end of the delay counting and adds a new coincidence at τ.

Figure 2.13a shows the standard HBT configuration used in quantum optics. Here, the classical light beam represented in Fig. 2.12 with arrows is replaced with a stream of photons. Modern experimental realizations use a beam splitter instead of a half-silvered mirror and avalanche photodiodes or superconducting nanowire single-photon detectors (SNSPDs) instead of photomultipliers. Additionally, Fig. 2.13b shows an exemplary experiment result, where the delay axis is divided into time bins so that the registered coincidences fall into an appropriate τ time slot and form a histogram.

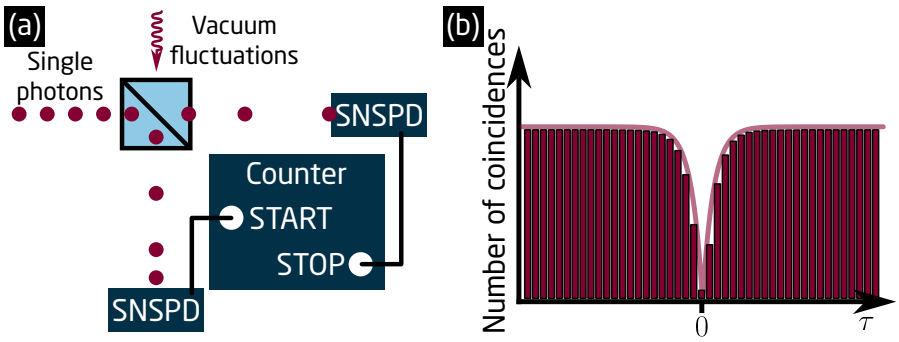

Figure 2.13: The Hanbury Brown and Twiss interferometer: **a**, the configuration applied in quantum optics, **b**, the result of the measurement: histogram of coincidences as a function of time delay τ.

Therefore, for a single-photon beam, the coincidences at all $\tau \neq 0$ values can be recorded but never at $\tau = 0$, standing in clear opposition to the classical theory of light, where $g^{(2)}(0) \geq 1$ Eq. (2.75), and is a direct consequence of the quantum nature of light. Here, the crucial assumption is that of long time intervals between photons, as otherwise, for photons traveling in bunches,

both detectors can detect photons at the same time so $g^{(2)}(0) \geq 1$ in accordance with the classical results. This distinction is central to the threefold classification of light according to the possible $g^{(2)}(0)$ value, summarized in Box 5:

Box 5: $g^{(2)}(0)$-based classification of light

- for $g^{(2)}(0) > 1$, the light is **bunched** and the source emits in a chaotic manner,
- for $g^{(2)}(0) = 1$, the light is **coherent**, and photons are randomly separated,
- for $g^{(2)}(0) < 1$, the light is **antibunched**, what is a purely quantum optical phenomenon, impossible to explain using the classical approach, given in Eq. (2.70).

Figure 2.14a presents the schemes of the photon streams forming the antibunched, coherent, and bunched light beams. The result of measuring an ideal single-photon source (totally suppressed photon bunches) is shown in Fig. 2.14b: the function is normalized to 1, $g^{(2)}(\tau \gg \tau_c) = 1$, and $g^{(2)}(0) = 0$.

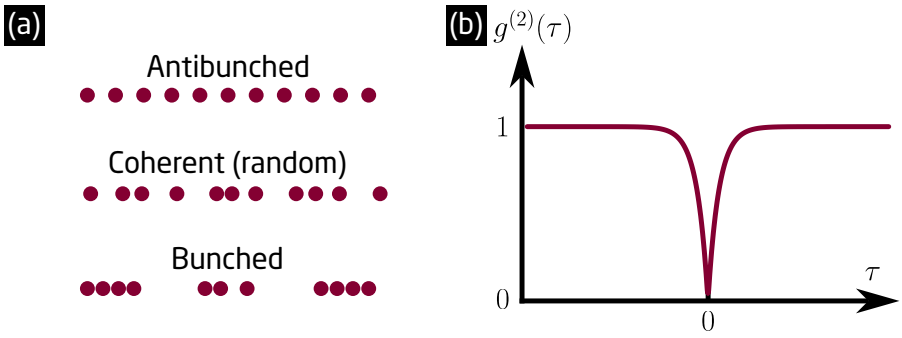

Figure 2.14: **a**, A schematic comparison of the photon streams for antibunched, coherent, and bunched light (top to bottom). The description *random* emphasizes the random time intervals between consecutive photons that follow the Poissonian statistics. For the antibunched light, the intervals are more uniform, while for the bunched light, they tend to clump together. **b**, The $g^{(2)}(\tau)$ function for an ideal single-photon source.

Antibunched light

As can be seen in Fig. 2.14a, the intervals between photons in the investigated antibunched beam are more regular compared to the coherent light and random intervals. The long time intervals translate to a small probability of detecting coincidences at small τ values which gradually increases with τ. This can be written in terms of $g^{(2)}(0)$ values as

$$g^{(2)}(0) < g^{(2)}(\tau), \tag{2.78}$$

$$g^{(2)}(0) < 1, \tag{2.79}$$

being a clear violation of the previously derived equations Eq. (2.75) and Eq. (2.76).

The first observation of photon antibunching in a resonance fluorescence experiment using the HBT configuration was shown in 1977 for a sodium atom by Kimble et al. [261]. When applied to evaluate the single-photon emission, the $g^{(2)}(\tau)$ function describes the purity P of this emission, defined as

$$P = 1 - g^{(2)}(0). \tag{2.80}$$

The information is both qualitative (the emitted photons are considered *single* if $g^{(2)}(0) < 0.5$) and quantitative (*to what extent* the photons are single), i. e., how pure the emission actually is – what is the probability of multiphoton emission of the source (bunches of photons). For an ideal single-photon source, $g^{(2)}(0) = 0$, what is possible if the probability of simultaneous detection of photons at both detectors is always zero.

2.5 Quantum dot–cavity coupling

After discussion of the QD properties and of the physics of excitons confined in QDs, the focus is brought to photonic nanocavities, especially the emitter-cavity weak interaction. This discussion is relevant for the CBGs investigated in this thesis, where a QD excitation weakly interacts with the cavity mode. The basic concepts of cavity quantum electrodynamics (c-QED) are introduced in this section, starting with the introduction of relevant terms for a planar cavity and covering the concepts of cavity quality factor, Q, and Purcell factor, F_P. They stem from atom physics and atom-cavity coupling but have been successfully applied to QDs placed in resonators and coupled to their modes.

Planar cavity

The basics of cavity physics are easier to introduce for planar cavities and then to be generalized for higher-dimensional cavities. Figure 2.15 presents the scheme of a simplest, 1D (planar) cavity formed between two semi-transparent mirrors M_1 and M_2 with reflectivity R_1 and R_2. The mirrors are separated by a cavity length L_cav, which can be tuned. The medium inside the cavity has a refractive index n. The mirror geometry allows for multiple light reflections inside the cavity.

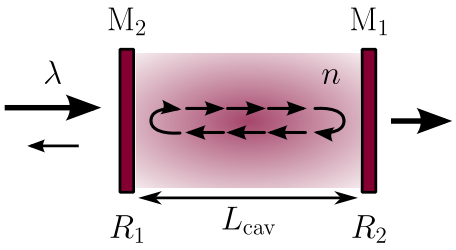

Figure 2.15: A planar cavity with two parallel end mirrors (Fabry-Pérot interferometer configuration).

Assuming the absence of absorption or scattering losses within the cavity, the cavity transmission T is equal to:

$$T = \frac{1}{1 + (4\mathscr{F}^2/\pi^2)\sin^2(\phi/2)}, \tag{2.81}$$

where $\phi = 4\pi n L_\mathrm{cav}/\lambda$ is the phase shift that the wave experiences on a cavity round-trip, and $\mathscr{F} = \pi \sqrt[4]{R_1 R_2}/(1-\sqrt{R_1 R_2})$ is the cavity finesse. The transmission is maximal ($T = 1$) if $\sin^2(\phi/2) = 0$, i. e., when $\phi = 2\pi m$, where m is an integer. The cavity length L_cav for the *resonance condition* is expressed as

$$L_\mathrm{cav} = m\lambda/2n, \tag{2.82}$$

and corresponds to the situation that traveling light is in phase during each cavity round-trip. Consequently, cavity resonance occurs when L_cav equals an integer number of intracavity half wavelengths.

The electromagnetic waves that satisfy Eq. (2.82) interfere constructively and gain a significant photon field amplitude. Such waves can be defined by the in-resonance wavelength, λ_m, or angular frequency, ω_m:

$$\lambda_m = \frac{2nL_\mathrm{cav}}{m} \xrightarrow{\omega = c/\lambda} \omega_m = m\frac{\pi c}{nL_\mathrm{cav}} \tag{2.83}$$

The cavity resonance conditions, Eqs. (2.82)–(2.83), lead to the concept of *cavity modes* – the modes of the light field that are selected by the cavity. When the resonance condition is fulfilled, the photon field intensity is enhanced by a factor of $4/(1-R)$ while outside the resonance, the intensity is diminished by a factor $(1-R)$ [262].

The spectral width of a cavity mode, $\Delta\omega$, can be estimated using the condition $T = 50\,\%$. From Eq. (2.81), this means that:

$$\phi = 2\pi m \pm \pi/\mathscr{F}, \tag{2.84}$$

hence the FWHM for the phase is

$$\Delta\phi_{\mathrm{FWHM}} = 2\pi/\mathscr{F}. \tag{2.85}$$

The $\Delta\omega$ can be calculated by exploiting the fact that the mode frequency ω_m is proportional to the phase ϕ and that the phase shift for the cavity round-trips for waves with frequencies ω_m and ω_{m-1} is 2π:

$$\frac{\Delta\omega}{\omega_m - \omega_{\mathrm{m-1}}} = \frac{\Delta\phi_{\mathrm{FWHM}}}{2\pi} = \frac{1}{\mathscr{F}}, \tag{2.86}$$

so that

$$\Delta\omega = \frac{\pi c}{nFL_{\mathrm{cav}}}. \tag{2.87}$$

The analysis of a Fabry-Pérot cavity shows that two figures of merit describe the properties of a linear cavity, the resonant mode frequency, ω_m, and the cavity finesse, $\mathscr{F}$. The latter controls the width of a cavity mode $\Delta\omega$. However, it is helpful to introduce the cavity quality factor, Q, defined as:

$$Q = \frac{\omega}{\Delta\omega}. \tag{2.88}$$

The Q factor is a figure of merit analogous to the finesse of a 1D cavity but working also for cavities of higher dimensions.

In the case of $R_1 = R_2 \equiv R \approx 1$, photons travel multiple times in the cavity before escaping through either of the mirrors. The cavity photon number decays exponentially with a time constant τ_{cav} being the cavity photon lifetime [262]:

$$\tau_{\mathrm{cav}} = \frac{nL_{\mathrm{cav}}}{c(R-1)}. \tag{2.89}$$

From this immediately follows the definition of photon decay rate κ:

$$\kappa = \frac{1}{\tau_{\mathrm{cav}}}. \tag{2.90}$$

By plugging Eq. (2.89) and Eq. (2.90) into Eq. (2.87) it can be found that for $R \approx 1$,

$$\Delta\omega = \kappa, \tag{2.91}$$

so that the κ controls the mode width $\Delta\omega$.

Emitter-cavity interaction

In this section, a basic model of c-QED is considered: the interaction between a cavity and an emitter (an atom or a QD) placed at the cavity center. The emitter can emit and absorb photons to and from the cavity mode. A particularly interesting situation is the one when the emitter emission energy overlaps with the energy of one of the cavity modes. In this case, the resonant exchange of energy between the emitter and the cavity mode is possible, being the source of the emitter-cavity coupling. The c-QED establishes that three parameters control the relative strength of this resonant interaction:

- the emitter-photon coupling parameter g_0,
- the photon decay rate κ,
- the non-resonant photon decay rate γ.

These parameters govern the dynamics of the system, and two limiting cases of the coupling can be described, depending on the relation between photon losses (κ, γ) and the interaction strength g_0:

- the strong coupling limit, when $g_0 \gg \max(\kappa, \gamma)$, and

- the weak coupling limit, when $g_0 \ll \max(\kappa, \gamma)$.

Based on this, there are two possibilities regarding the reversibility of the photon emission process. When photons are re-absorbed by the emitter before they leave the cavity, the emission process is reversible – it is the so-called *strong coupling* regime. On the other hand, in the *weak coupling* regime, photon emission is irreversible, as in spontaneous, free-space emission.

Figure 2.16a presents the scheme of a cavity with a two-level system (an emitter) placed at the cavity center, where the optical field density is maximal. The V_0 denotes the geometrical mode volume.

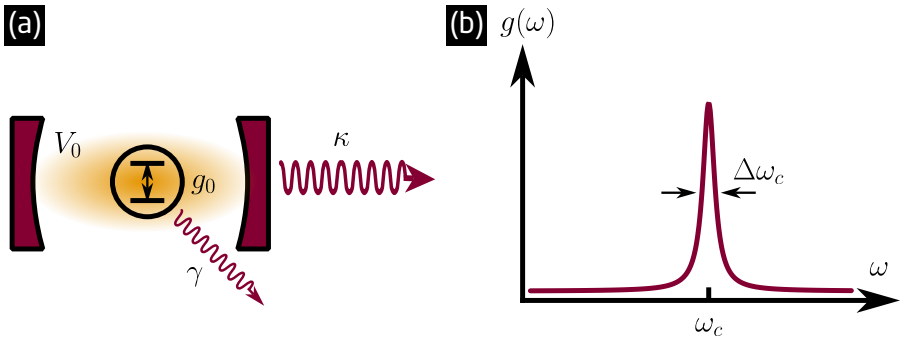

Figure 2.16: **a**, A two-level system (an emitter) in an optical cavity. **b**, Density of photonic states $g(\omega)$ as a function of the wave frequency for an optical cavity, with a mode of width $\Delta\omega_c$ visible at ω_c.

Photon losses κ, γ

Photon decay rate κ As can be seen from Eq. (2.88) and Eq. (2.91), the photon decay rate is governed by the same properties that determine the Q factor; indeed,

$$\kappa = \omega/Q, \tag{2.92}$$

so that a high-Q cavity leads to low κ.

Non-resonant photon decay rate γ The loss of photons due to the non-resonant decay with the rate γ can originate in several factors, among them are:

- the spatial mismatch between the direction of the emitted photon and the cavity mode,
- the spectral mismatch between the emitted photon energy and the cavity mode energy, for example, due to the radiative decay from other levels of the emitter, or the non-radiative decay. In this case, the two-level approximation is no longer valid.

Emitter-photon coupling strength g_0

Quantum harmonic oscillator and vacuum field oscillations To develop the theory on the coupling parameter g_0 in c-QED, it is instructive to recall a few important models of quantum optics, such as the quantum harmonic oscillator and zero-point vacuum field oscillations. It is a well-known property of a quantum harmonic oscillator that its energy is quantized in units of $\hbar\omega$:

$$E_n = \left(n + \frac{1}{2}\right)\hbar\omega. \tag{2.93}$$

From this equation, the oscillator zero-point energy of $(1/2)\hbar\omega$ is obtained. This energy is always present, even if no photons are excited ($n = 0$). In quantum optics, this energy is considered to originate from the random fluctuations of the electric field, called the vacuum field $\boldsymbol{E}_{\text{vac}}$. The field amplitude can be derived by taking a few assumptions, which are repeated here.

One can consider an evacuated optical cavity of mode volume V_0 with a negligible contribution of the thermal energy E_{th} to the total oscillator energy E_n ($E_{\text{th}} \ll E_n$). Additionally, if no additional energy sources are present, electromagnetic modes will be in the $n = 0$ state. Then, the total electric field energy in the cavity is $\int \frac{1}{2}\epsilon_0 E_{\text{vac}}^2 \, \mathrm{d}V_0$. However, the time-averaged energy contributions are equal for the electric and magnetic field, so that one can equate them to the energy of a quantum harmonic oscillator given in Eq. (2.93):

$$2 \times \int \frac{1}{2}\epsilon_0 E_{\text{vac}}^2 \, \mathrm{d}V_0 = \frac{1}{2}\hbar\omega, \tag{2.94}$$

and get

$$E_{\text{vac}} = \sqrt{\frac{\hbar\omega}{2\epsilon_0 V_0}}, \tag{2.95}$$

which connects the magnitude of the vacuum field $\boldsymbol{E}_{\text{vac}}$ with the cavity mode volume V_0.

Calculations of g_0 The zero-point fluctuations of the magnitude of the electromagnetic field $\boldsymbol{E}_{\text{vac}}$ are the source of the interaction between the emitter and the vacuum field that exists in the cavity. The energy interaction ΔE between the electric field $\boldsymbol{E}_{\text{vac}}$ and the electric dipole $\mathbf{d}$ with the dipole moment $\boldsymbol{\mu}$ of $\mu_{if,x} = -e\langle i|x|f\rangle$, with $|i\rangle$ and $|f\rangle$ being again the initial and final states, is[21]:

$$\Delta E = |\mu_{if}\boldsymbol{E}_{\text{vac}}|. \tag{2.96}$$

On the other hand, $\Delta E = \hbar g_0$, so applying Eq. (2.95):

$$g_0 = \sqrt{\frac{\mu_{if}^2\omega}{2\epsilon_0\hbar V_0}}, \tag{2.97}$$

which shows that the coupling strength g_0 depends on μ_{if}, ω, and V_0.

Strong coupling condition Assuming that the dominant photon loss mechanism is the photon decay with the rate κ, from Eq. (2.92) it follows that in the strong coupling regime $g_0 \gg \omega/Q$, and using Eq. (2.97):

$$Q \gg \sqrt{\frac{2\epsilon_0\hbar\omega V_0}{\mu_{if}^2}}, \tag{2.98}$$

imposing strict requirements on the cavity Q factor to observe strong coupling between the emitter and the cavity mode. Strong coupling is central to many physical phenomena and was also observed for QDs in micropillars [263], 2D photonic crystals [171, 264], and in open cavities [265], however, it will not be described further and the subsequent discussion will focus on weak coupling.

Weak coupling

This section aims to derive the formula for the Purcell factor. As stated in the previous section, the weak coupling condition is $g_0 \ll \max(\kappa, \gamma)$. Therefore, the characteristic emitter-cavity interaction time ($\sim 1/g_0$) is longer than the characteristic photon decay time at which photons are lost from the cavity τ_{cav} (if cavity photon decay is the main mechanism of photon losses) so that emission of a photon is irreversible. This situation is similar to the emission into free space, and so it is valid to treat this kind of interaction by the perturbation theory.

[21] Cf. Eqs. (2.47)–(2.49).

Free-space spontaneous emission

The theory of dipole emission into the free space is a good starting point for considering the emitter's spontaneous emission into the cavity mode. As defined in Eq. (2.45), the transition rate determined by Fermi's golden rule is $\Gamma = 2\pi/\hbar^2 |M_{if}|^2 g(\omega)$ and the photon density of states $g(\omega)$ for the free space is

$$g(\omega) = \frac{\omega^2 V_0}{\pi^2 c^3}. \tag{2.99}$$

One can take the vacuum field $\boldsymbol{E}_{\text{vac}}$ for $\boldsymbol{E}_0$ in the absence of other sources. Applying Eq. (2.47) and Eq. (2.95), and averaging over all possible dipole orientations with respect to the field direction leads to transition matrix element M_{if} of

$$M_{if}^2 = \frac{1}{3}\mu_{if}^2 \boldsymbol{E}_{\text{vac}} = \frac{\mu_{if}^2 \hbar\omega}{6\epsilon_0 V_0}. \tag{2.100}$$

Based on Eq. (2.45), the transition rate Γ and radiative recombination lifetime τ are now:

$$\Gamma^{\text{free}} = \frac{1}{\tau} = \frac{\mu_{if}^2 \omega^3}{3\pi\epsilon_0 \hbar c^3}. \tag{2.101}$$

It shows that Γ^{free} is proportional to ω^3 and to μ_{if}^2.

Purcell effect

The Purcell effect describes a change to the spontaneous emission properties of an emitter in the weak coupling limit. The first considerations of this problem for a two-level atom interacting with a single-mode[22] resonant cavity were performed by E. M. Purcell in 1946 [120].

The perturbative approach can be applied in the weak coupling regime, similar to the calculations performed in the previous section. We consider a cavity mode of frequency ω_c and quality factor Q. Fig. 2.16b shows the photon density of states $g(\omega)$ for such a cavity, and the integration of the photon density of states function over all frequencies for a single-mode cavity must yield 1:

$$\int_0^\infty g(\omega)\,\mathrm{d}\omega = 1. \tag{2.102}$$

This condition is satisfied by a normalized Lorentzian function:

$$g(\omega) = \frac{2}{\pi\Delta\omega_c} \frac{\Delta\omega_c^2}{4(\omega-\omega_c)^2 + \Delta\omega_c^2}, \tag{2.103}$$

and if the emission frequency of an emitter ω_0 is equal to the cavity frequency $\omega_0 = \omega_c$, the $g(\omega = \omega_0)$ reduces to:

$$g(\omega_0) = \frac{2}{\pi\Delta\omega_c}, \tag{2.104}$$

and on applying Eq. (2.88),

$$g(\omega_0) = \frac{2Q}{\pi\omega_0}. \tag{2.105}$$

The same reasoning as for an emitter in free space can be applied here, leading to the transition matrix element M_{if} calculated in analogy to Eq. (2.47) and Eq. (2.100) as

$$M_{if}^2 = \xi^2 \mu_{if}^2 \boldsymbol{E}_{\text{vac}}^2 = \xi^2 \frac{\mu_{if}^2 \hbar\omega}{2\epsilon_0 V_0}, \tag{2.106}$$

[22]The single-mode assumption means that there is only one mode of the cavity in the spectral vicinity of the emitter frequency. Potential other modes are neglected in this analysis.

where the factor ξ is the normalized dipole orientation:

$$\xi = \frac{|\mathbf{d} \cdot \boldsymbol{E}_0|}{|\mathbf{d}||\boldsymbol{E}_0|}, \tag{2.107}$$

and ξ^2 averages to 1/3 for a dipole randomly oriented in free space.

Applying the Lorentzian line shape, Eq. (2.103), the Q factor definition, Eq. (2.88), and transition matrix element M_{if}, Eq. (2.106), into the Fermi's golden rule, Eq. (2.45), the cavity transition rate Γ^{cav}:

$$\Gamma^{\text{cav}} = \frac{2Q\mu_{if}}{\hbar\epsilon_0 V_0}\xi^2 \frac{\Delta\omega_c^2}{4(\omega_0 - \omega_c)^2 + \Delta\omega_c^2}. \tag{2.108}$$

The Purcell factor F_{P} is defined as the ratio of transition rates for the emitter placed in a cavity, Γ^{cav}, and in free space, Γ^{free}:

$$F_{\text{P}} = \frac{\Gamma^{\text{cav}}}{\Gamma^{\text{free}}} = \frac{\tau^{\text{free}}}{\tau^{\text{cav}}}. \tag{2.109}$$

Therefore, for $F_{\text{P}} > 1$, the emission rate for an emitter in a cavity is enhanced (the characteristic lifetime τ^{cav} is shorter than τ^{free}) due to high photon density of states $g(\omega)$ at the cavity mode frequency.

Taking into account that $c/\omega = \lambda/2\pi n$, with λ being the free-space wavelength and n the refractive index of the cavity medium, and combining Eq. (2.101) and Eq. (2.108):

$$F_{\text{P}} = \frac{3Q}{4\pi^2 V_0}\left(\frac{\lambda}{n}\right)^3 \xi^2 \frac{\Delta\omega_c^2}{4(\omega_0 - \omega_c)^2 + \Delta\omega_c^2}. \tag{2.110}$$

This equation simplifies at resonance ($\omega_c = \omega_0$) and for $\xi = 1$ (dipole parallel to $\boldsymbol{E}_0$):

$$F_{\text{P}} = \frac{3Q}{4\pi^2 V_0}\left(\frac{\lambda}{n}\right)^3, \tag{2.111}$$

what is the final result of the calculations. Finally, based on Eq. (2.110), the requirements for F_{P} maximization and emitter-cavity coupling can be formulated as in Box 6.

Box 6: Requirements for maximization of the emitter-cavity coupling in the weak regime.

- **Maximization of achievable F_{P}:** a cavity should have a high quality factor Q and small modal volume V_0,
- **Dipole orientation:** the dipole $\mathbf{d}$ should be oriented parallel to the mode electric field $\boldsymbol{E}_0$ (maximal ξ in Eq. (2.107)), cf. point 4 in Box 4,
- **Spectral overlap:** the dipole transition frequency ω_0 should be equal to the cavity mode frequency ω_c for maximization of the Lorentzian term in Eq. (2.110).

Additionally,

- **Emitter placement:** the dipole should be placed at the point where the mode field $\boldsymbol{E}_0$ has maximal magnitude (typically in the cavity center).

CHAPTER 3

Methods

This Chapter describes the nanofabrication of QDs structures, including the epitaxial growth of QDs and the following processing. First, the crucial MOVPE process is described, followed by the full fabrication description with a summary in the form of a scheme. The subsequent section describes optical setups and tools used to characterize the fabricated structures and their spectroscopic investigations. This includes µPL (temperature-, excitation-power dependent, and polarization-resolved) and all its variations, such as macro-PL, time-resolved photoluminescence (TRPL), and imaging of µPL. Finally, the methods used for quantum optics experiments are described, such as $g^{(2)}(\tau)$ measurements, determination of η, and formulæ used to determine the single-photon purity P.

3.1 Fabrication of structures

All of the articles included in this research have utilized structures fabricated at the DTU Nanolab clean room, with the exception of P. Holewa *et al.*, *Optical and Electronic Properties of Symmetric InAs/(In,Al,Ga)As/InP Quantum Dots Formed by Ripening in Molecular Beam Epitaxy: A Potential System for Broad-Range Single-Photon Telecom Emitters*, **Physical Review Applied**, 14, 6 (2020)[1], for which the QDs have been grown at the University of Kassel in Germany.

Epitaxial growth

The QDs were grown in the low-pressure TurboDisc® rotating disk MOVPE reactor. The group V sources were hydride gases such as phosphine (PH_3), and arsine (AsH_3). Phosphorous was also supplied as metalorganic vapors of tertiarybutylphosphine, $(CH_3)_3CPH_2$ (TBP). Group III sources are metal-organic alkyls:

1. TMIn – solid,
2. trimethylgallium, $Ga(CH_3)_3$ (TMGa) – liquid,
3. trimethylaluminium, $Al_2(CH_3)_6$ (TMAl) – liquid,

with H_2 as a carrier gas.

The MOVPE was operated under the mass transport limit, i. e., the temperature of a rotating substrate is high enough that all the incoming precursors dissociate into the species. Additionally, due to the volatility of group V species (and constant dissociation from the heated crystal lattice), the crystal growth is governed by the group III species, with a group V overpressure – the molar ratio between the group V and group III species (the V/III ratio) typically $\gg 1$. Typical growth temperatures are in the range of 600-650 °C. However, to reach an extremely low QDs density, the growth temperature must be lowered, approaching the reaction limit of epitaxial growth. In this limit, the low substrate temperature limits the efficiency of group III precursor dissociation.

MOVPE reactor

The scheme of the MOVPE system employed in this thesis is shown in Fig. 3.1. In this system, hydrides are supplied from the house gas lines and can be diluted by the H_2 to obtain the desired

[1]This article is included in this thesis, p. 111.

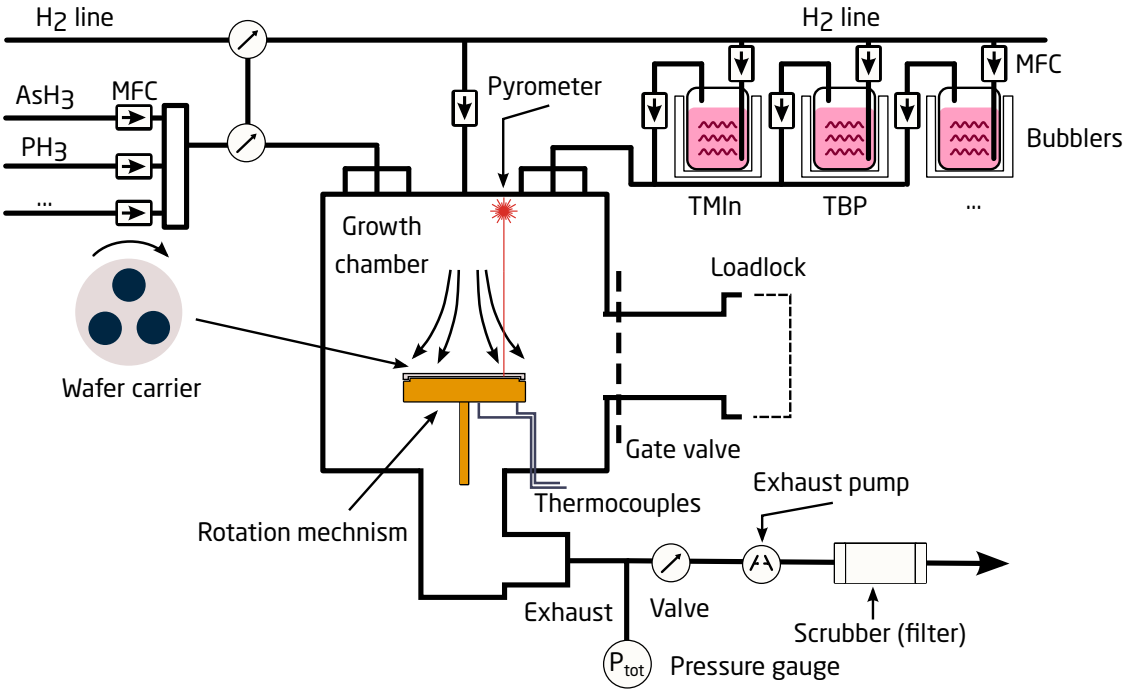

Figure 3.1: The scheme of the MOVPE TurboDisc® reactor used to grow the QDs investigated in this thesis.

mass flow. On the other hand, alkyls are stored as metal-organic liquids in the bubblers while H_2 is supplied into the bubbler and used to saturate the alkyl vapor. H_2 subsequently transports it to the growth chamber. Once the group III and V precursors are injected into the growth chamber, they are transported in the laminar flow to the boundary layer formed above a rotating wafer carrier with heated substrates, where they mix. At the wafer surface, several processes take place [181], starting with the pyrolysis (dissociation) of the precursors into elemental III and V group species, followed by the surface and gas phase diffusion and adsorption to and desorption from the surface. These processes are described in Section 2.1. Finally, the species are incorporated into the growing crystal. The exhaust gases are then sent into the filter (scrubber system), which removes highly toxic chemical compounds and elements.

The mass flows are controlled by mass flow controllers (MFCs) for all precursors to reach the transport-limited growth conditions at the boundary where the new adatoms join the crystal lattice. An inductively-heated graphite susceptor conducts the heat to the wafers, and two tools provide temperature T control:

- The emissivity-correcting pyrometer – is used to determine the wafer's temperature from a measurement of the thermal emissivity and the reflectance of the laser from the wafer surface. The temperature is determined using a patented solution [266], and the theory of this method is outlined in [267]. This method can be used for $T \gtrsim 510\,°C$.

- A pair of thermocouples located close to the bottom part of a rotating susceptor with wafers.

As the more accurate temperature determination using the pyrometer can be used only for high T, the thermocouples have to be carefully calibrated to gain the T and growth control for low-temperature ($< 510\,°C$) QDs.

The employed MOVPE reactor is equipped with a load lock to isolate the growth chamber from the clean room. This prevents exposing the growth chamber to the ambient atmosphere and speeds up loading and unloading the wafers.

Tuning the quantum dot growth parameters

To achieve Objective 1. of this thesis, the growth parameters of QDs are determined through empirical optimization, resulting in low QD density and emission at the telecom C-band. The following parameters are crucial to reach the desired QD properties:

1. **Growth temperature** – refers to the substrate temperature T during QD nucleation,
2. **Layer thickness** h – determined by the amount of group III elements (indium) supplied to the substrate under As ambient,
3. **V/III ratio** – the ratio of molar fluxes for the V and III groups, which is typically larger than 1 due to the high volatility of group V species,
4. **QD growth interruption conditions** – the conditions applied directly after the deposition of the QD material, before the InP capping, allowing the physical processes on the surface to last for a certain time. These conditions include GI (or annealing) time, temperature, and the As over-pressure.

Their influence on the properties of S-K InAs/InP QDs, investigated in [268], was introduced in Section 2.2 and, based on theory outlined in [195], can be summarized as:

1. **Growth temperature** is a crucial parameter that affects the reaction rates and thermodynamics of the system. It determines the density of QDs, inducing an opposite effect for sub- and supercritical QD. Before reaching the critical thickness h_c, the density increases with temperature, but after that, the opposite happens. The relaxed QD size R_g has a reverse temperature dependence but for subcritical QDs, attaining R_g requires a long exposition time. The growth temperature has no significant impact on h_c due to the temperature-independent WL thickness in the S-K growth of QDs.
2. **Layer thickness** h determines how much material is disposable for WL formation and following QDs nucleation. Crucial here is exceeding the h_{eq} thickness. Afterward, the relation between h and critical thickness h_c determines the nucleation regime: subcritical, supercritical, or near-critical ($h \sim h_c$). In this thesis, it was found that the near-critical regime is especially useful for reducing the QD density, primarily through the tuning of the V/III ratio. In the InAs/GaAs system characterized by a large lattice mismatch $\epsilon_0 = 7.2\%$, h_{eq} and h_c are similar, with $h_{eq} \approx 1.5$ ML and $h_c \approx 1.7$ ML [195, 269]. However, in the InAs/InP system with $\epsilon_0 = 3.2\%$, there is a larger difference between them [270]: $h_{eq} \approx 3$ ML and $h_c \approx 4$ ML. In the InAs/InP system, when the InP is exposed to the As flow, the considerable As-P interdiffusion leads to the formation of a 2D In(As,P) layer. The scanning transmission electron microscopy (STEM) analysis of structures analogous to those investigated in the thesis evidences that the In(As,P) layer thickness amounts to 4 ML with the composition of $InAs_{0.7}P_{0.3}$ [268]. The nucleation of QDs solely under As flow (without supplying In) was not observed. It was also shown that h_{eq} is achieved when less than 1.1 ML of InAs is deposited on the 4 ML-thick $InAs_{0.7}P_{0.3}$ layer, while passing the critical thickness h_c requires depositing of 1.1-1.65 ML of InAs [268].

   The QD density rapidly increases with h for $h < h_c$ and saturates above it, provided that the temperature is kept constant.
3. **V/III ratio** impacts the surface reconstruction [271] and affects, i. a., the migration of adatom migration. For the QDs investigated in this thesis, it allowed tuning the migration of indium adatoms on top of the WL, impacting the QD density heavily (two orders of magnitude). A high V/III ratio leads to the formation of QDs on the As-saturated surface, while the surface diffusion of In adatoms limits their GR (however, the influence of other surface processes on the diffusion is not fully understood). Conversely, a low V/III ratio results in an In-rich surface, and the transport of group V atoms from the gas phase limits the GR of QDs. Therefore, in this case, it is assumed that the GR is proportional to the As precursor flux F.

   The change between these regimes, particularly shifting toward high V/III ratios, was identified as an enabling factor for achieving the low surface density for both supercritical (down

to $\sim 10^9/\mathrm{cm}^2$) and near-critical (down to $\sim 10^7/\mathrm{cm}^2$) QDs at V/III = 100. The height of surface QDs, revealed by AFM, shows only minor oscillations in the range of 7-10 nm, while the density changes by two orders of magnitude.

4. **QD growth interruption conditions**. The size of QDs can be affected by changing the time of the GI (exposition time). This is due to the slower nucleation stage for the subcritical QDs. It can be controlled in a wide range without significantly impacting the surface density of islands by tuning the duration of the GI. This is possible because the mean lateral size of QDs is smaller than R_g in the case of immediate (or fast enough) overgrowth or cooling the structure down after switching off the In flux. The density of QDs should remain constant in the supercritical regime, as the island growth is much longer than the nucleation stage. However, the lateral QD size should increase when the exposition time is increased.

The above-listed parameters are determined for a specific MOVPE reactor and wafers. The parasitic deposition on the walls of the growth chamber induces the time drift of growth parameters and can induce the need for their fine-tuning. Additionally, working in a reaction-limited regime during the QD nucleation complicates the situation even more. There are many minor factors that have to be considered, but the ones enumerated here are most commonly used as tuning knobs to calibrate the QD properties. These parameters form a multi-dimensional space of parameters that often has no obvious influence on QD properties. Still, they require high tuning precision, and the strategy employed in this thesis was to change only one parameter at a time. For example, changing the temperature of the substrate by 1 °C during the QD material deposition can have a considerable impact on the properties of the obtained QDs, reflected in their emission energy.

Typical epitaxial growth procedure

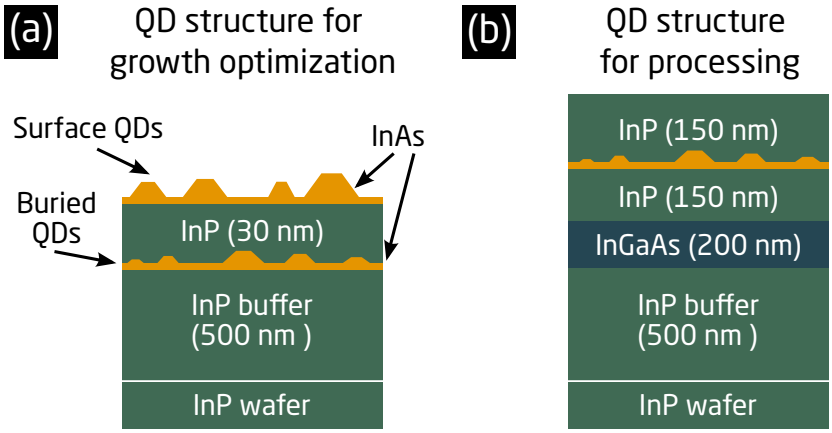

Figure 3.2: Cross-sections of the structures with QDs after the epitaxial growth. **a**, Structure typical for the optimization of epitaxial growth parameters. The structure contains buried QDs for optical studies and surface QDs for AFM characterization. **b**, Structure ready for subsequent processing steps, with InGaAs etch stop layer and buried QDs inside the InP cavity.

In Fig. 3.2, the cross-sections of structures with QDs grown for various purposes are compared. First, the optimal QD growth parameters need to be established. For that, the short recipe begins with thermal annealing and deoxidation of the (001)-oriented InP wafer followed by the growth of the InP buffer layer. Next, the optically active buried QDs are grown, capped by a few tens of InP ($\sim$30 nm). Nominally the same QDs are deposited atop the InP cap for structural characterization. To prevent any other surface reaction that could alter the size, shape, and density of surface QDs, the structure is cooled down immediately after the deposition step. The cross-section for this structure is shown in Fig. 3.2a.

The AFM is a standard surface QDs characterization tool that is sometimes supported by SEM. Although there is no direct correlation between the sizes of buried and surface QDs due to the inevitable impact of surface processes during cooling, the QD density in both layers is comparable. For more details on the comparison between the height of the surface and buried QDs, see P. Holewa *et al.*, *Optical and electronic properties of low-density InAs/InP quantum dot-like structures devoted to single-photon emitters at telecom wavelengths*, **Physical Review B**, 101, 19 (2020)[2], where the AFM statistics can be compared with the inferred buried QD sizes, determined from the STEM image, PL spectra, and 8-band $k{\cdot}p$ modeling. In that case, the median surface QD height determined from the AFM statistics was >9 nm, while the buried QDs, according to STEM and calculations, extruded 1-6 ML (0.3-1.8 nm) above the WL.

Once the optimal growth conditions are determined (i. e., low density of few-nm-high InAs islands, with a small size distribution and minimal in-plane elongation), the growth sequence can be repeated with slight modifications needed for further processing steps. In this case, the InP buffer layer is covered by a ∼200 nm-thick $In_{0.53}Ga_{0.47}As$ sacrificial layer lattice-matched to InP that serves as an etch-stop layer during the subsequent HCl etching of InP (substrate removal). Then, the InP layer is grown to a thickness determined by the cavity design. The QDs are placed in the middle of the weak vertical InP cavity, as depicted in Fig. 3.2b.

Exemplary conditions applied for a low-temperature QD growth in the calibration configuration (Figure 3.2a) involve wafer annealing at 650 °C under the PH_3 flux. During this step, the wafer rotation is increased to 1000 revolutions per minute (rpm). The deposition of a ∼500 nm-thick InP buffer layer on a substrate at 610 °C follows. Then, the temperature is decreased for the growth of a QD layer (e. g., at 483 °C) under the PH_3 flux. After reaching the growth temperature, the surface is stabilized under TBP for 180 s, then, under AsH_3 for 27 s.

The QDs can be nucleated either in the S-K growth mode or DE after deposition of InAs under TMIn and AsH_3 flows. Once nucleated, QDs are annealed for e. g. 60 s in AsH_3 ambient at the growth temperature. The minimal GI time is ∼3 s due to the switching of TBP flux between the QD material deposition and InP spacer. The employed GI can have a more complex temperature profile, for example, a temperature increase for 30 s to 515 °C and continuing the annealing for another 30 s. Subsequently, the InP capping layer is deposited, 10 nm at 515 °C, with the remaining desired thickness (typically 20 nm) deposited after increasing the temperature to 610 °C. This ends the growth sequence for the structure desired for further processing. However, for the test structure devoted to QD optimization, an additional QD layer is deposited on the capping layer at nominally the same growth condition mentioned above. After optional surface QD annealing, the temperature is immediately decreased, the susceptor rotation is slowed down, and it can be transferred from the growth chamber to the load lock.

Processing of the structures with quantum dots

Once the optimal growth parameters for the QDs growth are determined, and the processing-ready structure is grown, as presented in Fig. 3.2b, the subsequent fabrication steps are performed. There are two principal aims for this fabrication:

1. integration with a metallic mirror and with the Si platform to increase the photon extraction efficiency η, addressing the Objective **2.** of the thesis,

2. etching of cavities in the InP layer, addressing the Objective **3.**

The procedure described in this Section is a summary of the processing performed for the first time in P. Holewa *et al.*, *Bright Quantum Dot Single-Photon Emitters at Telecom Bands Heterogeneously Integrated with Si*, **ACS Photonics**, 9, 7 (2022)[3] and developed further as outlined in P. Holewa *et al.*, *Scalable quantum photonic devices emitting indistinguishable photons in the telecom C-band*, arXiv:2304.02515 (2023)[4]. A simplified representation of the process flow can be seen in Fig. 3.3.

[2]This article is included in this thesis, p. 95.
[3]This article is included in this thesis, p. 143.
[4]This article is included in this thesis, p. 153.

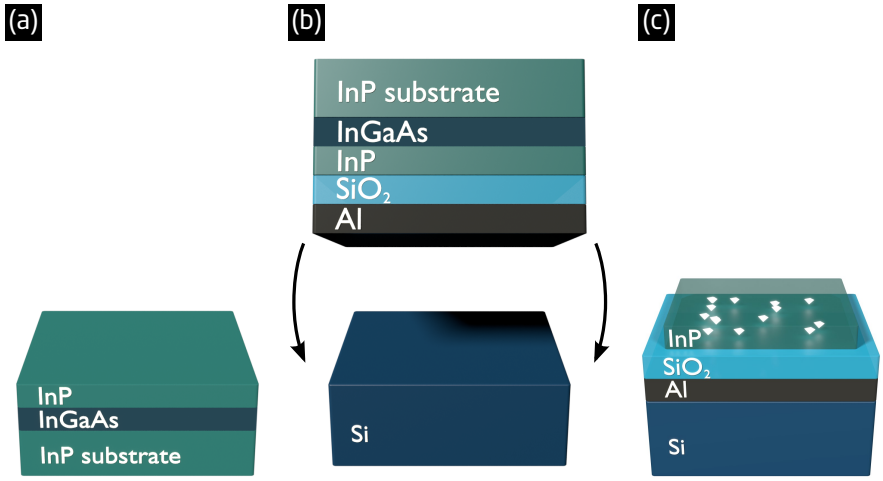

Figure 3.3: Schematic of the process flow applied to integrate the QDs with the Si substrate and to deposit the aluminum layer.

Deposition of SiO_2 and Al

The fabrication starts with an epitaxially grown structure shown in Fig. 3.3a – equivalent to Fig. 3.2b. At this point, it is cleaved into chips (quarters of a 2-inch wafer) to save the material for future processing iterations. To integrate the QD structure on Si, the SiO_2 layer is deposited on top of the InP-based structure using plasma-enhanced chemical vapor deposition (PECVD) at the rate of ∼1 nm/s with the thickness determined by the cavity calculations. This layer is covered by a 100 nm-thick (at least 20 nm, according to the modeling) aluminum layer deposited via electron-beam evaporation at the rate of 9 nm/s.

Integration with Si

After flipping the structure bottom-up, it is bonded to the Si substrate, see Fig. 3.3b. The bonding procedure includes, first, spin coating of the AP3000 adhesion promoter on Si and InP wafers, and benzocyclobutene (BCB) on Si wafer, and second, bonding of both structures at 250 °C in the vacuum under an applied force of ∼2 kN. Plasma ashing disposes of superfluous BCB from the back side of the InP wafer. Afterward, to achieve the InP membrane with QDs, the InP substrate is removed by 60-70 min-long dip in HCl followed by the InGaAs sacrificial layer etching for 30 s in (10%) H_2SO_4:H_2O_2 = 1:1[5]. Deionized (DI) water rinsing and drying with a nitrogen gun clean the structure.

At this point, the structure is a planar InP membrane with InAs QDs. It is positioned on top of the SiO_2 layer and the Al mirror underneath. The structure is integrated with the Si carrier and ready for further processing – fabrication of either mesas (for non-deterministic approach, see P. Holewa *et al.*, *Bright Quantum Dot Single-Photon Emitters at Telecom Bands Heterogeneously Integrated with Si*, **ACS Photonics**, 9, 7 (2022)[6]), or of imaging fields for µPL imaging, as in P. Holewa *et al.*, *Scalable quantum photonic devices emitting indistinguishable photons in the telecom C-band*, arXiv:2304.02515 (2023)[7]. The structure with imaging fields is shown in Fig. 3.3c with bright pyramids that represent InAs QDs randomly distributed on the InP surface.

[5]Equivalent to H_2SO_4:H_2O_2:H_2O=1:8:80.
[6]This article is included in this thesis, p. 143.
[7]This article is included in this thesis, p. 153.

Electron-beam lithography

In this thesis, the EBL process with the investigated structures was performed using the JEOL JBX-9500FSZ e-beam writer. The crucial parameters of the system are the acceleration voltage of 100 kV, beam current in the range of 0.1-60 nA, minimum beam diameter of 4 nm (for 100 pA beam current), stage position accuracy of 0.5 nm, and writing field area of (1×1) mm^2 (enabling the exposure without stitching errors). The available dose range is 10^{-3}-10^5 µC/cm^2 with a scanning speed of 100 MHz. Together with automatic beam optimization and proximity error correction, these parameters allow obtaining lines down to 10 nm with the Chemical Semi Amplified Resist (CSAR) AR-P 6200 resist. A comprehensive review of the principles of the EBL can be found in Ref. [272].

Generally, the standard EBL process flow requires spin-coating the resist, exposing it with the e-beam, and developing it. For the hydrogen silsesquioxane (HSQ) negative-tone resist, the manual spin-coaters were used with the adjusted recipe to fabricate the desired resist thickness (100 nm). For the positive-tone resist, the CSAR resist was used, and the automatic spin-coaters were employed. In each case, the wafers were baked before the spin-coating.

The spin-coated chips were loaded into the aluminum or titanium chip cassette of the JEOL JBX-9500 EBL system. Once the cassette is loaded into the load lock (by a clean-room employee, according to the safety rules), the automatic handling system transfers it into the process chamber and onto the stage. Then, the semi-automatic calibration of the system is executed, which involves, i. a., measurements of the e-beam current, stage drift, height map, detection of stage AMs, etc. Additional steps are needed for the exposure with alignment, which is indispensable for the deterministic fabrication of cavities. They include the detection of wafer global AMs ("P" and "Q") and chip AMs. Once the machine is ready, the magazine file (created from the mask file[8] and system-specific exposure instructions files[9] are used to control the e-beam. After the exposure, the cassette is unloaded, and the exposed resist is developed. HSQ requires 2 min 40 s dip in water-diluted AZ400K, while CSAR is developed automatically for 60 s in TMAH.

ICP-RIE etching

The structures were etched in high-power inductively coupled plasma-reactive ion etching (ICP-RIE). This technique provides precise control over the physical and chemical etching of the material, resulting in a high-quality pattern transfer. It is a reactive ion etching (RIE) modification commonly used for semiconductor manufacturing. In the ICP-RIE, radicals and ions are generated by the plasma ignition inside the process chamber. They are highly reactive species that are accelerated toward the platen electrode that holds the structure.

While in RIE, there is only one power supply to generate the plasma and to accelerate the species toward the electrode, in ICP-RIE, independent control of plasma generation (flux of species) and acceleration (ion energy) is established with an additional power supply. Therefore, a much higher density of radicals and ions is achievable in ICP-RIE compared to RIE (2-3 orders of magnitude) with lower ion bombardment energy and reduced chamber pressure. Hence the ICP-RIE processing is easier to control and more flexible, providing minor damage to the sample and high etch rates.

The process recipe applied in processing the structures with QDs was developed in DTU (optimized platen power, established etch rates) and slightly adjusted for the current needs. For the etching of InP, the HBr plasma is used, and the etching progress can be monitored with a laser point detection system if a negative-tone resist is used. There, the interferometry-based metrology of the laser beam reflected from the sample surface allows for calculating *in-situ* the thickness of the etched material and, additionally, the rapid change of the fringe oscillation period is a footprint of the material refractive index change. This allows for manually terminating the etching at the right moment, however, the signal is obtained only from a single point on the structure.

The pattern transfer to InP is performed at 180 °C as the formed etch products have to be volatile (in this case, $InBr_3$). The load lock is used, and the etching is preceded by the oxygen cleaning of the process chamber and chamber preconditioning to ensure the repeatability of etching results.

[8] The `*.gds` file.
[9] The `*.sdf` and `*.jdf` files.

Directly after the etching, the structure is transferred back into the load lock, which is vented afterward. The sample is removed from the load lock immediately as it has to be dipped promptly into the DI water to prevent the continuation of the InP etching by residual HBr species. The HSQ resist residuals can be removed in a buffered oxide etch (BOE or BHF).

Deterministic fabrication of the cavities

A similar processing has been performed during the research presented in P. Holewa *et al.*, *Scalable quantum photonic devices emitting indistinguishable photons in the telecom C-band*, arXiv:2304.02515 (2023)[10] to fabricate the structure ready for localization of QDs in µPL imaging. However, once the QD positions were determined with respect to the AMs (described in Section 3.2), the deterministic workflow at DTU is continued by the nanofabrication of cavities.

For a deterministic cavity fabrication process, a 110 nm-thick SiN_x layer is deposited in PECVD on top of InP as a hard mask, and the CSAR e-beam resist is spin-coated. The resist is exposed in EBL, using AMs in the form of InP crosses standing on SiO_2 (located close but outside the imaging fields). This step requires more attention during the EBL session as all AMs have to be of high quality for the alignment exposure to work. The resist is developed, and the cavities are transferred to the SiN_x hard mask using ICP-RIE employing SF_6 plasma. Next, the CSAR residues are removed using the Remover 1165 followed by 10 min plasma ashing for the resist descum. Subsequently, the pattern is transferred into the InP in ICP-RIE by HBr plasma.

The fabrication scheme that has been developed for the fabrication of the structures is presented in Fig. 3.4. The author of the thesis has performed all steps written in rectangles, however, the configuration of the steps was always adjusted for the specific aims. The process flow was first adapted from solutions existing at DTU and developed for the needs of the research described in P. Holewa *et al.*, *Bright Quantum Dot Single-Photon Emitters at Telecom Bands Heterogeneously Integrated with Si*, **ACS Photonics**, 9, 7 (2022)[11]. It was used to the full extent in P. Holewa *et al.*, *Scalable quantum photonic devices emitting indistinguishable photons in the telecom C-band*, arXiv:2304.02515 (2023)[12].

3.2 Optical characterization

This section provides a brief description of the optical setup configurations, which are illustrated in Fig. 3.5. The figures show a general outline of a µPL setup (Fig. 3.5a) and the imaging setup (Fig. 3.5b). The depicted µPL setup is greatly simplified and only includes essential elements. The form was chosen since the reported research required many reconfigurations and setup adjustments, so showing all used versions is impractical. Instead, the following paragraphs give details of the setups and describe the equipment used. The exemplary realizations of the µPL setups can be found in SM to the thesis papers, which are included in Appendix A.1 and Appendix A.2.

Microphotoluminescence setup

For a µPL investigation, a structure was held in a helium-flow cryostat allowing for controlled sample temperatures in the range of 4.2-360 K. The structures were optically excited through a long-working-distance, infinity-corrected, high-numerical-aperture (NA = 0.4, NA = 0.65, or NA = 0.7) microscope objective (Mitutoyo) with 20×, 50×, or 100× magnification, respectively, with one of the continuous-wave (cw) semiconductor laser diode lines: 532 nm, 640 nm, 660 nm, 787 nm, or 805 nm. The transmission of the microscope objective is ∼57 % at 1.55 µm.

For the pulsed excitation, the structures are excited either by a train of ∼50 ps-long pulses with a repetition frequency of 80 MHz or 40 MHz and the central photon wavelength of 805 nm (PicoQuant laser diode), or ∼2 ps-long pulses with a repetition frequency of 76 MHz (∼13.16 ns pulse separation) and the central photon wavelength of 830 nm (Coherent Ti:Sapphire). The great

[10] This article is included in this thesis, p. 153.
[11] This article is included in this thesis, p. 143.
[12] This article is included in this thesis, p. 153.

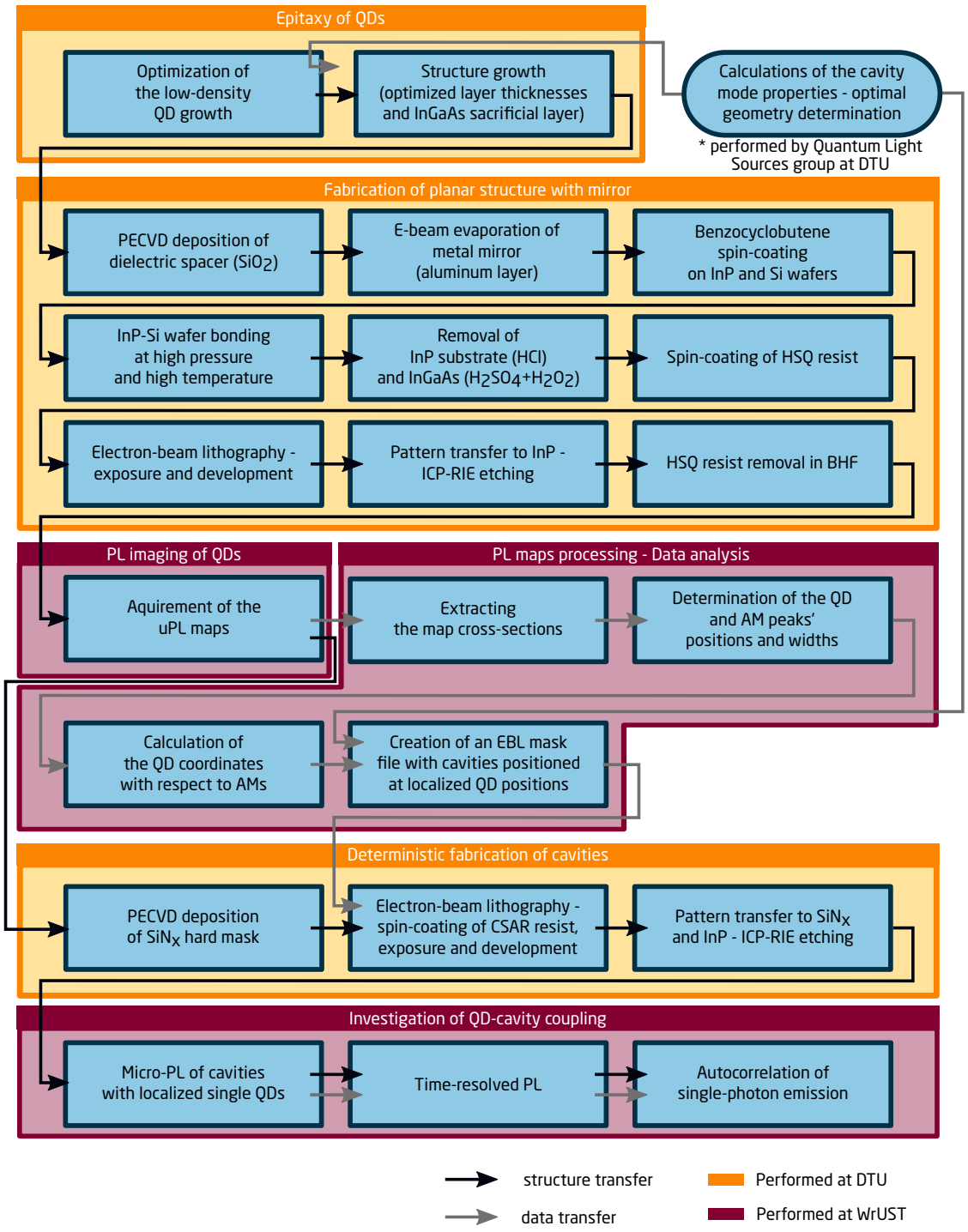

Figure 3.4: The scheme with the process flow used for the deterministic fabrication of cavities with QDs.

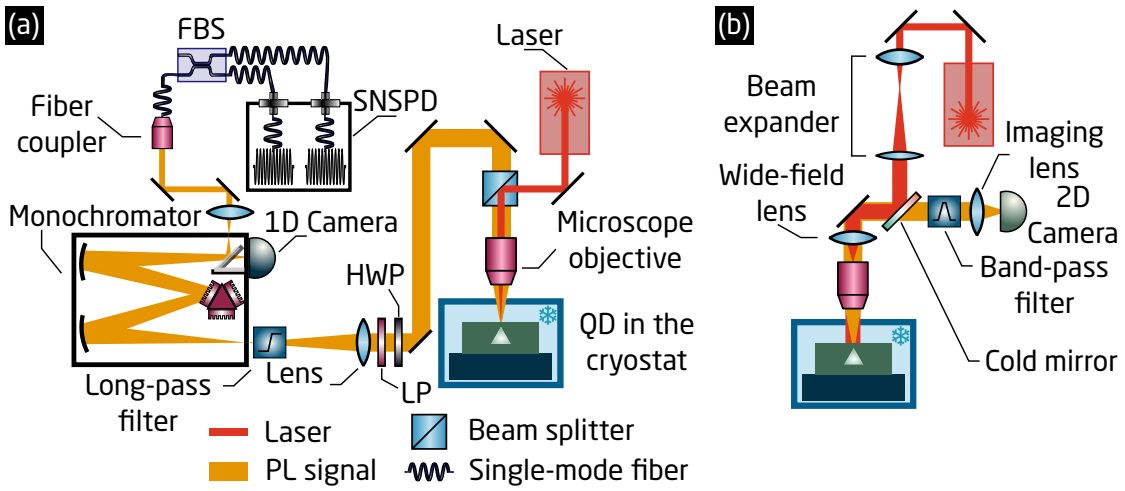

Figure 3.5: The general and simplified schemes of the µPL setups showcasing the crucial elements and comparing **a**, the typical spectroscopic configuration with **b**, the imaging configuration. HWP – half-wave plate, LP – linear polarizer, FBS – fiber beam splitter, SNSPD – a pair of superconducting nanowire single-photon detectors.

advantage of this laser is its tunability in the broad range of 700-1050 nm. The tuning range can be further extended to ∼1600 nm with the optical parametric oscillator (OPO). The estimated diffraction-limited laser beam waist at the sample surface is ∼2 µm when the laser beam is focused with a microscope objective of NA = 0.65.

Emission from the structure is collected by the same objective and directed by a set of mirrors for spectral analysis to one of the monochromators: either with a 1 m (Horiba Jobin Yvon), 0.3 m, or 0.5 m (Princeton Instruments) focal length. The monochromator is equipped with a liquid-nitrogen-cooled InGaAs multichannel array detector with the typical detection range of 0.8-1.65 µm, providing spectral resolution of ∼25 µeV for the 1 m focal length monochromator and the grating characterized by the highest dispersion (600 grooves/mm).

Identification of excitonic complexes

The µPL experiments provide various established routes to identify the transition lines visible in the spectrum. They are based on the excitation power-dependent and polarization-resolved µPL spectra. The theory underlining the expected behavior for the excitation-power dependent µPL is explained in Section 2.3. The expected behavior for the polarization series is based on lifting the spin degeneracy for a neutral exciton state by the EI, as well as lack thereof for charged complexes, which is explained in Section 2.3 and summarized in Fig. 2.10. The knowledge of calculated complexes' binding energies can support the identification by indicating the energy range where trion or biexciton emission is plausible.

A decisive proof that the observed lines originate from the same QD can be obtained by measuring the second-order cross-correlation function in a setup analogous to the one shown in Fig. 3.5a. However, the intensities of two different lines have to be cross-correlated, which means that the fiber-beam splitter (after the light filtering) is of no use and has to be removed. Instead, two monochromators are used to act as band-pass filters for the correlated lines while the signal is divided with a free-space beam splitter, with reflected and transmitted signals feeding each of them. Two fiber couplings are needed for the light that is transmitted through the monochromators.

The expected histogram for the biexciton-exciton cascade is a strong asymmetric pattern of bunching-antibunching at zero delay. Suppose X photon detection is the starting signal, and XX is the stopping one. In that case, the correlation function for negative delay reflects the probability of registering a photon emitted from X after registering a photon emitted from a XX. The correlation function increases for negative delays, reaching a maximum for $\tau < 0$ ns. This reflects the increased

probability of X emitting immediately after XX, forming the XX-X cascade. For positive delays, the correlation function has a minimum, reflecting the low probability of the X-XX cascade. Then, the function increases to 1, which corresponds to an increase in the probability of XX emission after a long time after the X emission.

For the cross-correlation of a neutral exciton X and a trion CX, the expected histogram has a dip at zero delay (antibunching) due to the exclusive nature of the complexes, with different dip rise times for positive and negative delays. Suppose X photon detection is again the starting signal and CX is the stopping one. The probability of registering a photon emitted from an exciton after the detection of the photon emitted from the trion is reflected on the negative part of the histogram delay axis and the opposite for the positive part. The cross-correlation function takes the form of a slightly asymmetric minimum reflecting the faster single-carrier capture immediately after CX emission than the three-carrier capture rate after the X emission.

The exemplary cross-correlation histograms for X-CX and X-XX are shown in Fig. S2 of the SM, included in Appendix A.1.

Degree of linear polarization

Apart from the identification of complexes, the degree of linear polarization is additional information that can be gained from the polarization-resolved µPL measurement. Generally, the polarization state of light can be described using three bases, two linear polarization $\pi_{x,y}$ basis, horizontal-vertical, $|H\rangle$, $|V\rangle$ and diagonal-antidiagonal, $|D\rangle$, $|A\rangle$, as well as the circular polarization $\sigma^{\pm}$, right-hand and left-hand circularly polarized. The polarization state of light can be conveniently described using the Stokes vector, $[S_0, S_1, S_2, S_3]$, where the total light intensity $I = S_0$, and the parameters S_1 to S_3 correspond to the dominance of one of the polarization basis states in the investigated beam. In particular, S_1 and S_2 describe the prevalence of $|H\rangle$ over $|V\rangle$ and $|D\rangle$ over $|A\rangle$ polarization, respectively,

$$\begin{aligned} S_0 &= I_H + I_V, \\ S_1 &= I_H - I_V, \\ S_2 &= I_D - I_A. \end{aligned} \tag{3.1}$$

The DOLP is defined as

$$\mathrm{DOLP} = \frac{\sqrt{S_1^2 + S_2^2}}{S_0}, \tag{3.2}$$

and can be extracted from the PL spectra as the contrast between maximum and minimum PL intensities $I_{\max}$ and $I_{\min}$ of the linearly-polarized beam normalized by the total PL intensity $I_{\max} + I_{\min}$:

$$\mathrm{DOLP} = \frac{I_{\max} - I_{\min}}{I_{\max} + I_{\min}}. \tag{3.3}$$

For QDs, DOLP is, i. a., a measure of the HH-LH states mixing.

To measure the polarization properties of emitted light, a HWP is mounted in front of a fixed high-contrast-ratio (10^6:1) LP at the monochromator entrance slit. First, the LP is placed at the entrance of the monochromator, and the diffraction grating properties determine the LP angle in order to maximize the monochromator transmission efficiency. The HWP is rotated, and in this way, the linear polarization of the signal beam is selected. Except for the information on the DOLP, this measurement also discloses the FSS energy for the X state.

Photoluminescence in the macro configuration

For the initial characterization of the structures, where the averaged spectral emission from the ensemble of QDs is analyzed, the microscope objective is replaced with an optical lens. With this solution, the estimated laser beam waist at the sample surface is much larger than in the µPL experiment, with a typical range of 100-200 µm (depending on the lens focal length, the laser beam width, and the laser wavelength).

The PL measurement is also possible in a long-wavelength spectral range, up to ∼2.1 µm via the lock-in technique, using a thermoelectrically cooled InAs-based single-channel detector. The typical reference modulation frequency is ∼2 kHz.

Imaging of the microphotoluminescence

Setup configuration

To localize the QD positions with respect to the field edges, the wide-field bright microscope configuration, presented in Fig. 3.5b, was employed. For that, the structure was placed in a standard optical cryostat mounted on a *x*-*y*-*z* movable stage for targeting fabricated fields that are imaged consecutively. The surface of the sample was illuminated non-resonantly using the high numerical aperture (NA = 0.65) high-resolution microscope objective optimized for NIR (57 % transmission, 10 mm working distance) with 50× magnification and the 660 nm laser line. First, the laser beam is shaped by a beam expander. To create a uniform laser illumination of the sample's surface, the laser is focused with an additional lens at the objective's rear to create the wide-field configuration. It provides nearly homogeneous surface illumination and high photon collection efficiency across a (50×50) µm^2 field. The same objective collects the spatially distributed QD µPL and scattered light from the field edges (used as AMs).

Subsequently, the PL signal passes through a cold mirror cutting off the laser light, while a narrow band-pass filter centered at (1550 ± 8) nm is applied to detect only QD emission at the center of the C-band. The PL signal is projected onto the NIR-optimized 2D thermoelectrically-cooled InGaAs-based camera array, characterized by a (12.8×10.24) mm^2 chip with pixels of (20×20) µm^2 in size. With the 4× magnification lens in front of the detector chip, the setup has a 200× magnification, enabling the optimal filling of the entire chip with a single projected field, hence providing optimal conditions for the QD localization. The setup can be easily changed into the spectroscopic mode by introducing a collimated laser beam on the microscope objective and directing the gathered optical signal to the monochromator equipped with a 1D InGaAs multichannel array detector, forming a configuration analogous to the one shown in Fig. 3.5a.

The field borders, treated as AMs, are also visible. After the adjustment of the data acquisition time and laser power, the µPL maps are recorded for many imaging fields. With the applied narrowband filtering, each of the fields contains only a few bright emitting spots. They can be checked in the spectroscopic configuration of the setup, and the QD character of emission is verified by the power- and temperature-dependent µPL series.

QD localization

The data analysis of the µPL maps is outlined in the Fig. 3.4. The localization of QDs is performed by taking the vertical and horizontal cross-sections of the µPL map, centered on a QD emission spot so that each cross-section contains the QD of interest and two field borders – AMs. The cross-sections are taken by averaging the signal over 10 px in the direction perpendicular to the cross-section to increase the signal-to-noise ratio (SNR). Then, the Gaussian profiles are used to find the positions of the QD and both AMs in the perpendicular directions.

It was found that the average SNR for QD emission spots is 10.6, emphasizing the importance of the 7× emission enhancement in the planar structure as compared to bulk InP, what was shown in P. Holewa *et al.*, *Bright Quantum Dot Single-Photon Emitters at Telecom Bands Heterogeneously Integrated with Si*, **ACS Photonics**, 9, 7 (2022)[13]. It is found that for the brightest 10 % of QD spots the QD position fit uncertainty is < 54 nm for horizontal and < 37 nm for vertical cross-section. The median fit uncertainty for AMs is 24.1 nm and 35.1 nm respectively, what can be translated to the 1D uncertainty of the QD localization $\Delta Q_H < 61.1$ nm and $\Delta Q_V < 53.2$ nm for both cross-sections. Then, using the formula $\Delta Q = \sqrt{(\Delta Q_h)^2 + (\Delta Q_v)^2}$, one can calculate the 2D QD localization accuracy of $\Delta Q < 80.1$ nm. Finally, taking into account the EBL alignment accuracy

[13]This article is included in this thesis, p. 143.

of $\Delta C = 40\,\text{nm}$ [273], the estimated overall accuracy of the deterministic cavity fabrication (2D CBG placement accuracy) is $\Delta R = \sqrt{(\Delta Q)^2 + (\Delta C)^2} < 90.3\,\text{nm}$.

The details on the localization algorithm, discussion of the involved uncertainties, and the accuracy of cavity positioning are given in SM for the article P. Holewa *et al.*, *Scalable quantum photonic devices emitting indistinguishable photons in the telecom C-band*, arXiv:2304.02515 (2023)[14], Appendix A.2, Section S-III. Additionally, it was found that the median width of the QD spot is only ∼35 % larger than the diffraction-limited spot size (see Appendix A.2, Section S-IV for details) what is caused most probably by the imperfect setup configuration, especially the presence of cryostat window between the QDs and microscope objective (compare with the "first generation setup" in Ref. [176]).

Time-resolved photoluminescence and the correlation spectroscopy

The TRPL is measured by a time-correlated single photon counting method. The structure is excited by a train of laser pulses, typically non-resonantly. The time width of the pulse has to be much smaller than the timescale of the system dynamics. A typical lifetime of an exciton complex in its ground state in InAs/InP QDs is longer than 1 ns so both described laser light sources (laser diode with ∼50 ps-long pulses or Ti:Sa laser with ∼ 2-ps-long pulses) were employed for the excitation of QDs.

A monochromator spectrally filters photons, and the second output port of the monochromator is equipped with a fiber coupling system, transmitting the signal to an NbN-based SNSPD with ∼92 % quantum efficiency in the 1.5-1.6 µm range and ∼ 200 dark counts per second (cps) (Scontel). A multichannel picosecond event timer (PicoHarp 300 by PicoQuant) – an electric circuit capable of counting the time differences between pulses, working as a time-to-amplitude converter – analyzes the single photon counts. The overall time resolution of the setup is ∼80 ps.

The correlation histograms are recorded in an analogous setup, in the HBT configuration, see Fig. 2.13. For that, the QD signal has to be split into two paths and detected by two SNSPDs. The detectors, a pair of SNSPDs with ∼87 % and ∼92 % quantum efficiency, generate an electric pulse in response to the photon absorption. The pulses are passed to the PicoHarp 300 multichannel picosecond event timer. In this approach, one of the pulses is a "START" event, the second – a "STOP" event, and the Time-Tagged Time-Resolved (TTTR) data acquisition mode is applied. The events are stored directly along with additional time information, the time tag, instead of being sorted into a histogram, as is done for the lifetime measurements. This approach is more powerful and, i. a., allows for the reconstruction of also the negative part of the time axis. The measured time differences are collected to reflect the time correlation of the two beams' intensities in full statistics. The data is plotted as a histogram of coincidences as a function of delay τ. The second-order correlation function $g^{(2)}(\tau)$ obtained after the normalization of the histogram was described theoretically in Section 2.4.

During the reported research, the signal was split either before the spectral filtering (using two monochromators, see Appendix A.1), or after the filtering (using a fiber-based beam splitter, see Appendix A.2). In the latter case, the fiber filter with ∼0.3 nm-wide transmission window was used for spectral filtering of the signal.

Determination of the photon extraction efficiency

The estimation of photon extraction efficiency η is typically performed in the same setup as the correlation experiments because a SNSPD has to be employed. To determine the value of η, the QDs are excited non-resonantly with a pulsed laser diode with $f_{\text{rep}} = 80\,\text{MHz}$ repetition rate at the saturation power for each QD. The emission is collected with the microscope objective (NA = 0.4), and the SNSPDs count rates are summed for CX and X lines (n_{QD}), as only one excitonic complex can radiatively decay at a time, contributing to the QD-generated photon flux. The counts are corrected by the efficiency of the optical setup η_{Setup}. Taking into account the laser repetition f_{rep},

[14] This article is included in this thesis, p. 153.

η for a QD is estimated as

$$\eta = \frac{n_{\mathrm{QD}}}{f \times \eta_{\mathrm{Setup}}}. \tag{3.4}$$

It is difficult to determine the internal quantum efficiency of a QD (i. e., the rate of non-radiative recombination) experimentally. At the same time, a non-unity value decreases the registered photon flux and hence η. The employed method assumes unity QDs internal quantum efficiency ($\eta_{\mathrm{int}} = 100\,\%$), what translates to the fact that the QD photon repetition rate equals f_{rep}. The assumption of $\eta_{\mathrm{int}} = 100\,\%$ thus determines a lower limit of η due to a possible overestimation of the expected QD photon flux n_{QD}. Finally, the measured QD values for the QDs should be corrected by the factor $\sqrt{1-g^{(2)}(0)}$ to account for the secondary photons due to the refilling of the QD states that enhance the measured photon flux [155, 274].

Setup efficiency

To estimate the optical setup efficiency η_{Setup}, two methods were used and are described in this section. The first is based on the calibration of SNSPD counts [114], and the second relies on the product of transmission (or efficiency) of all elements. The multiplication of the transmission and efficiency values should lead to the same η_{Setup} as determined using the calibration method, so the choice depends on the experimental convenience.

Calibration of SNSPD counts In this case, the setup efficiency η_{Setup} is estimated by reflecting a laser tuned to the investigated QD emission range off a silver mirror placed in the setup instead of the structure. The laser beam is attenuated with neutral density filters to achieve the SNSPDs count rate in the MHz range. This number is corrected by the measured mirror reflectivity, attenuation of filters, transmission of the cryostat window, and microscope objective, i. e., all elements that have to be inserted into the optical path during the measurement of QD-emitted photons. The setup efficiency can be estimated based on the laser power coming on the silver mirror, transmission of the elements, and the attenuation factor.

Transmission and efficiency of setup elements The setup efficiency η_{Setup} can also be calculated by multiplying the transmission of all optical elements and the efficiency of fiber in-coupling and SNSPD used. In this method, the first point is to reflect the laser beam tuned to the QD emission wavelength off a silver mirror placed in the setup instead of the structure. The signal emitted by the sample passes through the following elements of the setup on the way to the detector, which are given with the exemplary transmission/efficiency values: cryostat window (spectrally averaged transmission $T \approx 90\,\%$), microscope objective ($T \approx 55\,\%$ at 1.55 µm), two beam splitters (introducing the optical excitation and splitting the QD signal, $T \approx 40\,\%$ each), monochromator ($T \approx$ 15-40 %), fiber in-coupling (efficiency 15-50 %) and SNSPDs (efficiency ∼92 %). The broad range given for the fiber in-coupling efficiency originates from the setup instability. Reaching high coupling is challenging as the mode field diameter for the used single-mode fibers is only $(10.4 \pm 0.5)\,\mu\mathrm{m}$[15], requiring the micrometer-range precision of the setup adjustment. The resulting η_{Setup} was estimated to $(1.10 \pm 0.17)\,\%$ for P. Holewa *et al.*, *Scalable quantum photonic devices emitting indistinguishable photons in the telecom C-band*, arXiv:2304.02515 (2023), where the uncertainty was calculated by propagating the assumed uncertainties of the consecutive elements (for details, see Appendix A.2). The QD emission lines measured during the η estimation always have at least a few thousand cps registered on the SNSPD.

Determination of the single-photon purity

The correlation histograms obtained with pulsed laser excitation are fitted with the function [95, 275]:

$$C(\tau) = B + A\left[\exp\left(-|\tau|/\tau_{\mathrm{dec}}\right) - \exp\left(-|\tau|/\tau_{\mathrm{cap}}\right)\right] + H\sum_{n\neq 0}\exp\left(-|\tau - n\tau_0|/\tau_{\mathrm{dec}}\right), \tag{3.5}$$

[15] Value for the Corning® SMF-28® Ultra Optical Fiber available in the Product Information.

where B is the level of background coincidences, A is a scaling parameter related to secondary photon emission, $n \neq 0$ is the peak number and H is the average height of the peaks at $\tau_n = n\tau_0$. The second-order correlation function $g^{(2)}(\tau)$ is then obtained by normalizing $C(\tau)$ with H.

To calculate the $g^{(2)}(\tau)$ value at zero time delay, $g^{(2)}(0)$, under the pulsed QD excitation, the coincidences registered during the time T_0 corresponding to a full laser excitation cycle ($T_0 = 1/f_{\mathrm{rep}}$) are taken into account. The histogram integration is performed so that the value $g^{(2)}(0)_{\mathrm{area}}$ can be obtained when including the histogram background contribution B:

$$g^{(2)}(0)_{\mathrm{area}} = \int_{-T_0/2}^{T_0/2} \left[B + A\left[\exp\left(-|\tau|/\tau_{\mathrm{dec}}\right) - \exp\left(-|\tau|/\tau_{\mathrm{cap}}\right)\right]\right] \mathrm{d}\tau \,/ \int_{-T_0/2}^{T_0/2} \left[B + H\exp\left(-|\tau|/\tau_{\mathrm{dec}}\right)\right] \mathrm{d}\tau\,, \tag{3.6}$$

and with the background contribution subtracted:

$$g^{(2)}(0)_{\mathrm{area}} = \int_{-T_0/2}^{T_0/2} A\left[\exp\left(-|\tau|/\tau_{\mathrm{dec}}\right) - \exp\left(-|\tau|/\tau_{\mathrm{cap}}\right)\right] \mathrm{d}\tau \,/ \int_{-T_0/2}^{T_0/2} H\exp\left(-|\tau|/\tau_{\mathrm{dec}}\right) \mathrm{d}\tau\,. \tag{3.7}$$

For the histograms recorded in cw mode, the standard fitting formula is used:

$$C(\tau) = N\left[1 - \left(1 - g^{(2)}_{\mathrm{fit}}(0)\right)\exp\left(-|\tau|/t_{\mathrm{rise}}\right)\right], \tag{3.8}$$

where N is the average coincidence level at $|\tau| \gg 0$ allowing for $C(t)$ histogram normalization and hence obtaining the $g^{(2)}(\tau)$ function, and t_{rise} is the antibunching time constant, $t_{\mathrm{rise}} = 1/\Gamma + G_{\mathrm{eff}}$, with the electron-hole radiative recombination rate Γ and the effective pump rate G_{eff}.

In all cases, the purity is extracted as $P = 1 - g^{(2)}(0)$, so for the pulsed excitation it is $P_{\mathrm{pulsed}} = 1 - g^{(2)}(0)_{\mathrm{area}}$.

CHAPTER 4
Summary of the results

The thesis comprises five articles that summarize my research conducted during Ph.D. studies. Four of these articles have been published in international peer-reviewed journals and form the core of the thesis, fulfilling the legal requirements for the thesis submitted as a series of articles. These papers deal with Objective 1. and Objective 2. of the thesis. The most recent results concerning Objective 3. have yet to be published and are included in the thesis as an arXiv preprint. This completes my research on the nanofabrication for QIP at the 3rd telecom window.

This chapter presents an overview of the obtained results, which are classified according to the article they have been published in. Each article is described individually, and together, they comprehensively describe the nanofabrication of QD-based structures and their optical properties. The order of articles is organized to gradually shift the emphasis from the fundamental physics of excitons confined in the QDs towards the application-relevant point of view. This also complies with the chronological order of publication.

The results of the research reported in the thesis are divided into three major groups based on their relevance to the thesis objectives formulated on p. 13:

1. **Establishing an optimal QD growth strategy for low-density InAs/InP QDs emitting at C-band, understanding their optical properties, enhancing their in-plane symmetry. (Objective 1.)**

   - P. Holewa *et al.*, *Optical and electronic properties of low-density InAs/InP quantum dot-like structures devoted to single-photon emitters at telecom wavelengths*, **Physical Review B**, 101, 19 (2020).
   - P. Holewa *et al.*, *Optical and Electronic Properties of Symmetric InAs/(In,Al,Ga)As/InP Quantum Dots Formed by Ripening in Molecular Beam Epitaxy: A Potential System for Broad-Range Single-Photon Telecom Emitters*, **Physical Review Applied**, 14, 6 (2020).
   - P. Holewa *et al.*, *Droplet epitaxy symmetric InAs/InP quantum dots for quantum emission in the third telecom window: morphology, optical and electronic properties*, **Nanophotonics**, 11, 8 (2022).

   In this group, two low-density QD systems (InAs/InP and InAs/(In,Al,Ga)As/InP) have been investigated. Both QD systems share characteristic properties, such as multimodal PL emission extending over a wide spectral range in NIR, redistribution of carriers via WL states, and exciton dynamics. The third publication discusses DE QDs with high in-plane symmetry favorable for entangled photon pairs emission.
   All the examined structures with QDs are useful for QIP applications, particularly as sources of single photons for the systems requiring low-loss and long-range quantum data links implemented in silicon chips or between network nodes connected via silica fibers. This is because their emission wavelength falls within the 3rd telecommunication window (approx. 1.55 µm), providing minimal optical losses in the transmission medium.

2. **Development of a semiconductor platform for a broadband enhancement of the photon extraction efficiency. (Objective 2.)**

   - P. Holewa *et al.*, *Bright Quantum Dot Single-Photon Emitters at Telecom Bands Heterogeneously Integrated with Si*, **ACS Photonics**, 9, 7 (2022).

This publication shows the potential of the developed InP/Al/Si platform for enhancing photon extraction efficiency η for single photons generated in InAs QDs at the 3rd telecom window. It describes the integration of QDs with a metallic mirror and the investigation of QD optical properties.

3. **Localization of QDs and deterministic fabrication of optimized nanocavities at the QD nucleation site, investigating the cavity-coupled QDs. (Objective 3.)**

   - P. Holewa *et al.*, *Scalable quantum photonic devices emitting indistinguishable photons in the telecom C-band*, arXiv:2304.02515 (2023).

   This part of the research was focused on the μPL imaging approach to localize the QDs optically active at the C-band and the deterministic fabrication of CBGs over them to demonstrate control over the QD-cavity coupling, leading to a significant enhancement in photon extraction efficiency η and the generation rate of single photons.

4.1 Low-density InAs/InP quantum-dot-like structures

The investigated low-density InAs/InP QDs were obtained by MOVPE in the S-K growth mode. In this case, the emission of QDs is dispersed between seven PL bands, which are spectrally distributed in the 1.2-1.9 μm range. These bands originate from the ground-state emission of consecutive QD "families", as was confirmed by the power-dependent PL experiment (the linear dependence of the PL intensity vs. the excitation power). The families are formed by QDs whose height differs by a single ML of InAs. It was suggested by a good agreement between experimental data and theoretical calculations.[1] Additionally, the WL absorption edge was determined in the PLE experiment and was an input parameter for the modeling of the WL band structure in the 8-band $k{\cdot}p$ approach. The single-particle band structure calculations were performed in the nextnano environment. It allowed determining the WL thickness and composition.

The temperature-dependent PL experiment allowed assessing the energy scales relevant to the energy band diagram of the QD system. The experiment revealed activation energies leading to the PL quench and enhancement for subsequent families of QDs. Based on that, it was found that at elevated temperatures, carriers are undergoing redistribution among the dot families via the WL, leaving empty the QDs with a shallow confining potential and filling those with a deeper one.

TRPL studies disclosed the existence of two excitation decay channels for the QD families, characterized by two different decay time constants. The entropy maximization method (MEM) applied to data analysis provided that the decay time constants show unexpected flat spectral dispersion, much different than previously observed for InAs/InP dots [276]. The explanation of the dispersion lies in two contradictory effects:[2]

1. weak electron confinement in the dots (leakage of the electron wavefunction from the QD material to the barrier area, which results in the reduction of the electron and hole wavefunction overlap integral, and the elongation of τ), and

2. the weak exciton binding regime in investigated dots, resulting in the expected dependence $\tau(E) \sim E^{-2}$, where E is QD emission energy (cf. Eq. (2.58)).

In the μPL experiment, single emission lines from the QDs were observed across the S-, C-, and L-bands of the 3rd telecom window. These lines were attributed to the recombination of excitonic complexes confined in QDs. This conclusion was drawn from the excitation power- and polarization-resolved μPL (see Section 2.3 and Fig. 2.10 and the following discussion). Additionally, the μPL studies provided insight into the XX binding energy that reached 3.5 meV and the X FSS energy that amounted to (44 ± 5) μeV. The DOLP was determined for a few CX states and ranged from 5-31 %, indicating HH-LH mixing (see Section 3.2) [277, 278].

In the temperature-dependent μPL experiment, the activation energies of the μPL quench processes for a chosen CX line were determined. Two activation energies were found: 1 meV and

[1] The calculations were done by Michał Gawełczyk.
[2] This explanation was possible thanks to the theory developed by Michał Gawełczyk.

23 meV. The higher energy was interpreted as the excitation of the CX to a high-energy confined state[3].

> **Related article:** P. Holewa, M. Gawełczyk, C. Ciostek, P. Wyborski, S. Kadkhodazadeh, E. Semenova, M. Syperek, *Optical and electronic properties of low-density InAs/InP quantum dot-like structures devoted to single-photon emitters at telecom wavelengths*, **Physical Review B**, 101, 19 (2020).
> This article is included in the thesis, starting from p. 95.

> **Contribution:** PL experiments for the investigated QDs in a broad spectral range, observation of QD families, and further research to explain their origin and mutual relations: temperature-, excitation-power dependent PL, polarization-resolved PL, PLE, TRPL, 8-band $k{\cdot}p$ calculations of the WL states and initial investigations of QD single-particle states (in nextnano), interpretation of the obtained results, analysis of all PL, PLE, TRPL and µPL experimental data, preparation of the manuscript, response to the review.

4.2 Symmetric InAs/(In,Al,Ga)As/InP quantum dots

Exciting findings were discovered when studying InAs QDs embedded in the (In,Al,Ga)As matrix lattice-matched to the InP substrate. These structures were grown by MBE using the QD ripening method, which resulted in both the QD emission wavelength at 1.55 µm and high in-plane symmetry of the QDs [102, 103].[4] The research provided a comprehensive overview of the optical properties of such structures and includes a noteworthy discovery about the height differences between consecutive QD families of 2 ML of InAs, indicating the long-range crystal structure ordering.

The investigated QDs show the PL emission centered at ∼1.5 µm, with five emission bands distributed in the 1.55-2 µm spectral range. The power-dependent PL showed the linear increase of each band intensity vs. excitation power, indicating that the bands are contributed by the ground state emission of the QDs. Based on that, the working hypothesis has been established that the QDs are grouped into height-dependent families, similar to P. Holewa *et al.*, *Optical and electronic properties of low-density InAs/InP quantum dot-like structures devoted to single-photon emitters at telecom wavelengths*, **Physical Review B**, 101, 19 (2020).

Further studies revealed that explaining the observed differences between PL band energies was initially impossible, assuming that QD families differ by a *single* InAs monolayer. Instead, it was discovered that the observed differences could be explained if successive QDs families differ by *two* InAs monolayers in height. This conclusion indicated the existence of a long-range ordering [279, 280] in the investigated system and was **the first observation of such phenomenon for QDs in general.** The long-range ordering is present in the (In,Al,Ga)As matrix surrounding the QDs. It can be described as the arrangement of the barrier material into alternating layers: rich and poor in indium. Due to such an atomic arrangement (previously observed for ternaries [279, 281, 282] and quaternaries [283]), it is impossible to change the height of the InAs QD by one monolayer.

Performed spectroscopic studies were analogous to those applied to QDs investigated in P. Holewa *et al.*, *Optical and electronic properties of low-density InAs/InP quantum dot-like structures devoted to single-photon emitters at telecom wavelengths*, **Physical Review B**, 101, 19 (2020). These included polarization-resolved PL, which indicated that the QD emission had a negligible DOLP, as demonstrated in [102]. In the TRPL experiments, the recorded PL decay traces were described by the mono-exponential decay function, and the extracted PL decay times had negligible energy dispersion. When examining elongated QDs (and especially QDashes), it is common to extract two time constants from the decay traces. The lack of such observation coupled with the low DOLP suggested that the QDs under study have a high in-plane symmetry.

Finally, temperature-dependent PL revealed carrier redistribution between QDs families at elevated temperatures via the WL states. The holes were identified as contributing the most to the

[3] The QD band-structure calculations including excitonic effects were performed by Michał Gawełczyk.
[4] The MBE growth was carried out in the group of Mohamed Benyoucef at the University of Kassel, Germany.

redistribution taking into account the extracted activation energies for the observed PL quench process and their comparison to the QDs band structure calculations.[5]

Related article: P. Holewa, M. Gawełczyk, A. Maryński, P. Wyborski, J. P. Reithmaier, G. Sęk, M. Benyoucef, M. Syperek, *Optical and Electronic Properties of Symmetric InAs/(In,Al,Ga)As/InP Quantum Dots Formed by Ripening in Molecular Beam Epitaxy: A Potential System for Broad-Range Single-Photon Telecom Emitters*, **Physical Review Applied**, 14, 6 (2020).
This article is included in the thesis, starting from p. 111.

Contribution: The PL studies for the QD ensemble in a wide spectral range, observation of the QD families, and further research to explain their origin: modeling their electronic structure using the 8-band $k{\cdot}p$ method. Discovery and description of the first long-range ordering of the crystal lattice in the case of QDs, based on the consistency between results from spectroscopic studies and theoretical modeling (using the 8-band $k{\cdot}p$ approach implemented in the nextnano software). Spectroscopic examinations: temperature-dependent, polarization-resolved, power-dependent, and TRPL, interpretation of the obtained results, analysis of all experimental data, preparation of the manuscript, response to the review.
Author of this thesis is a corresponding author of this article.

4.3 Droplet epitaxy symmetric InAs/InP quantum dots

The work on the low-density droplet epitaxy InAs/InP QDs of high in-plane symmetry demonstrates the potential of a novel epitaxial method with applications to nanophotonics, particularly quantum optical communication and QIP based on an entangled photon state.

Although the successful synthesis of epitaxial S-K InAs/InP QDs results in excellent single-photon emission at C-band [95], the DE QDs are very promising sources of entangled photon pair emission [59] as their confining potential is more symmetric compared to S-K QDs [76]. The symmetry of a QD confining potential is the primary factor determining the X FSS [2]. The more symmetric the QD is, the FSS is lower and ideally tends to zero. This condition is critical for achieving polarization-entangled photon pairs originating from the XX-X recombination cascade in a QD.

Therefore, a new QD growth approach in the MOVPE was required to allow for control over the QD parameters. The stress was primarily put on tailoring the shape of a QD in MOVPE and addressing its size and surface density while maintaining emission in the C-band.

Implementation of a QD growth method based on the DE approach allowed to fulfill several essential requirements for QD-based quantum emitters operating in the telecom spectral range. The applied procedure led to the following:

- low QD surface density $2.8 \times 10^8/\mathrm{cm}^2$,
- control over the photon emission wavelength in the required spectral range near the center of the 3$^{\mathrm{rd}}$ telecom spectral window,
- high purity of single-photon emission,
- potential for entangled photon pairs generation.

The work first involved developing the DE scheme with the In droplet deposition performed at a low temperature (360 °C), followed by the research to find the optimal AsH_3 flux parameters in the MOVPE reactor to achieve high QD symmetry and emission in the C-band simultaneously. Although no additional annealing was initially applied after the droplet crystallization, its inclusion was found necessary to achieve symmetric QDs. The conditions of the annealing were optimized

[5] Calculated by Michał Gawełczyk.

and found out as annealing the In droplets under AsH_3 ambient during ramping up the temperature to 550 °C, followed by 180 s waiting time under AsH_3 flux (annealing).

The characterization of QDs morphology was examined in detail by AFM, high-resolution STEM and energy-dispersive x-ray spectroscopy (EDX).[6] The experimental data were supported by detailed theoretical treatment of the DE QDs nucleation process, including changes in the DE morphology upon annealing.[7]

The optical investigations involved studies on the emission properties of QD ensemble, including the temperature- and power-dependent PL, TRPL, and polarization-resolved PL. To study the optical properties of individual QDs, mesa structures were fabricated to limit the QDs density within an excitation spot. Consequently, high-spatially-resolved experiments could be performed, like temperature- and power-dependent µPL, TRPL, and the polarization-resolved µPL. In addition, autocorrelation spectroscopy was carried out for the most intense and well-isolated QDs to elaborate on single-photon emission properties. The spectroscopic data were supported by modeling of the QDs band structure with input from the QD morphology characterization.[8]

In particular, the QDs ensemble emission polarization properties, measured and theoretically simulated, suggest negligible FSS, a figure of merit for entangled photon pairs generation. The measured optical response from a single QD located in a fabricated mesa structure showed the high purity of single photons, $P = (92.5 \pm 7.5)\,\%$. In addition, the FSS of (50 ± 5) µeV determined for an X line was related to the post-processing-induced imperfections and not the intrinsic property of the QD itself. Despite that, based on the temperature-dependent µPL, it was shown that the QDs could operate as high-purity photon state generators even at elevated temperatures up to 80 K.

Related article: P. Holewa, S. Kadkhodazadeh, M. Gawełczyk, P. Baluta, A. Musiał, V. G. Dubrovskii, M. Syperek, E. Semenova, *Droplet epitaxy symmetric InAs/InP quantum dots for quantum emission in the third telecom window: morphology, optical and electronic properties*, **Nanophotonics**, 11, 8 (2022).
This article is included in the thesis, starting from p. 127.

Contribution: Optimization of the QD growth method and the growth of QDs, AFM measurements, all optical studies: PL and µPL, identification and study of exciton complexes, correlation and TRPL, data analysis and interpretation, manuscript preparation, response to the review.
Author of this thesis is a corresponding author of this article.

4.4 Bright quantum dot single-photon emitters heterogeneously integrated on Si

This article is a continuation of the work on the epitaxy of self-assembled InAs/InP QDs, expanding the field of research on the development of heterogeneous integration of photon emitters with other material platforms towards enhancement of photon extraction efficiency η. The latter is an indispensable step that paves the way for the localization of a single telecom photon emitter in a planar structure through the optical imaging technique prior to the deterministic shaping of its environment. As explained in the Motivation, the challenge of low photon flux escaping the semiconductor structure can be routinely addressed for QDs emitting in the $< 1\,\mu m$ range (for example, DBR for GaAs-based QDs).

In this work, the multi-step nanofabrication described in Section 3.1 was explored, transforming the epitaxial wafer with QDs into a stack with an InP slab and the aluminum mirror under the QDs layer, all integrated with the Si platform. It led to a proof-of-principle structure with InAs/InP QDs emitting in the 3rd telecom band that were heterogeneously integrated to a silicon carrier. Therefore, this paper deals with a versatile and robust solution for achieving high levels of η ($\sim$10% for an objective NA of 0.4 with room for further improvement) for QDs emitting at

[6] STEM and EDX done by Shima Kadkhodazadeh.
[7] Kinetic nucleation theory developed by Vladimir Dubrovskii.
[8] Calculations of the QDs band structure in 8-band $k{\cdot}p$ were performed by Michał Gawełczyk.

1.55 µm, increasing the average brightness of QDs by the factor of ∼ 7.4. The structure offered the possibility to study the optical properties of QD-based single photon emitters in telecom due to high photon extraction efficiency elevating the source brightness on a state-of-the-art level at that time.

The significance and novelty of this work can be summarized as follows:

- A novel hybrid structure with InAs/InP QDs was proposed and fabricated, marking the first heterogeneous integration of single InAs/InP QDs emitting in the 3rd telecom band with a silicon substrate. One previous attempt for integrating with Si an InAs/InP QD, emitting in the O-band near 1300 nm, has been made using the pick-and-place technique [284].
- The obtained results are important for a simplified, small-footprint, cost-effective, and scalable manufacturing process for triggered single-photon emission that is suitable for Si-based on-chip photonic QIP and distributed quantum computation utilizing low-loss, fiber-based optical networks.
- The fabricated single-photon source architecture, surpassing other approaches in its technological simplicity, achieved the record η value of ∼11 % at 1500 nm and ∼7 % at 1550 nm with the NA = 0.4. These efficiencies are highly competitive with those presented to date for InAs/InP QDs in the 3rd telecom band: Ref. [106] reported η ∼11 % at 1560 nm but with NA = 0.55. Additionally, that approach is not suitable for monolithic integration due to the low mechanical stability of the utilized horn structure. In turn, Ref. [113] has provided η = 13 % at 1560 nm and NA = 0.4 for an InAs/InP QD atop of an InP/(In,Al,Ga)As DBR. However, this approach is limited to a narrow spectral window provided by the DBR stop-band and requires demanding fabrication for the DBR due to the low refractive index contrast of the InP-lattice-matched material layers.
- The high-purity triggered single-photon emission was demonstrated with $g^{(2)}(\tau = 0) < 0.02$ without any corrections at cw excitation at the liquid helium temperature and preserved up to 50 K, and the record-high purity at 80 K of $P = (0.75 \pm 0.19)$ was shown for QDs emitting at 1.55 µm (the previous record at 1.55 µm was 66 %, demonstrated in Ref. [100]).
- For pulsed excitation, the achieved as-measured $g^{(2)}(0) = (0.205 \pm 0.020)$, and $g^{(2)}(0) = (0.114 \pm 0.020)$ with background coincidences subtracted.

The applied approach is prospective for high-brightness, high-purity SPSs at 1.55 µm range, utilizing a well-developed and cost-effective silicon platform. It also paves the way for the fabrication of photonic microcavities (e. g., CBGs or nanopillars) with optimized microcavity design to further enhance the η level in deterministic processing in µPL imaging, what was realized in P. Holewa *et al.*, *Scalable quantum photonic devices emitting indistinguishable photons in the telecom C-band*, arXiv:2304.02515 (2023), and the deterministic fabrication of dedicated microcavities with prospects of the η close to unity.

> **Related article:** P. Holewa, A. Sakanas, U. M. Gür, P. Mrowiński, A. Huck, B. Wang, A. Musiał, K. Yvind, N. Gregersen, M. Syperek, E. Semenova, *Bright Quantum Dot Single-Photon Emitters at Telecom Bands Heterogeneously Integrated with Si*, **ACS Photonics**, 9, 7 (2022).
> This article is included in the thesis, starting from p. 143.
>
> **Supplemental Material** for this article is included in the Appendix A.1, p. 167.
>
> **Contribution:** Optimization of the QD growth and the growth of the QDs described in the article (S-K mode), participation in the design of the structure, fabrication as described in Section 3.1, all optical studies: characterization in µPL, identification and study of exciton complexes in temperature-, power-dependent and polarization-resolved µPL, correlation spectroscopy, determination of photon extraction efficiency from the structure, data analysis and interpretation, preparation of the manuscript, response to the review.
> **Author of this thesis is a corresponding author of this article.**

4.5 Quantum dots in nanocavities resulting from deterministic processing

The scalability of the QD-based technologies requires deterministic processing. However, the random nucleation site of semiconductor QDs is a common obstacle in the development of efficient quantum light sources, especially restraining the deterministic fabrication of photonic devices based on QDs. Although a QD operating in NIR ($< 1\,\mu m$) can be identified and localized using a high-quality 2D Si-based CCD camera or localized by scanning techniques, the localization of QDs emitting in the telecommunication-relevant C-band (outside the detection range of the Si-based detectors) is especially demanding but crucial for establishing the deterministic workflow. See Section 1.3 for more details.

To address this problem, which is also central to the Objective **3.** of this thesis, a fully-deterministic fabrication of numerically-optimized hybrid CBGs at the nucleation site of single InAs/InP QDs emitting at telecom C-band was performed. The µPL imaging was employed to efficiently localize hundreds of QDs, visible as nearly diffraction-limited spots on a chip of the 2D InGaAs camera, and used EBL to fabricate CBGs there. For that, the nanofabrication of the structure for imaging was performed, and the µPL imaging setup working at 1.55 µm was developed[9]. The positions of QDs with respect to the AMs were found using a LabTalk script that takes as an input the µPL maps and rough estimations of the QD positions, analyzes them and outputs the QD positions with respect to the AMs (imaging field borders). Afterward, a Python script processes this data and outputs the mask file for EBL.

The CBGs with the optimized geometry[10] were etched afterward in the InP layer at the localized QD spots. The related preprint describes the overall performed processing while the methodology, details on the localization algorithm, discussion of the involved uncertainties, and the accuracy of cavity positioning are given in SM. Additionally, the scheme presented in Fig. 3.4 summarizes the procedure described here. he overall accuracy of the cavity placement is estimated at 90 nm, and the total process yield at 30 %. The related preprint describes the overall performed processing while the methodology, details on the localization algorithm, discussion of the involved uncertainties, and the accuracy of cavity positioning are given in SM. Additionally, the scheme presented in Fig. 3.4 summarizes the procedure described here.

The QD-cavity coupling in TRPL was shown by the shortening of the radiative decay rate of the CX lines, with the Purcell enhancement estimated to $F_p = 5$. QDs coupled with the cavity modes are bright and pure sources of single photons with the photon extraction efficiency of $\eta = (16.6 \pm 2.7)\,\%$ into NA = 0.4. The single-photon purity under non-resonant excitation has been estimated to $P = (95 \pm 2)\,\%$ at half the saturation power and $P = (83 \pm 3)\,\%$ for the CX line saturation power. Additional quantum-optical experiments were carried out without the participation of this thesis' author, with the single-photon purity of $P = (99.68 \pm 0.06)\,\%$ under the longitudinal optical (LO)-phonon-assisted excitation and the two-photon interference visibility of $(19.3 \pm 2.6)\,\%$.

The reported work can be seen as a direct continuation of the research on the heterogeneous platform with metallic mirror reported in P. Holewa *et al.*, *Bright Quantum Dot Single-Photon Emitters at Telecom Bands Heterogeneously Integrated with Si*, **ACS Photonics**, 9, 7 (2022), which could be used during the µPL imaging due to the enhanced photon extraction efficiency η. Moreover, the presented approach paves the way for fast and scalable fabrication of photonic devices based on QDs, operating at 3rd telecom window. This implies a clear application potential of these results in the medium term.

> **Related preprint:** P. Holewa, E. Zięba-Ostój, D. Vajner, M. Wasiluk, B. Gaál, A. Sakanas, M. Burakowski, P. Mrowiński, B. Krajnik, M. Xiong, A. Huck, K. Yvind, N. Gregersen, A. Musiał, T. Heindel, M. Syperek, E. Semenova, *Scalable quantum photonic devices emitting indistinguishable photons in the telecom C-band*, arXiv:2304.02515 (2023).
> This preprint is included in the thesis, starting from p. 153.

[9] In cooperation with Bartosz Krajnik and Paweł Mrowiński, WUST.
[10] The cavity design was provided by Benedek Gaál and Niels Gregersen, DTU Electro.

Supplemental Material for this preprint is included in the Appendix A.2, p. 180.

Contribution: Optimization of the QD growth and the growth of the QDs structure for further processing, similar to the one performed in P. Holewa *et al.*, *Bright Quantum Dot Single-Photon Emitters at Telecom Bands Heterogeneously Integrated with Si*, **ACS Photonics**, 9, 7 (2022), µPL imaging, devising the data analysis approach to localize the QDs, as outlined in Section 3.2, writing the Labtalk scripts to analyze the µPL maps and determine the absolute positions of QDs, creation of EBL masks with deterministic cavities in Python, fabrication of cavities according to the description given in Section 3.1.
Optical studies of the cavities: their characterization in µPL, identification and study of exciton complexes in temperature-, power-dependent, and polarization-resolved µPL, correlation spectroscopy (non-resonant excitation), determination of photon extraction efficiency for the QDs in cavities, data analysis and interpretation, preparation of the manuscript.
Author of this thesis is a corresponding author of this article.

Bibliography

(1) O'Brien, J. L.; Furusawa, A.; Vučković, J. *Nat. Photonics* **2009**, *3*, 687–695 (cit. on p. 3).

(2) Senellart, P.; Solomon, G.; White, A. *Nat. Nanotechnol.* **2017**, *12*, 1026–1039 (cit. on pp. 3, 4, 6, 27, 74).

(3) Knill, E.; Laflamme, R.; Milburn, G. J. *Nature* **2001**, *409*, 46–52 (cit. on p. 3).

(4) Kok, P.; Munro, W. J.; Nemoto, K.; Ralph, T. C.; Dowling, J. P.; Milburn, G. J. *Rev. Mod. Phys.* **2007**, *79*, 135–174 (cit. on pp. 3, 6).

(5) Aharonovich, I.; Englund, D.; Toth, M. *Nat. Photonics* **2016**, *10*, 631–641 (cit. on p. 3).

(6) Kimble, H. J. *Nature* **2008**, *453*, 1023–1030 (cit. on p. 3).

(7) Wehner, S.; Elkouss, D.; Hanson, R. *Science* **2018**, *362*, eaam9288 (cit. on pp. 3, 4).

(8) Gisin, N.; Ribordy, G.; Tittel, W.; Zbinden, H. *Rev. Mod. Phys.* **2002**, *74*, 145–195 (cit. on p. 3).

(9) Serafini, A.; Mancini, S.; Bose, S. *Phys. Rev. Lett.* **2006**, *96*, 010503 (cit. on p. 3).

(10) Ekert, A. K. *Phys. Rev. Lett.* **1991**, *67*, 661–663 (cit. on p. 3).

(11) Lu, C.-Y.; Cao, Y.; Peng, C.-Z.; Pan, J.-W. *Rev. Mod. Phys.* **2022**, *94*, 035001 (cit. on p. 4).

(12) Cao, X.; Zopf, M.; Ding, F. *J. Semicond.* **2019**, *40*, 071901 (cit. on pp. 4, 6).

(13) Arakawa, Y.; Holmes, M. J. *Appl. Phys. Rev.* **2020**, *7*, 021309 (cit. on pp. 4, 6).

(14) Martini, F. D.; Giuseppe, G. D.; Marrocco, M. *Phys. Rev. Lett.* **1996**, *76*, 900–903 (cit. on p. 4).

(15) Brunel, C.; Lounis, B.; Tamarat, P.; Orrit, M. *Phys. Rev. Lett.* **1999**, *83*, 2722–2725 (cit. on p. 4).

(16) Lounis, B.; Moerner, W. E. *Nature* **2000**, *407*, 491–493 (cit. on p. 4).

(17) Kurtsiefer, C.; Mayer, S.; Zarda, P.; Weinfurter, H. *Phys. Rev. Lett.* **2000**, *85*, 290–293 (cit. on p. 4).

(18) Beveratos, A.; Kühn, S.; Brouri, R.; Gacoin, T.; Poizat, J.-P.; Grangier, P. *Eur. Phys. J. D* **2002**, *18*, 191–196 (cit. on p. 4).

(19) Kuhn, A.; Hennrich, M.; Rempe, G. *Phys. Rev. Lett.* **2002**, *89*, 067901 (cit. on p. 4).

(20) Michler, P.; Imamoğlu, A.; Mason, M.; Carson, P.; Strouse, G.; Buratto, S. *Nature* **2000**, *406*, 968 (cit. on p. 4).

(21) Michler, P.; Kiraz, A.; Becher, C.; Schoenfeld, W. V.; Petroff, P. M. *Science* **2000**, *290*, 2282–2285 (cit. on pp. 4, 6).

(22) Santori, C.; Pelton, M.; Solomon, G.; Dale, Y.; Yamamoto, Y. *Phys. Rev. Lett.* **2001**, *86*, 1502–1505 (cit. on p. 4).

(23) Yuan, Z.; Kardynal, B.; Stevenson, R. M.; Shields, A.; Lobo, C. J.; Cooper, K.; Beattie, N. S.; Ritchie, D. A.; Pepper, M. *Science* **2002**, *295*, 102–105 (cit. on p. 4).

(24) Fasel, S.; Alibart, O.; Tanzilli, S.; Baldi, P.; Beveratos, A.; Gisin, N.; Zbinden, H. *New J. Phys.* **2004**, *6*, 163–163 (cit. on p. 5).

(25) Alibart, O.; Ostrowsky, D. B.; Baldi, P.; Tanzilli, S. *Opt. Lett.* **2005**, *30*, 1539 (cit. on p. 5).

(26) Pelc, J. S.; Yu, L.; Greve, K. D.; McMahon, P. L.; Natarajan, C. M.; Esfandyarpour, V.; Maier, S.; Schneider, C.; Kamp, M.; Höfling, S.; Hadfield, R. H.; Forchel, A.; Yamamoto, Y.; Fejer, M. M. *Opt. Express* **2012**, *20*, 27510–27519 (cit. on p. 5).

(27) Vallés, A.; Hendrych, M.; Svozilík, J.; Machulka, R.; Abolghasem, P.; Kang, D.; Bijlani, B. J.; Helmy, A. S.; Torres, J. P. *Opt. Express* **2013**, *21*, 10841 (cit. on p. 5).

(28) Ngah, L. A.; Alibart, O.; Labonté, L.; D'Auria, V.; Tanzilli, S. *Laser Photonics Rev.* **2015**, *9*, L1–L5 (cit. on p. 5).

(29) Fiorentino, M.; Voss, P.; Sharping, J.; Kumar, P. *IEEE Photon. Technol. Lett.* **2002**, *14*, 983–985 (cit. on p. 5).

(30) Sharping, J. E.; Lee, K. F.; Foster, M. A.; Turner, A. C.; Schmidt, B. S.; Lipson, M.; Gaeta, A. L.; Kumar, P. *Opt. Express* **2006**, *14*, 12388 (cit. on p. 5).

(31) Takesue, H.; Tokura, Y.; Fukuda, H.; Tsuchizawa, T.; Watanabe, T.; Yamada, K.; Itabashi, S.-i. *Appl. Phys. Lett.* **2007**, *91*, 201108 (cit. on p. 5).

(32) Pomarico, E.; Sanguinetti, B.; Guerreiro, T.; Thew, R.; Zbinden, H. *Opt. Express* **2012**, *20*, 23846 (cit. on p. 5).

(33) Gerrits, T. et al. *Opt. Express* **2011**, *19*, 24434 (cit. on p. 5).

(34) Guerreiro, T.; Martin, A.; Sanguinetti, B.; Bruno, N.; Zbinden, H.; Thew, R. T. *Opt. Express* **2013**, *21*, 27641 (cit. on p. 5).

(35) Christ, A.; Silberhorn, C. *Phys. Rev. A* **2012**, *85*, 023829 (cit. on p. 5).

(36) Yin, C.; Rancic, M.; de Boo, G. G.; Stavrias, N.; McCallum, J. C.; Sellars, M. J.; Rogge, S. *Nature* **2013**, *497*, 91–94 (cit. on p. 5).

(37) Dibos, A.; Raha, M.; Phenicie, C.; Thompson, J. *Phys. Rev. Lett.* **2018**, *120*, 243601 (cit. on p. 5).

(38) Ourari, S.; Dusanowski, Ł.; Horvath, S. P.; Uysal, M. T.; Phenicie, C. M.; Stevenson, P.; Raha, M.; Chen, S.; Cava, R. J.; de Leon, N. P.; Thompson, J. D. Indistinguishable telecom band photons from a single erbium ion in the solid state, 2023 (cit. on p. 5).

(39) He, X.; Hartmann, N. F.; Ma, X.; Kim, Y.; Ihly, R.; Blackburn, J. L.; Gao, W.; Kono, J.; Yomogida, Y.; Hirano, A.; Tanaka, T.; Kataura, H.; Htoon, H.; Doorn, S. K. *Nat. Photonics* **2017**, *11*, 577–582 (cit. on p. 5).

(40) Zhao, H.; Pettes, M. T.; Zheng, Y.; Htoon, H. *Nat. Commun.* **2021**, *12*, 6753 (cit. on p. 5).

(41) Arakawa, Y.; Sakaki, H. *Appl. Phys. Lett.* **1982**, *40*, 939–941 (cit. on p. 5).

(42) Asada, M.; Miyamoto, Y.; Suematsu, Y. *IEEE J. Quantum Electron.* **1986**, *22*, 1915–1921 (cit. on p. 5).

(43) Liu, G.; Stintz, A.; Li, H.; Malloy, K.; Lester, L. *Electron. Lett* **1999**, *35*, 1163–1165 (cit. on p. 5).

(44) Shchekin, O.; Park, G.; Huffaker, D.; Mo, Q.; Deppe, D. *IEEE Photon. Technol. Lett.* **2000**, *12*, 1120–1122 (cit. on p. 5).

(45) Mukai, K.; Nakata, Y.; Otsubo, K.; Sugawara, M.; Yokoyama, N.; Ishikawa, H. *IEEE J. Quantum Electron.* **2000**, *36*, 472–478 (cit. on p. 5).

(46) Reed, M.; Randall, J.; Aggarwal, R.; Matyi, R.; Moore, T.; Wetsel, A. *Phys. Rev. Lett.* **1988**, *60*, 535–537 (cit. on pp. 5, 6).

(47) Santori, C.; Fattal, D.; Vučković, J.; Solomon, G. S.; Yamamoto, Y. *Nature* **2002**, *419*, 594 (cit. on p. 6).

(48) *Single Semiconductor Quantum Dots*; Michler, P., Ed.; Springer Berlin Heidelberg: 2009 (cit. on p. 6).

(49) Somaschi, N. et al. *Nat. Photonics* **2016**, *10*, 340–345 (cit. on pp. 6, 8, 10, 11).

(50) Ding, X.; He, Y.; Duan, Z.-C.; Gregersen, N.; Chen, M.-C.; Unsleber, S.; Maier, S.; Schneider, C.; Kamp, M.; Höfling, S.; Lu, C.-Y.; Pan, J.-W. *Phys. Rev. Lett.* **2016**, *116*, 020401 (cit. on pp. 6, 8, 10).

(51) Wang, H.; Duan, Z.-C.; Li, Y.-H.; Chen, S.; Li, J.-P.; He, Y.-M.; Chen, M.-C.; He, Y.; Ding, X.; Peng, C.-Z.; Schneider, C.; Kamp, M.; Höfling, S.; Lu, C.-Y.; Pan, J.-W. *Phys. Rev. Lett.* **2016**, *116*, 213601 (cit. on p. 6).

(52) Schweickert, L.; Jöns, K. D.; Zeuner, K. D.; Covre da Silva, S. F.; Huang, H.; Lettner, T.; Reindl, M.; Zichi, J.; Trotta, R.; Rastelli, A.; Zwiller, V. *Appl. Phys. Lett.* **2018**, *112*, 093106 (cit. on pp. 6, 10).

(53) Basso Basset, F.; Rota, M. B.; Schimpf, C.; Tedeschi, D.; Zeuner, K. D.; Covre da Silva, S. F.; Reindl, M.; Zwiller, V.; Jöns, K. D.; Rastelli, A.; Trotta, R. *Phys. Rev. Lett.* **2019**, *123*, 160501 (cit. on pp. 6, 29).

(54) Liu, J.; Su, R.; Wei, Y.; Yao, B.; da Silva, S. F. C.; Yu, Y.; Iles-Smith, J.; Srinivasan, K.; Rastelli, A.; Li, J.; Wang, X. *Nat. Nanotechnol.* **2019**, *14*, 586–593 (cit. on pp. 6, 9–12).

(55) Tomm, N.; Javadi, A.; Antoniadis, N. O.; Najer, D.; Löbl, M. C.; Korsch, A. R.; Schott, R.; Valentin, S. R.; Wieck, A. D.; Ludwig, A.; Warburton, R. J. *Nat. Nanotechnol.* **2021**, *16*, 399–403 (cit. on pp. 6, 8).

(56) Akopian, N.; Lindner, N.; Poem, E.; Berlatzky, Y.; Avron, J.; Gershoni, D.; Gerardot, B.; Petroff, P. *Phys. Rev. Lett.* **2006**, *96*, 130501 (cit. on p. 6).

(57) Stevenson, R. M.; Young, R. J.; Atkinson, P.; Cooper, K.; Ritchie, D. A.; Shields, A. J. *Nature* **2006**, *439*, 179 (cit. on pp. 6, 28).

(58) Salter, C. L.; Stevenson, R. M.; Farrer, I.; Nicoll, C. A.; Ritchie, D. A.; Shields, A. J. *Nature* **2010**, *465*, 594–597 (cit. on p. 6).

(59) Müller, T.; Skiba-Szymanska, J.; Krysa, A. B.; Huwer, J.; Felle, M.; Anderson, M.; Stevenson, R. M.; Heffernan, J.; Ritchie, D. A.; Shields, A. J. *Nat. Commun.* **2018**, *9*, 862 (cit. on pp. 6–8, 28, 74).

(60) Wang, H. et al. *Phys. Rev. Lett.* **2019**, *122*, 113602 (cit. on pp. 6, 9, 10, 27).

(61) Zeuner, K. D.; Jöns, K. D.; Schweickert, L.; Hedlund, C. R.; Lobato, C. N.; Lettner, T.; Wang, K.; Gyger, S.; Schöll, E.; Steinhauer, S.; Hammar, M.; Zwiller, V. *ACS Photonics* **2021**, *8*, 2337–2344 (cit. on pp. 6, 7).

(62) Schwartz, I.; Cogan, D.; Schmidgall, E. R.; Don, Y.; Gantz, L.; Kenneth, O.; Lindner, N. H.; Gershoni, D. *Science* **2016**, *354*, 434–437 (cit. on p. 6).

(63) Javadi, A.; Söllner, I.; Arcari, M.; Hansen, S. L.; Midolo, L.; Mahmoodian, S.; Kiršanskė, G.; Pregnolato, T.; Lee, E. H.; Song, J. D.; Stobbe, S.; Lodahl, P. *Nat. Commun.* **2015**, *6*, 8655 (cit. on p. 6).

(64) Wang, H. et al. *Nat. Photonics* **2017**, *11*, 361–365 (cit. on p. 6).

(65) Loredo, J.; Broome, M.; Hilaire, P.; Gazzano, O.; Sagnes, I.; Lemaitre, A.; Almeida, M.; Senellart, P.; White, A. *Phys. Rev. Lett.* **2017**, *118*, 130503 (cit. on p. 6).

(66) He, Y. et al. *Phys. Rev. Lett.* **2017**, *118*, 190501 (cit. on p. 6).

(67) Wang, Z. M.; Qin, J.; Ding, Y.; Chen, Z.-s.; You, X.; He, Y. M.; Jiang, X.; You, L.; Schneider, C.; Renema, J. J.; Höfling, S.; Lu, C. Y.; Pan, J. W. *Phys. Rev. Lett.* **2019**, *123*, 250503 (cit. on p. 6).

(68) Lodahl, P. *Quantum Sci. Technol.* **2017**, *3*, 013001 (cit. on p. 6).

(69) Zhai, L.; Nguyen, G. N.; Spinnler, C.; Ritzmann, J.; Löbl, M. C.; Wieck, A. D.; Ludwig, A.; Javadi, A.; Warburton, R. J. *Nat. Nanotechnol.* **2022**, *17*, 829–833 (cit. on p. 6).

(70) Cogan, D.; Su, Z.-E.; Kenneth, O.; Gershoni, D. *Nat. Photonics* **2023**, *17*, 324–329 (cit. on p. 6).

(71) Buckley, S.; Rivoire, K.; Vučković, J. *Rep. Prog. Phys.* **2012**, *75*, 126503 (cit. on p. 6).

(72) Sapienza, L.; Davanço, M.; Badolato, A.; Srinivasan, K. *Nat. Commun.* **2015**, *6*, 7833 (cit. on pp. 6, 9, 11, 12).

(73) Yamamoto, Y.; Santori, C.; Solomon, G.; Vuckovic, J.; Fattal, D.; Waks, E.; Diamanti, E. *Prog. Inform.* **2005**, *1* (cit. on p. 6).

(74) Semenova, E. S.; Hostein, R.; Patriarche, G.; Mauguin, O.; Largeau, L.; Robert-Philip, I.; Beveratos, A.; Lemaître, A. *J. Appl. Phys.* **2008**, *103*, 103533 (cit. on pp. 6, 7).

(75) Portalupi, S. L.; Jetter, M.; Michler, P. *Semicond. Sci. Technol.* **2019**, *34*, 053001 (cit. on pp. 6, 8).

(76) Skiba-Szymanska, J.; Stevenson, R. M.; Varnava, C.; Felle, M.; Huwer, J.; Müller, T.; Bennett, A. J.; Lee, J. P.; Farrer, I.; Krysa, A. B.; Spencer, P.; Goff, L. E.; Ritchie, D. A.; Heffernan, J.; Shields, A. J. *Phys. Rev. Appl.* **2017**, *8*, 014013 (cit. on pp. 6, 7, 28, 29, 74).

(77) Semenova, E. S. et al. *Nanotechnology* **2004**, *15*, S283–S287 (cit. on pp. 6, 7).

(78) Paul, M.; Olbrich, F.; Höschele, J.; Schreier, S.; Kettler, J.; Portalupi, S. L.; Jetter, M.; Michler, P. *Appl. Phys. Lett.* **2017**, *111*, 033102 (cit. on pp. 6, 7).

(79) Zeuner, K. D.; Paul, M.; Lettner, T.; Hedlund, C. R.; Schweickert, L.; Steinhauer, S.; Yang, L.; Zichi, J.; Hammar, M.; Jöns, K. D.; Zwiller, V. *Appl. Phys. Lett.* **2018**, *112*, 173102 (cit. on pp. 6, 7).

(80) Sittig, R.; Nawrath, C.; Kolatschek, S.; Bauer, S.; Schaber, R.; Huang, J.; Vijayan, P.; Pruy, P.; Portalupi, S. L.; Jetter, M.; Michler, P. *Nanophotonics* **2022**, *11*, 1109–1116 (cit. on p. 6).

(81) Wyborski, P.; Podemski, P.; Wroński, P. A.; Jabeen, F.; Höfling, S.; Sęk, G. *Materials* **2022**, *15*, 1071 (cit. on p. 6).

(82) Wroński, P. A.; Wyborski, P.; Musiał, A.; Podemski, P.; Sęk, G.; Höfling, S.; Jabeen, F. *Materials* **2021**, *14*, 5221 (cit. on pp. 6, 7).

(83) Mrowiński, P.; Musiał, A.; Gawarecki, K.; Dusanowski, Ł.; Heuser, T.; Srocka, N.; Quandt, D.; Strittmatter, A.; Rodt, S.; Reitzenstein, S.; Sęk, G. *Phys. Rev. B* **2019**, *100*, 115310 (cit. on pp. 6–8).

(84) Nishi, K.; Saito, H.; Sugou, S.; Lee, J.-S. *Appl. Phys. Lett.* **1999**, *74*, 1111–1113 (cit. on p. 7).

(85) Ustinov, V. M.; Maleev, N. A.; Zhukov, A. E.; Kovsh, A. R.; Egorov, A. Y.; Lunev, A. V.; Volovik, B. V.; Krestnikov, I. L.; Musikhin, Y. G.; Bert, N. A.; Kop'ev, P. S.; Alferov, Z. I.; Ledentsov, N. N.; Bimberg, D. *Appl. Phys. Lett.* **1999**, *74*, 2815–2817 (cit. on p. 7).

(86) Guffarth, F.; Heitz, R.; Schliwa, A.; Stier, O.; Ledentsov, N. N.; Kovsh, A. R.; Ustinov, V. M.; Bimberg, D. *Phys. Rev. B* **2001**, *64*, 085305 (cit. on p. 7).

(87) Tatebayashi, J.; Nishioka, M.; Arakawa, Y. *Appl. Phys. Lett.* **2001**, *78*, 3469–3471 (cit. on p. 7).

(88) Sęk, G.; Ryczko, K.; Motyka, M.; Andrzejewski, J.; Wysocka, K.; Misiewicz, J.; Li, L. H.; Fiore, A.; Patriarche, G. *J. Appl. Phys.* **2007**, *101*, 063539 (cit. on p. 7).

(89) Ward, M.; Dean, M.; Stevenson, R.; Bennett, A.; Ellis, D.; Cooper, K.; Farrer, I.; Nicoll, C.; Ritchie, D.; Shields, A. *Nat. Commun.* **2014**, *5*, 3316 (cit. on p. 7).

(90) Seravalli, L.; Trevisi, G.; Frigeri, P.; Rivas, D.; Muñoz-Matutano, G.; Suárez, I.; Alén, B.; Canet-Ferrer, J.; Martínez-Pastor, J. P. *Appl. Phys. Lett.* **2011**, *98*, 173112 (cit. on p. 7).

(91) Nawrath, C.; Joos, R.; Kolatschek, S.; Bauer, S.; Pruy, P.; Hornung, F.; Fischer, J.; Huang, J.; Vijayan, P.; Sittig, R.; Jetter, M.; Portalupi, S. L.; Michler, P. High emission rate from a Purcell-enhanced, triggered source of pure single photons in the telecom C-band, 2022 (cit. on pp. 7, 9, 10).

(92) Olbrich, F.; Höschele, J.; Müller, M.; Kettler, J.; Portalupi, S. L.; Paul, M.; Jetter, M.; Michler, P. *Appl. Phys. Lett.* **2017**, *111*, 133106 (cit. on p. 7).

(93) Nawrath, C.; Vural, H.; Fischer, J.; Schaber, R.; Portalupi, S. L.; Jetter, M.; Michler, P. *Appl. Phys. Lett.* **2021**, *118*, 244002 (cit. on p. 7).

(94) Nawrath, C.; Olbrich, F.; Paul, M.; Portalupi, S. L.; Jetter, M.; Michler, P. *Appl. Phys. Lett.* **2019**, *115*, 023103 (cit. on p. 7).

(95) Miyazawa, T.; Takemoto, K.; Nambu, Y.; Miki, S.; Yamashita, T.; Terai, H.; Fujiwara, M.; Sasaki, M.; Sakuma, Y.; Takatsu, M.; Yamamoto, T.; Arakawa, Y. *Appl. Phys. Lett.* **2016**, *109*, 132106 (cit. on pp. 7, 68, 74).

(96) Musiał, A.; Holewa, P.; Wyborski, P.; Syperek, M.; Kors, A.; Reithmaier, J. P.; Sęk, G.; Benyoucef, M. *Adv. Quantum Technol.* **2019**, *3*, 1900082 (cit. on pp. 7, 8).

(97) Anderson, M.; Müller, T.; Huwer, J.; Skiba-Szymanska, J.; Krysa, A. B.; Stevenson, R. M.; Heffernan, J.; Ritchie, D. A.; Shields, A. J. *npj Quantum Inf.* **2020**, *6*, 14 (cit. on p. 7).

(98) Anderson, M.; Müller, T.; Skiba-Szymanska, J.; Krysa, A. B.; Huwer, J.; Stevenson, R. M.; Heffernan, J.; Ritchie, D. A.; Shields, A. J. *Phys. Rev. Appl.* **2020**, *13*, 1 (cit. on p. 7).

(99) Dusanowski, Ł.; Musiał, A.; Maryński, A.; Mrowiński, P.; Andrzejewski, J.; Machnikowski, P.; Misiewicz, J.; Somers, A.; Höfling, S.; Reithmaier, J. P.; Sęk, G. *Phys. Rev. B* **2014**, *90*, 125424 (cit. on p. 7).

(100) Dusanowski, Ł.; Syperek, M.; Misiewicz, J.; Somers, A.; Höfling, S.; Kamp, M.; Reithmaier, J. P.; Sęk, G. *Appl. Phys. Lett.* **2016**, *108*, 163108 (cit. on pp. 7, 76).

(101) Kubota, R.; Saiki, T.; Regreny, P.; Benamrouche, A.; Gendry, M. *Jpn. J. Appl. Phys.* **2010**, *49*, 041201 (cit. on p. 7).

(102) Yacob, M.; Reithmaier, J. P.; Benyoucef, M. *Appl. Phys. Lett.* **2014**, *104*, 022113 (cit. on pp. 7, 73).

(103) Benyoucef, M.; Yacob, M.; Reithmaier, J. P.; Kettler, J.; Michler, P. *Appl. Phys. Lett.* **2013**, *103*, 162101 (cit. on pp. 7, 73).

(104) Takemoto, K.; Sakuma, Y.; Hirose, S.; Usuki, T.; Yokoyama, N.; Miyazawa, T.; Takatsu, M.; Arakawa, Y. *Jpn. J. Appl. Phys.* **2004**, *43*, L993–L995 (cit. on p. 7).

(105) Miyazawa, T.; Takemoto, K.; Sakuma, Y.; Hirose, S.; Usuki, T.; Yokoyama, N.; Takatsu, M.; Arakawa, Y. *Jpn. J. Appl. Phys.* **2005**, *44*, L620–L622 (cit. on p. 7).

(106) Takemoto, K.; Takatsu, M.; Hirose, S.; Yokoyama, N.; Sakuma, Y.; Usuki, T.; Miyazawa, T.; Arakawa, Y. *J. Appl. Phys.* **2007**, *101*, 081720 (cit. on pp. 7, 10, 76).

(107) Gurioli, M.; Wang, Z.; Rastelli, A.; Kuroda, T.; Sanguinetti, S. *Nat. Mater.* **2019**, *18*, 799–810 (cit. on pp. 7, 10, 27).

(108) Ha, N.; Liu, X.; Mano, T.; Kuroda, T.; Mitsuishi, K.; Castellano, A.; Sanguinetti, S.; Noda, T.; Sakuma, Y.; Sakoda, K. *Appl. Phys. Lett.* **2014**, *104*, 143106 (cit. on p. 7).

(109) Liu, X.; Ha, N.; Nakajima, H.; Mano, T.; Kuroda, T.; Urbaszek, B.; Kumano, H.; Suemune, I.; Sakuma, Y.; Sakoda, K. *Phys. Rev. B* **2014**, *90*, 081301 (cit. on pp. 7, 28).

(110) Ha, N.; Mano, T.; Dubos, S.; Kuroda, T.; Sakuma, Y.; Sakoda, K. *Appl. Phys. Express* **2020**, *13*, 025002 (cit. on p. 7).

(111) Sala, E. M.; Na, Y. I.; Godsland, M.; Trapalis, A.; Heffernan, J. *Phys. Status. Solidi Rapid Res. Lett.* **2020**, *14*, 2000173 (cit. on pp. 7, 29).

(112) Kors, A.; Reithmaier, J. P.; Benyoucef, M. *Appl. Phys. Lett.* **2018**, *112*, 172102 (cit. on p. 8).

(113) Musiał, A.; Mikulicz, M.; Mrowiński, P.; Zielińska, A.; Sitarek, P.; Wyborski, P.; Kuniej, M.; Reithmaier, J. P.; Sęk, G.; Benyoucef, M. *Appl. Phys. Lett.* **2021**, *118*, 221101 (cit. on pp. 8, 10, 76).

(114) Gschrey, M.; Thoma, A.; Schnauber, P.; Seifried, M.; Schmidt, R.; Wohlfeil, B.; Krüger, L.; Schulze, J.-H.; Heindel, T.; Burger, S.; Schmidt, F.; Strittmatter, A.; Rodt, S.; Reitzenstein, S. *Nat. Commun.* **2015**, *6*, 7662 (cit. on pp. 8, 11, 68).

(115) Fischbach, S.; Schlehahn, A.; Thoma, A.; Srocka, N.; Gissibl, T.; Ristok, S.; Thiele, S.; Kaganskiy, A.; Strittmatter, A.; Heindel, T., et al. *ACS Photonics* **2017**, *4*, 1327–1332 (cit. on pp. 8, 11).

(116) Srocka, N.; Musiał, A.; Schneider, P.-I.; Mrowiński, P.; Holewa, P.; Burger, S.; Quandt, D.; Strittmatter, A.; Rodt, S.; Reitzenstein, S.; Sęk, G. *AIP Adv.* **2018**, *8*, 085205 (cit. on pp. 8, 11).

(117) Sartison, M.; Portalupi, S. L.; Gissibl, T.; Jetter, M.; Giessen, H.; Michler, P. *Sci. Rep.* **2017**, *7*, 39916 (cit. on pp. 8, 11).

(118) Claudon, J.; Bleuse, J.; Malik, N. S.; Bazin, M.; Jaffrennou, P.; Gregersen, N.; Sauvan, C.; Lalanne, P.; Gérard, J.-M. *Nat. Photonics* **2010**, *4*, 174–177 (cit. on pp. 8–10).

(119) Bleuse, J.; Claudon, J.; Creasey, M.; Malik, N. S.; Gérard, J.-M.; Maksymov, I.; Hugonin, J.-P.; Lalanne, P. *Phys. Rev. Lett.* **2011**, *106*, 103601 (cit. on p. 8).

(120) Purcell, E. M. *Phys. Rev.* **1946**, *69*, 681 (cit. on pp. 8, 53).

(121) Strauf, S.; Stoltz, N. G.; Rakher, M. T.; Coldren, L. A.; Petroff, P. M.; Bouwmeester, D. *Nat. Photonics* **2007**, *1*, 704–708 (cit. on pp. 8, 10).

(122) Dousse, A.; Suffczyński, J.; Beveratos, A.; Krebs, O.; Lemaître, A.; Sagnes, I.; Bloch, J.; Voisin, P.; Senellart, P. *Nature* **2010**, *466*, 217–220 (cit. on pp. 8, 11).

(123) Heindel, T.; Schneider, C.; Lermer, M.; Kwon, S. H.; Braun, T.; Reitzenstein, S.; Höfling, S.; Kamp, M.; Forchel, A. *Appl. Phys. Lett.* **2010**, *96*, 011107 (cit. on pp. 8, 10).

(124) Gazzano, O.; de Vasconcellos, S. M.; Arnold, C.; Nowak, A.; Galopin, E.; Sagnes, I.; Lanco, L.; Lemaître, A.; Senellart, P. *Nat. Commun.* **2013**, *4*, 1425 (cit. on pp. 8, 11).

(125) Kim, J.-H.; Cai, T.; Richardson, C. J. K.; Leavitt, R. P.; Waks, E. *Optica* **2016**, *3*, 577 (cit. on pp. 8, 10).

(126) Unsleber, S.; He, Y.-M.; Gerhardt, S.; Maier, S.; Lu, C.-Y.; Pan, J.-W.; Gregersen, N.; Kamp, M.; Schneider, C.; Höfling, S. *Opt. Express* **2016**, *24*, 8539 (cit. on pp. 8, 11).

(127) Chen, Z.-S.; Ma, B.; Shang, X.-J.; Ni, H.-Q.; Wang, J.-L.; Niu, Z.-C. *Nanoscale Res. Lett.* **2017**, *12*, 378 (cit. on pp. 8, 10).

(128) Munsch, M.; Malik, N. S.; Dupuy, E.; Delga, A.; Bleuse, J.; Gérard, J.-M.; Claudon, J.; Gregersen, N.; Mørk, J. *Phys. Rev. Lett.* **2013**, *110*, 177402 (cit. on p. 8).

(129) Gregersen, N.; McCutcheon, D. P. S.; Mørk, J.; Gérard, J.-M.; Claudon, J. *Opt. Express* **2016**, *24*, 20904 (cit. on p. 8).

(130) Osterkryger, A. D.; Claudon, J.; Gérard, J.-M.; Gregersen, N. *Opt. Lett.* **2019**, *44*, 2617 (cit. on p. 8).

(131) Gaál, B.; Jacobsen, M. A.; Vannucci, L.; Claudon, J.; Gérard, J.-M.; Gregersen, N. *Appl. Phys. Lett.* **2022**, *121*, 170501 (cit. on p. 8).

(132) Jurkat, J.; Moczała-Dusanowska, M.; Jacobsen, M. A.; Predojević, A.; Huber, T.; Gregersen, N.; Höfling, S.; Schneider, C. *Phys. Rev. Materials* **2021**, *5*, 064603 (cit. on p. 8).

(133) Claudon, J.; Gregersen, N.; Lalanne, P.; Gérard, J.-M. *ChemPhysChem* **2013**, *14*, 2393–2402 (cit. on p. 9).

(134) Versteegh, M. A. M.; Reimer, M. E.; Jöns, K. D.; Dalacu, D.; Poole, P. J.; Gulinatti, A.; Giudice, A.; Zwiller, V. *Nat. Commun.* **2014**, *5*, 5298 (cit. on p. 9).

(135) Huber, T.; Predojević, A.; Khoshnegar, M.; Dalacu, D.; Poole, P. J.; Majedi, H.; Weihs, G. *Nano Lett.* **2014**, *14*, 7107–7114 (cit. on p. 9).

(136) Ginés, L.; Moczała-Dusanowska, M.; Dlaka, D.; Hošák, R.; Gonzales-Ureta, J. R.; Lee, J.; Ježek, M.; Harbord, E.; Oulton, R.; Höfling, S.; Young, A. B.; Schneider, C.; Predojević, A. *Phys. Rev. Lett.* **2022**, *129*, 033601 (cit. on p. 9).

(137) Wang, B.-Y.; Häyrynen, T.; Vannucci, L.; Jacobsen, M. A.; Lu, C.-Y.; Gregersen, N. *Appl. Phys. Lett.* **2021**, *118*, 114003 (cit. on p. 9).

(138) Schall, J. et al. *Adv. Quantum Technol.* **2021**, *4*, 2100002 (cit. on pp. 9, 11).

(139) Davanço, M.; Rakher, M. T.; Schuh, D.; Badolato, A.; Srinivasan, K. *Appl. Phys. Lett.* **2011**, *99*, 041102 (cit. on pp. 9, 10).

(140) Kolatschek, S.; Hepp, S.; Sartison, M.; Jetter, M.; Michler, P.; Portalupi, S. L. *J. Appl. Phys.* **2019**, *125*, 045701 (cit. on pp. 9, 11).

(141) Wang, H. et al. *Nat. Photonics* **2019**, *13*, 770–775 (cit. on pp. 9–11).

(142) Moczała-Dusanowska, M.; Dusanowski, Ł.; Iff, O.; Huber, T.; Kuhn, S.; Czyszanowski, T.; Schneider, C.; Höfling, S. *ACS Photonics* **2020**, *7*, 3474–3480 (cit. on pp. 9, 10).

(143) Xu, S.-W.; Wei, Y.-M.; Su, R.-B.; Li, X.-S.; Huang, P.-N.; Liu, S.-F.; Huang, X.-Y.; Yu, Y.; Liu, J.; Wang, X.-H. *Photon. Res.* **2022**, *10*, B1–B6 (cit. on pp. 9–12).

(144) Zinoni, C.; Alloing, B.; Monat, C.; Zwiller, V.; Li, L. H.; Fiore, A.; Lunghi, L.; Gerardino, A.; de Riedmatten, H.; Zbinden, H.; Gisin, N. *Appl. Phys. Lett.* **2006**, *88*, 131102 (cit. on p. 10).

(145) Rickert, L.; Kupko, T.; Rodt, S.; Reitzenstein, S.; Heindel, T. *Opt. Express* **2019**, *27*, 36824 (cit. on p. 10).

(146) Blokhin, S. A.; Bobrov, M. A.; Maleev, N. A.; Donges, J. N.; Bremer, L.; Blokhin, A. A.; Vasil'ev, A. P.; Kuzmenkov, A. G.; Kolodeznyi, E. S.; Shchukin, V. A.; Ledentsov, N. N.; Reitzenstein, S.; Ustinov, V. M. *Opt. Express* **2021**, *29*, 6582 (cit. on p. 10).

(147) Kolatschek, S.; Nawrath, C.; Bauer, S.; Huang, J.; Fischer, J.; Sittig, R.; Jetter, M.; Portalupi, S. L.; Michler, P. *Nano Lett.* **2021**, *21*, 7740–7745 (cit. on p. 10).

(148) Barbiero, A.; Huwer, J.; Skiba-Szymanska, J.; Ellis, D. J. P.; Stevenson, R. M.; Müller, T.; Shooter, G.; Goff, L. E.; Ritchie, D. A.; Shields, A. J. *ACS Photonics* **2022**, *9*, 3060–3066 (cit. on p. 10).

(149) Bremer, L.; Jimenez, C.; Thiele, S.; Weber, K.; Huber, T.; Rodt, S.; Herkommer, A.; Burger, S.; Höfling, S.; Giessen, H.; Reitzenstein, S. *Opt. Express* **2022**, *30*, 15913 (cit. on p. 10).

(150) Barbiero, A.; Huwer, J.; Skiba-Szymanska, J.; Müller, T.; Stevenson, R. M.; Shields, A. J. *Opt. Express* **2022**, *30*, 10919 (cit. on p. 10).

(151) Dalacu, D.; Mnaymneh, K.; Sazonova, V.; Poole, P. J.; Aers, G. C.; Lapointe, J.; Cheriton, R.; SpringThorpe, A. J.; Williams, R. *Phys. Rev. B* **2010**, *82*, 033301 (cit. on p. 10).

(152) Birowosuto, M. D.; Sumikura, H.; Matsuo, S.; Taniyama, H.; van Veldhoven, P. J.; Nötzel, R.; Notomi, M. *Sci. Rep.* **2012**, *2*, 321 (cit. on p. 10).

(153) Fischbach, S.; Kaganskiy, A.; Tauscher, E. B. Y.; Gericke, F.; Thoma, A.; Schmidt, R.; Strittmatter, A.; Heindel, T.; Rodt, S.; Reitzenstein, S. *Appl. Phys. Lett.* **2017**, *111*, 011106 (cit. on p. 10).

(154) Chen, Y.; Zopf, M.; Keil, R.; Ding, F.; Schmidt, O. G. *Nat. Commun.* **2018**, *9*, 2994 (cit. on p. 10).

(155) Yang, J.; Nawrath, C.; Keil, R.; Joos, R.; Zhang, X.; Höfer, B.; Chen, Y.; Zopf, M.; Jetter, M.; Portalupi, S. L.; Ding, F.; Michler, P.; Schmidt, O. G. *Opt. Express* **2020**, *28*, 19457 (cit. on pp. 10, 68).

(156) Reimer, M. E.; Bulgarini, G.; Akopian, N.; Hocevar, M.; Bavinck, M. B.; Verheijen, M. A.; Bakkers, E. P.; Kouwenhoven, L. P.; Zwiller, V. *Nat. Commun.* **2012**, *3*, 737 (cit. on p. 10).

(157) Kremer, P. E.; Dada, A. C.; Kumar, P.; Ma, Y.; Kumar, S.; Clarke, E.; Gerardot, B. D. *Phys. Rev. B* **2014**, *90*, 201408 (cit. on p. 10).

(158) Kuhlmann, A. V.; Prechtel, J. H.; Houel, J.; Ludwig, A.; Reuter, D.; Wieck, A. D.; Warburton, R. J. *Nat. Commun.* **2015**, *6*, 8204 (cit. on p. 10).

(159) Ollivier, H.; Priya, P.; Harouri, A.; Sagnes, I.; Lemaître, A.; Krebs, O.; Lanco, L.; Lanzillotti-Kimura, N.; Esmann, M.; Senellart, P. *Phys. Rev. Lett.* **2022**, *129*, 057401 (cit. on p. 10).

(160) Liu, F.; Brash, A. J.; O'Hara, J.; Martins, L. M. P. P.; Phillips, C. L.; Coles, R. J.; Royall, B.; Clarke, E.; Bentham, C.; Prtljaga, N.; Itskevich, I. E.; Wilson, L. R.; Skolnick, M. S.; Fox, A. M. *Nat. Nanotechnol.* **2018**, *13*, 835–840 (cit. on p. 10).

(161) Lodahl, P.; Mahmoodian, S.; Stobbe, S. *Rev. Mod. Phys.* **2015**, *87*, 347–400 (cit. on p. 10).

(162) Liu, J.; Konthasinghe, K.; Davan ço, M.; Lawall, J.; Anant, V.; Verma, V.; Mirin, R.; Nam, S. W.; Song, J. D.; Ma, B.; Chen, Z. S.; Ni, H. Q.; Niu, Z. C.; Srinivasan, K. *Phys. Rev. Appl.* **2018**, *9*, 064019 (cit. on p. 10).

(163) Liu, S.; Srinivasan, K.; Liu, J. *Laser Photonics Rev.* **2021**, *15*, 2100223 (cit. on p. 10).

(164) Gschrey, M.; Gericke, F.; Schußler, A.; Schmidt, R.; Schulze, J.-H.; Heindel, T.; Rodt, S.; Strittmatter, A.; Reitzenstein, S. *Appl. Phys. Lett.* **2013**, *102*, 251113 (cit. on p. 11).

(165) Rodt, S.; Reitzenstein, S. *Nano Express* **2021**, *2*, 014007 (cit. on p. 11).

(166) Musiał, A. et al. *Adv. Quantum Technol.* **2020**, *3*, 2000018 (cit. on p. 11).

(167) Nogues, G.; Merotto, Q.; Bachelier, G.; Lee, E. H.; Song, J. D. *Appl. Phys. Lett.* **2013**, *102*, 231112 (cit. on p. 11).

(168) Lee, K. H.; Green, A. M.; Taylor, R. A.; Sharp, D. N.; Scrimgeour, J.; Roche, O. M.; Na, J. H.; Jarjour, A. F.; Turberfield, A. J.; Brossard, F. S. F.; Williams, D. A.; Briggs, G. A. D. *Appl. Phys. Lett.* **2006**, *88*, 193106 (cit. on p. 11).

(169) Dousse, A.; Lanco, L.; Suffczyński, J.; Semenova, E.; Miard, A.; Lemaître, A.; Sagnes, I.; Roblin, C.; Bloch, J.; Senellart, P. *Phys. Rev. Lett.* **2008**, *101*, 30–33 (cit. on p. 11).

(170) Dousse, A.; Suffczyński, J.; Braive, R.; Miard, A.; Lemaître, A.; Sagnes, I.; Lanco, L.; Bloch, J.; Voisin, P.; Senellart, P. *Appl. Phys. Lett.* **2009**, *94*, 121102 (cit. on p. 11).

(171) Hennessy, K.; Badolato, A.; Winger, M.; Gerace, D.; Atatüre, M.; Gulde, S.; Fält, S.; Hu, E. L.; Imamoğlu, A. *Nature* **2007**, *445*, 896–899 (cit. on pp. 11, 52).

(172) Badolato, A.; Hennessy, K.; Atatüre, M.; Dreiser, J.; Hu, E.; Petroff, P. M.; Imamoğlu, A. *Science* **2005**, *308*, 1158–1161 (cit. on p. 11).

(173) Pfeiffer, M.; Lindfors, K.; Zhang, H.; Fenk, B.; Phillipp, F.; Atkinson, P.; Rastelli, A.; Schmidt, O. G.; Giessen, H.; Lippitz, M. *Nano Lett.* **2013**, *14*, 197–201 (cit. on p. 11).

(174) Kojima, T.; Kojima, K.; Asano, T.; Noda, S. *Appl. Phys. Lett.* **2013**, *102*, 011110 (cit. on p. 11).

(175) Zadeh, I. E.; Elshaari, A. W.; Jöns, K. D.; Fognini, A.; Dalacu, D.; Poole, P. J.; Reimer, M. E.; Zwiller, V. *Nano Lett.* **2016**, *16*, 2289–2294 (cit. on p. 11).

(176) Liu, J.; Davanço, M. I.; Sapienza, L.; Konthasinghe, K.; Cardoso, J. V. D. M.; Song, J. D.; Badolato, A.; Srinivasan, K. *Rev. Sci. Instrum.* **2017**, *88*, 023116 (cit. on pp. 11, 12, 67).

(177) He, Y.-M.; Liu, J.; Maier, S.; Emmerling, M.; Gerhardt, S.; Davanço, M.; Srinivasan, K.; Schneider, C.; Höfling, S. *Optica* **2017**, *4*, 802 (cit. on p. 12).

(178) Manasevit, H. M.; Simpson, W. I. *J. Electrochem. Soc.* **1969**, *116*, 1725 (cit. on p. 15).

(179) Seki, Y.; Tanno, K.; Iida, K.; Ichiki, E. *J. Electrochem. Soc.* **1975**, *122*, 1108–1112 (cit. on p. 15).

(180) Dupuis, R. D.; Dapkus, P. D. *Appl. Phys. Lett.* **1978**, *32*, 406–407 (cit. on p. 15).

(181) Breiland, W. G.; Coltrin, M. E.; Creighton, J.; Hou, H. Q.; Moffat, H. K.; Tsao, J. Y. *Mater. Sci. Eng. R Rep.* **1999**, *24*, 241–274 (cit. on pp. 16, 56).

(182) Eversteyn, F. C.; Severin, P. J. W.; v. d. Brekel, C. H. J.; Peek, H. L. *J. Electrochem. Soc.* **1970**, *117*, 925 (cit. on p. 16).

(183) Shaw, D. W. *J. Cryst. Growth* **1975**, *31*, 130–141 (cit. on p. 16).

(184) Shchukin, V.; Schöll, E.; Kratzer, P. In *Semiconductor Nanostructures*; Springer Berlin Heidelberg: 2008, pp 1–39 (cit. on p. 22).

(185) Shchukin, V. A.; Bimberg, D. *Rev. Mod. Phys.* **1999**, *71*, 1125–1171 (cit. on pp. 22, 23).

(186) Pehlke, E.; Moll, N.; Kley, A.; Scheffler, M. *Appl. Phys. A* **1997**, *65*, 525–534 (cit. on p. 23).

(187) Moll, N.; Scheffler, M.; Pehlke, E. *Phys. Rev. B* **1998**, *58*, 4566–4571 (cit. on p. 23).

(188) Liu, Q. K. K.; Moll, N.; Scheffler, M.; Pehlke, E. *Phys. Rev. B* **1999**, *60*, 17008–17015 (cit. on p. 23).

(189) Bauer, E. *Zeitschrift für Kristallographie-Crystalline Materials* **1958**, *110*, 372–394 (cit. on p. 23).

(190) Stranski, I. N.; Krastanow, L. *Monatshefte für Chemie und verwandte Teile anderer Wissenschaften* **1937**, *71*, 351–364 (cit. on p. 23).

(191) Goldstein, L.; Glas, F.; Marzin, J. Y.; Charasse, M. N.; Roux, G. L. *Appl. Phys. Lett.* **1985**, *47*, 1099–1101 (cit. on p. 24).

(192) Eaglesham, D. J.; Cerullo, M. *Phys. Rev. Lett.* **1990**, *64*, 1943–1946 (cit. on p. 24).

(193) Asaro, R. J.; Tiller, W. A. *Metall. and Mater. Trans. B* **1972**, *3*, 1789–1796 (cit. on p. 24).

(194) Grinfeld, M. A. *J. Nonlinear Sci.* **1993**, *3*, 35–83 (cit. on p. 24).

(195) Dubrovskii, V. G., *Nucleation Theory and Growth of Nanostructures*; Springer Berlin Heidelberg: 2014 (cit. on pp. 24, 26, 27, 57).

(196) Shchukin, V. A.; Ledentsov, N. N.; Kop'ev, P. S.; Bimberg, D. *Phys. Rev. Lett.* **1995**, *75*, 2968–2971 (cit. on p. 25).

(197) Shchukin, V.; Ledentsov, N.; Grundmann, M.; Kop'ev, P.; Bimberg, D. *Surf. Sci.* **1996**, *352-354*, 117–122 (cit. on p. 25).

(198) Nowak, A. K.; Portalupi, S. L.; Giesz, V.; Gazzano, O.; Savio, C. D.; Braun, P.-F.; Karrai, K.; Arnold, C.; Lanco, L.; Sagnes, I.; Lemaître, A.; Senellart, P. *Nat. Commun.* **2014**, *5*, 3240 (cit. on p. 27).

(199) Juska, G.; Dimastrodonato, V.; Mereni, L. O.; Gocalinska, A.; Pelucchi, E. *Nat. Photonics* **2013**, *7*, 527–531 (cit. on p. 28).

(200) Bennett, A. J.; Pooley, M. A.; Stevenson, R. M.; Ward, M. B.; Patel, R. B.; de la Giroday, A. B.; Sköld, N.; Farrer, I.; Nicoll, C. A.; Ritchie, D. A.; Shields, A. J. *Nat. Phys.* **2010**, *6*, 947–950 (cit. on p. 28).

(201) Zhang, J.; Wildmann, J. S.; Ding, F.; Trotta, R.; Huo, Y.; Zallo, E.; Huber, D.; Rastelli, A.; Schmidt, O. G. *Nat. Commun.* **2015**, *6*, 10067 (cit. on p. 28).

(202) Muller, A.; Fang, W.; Lawall, J.; Solomon, G. S. *Phys. Rev. Lett.* **2009**, *103*, 217402 (cit. on p. 28).

(203) Koguchi, N.; Takahashi, S.; Chikyow, T. *J. Cryst. Growth* **1991**, *111*, 688–692 (cit. on p. 28).

(204) Somaschini, C.; Bietti, S.; Koguchi, N.; Sanguinetti, S. *Nano Lett.* **2009**, *9*, 3419–3424 (cit. on p. 28).

(205) Kuroda, T.; Mano, T.; Ha, N.; Nakajima, H.; Kumano, H.; Urbaszek, B.; Jo, M.; Abbarchi, M.; Sakuma, Y.; Sakoda, K.; Suemune, I.; Marie, X.; Amand, T. *Phys. Rev. B* **2013**, *88*, 041306(R) (cit. on p. 28).

(206) Ha, N.; Mano, T.; Wu, Y.-N.; Ou, Y.-W.; Cheng, S.-J.; Sakuma, Y.; Sakoda, K.; Kuroda, T. *Appl. Phys. Express* **2016**, *9*, 101201 (cit. on p. 28).

(207) Ohtake, A.; Ozeki, M.; Nakamura, J. *Phys. Rev. Lett.* **2000**, *84*, 4665–4668 (cit. on p. 28).

(208) Jahromi, I. R.; Juska, G.; Varo, S.; Basset, F. B.; Salusti, F.; Trotta, R.; Gocalinska, A.; Mattana, F.; Pelucchi, E. *Appl. Phys. Lett.* **2021**, *118*, 073103 (cit. on p. 29).

(209) Schliwa, A.; Winkelnkemper, M.; Lochmann, A.; Stock, E.; Bimberg, D. *Phys. Rev. B* **2009**, *80*, 161307 (cit. on p. 29).

(210) Wang, Z. M.; Holmes, K.; Mazur, Y. I.; Ramsey, K. A.; Salamo, G. J. *Nanoscale Res. Lett.* **2006**, *1*, 57–61 (cit. on p. 29).

(211) Wang, Z. M.; Liang, B. L.; Sablon, K. A.; Salamo, G. J. *Appl. Phys. Lett.* **2007**, *90*, 113120 (cit. on p. 29).

(212) Huo, Y. H.; Rastelli, A.; Schmidt, O. G. *Appl. Phys. Lett.* **2013**, *102*, 152105 (cit. on p. 29).

(213) Heyn, C.; Stemmann, A.; Köppen, T.; Strelow, C.; Kipp, T.; Grave, M.; Mendach, S.; Hansen, W. *Appl. Phys. Lett.* **2009**, *94*, 183113 (cit. on p. 29).

(214) Basset, F. B.; Valeri, M.; Roccia, E.; Muredda, V.; Poderini, D.; Neuwirth, J.; Spagnolo, N.; Rota, M. B.; Carvacho, G.; Sciarrino, F.; Trotta, R. *Sci. Adv.* **2021**, *7*, eabe6379 (cit. on p. 29).

(215) Luttinger, J. M.; Kohn, W. *Phys. Rev.* **1955**, *97*, 869–883 (cit. on p. 31).

(216) Wojs, A.; Hawrylak, P.; Fafard, S.; Jacak, L. *Phys. Rev. B* **1996**, *54*, 5604–5608 (cit. on p. 31).

(217) Korkusiński, M.; Hawrylak, P. *Phys. Rev. B* **2001**, *63*, 195311 (cit. on p. 31).

(218) Franceschetti, A.; Zunger, A. *Phys. Rev. Lett.* **1997**, *78*, 915–918 (cit. on pp. 31, 33).

(219) Wang, L.-W.; Kim, J.; Zunger, A. *Phys. Rev. B* **1999**, *59*, 5678–5687 (cit. on p. 31).

(220) Williamson, A. J.; Wang, L. W.; Zunger, A. *Phys. Rev. B* **2000**, *62*, 12963–12977 (cit. on pp. 31–34).

(221) Bester, G.; Nair, S.; Zunger, A. *Phys. Rev. B* **2003**, *67*, 161306(R) (cit. on p. 31).

(222) Bester, G.; Zunger, A. *Phys. Rev. B* **2005**, *71*, 045318 (cit. on p. 31).

(223) Franceschetti, A.; Fu, H.; Wang, L. W.; Zunger, A. *Phys. Rev. B* **1999**, *60*, 1819–1829 (cit. on pp. 31, 33, 35).

(224) Fu, H.; Zunger, A. *Phys. Rev. B* **1997**, *56*, 1496–1508 (cit. on pp. 31, 32).

(225) Kane, E. *J. Phys. Chem. Solids* **1956**, *1*, 82–99 (cit. on p. 32).

(226) Kane, E. O. *J. Phys. Chem. Solids* **1957**, *1*, 249–261 (cit. on p. 32).

(227) Trebin, H.-R.; Rössler, U.; Ranvaud, R. *Phys. Rev. B* **1979**, *20*, 686–700 (cit. on p. 32).

(228) Bahder, T. B. *Phys. Rev. B* **1990**, *41*, 11992–12001 (cit. on p. 32).

(229) Burt, M. G. *J. Phys.: Condens. Matter* **1992**, *4*, 6651–6690 (cit. on p. 32).

(230) Foreman, B. A. *Phys. Rev. B* **1993**, *48*, 4964–4967 (cit. on p. 32).

(231) Gershoni, D.; Henry, C.; Baraff, G. *IEEE J. Quantum Electron.* **1993**, *29*, 2433–2450 (cit. on p. 32).

(232) Stier, O.; Bimberg, D. *Phys. Rev. B* **1997**, *55*, 7726–7732 (cit. on p. 32).

(233) Jiang, H.; Singh, J. *Phys. Rev. B* **1997**, *56*, 4696–4701 (cit. on p. 32).

(234) Pryor, C.; Kim, J.; Wang, L. W.; Williamson, A. J.; Zunger, A. *J. Appl. Phys.* **1998**, *83*, 2548–2554 (cit. on p. 32).

(235) Stier, O.; Grundmann, M.; Bimberg, D. *Phys. Rev. B* **1999**, *59*, 5688–5701 (cit. on p. 32).

(236) Grundmann, M.; Stier, O.; Bimberg, D. *Phys. Rev. B* **1995**, *52*, 11969–11981 (cit. on p. 32).

(237) Bester, G.; Wu, X.; Vanderbilt, D.; Zunger, A. *Phys. Rev. Lett.* **2006**, *96*, 187602 (cit. on p. 32).

(238) Schliwa, A.; Winkelnkemper, M.; Bimberg, D. *Phys. Rev. B* **2007**, *76*, 205324 (cit. on p. 32).

(239) Birner, S.; Zibold, T.; Andlauer, T.; Kubis, T.; Sabathil, M.; Trellakis, A.; Vogl, P. *IEEE Trans. Electron Devices* **2007**, *54*, 2137–2142 (cit. on p. 33).

(240) Hu, Y. Z.; Lindberg, M.; Koch, S. W. *Phys. Rev. B* **1990**, *42*, 1713–1723 (cit. on p. 35).

(241) Martin, E.; Delerue, C.; Allan, G.; Lannoo, M. *Phys. Rev. B* **1994**, *50*, 18258–18267 (cit. on p. 35).

(242) Chen, Y.; Gil, B.; Lefebvre, P.; Mathieu, H. *Phys. Rev. B* **1988**, *37*, 6429–6432 (cit. on p. 37).

(243) Van Kesteren, H. W.; Cosman, E. C.; van der Poel, W. A. J. A.; Foxon, C. T. *Phys. Rev. B* **1990**, *41*, 5283–5292 (cit. on p. 37).

(244) Andreani, L. C.; Bassani, F. *Phys. Rev. B* **1990**, *41*, 7536–7544 (cit. on p. 37).

(245) Blackwood, E.; Snelling, M. J.; Harley, R. T.; Andrews, S. R.; Foxon, C. T. B. *Phys. Rev. B* **1994**, *50*, 14246–14254 (cit. on p. 37).

(246) Bayer, M.; Kuther, A.; Forchel, A.; Gorbunov, A.; Timofeev, V. B.; Schäfer, F.; Reithmaier, J. P.; Reinecke, T. L.; Walck, S. N. *Phys. Rev. Lett.* **1999**, *82*, 1748–1751 (cit. on p. 37).

(247) Bayer, M.; Ortner, G.; Stern, O.; Kuther, A.; Gorbunov, A. A.; Forchel, A.; Hawrylak, P.; Fafard, S.; Hinzer, K.; Reinecke, T. L.; Walck, S. N.; Reithmaier, J. P.; Klopf, F.; Schäfer, F. *Phys. Rev. B* **2002**, *65*, 195315 (cit. on p. 37).

(248) Gammon, D.; Snow, E. S.; Shanabrook, B. V.; Katzer, D. S.; Park, D. *Phys. Rev. Lett.* **1996**, *76*, 3005–3008 (cit. on p. 37).

(249) Dexter, D. In *Advances in Research and Applications*, Seitz, F., Turnbull, D., Eds.; Solid State Physics, Vol. 6; Academic Press: 1958, pp 353–411 (cit. on p. 40).

(250) Loudon, R., *The Quantum Theory of Light*; Oxford University Press: 2000 (cit. on p. 41).

(251) Karrai, K.; Warburton, R. J. *Superlattices Microstruct.* **2003**, *33*, 311–337 (cit. on p. 41).

(252) Narvaez, G. A.; Bester, G.; Zunger, A. *Phys. Rev. B* **2005**, *72*, 245318 (cit. on p. 41).

(253) Dekel, E.; Regelman, D. V.; Gershoni, D.; Ehrenfreund, E.; Schoenfeld, W. V.; Petroff, P. M. *Phys. Rev. B* **2000**, *62*, 11038–11045 (cit. on p. 41).

(254) Sęk, G.; Musiał, A.; Podemski, P.; Misiewicz, J. *J. Appl. Phys.* **2010**, *108*, 033507 (cit. on p. 42).

(255) Abbarchi, M.; Mastrandrea, C.; Kuroda, T.; Mano, T.; Vinattieri, A.; Sakoda, K.; Gurioli, M. *J. Appl. Phys.* **2009**, *106*, 053504 (cit. on p. 43).

(256) Varshni, Y. *Physica* **1967**, *34*, 149–154 (cit. on p. 43).

(257) O'Donnell, K. P.; Chen, X. *Appl. Phys. Lett.* **1991**, *58*, 2924–2926 (cit. on pp. 43, 44).

(258) Lautenschlager, P.; Garriga, M.; Logothetidis, S.; Cardona, M. *Phys. Rev. B* **1987**, *35*, 9174–9189 (cit. on p. 44).

(259) Brown, R. H.; Twiss, R. *The London, Edinburgh, and Dublin Philosophical Magazine and Journal of Science* **1954**, *45*, 663–682 (cit. on pp. 44, 45).

(260) Hanbury-Brown, R.; Twiss, R. Q. *Nature (London)* **1956**, *177*, 27–29 (cit. on pp. 44, 45).

(261) Kimble, H. J.; Dagenais, M.; Mandel, L. *Phys. Rev. Lett.* **1977**, *37*, 691–695 (cit. on p. 48).

(262) Fox, M., *Quantum Optics. An Introduction*; Oxford University Press: 2013 (cit. on pp. 49, 50).

(263) Reithmaier, J. P.; Sęk, G.; Löffler, A.; Hofmann, C.; Kuhn, S.; Reitzenstein, S.; Keldysh, L. V.; Kulakovskii, V. D.; Reinecke, T. L.; Forchel, A. *Nature* **2004**, *432*, 197–200 (cit. on p. 52).

(264) Yoshie, T.; Scherer, A.; Hendrickson, J.; Khitrova, G.; Gibbs, H. M.; Rupper, G.; Ell, C.; Shchekin, O. B.; Deppe, D. G. *Nature* **2004**, *432*, 200–203 (cit. on p. 52).

(265) Najer, D.; Söllner, I.; Sekatski, P.; Dolique, V.; Löbl, M. C.; Riedel, D.; Schott, R.; Starosielec, S.; Valentin, S. R.; Wieck, A. D.; Sangouard, N.; Ludwig, A.; Warburton, R. J. *Nature* **2019**, *575*, 622–627 (cit. on p. 52).

(266) William G. Breiland Alexander I. Gurary, V. B. Temperature determination using pyrometry US Patent, 6,398,406 B1, 2000 (cit. on p. 56).

(267) Breiland, W. G. *Reflectance-Correcting Pyrometry in Thin Film Deposition Applications*; tech. rep.; 2003 (cit. on p. 56).

(268) Berdnikov, Y.; Holewa, P.; Kadkhodazadeh, S.; Śmigiel, J. M.; Frąckowiak, A.; Sakanas, A.; Yvind, K.; Syperek, M.; Semenova, E. Fine-tunable near-critical Stranski-Krastanov growth of InAs/InP quantum dots, 2023 (cit. on p. 57).

(269) Song, H. Z.; Usuki, T.; Nakata, Y.; Yokoyama, N.; Sasakura, H.; Muto, S. *Phys. Rev. B* **2006**, *73*, 115327 (cit. on p. 57).

(270) Hasan, S.; Merckling, C.; Pantouvaki, M.; Meersschaut, J.; Campenhout, J. V.; Vandervorst, W. *J. Cryst. Growth* **2019**, *509*, 133–140 (cit. on p. 57).

(271) Yeu, I. W.; Park, J.; Han, G.; Hwang, C. S.; Choi, J.-H. *Sci. Rep.* **2017**, *7*, 10691 (cit. on p. 57).

(272) Constancias, C.; Landis, S.; Manakli, S.; Martin, L.; Pain, L.; Rio, D. In *Lithography*; John Wiley & Sons, Inc.: 2013, pp 101–182 (cit. on p. 61).

(273) Sakanas, A.; Semenova, E.; Ottaviano, L.; Mørk, J.; Yvind, K. *Microelectron. Eng.* **2019**, *214*, 93–99 (cit. on p. 67).

(274) Kumano, H.; Harada, T.; Suemune, I.; Nakajima, H.; Kuroda, T.; Mano, T.; Sakoda, K.; Odashima, S.; Sasakura, H. *Appl. Phys. Express* **2016**, *9*, 032801 (cit. on p. 68).

(275) Dalgarno, P. A.; McFarlane, J.; Brunner, D.; Lambert, R. W.; Gerardot, B. D.; Warburton, R. J.; Karrai, K.; Badolato, A.; Petroff, P. M. *Appl. Phys. Lett.* **2008**, *92*, 193103 (cit. on p. 68).

(276) Gong, M.; Zhang, W.; Guo, G. C.; He, L. *Appl. Phys. Lett.* **2011**, *99*, 231106 (cit. on p. 72).

(277) Belhadj, T.; Amand, T.; Kunold, A.; Simon, C.-M.; Kuroda, T.; Abbarchi, M.; Mano, T.; Sakoda, K.; Kunz, S.; Marie, X.; Urbaszek, B. *Appl. Phys. Lett.* **2010**, *97*, 051111 (cit. on p. 72).

(278) Koudinov, A. V.; Akimov, I. A.; Kusrayev, Y. G.; Henneberger, F. *Phys. Rev. B* **2004**, *70*, 241305 (cit. on p. 72).

(279) Kuan, T. S.; Kuech, T. F.; Wang, W. I.; Wilkie, E. L. *Phys. Rev. Lett.* **1985**, *54*, 201–204 (cit. on p. 73).

(280) Stringfellow, G. B. *J. Vac. Sci. Technol. B* **1991**, *9*, 2182 (cit. on p. 73).

(281) Han, W. S.; Lee, B.; Baek, J. H.; Lee, J.-H.; Jung, B. S.; Lee, E.-H.; O, B. *Appl. Phys. Lett.* **1998**, *72*, 1905–1907 (cit. on p. 73).

(282) Kuan, T. S.; Wang, W. I.; Wilkie, E. L. *Appl. Phys. Lett.* **1987**, *51*, 51–53 (cit. on p. 73).

(283) Shahid, M. A.; Mahajan, S.; Laughlin, D. E.; Cox, H. M. *Phys. Rev. Lett.* **1987**, *58*, 2567–2570 (cit. on p. 73).

(284) Kim, J.-H.; Aghaeimeibodi, S.; Richardson, C. J. K.; Leavitt, R. P.; Englund, D.; Waks, E. *Nano Lett.* **2017**, *17*, 7394–7400 (cit. on p. 76).

Part II

Core publications

ARTICLE 1

Low-density InAs/InP quantum-dot-like structures

PHYSICAL REVIEW B **101**, 195304 (2020)

Optical and electronic properties of low-density InAs/InP quantum-dot-like structures designed for single-photon emitters at telecom wavelengths

P. Holewa,[1] M. Gawełczyk,[2,1,*] C. Ciostek,[1,†] P. Wyborski,[1] S. Kadkhodazadeh,[3] E. Semenova,[4,‡] and M. Syperek[1,§]

[1]*Laboratory for Optical Spectroscopy of Nanostructures, Department of Experimental Physics, Wrocław University of Science and Technology, Wybrzeże Wyspiańskiego 27, 50-370 Wrocław, Poland*

[2]*Department of Theoretical Physics, Wrocław University of Science and Technology, 50-370 Wrocław, Poland*

[3]*DTU Nanolab–National Centre for Nano Fabrication and Characterization, Technical University of Denmark, Kongens Lyngby DK-2800, Denmark*

[4]*DTU Fotonik, Technical University of Denmark, Kongens Lyngby DK-2800, Denmark*

(Received 16 December 2019; revised manuscript received 27 February 2020; accepted 18 March 2020; published 11 May 2020)

Due to their band-structure and optical properties, InAs/InP quantum dots (QDs) constitute a promising system for single-photon generation at the third telecom window of silica fibers and for applications in quantum communication networks. However, obtaining the necessary low in-plane density of emitters remains a challenge. Such structures are also still less explored than their InAs/GaAs counterparts regarding optical properties of confined carriers. Here, we report on the growth via metal-organic vapor phase epitaxy and investigation of low-density InAs/InP QD-like structures, emitting in the range of 1.2–1.7 μm, which includes the S, C, and L bands of the third optical window. We observe multiple photoluminescence (PL) peaks originating from flat QDs with the height of a few material monolayers. Temperature-dependent PL reveals a redistribution of carriers between families of QDs. Via time-resolved PL, we obtain radiative lifetimes nearly independent of emission energy in contrast to previous reports on InAs/InP QDs, which we attribute to strongly height-dependent electron-hole correlations. Additionally, we observe neutral and charged exciton emission from spatially isolated emitters. Using the eight-band $\boldsymbol{k}\cdot\boldsymbol{p}$ model and configuration-interaction method, we successfully reproduce the energies of emission lines, the dispersion of exciton lifetimes, the carrier activation energies, as well as the biexciton binding energy, which allows for a detailed and comprehensive analysis of the underlying physics.

DOI: 10.1103/PhysRevB.101.195304

I. INTRODUCTION

Semiconductor epitaxial self-assembled quantum dots (QDs) have attracted attention for decades. Among many factors, this interest is driven by their ability to emit single photons of high purity and indistinguishability [1–3], and by the possibilities of their integration with existing semiconductor platforms. The proposed applications require further development of QDs to meet specific requirements, e.g., emission wavelength or spatial isolation of an emitter. A currently vital example is a nonclassical single photon source desired for quantum-secured data transfer and quantum information processing in open systems exploiting the existing architecture of mid- and long-haul silica- fiber-based optical networks. To achieve this specific application target, a QD should emit in the low-loss third spectral window of silica fibers (1.46–1.625 μm) commonly divided into three subbands: S (1460–1530 nm), C (1530–1565 nm), and L (1565–1625 nm). This can be reached by employing an InGaAs metamorphic layer approach for the well-known InAs/GaAs QD structure [4]. Recently, QDs made by this technique have shown high fidelity photon entanglement [5]. However, this growth method is technologically demanding and still prone to structural defects [6], which obstructs its migration to the realm of applications.

Emission in the third telecom window can naturally be achieved by using InAs QDs grown on the InP substrate without applying additional strain engineering to the band gap. However, due to more than two times smaller lattice mismatch in comparison to standard InAs/GaAs QDs, the InAs/InP dots form dense arrays of flat and sizable in-plane material islands. Consequently, the in-plane spatial isolation and quality of such dots are hardly achievable but still indispensable for a single-photon source application.

Up to now, the reduced planar density of InAs/InP QDs emitting in the targeted spectral range has been achieved in molecular beam epitaxy (MBE) through modifications of the growth scheme or post-growth annealing of the structure [7–9]. A similar approach has been used in metal-organic vapor phase epitaxy (MOVPE), where the combination of annealing with double-capping was applied to enhance the uniformity of QD sizes [10,11]. Both techniques have yielded good optical quality InAs/InP QD-based emitters [8,12,13].

*michal.gawelczyk@pwr.edu.pl
†Present address: Experimental Physics 3, University of Würzburg, Am Hubland, 97074 Würzburg, Germany.
‡esem@fotonik.dtu.dk
§marcin.syperek@pwr.edu.pl

Here, we explore the MOVPE growth of InAs/InP QD-like nanostructures, modified by introducing the additional interruption step leading to formation of sparse islands emitting light within the third telecom band. The strain-driven formation of islands (the Stranski-Krastanov mechanism) from the InAs(P) layer is partially suppressed by high V/III ratio to ensure low surface density of QDs below 10^9 cm^{-2}. This results in good spatial isolation of single emitters allowing for examination of their optical properties.

Apart from their relevance for applications, InAs QDs grown on InP itself or in alloys lattice-matched to InP, e.g., InGaAlAs with various cation proportions, are interesting for fundamental research, as they provide carrier confinement distinct from the one known from well-explored and described GaAs-based systems. Recent studies have provided explanation of some of their properties, such as partially polarized emission [14], exciton recombination characterized by two distinct lifetimes in the case of asymmetric dots [15] or the structure of excited states [16]. They have also raised a question regarding the exciton confinement regime [17,18]. These results were, however, obtained mostly for very dense ensembles of elongated QDs [19], and thus characterization of carrier confinement and the resulting optical properties of low-density QDs, growing in a different geometry such as those considered here, is needed. In this work, we combine both goals and provide a comprehensive description of this specific low-density QD-like system, focusing both on its relevance for potential applications and on fundamental properties of carrier confinement leading to the observed properties of emission.

The investigated InAs/InP QDs are formed on a 3-ML-thick InAs(P) wetting layer (WL) and have a truncated pyramidal shape with a hexagonal base. The ensemble photoluminescence (PL) from the dots is concentrated in multiple narrow bands corresponding to QDs with height of consecutive integer numbers of monolayers (MLs) of material, according to our calculation. By fine-tuning the agreement of calculated exciton energies with positions of PL peaks, we establish that QDs in-plane size scales linearly with their height. Additionally, from time-resolved PL studies, we assess exciton lifetimes on the order of 1 ns with a very weak dispersion of values. While in general a dispersive character of the latter is expected due to strong scaling of radiative recombination rates with emission wavelength [20], we find theoretically that the virtually energy-independent values measured here result from the interplay between the said general trend and a strong change in the strength of Coulomb electron-hole correlations, known to enhance exciton-light coupling, with increasing QD height. We observe also a thermally driven redistribution of carriers, exhibited in thermal quenching of PL from the highest-energy peaks and a combination of enhancement and quenching for the others. For the latter, the extracted activation energies correspond well to those calculated by us for escape of electrons to the WL, while for the other we rather deal with excitation of whole excitons. At the same time, the energies corresponding to PL enhancement for each of the bands correspond to energies of thermal escape of single carriers from QDs forming the higher-energy neighboring band, which illustrates the migration of carriers between families of QDs. Finally, by means of high-resolution microphotoluminescence (μPL) measurements performed on samples with fabricated submicrometer mesas, we observe emission lines originating from recombination of neutral and charged excitonic complexes within single QDs. Charged excitons (CX) are observed in each of the subbands of the third telecom window with emission persisting up to $T = 70$ K.

The paper is organized as follows. In Sec. II, we describe the investigated structure and experimental methods. Next, in Sec. III, we describe the formalism employed for theoretical calculations. In Sec. IV, we report experimental results and provide explanations based on theoretical calculations. Finally, we summarize our findings in Sec. V.

II. INVESTIGATED STRUCTURE AND OPTICAL EXPERIMENTS

In this section, we discuss the QD growth method, and the morphological characteristics of the structures under consideration, as well as we describe the experimental methods used.

A. Investigated structure

The structure was grown in the low-pressure MOVPE TurboDisc® reactor using standard precursors: arsine (AsH_3), phosphine (PH_3), tertiarybutylphosphine (TBP), and trimethylindium (TMI). The growth sequence started from the deposition of a 0.5-μm-thick InP buffer layer on an (001)-oriented InP substrate at 600°C. Subsequently, the temperature was decreased to 480°C and stabilized first under TBP and afterwards AsH_3 ambient. A layer of QDs on a wetting layer (WL) was formed after deposition of a nominally 1.04-ML-thick InAs layer at TMIn and AsH_3 flow rates of 12.2 and 4461 μmol/min, respectively, with the V/III ratio of 366. After that, a 6-s-long growth interruption was introduced prior to the deposition of a 10-nm-thick InP cap layer. The temperature was then increased to 600°C, and 30 nm of InP was deposited. Finally, an array of surface QDs was deposited using the same growth parameters for characterization by atomic force microscopy (AFM).

The structural and morphological characteristics of the structures are summarized in Fig. 1 and further elaborated in Ref. [21]. Figure 1(a) shows a 5 μm × 3.5 μm areal scan of surface QDs measured with the AFM. The dots are relatively large and slightly elongated in the $[1\bar{1}0]$ direction and are sparsely scattered with a surface density of $\lesssim 10^9$ cm^{-2}. Statistical analysis of their geometry presented in Fig. 1(c) showed length L in the range of 55–85 nm, while width W is spread between 45 and 55 nm. This gives an average in-plane aspect ratio of ∼1.25. The median QD height H is relatively large and exceeds 9 nm. Setting the aspect ratio of $L/W = 1.25$, we calculate L from measured QD areas and check their correlation with H by plotting in Fig. 1(d) the dependence $H(L)$ in the form of a scatter plot. Based on this we deduce a linear dependence between H and L for surface QDs, which is plotted to guide the eye with a solid line.

The magnified image of surface QDs shown in the inset of Fig. 1(a) reveals their diamond-like shape ended from top by a dome, which we schematically present in Fig. 1(e). Although these dots are optically inactive, we assume that their in-plane

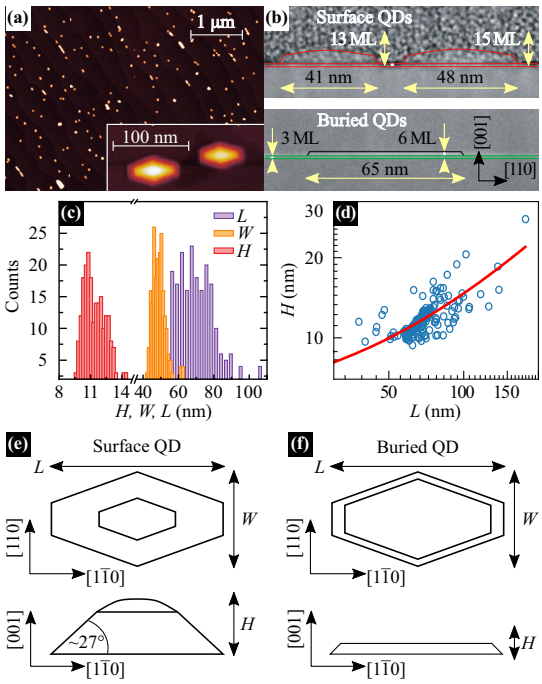

FIG. 1. (a) AFM image of 5 × 3.5 μm^2 sample area with surface QDs. (Inset) Magnified part revealing geometry of single QDs. (b) TEM image of the sample cross-section with surface and buried QDs. (c) Histograms of width W, length L, and height H of surface QDs based on the AFM data. (d) Dependence of surface QDs height on their in-plane size based on AFM data (symbols) with a linear trend (line). (e) and (f) Assumed shapes for the surface and buried QDs, respectively.

dimensions are similar to those of their buried counterparts, which are responsible for the strong optical response.

A high-angle annular dark-field scanning transmission electron microscopy (HAADF STEM) image of the structure is presented in Fig. 1(b), providing a cross-sectional view in [1$\bar{1}$0] crystallographic direction. The contrast in HAADF STEM images is primarily related to the atomic number, and can thus be used directly to measure the dimensions of the QDs, as the contrast arising from the strain is negligible here [23]. The upper panel reveals surface QDs, while the bottom one shows a single buried dot. Although some similarities between both types of dots are discernible, significant differences between them can also be observed. Both types of dots are of similar size in the growth plane. However, the height of buried QDs is much smaller than that of the surface ones. Additionally, the buried ones are flat on top [Fig. 1(f)], in contrast to dome-shaped surface dots [Fig. 1(e)]. These differences most probably result from longer growth interruption after the nucleation of the surface QDs. In this case, the material may be partially redistributed from the WL to the top of QDs, driven by strain relaxation. However, we can assume that the lateral sizes of surface dots are the same as of buried dots. The buried QD shown protrudes by 6 ML from the WL top surface. We estimate that QDs are of pure InAs, based on the lattice spacing analysis of the STEM images available in Ref. [21].

B. Optical experiments

For time-integrated PL, photoluminescence excitation (PLE), and time-resolved PL (TRPL) experiments the structure was held in a helium closed-cycle refrigerator allowing for control of temperature in the range of 10–300 K. The sample was excited by a train of ∼2-ps-long pulses generated by the optical parametric oscillator (OPO) providing a photon energy in the range of 0.9–1.2 eV. The pulse generation frequency was either 76 MHz or lower. The light emitted from the sample was collected in a standard lens-based far-field optical setup and dispersed by a 0.3-m-focal-length monochromator. Time-integrated PL was measured in a wide spectral range of 0.5–1.1 eV via the lock-in technique at the reference modulation frequency of 2 kHz, using a thermoelectrically cooled InGaAs-based single-channel detector. The same experimental setup was employed for the PLE measurements. In this case, the monochromator was fixed to a certain detection energy (E_{det}) while the structure was excited by scanning the photon energy across the OPO's spectral range. The TRPL was measured by a time-correlated single photon counting method. Photons were spectrally filtered by the monochromator and subsequently directed onto the NbN superconducting detector. The multichannel event timer was synchronized to the pulse train to produce photon event statistics. The overall temporal resolution of the TRPL setup was ∼80 ps.

For the PL with high spatial resolution (μPL) the sample was kept in a He-flow cryostat allowing for control of the sample temperature in the range of 5–300 K. Sample was excited by the continuous wave (CW) semiconductor laser, and the emission was collected by a near-infrared-optimized microscope objective with high numerical aperture of NA = 0.4. The μPL signal was spectrally analyzed by a 1-m-focal-length monochromator and registered by a liquid-nitrogen-cooled InGaAs-based linear detector operating in the spectral range from 1.24 eV down to 0.75 eV. Polarization properties of emitted light were analyzed by rotating the half-wave retarder mounted before a fixed high-contrast-ratio (10^6:1) linear polarizer placed in front of the monochromator's entrance.

III. THEORY

In this section, we describe the theoretical framework used to model investigated QDs and their electronic and optical properties.

A. Modeling of QDs

The modeling of nanostructures in question was preceded by evaluation of our initial assumption on their height varying by single MLs and by establishing the thickness of the WL. For this, numerical calculations within the eight-band $\boldsymbol{k}\cdot\boldsymbol{p}$ method with use of the commercially available *nextnano* software have been performed [24]. As a result, via comparison

with experimental data, a WL thickness of 3 MLs has been determined.

To model the buried QDs we have used the available structural data presented in Sec. II. While the in-plane shape is not well-established, we followed the premise derived from surface dots and assumed an elongated hexagonal base with aspect ratio of $L/W = 5/4$. The height, based on the cross-sectional data, is of a few MLs of InAs. Additionally, from the spacing of PL peaks we formed an assumption that the dots are of height equal to consecutive integer numbers of MLs. Thus, we have modeled a series of such QDs protruding by N MLs above the WL of 3-ML thickness, for $N = 1$–9. For each height, we simulated QDs with in-plane sizes varied uniformly from 15 nm × 12 nm up to 60 nm × 48 nm in seven linear steps. Again following the properties of surface QDs, we set the inclination of QD side walls to 27°, which is however of little relevance in view of their small height. Regarding the material composition, we assumed that QDs and WL are composed of pure InAs.

B. Single-particle states and complexes

The lattice mismatch between InAs and InP is only approximately 3%, nonetheless we have calculated the structural strain within the standard continuous elasticity theory via minimization of elastic energy. Next, piezoelectric field resulting from the presence of shear strain in a noncentrosymmetric material has been calculated up to second-order terms in strain-tensor elements. With this, to calculate the electron and hole eigenstates, and then states of their complexes, we have used a numerical implementation [28] of the eight-band $\boldsymbol{k}\cdot\boldsymbol{p}$ theory with envelope-function approximation [29,30]. To fix the spin configuration, a weak (20 mT) magnetic field was used. The Dresselhaus spin-orbit interaction enters via perturbative terms in Hamiltonian blocks that couple the conduction band to valence bands, while the impact of structural strain is included via the standard Bir-Pikus Hamiltonian [31]. The explicit form of the Hamiltonian and description of the numerical implementation may be found in Ref. [32], while the material parameters used are given in Table I along with their sources. Numerical diagonalization yields the conduction- and valence-band electron eigenstates in the form of pseudospinors with components holding the envelope functions for each of the subbands. Hole states were obtained by application of time reversal operation to valence-band electron states.

Next, the calculated electron and hole single-particle states have been used to calculate the neutral- and charged-exciton, as well as biexciton states in the configuration-interaction approach. To this end, electron-hole Coulomb and phenomenological anisotropic exchange interactions have been diagonalized in the basis of 40 × 40 electron-hole configurations, which yielded carrier-complex states expanded in the configuration-space basis. Finally, for each of the states the coupling to light has been evaluated in the dipole approximation, and the resultant dipole moments were used to calculate radiative lifetimes of carrier-complex states [33].

TABLE I. Material parameters used in the modeling of nanostructures and calculation of single-particle and exciton states.

Parameter	Unit	InAs	InP	Source
a	Å	6.06	5.87	[25]
E_g	eV	0.417	1.42	[25]
VBO	eV	−0.59	−0.94	[25]
E_p	eV	21.5	20.7	[25]
m_e^*		0.0229	0.0803	[26]
Δ	eV	0.39	0.11	[25]
γ_1		20.4	4.95	[26]
γ_2		8.3	1.65	[26]
γ_3		9.1	2.35	[26]
e_{14}	C/m^2	−0.111	0.016	[27]
B_{114}	C/m^2	−1.17	−1.54	[27]
B_{124}	C/m^2	−4.31	−3.62	[27]
B_{156}	C/m^2	−0.46	−1.02	[27]
C_k	eV Å	−0.0112	−0.0144	[26]
a_c	eV	−5.08	−6.0	[25]
a_v	eV	1.0	0.6	[25]
b_v	eV	−1.8	−2	[25]
d_v	eV	−3.6	−5	[25]
c_{11}	GPa	833	1011	[25]
c_{12}	GPa	453	561	[25]
c_{44}	GPa	396	456	[25]
ε_r		14.6	12.4	[26]

IV. RESULTS AND DISCUSSION

In this section, we present both experimental and theoretical results. Their confrontation and mutual feedback are used as a base to discuss in detail the revealed properties of the system.

A. Emission from ensemble of QDs

We begin with presenting the results of PL measurements performed on the ensemble of QDs in question. These are presented in Fig. 2(a), where at $T = 10$ K a multimodal distribution of intensity with well-pronounced seven PL maxima (labeled A to G) is visible. The peaks spread across the energy range of ∼0.65–1.05 eV, and, notably, those labeled with D, E, and F coincide with the S, C, and L bands of the third telecom window, respectively. Combining this observation with knowledge on the growth process, we conjecture that each of the PL bands corresponds to emission from a distinct family of QDs. Such multi-peaked PL was previously observed for InAs/InP QDs grown via chemical beam epitaxy (CBE) [34,35], MBE [36,37], and MOVPE [38,39], as well as for InAs/GaAs QDs [40]. Based on our initial theoretical estimations, to form such a pattern of bands in emission, QDs have to be of height varying by a single InAs ML (≈0.3 nm), and each peak corresponds to a given QD height. Increase of temperature up to $T = 300$ K results in the PL pattern presented in Fig. 2(b), which still reflects the multimodal QD-height distribution. Thus, the confinement for carriers is strong enough, so that they are still localized, as it could be expected for QDs of size and composition assumed here.

To strengthen our interpretation of the ground-state nature of emission for all observed PL peaks, in Fig. 3, we plot

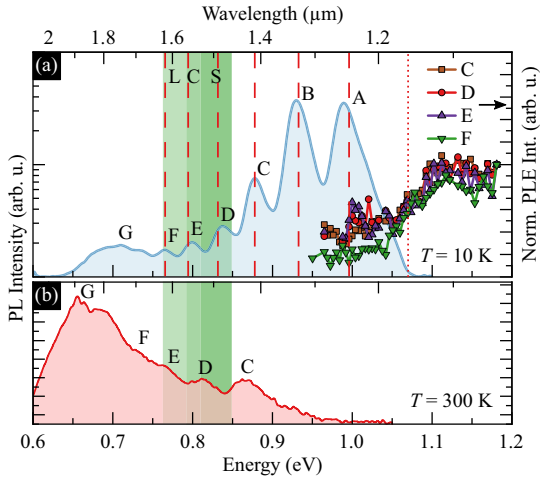

FIG. 2. (a) Low-temperature ($T = 10$ K) PL spectrum (solid line, logarithmic scale) and PLE signals for the ensemble of QDs obtained for collection from lines C–F (symbols). Vertical dashed lines mark theoretically calculated exciton energies for modeled QDs, and dotted line marks the wetting layer absorption edge. Shaded areas represent the S (1460–1530nm), C (1530–1565nm) and L (1565–1625nm) bands of the third telecom window. (b) PL spectrum measured at $T = 300$ K.

the excitation power-dependent PL spectra. The emission pattern does not change qualitatively over three orders of magnitude of the excitation powers [Fig. 3(a)], exhibiting the same multi-peak structure, with two peaks emitting at highest energies being always the brightest at low T. Furthermore, the dependence of the integrated PL intensity on the excitation power [Fig. 3(b)] for the all PL peaks is linear in the whole investigated power range (over four orders of magnitude), with none of peaks saturating. These observations, combined with temperature-dependent characteristics of PL (see Fig. 4), single QD studies and agreement of numerical calculations with experimental findings, presented in the following part of this article, prove the ground-state character of emission for all PL peaks.

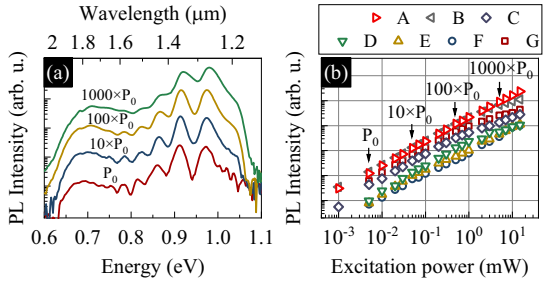

FIG. 3. (a) Power-dependent PL spectra at $T = 10$ K for excitation powers increasing by a factor of 10. (b) Integrated PL intensity for all peaks as a function of the excitation power.

Next, we focus on absorption properties of the dots, which are reflected in the PLE spectra. They were measured by registering the entire emission spectrum while scanning the excitation energy. Since no changes in the positions of PL peaks nor in their shapes were observed for QD families in question, each PLE trace presented in Fig. 2(a) is a plot of the PL peak intensity at a fixed detection energy versus the excitation energy. A strong absorption edge at about 1.07 eV is present for all traces, which corresponds to the fundamental band gap of the WL. Moreover, since all traces are very similar, the WL beneath different QD families apparently has a similar thickness and chemical composition. Theoretical calculations of the InAs/InP WL fundamental gap as a function of the WL thickness (d_{WL}) and its further comparison to the measured absorption edge lead to $d_{\mathrm{WL}} \approx 3$ ML. This value agrees with the WL thickness obtained from the cross-sectional TEM presented in Fig. (1 b).

The quantitative agreement between positions of PL peaks and calculated exciton energies, visible in Fig. 2(a), has been achieved in the following way. As described in Sec. III, we have modeled a series of QDs with heights of consecutive integer numbers of InAs MLs and with varying in-plane size. This resulted in a smooth dependence of exciton ground-state energy on both varied QD dimensions. The latter could thus be interpolated via fitting of expected analytical dependence

$$E(H, L) \simeq \sum_{ij} a_{ij} H^{-i} L^{-j}, \tag{1}$$

where a_{ij} are the fit coefficients, whose nonnegative integer indices i and j do not exceed $i + j = 2$. Next, we look for a smooth $L = f(H)$ dependence. From the surface-QD structural data we draw an assumption that it may be linear [see Fig. 1(d)], thus we plug $L = AH + B$ into Eq. (1), and fit the resultant one-variable function of H to the dependence of PL-peak positions on the assumed $(N + 3)$ ML height of corresponding QDs (a QD protrudes by N MLs over the top of 3-ML-high WL). As a result, we obtain $L[\mathrm{nm}] = (3.2 \pm 0.5)N + (28 \pm 2)$, for which the final calculated energies are shown in Fig. 2(a), in a more than satisfactory agreement with positions of all peaks. The final series of sizes for modeled QDs established here is then used for calculation of other quantities presented in the following sections.

B. Temperature-driven effects

Here, we move to the temperature-driven processes in the system. In Fig. 4(a), we present the measured temperature-dependent PL spectra, where a strong redshift of emission is present, initially marked in Fig. 2(b). Moreover, an overall intensity drop of emitted light is observed. We attribute this PL quenching to redistribution of carriers between QDs, during which part of them escapes from the low-dimensional traps completely. Such processes may result from differences in confinement potential depth for distinct QD families. We explain the data similarly as in Ref. [41], with an assumption of transfer taking place via 2D wetting layer states. This transfer should involve thermal activation of carriers from QDs to the WL, their migration via WL states followed by their re-trapping with the highest probability by larger QDs with deeper confining potential, where the carriers finally

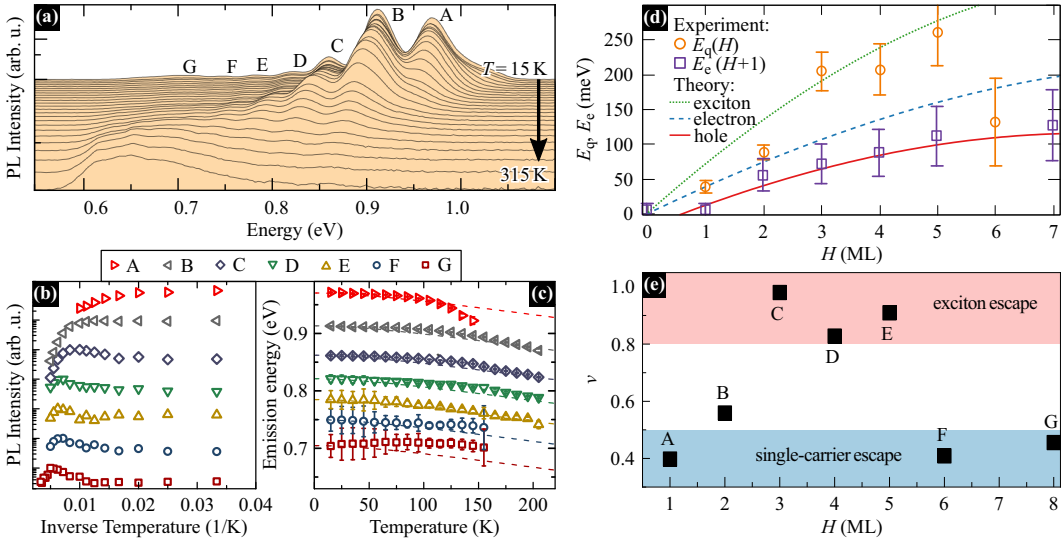

FIG. 4. Temperature dependence of PL emission from QDs. (a) Stacked PL spectra plotted in the Arrhenius form. (b) Temperature dependence of PL intensity for maxima A–G. (c) Thermal shift of emission energies (points) with Varshni lines: Eq. (2) (dashed lines). (d) Fitted activation energies for PL quench E_q (circles) and PL enhancement E_e (squares; shifted horizontally by one ML), and calculated energies for excitation to the WL ground state for excitons (dotted line), electrons (dashed), and holes (solid) in their ground states in a QD, versus QD height. (e) Analysis of phenomenological parameter ν.

recombine. The activation-capture processes can be repeated many times before the radiative recombination. As a result, the temperature-dependent subtle interplay between activation and capture probabilities for each QD family is crucial for the relative PL intensities of peaks.

Note that other scenarios, such as the lateral tunneling of carriers or excitons can be excluded. In our sample, the average dot-to-dot variation is about 300 nm, much larger than ∼10 nm required for this kind of lateral transport [42]. For the same reason, we exclude long-range dipole-dipole coupling [43,44]. Moreover, due to energy differences between QD ground states and the InP matrix, the lateral hopping of carriers seems improbable. Finally, we can exclude any significant impact of radiative recombination of excitons during the redistribution processes, as the characteristic times for carrier release from localized states and capture processes are both in the range of ≈20 ps [41], i.e., two orders of magnitude faster than radiative recombination times observed by us for all QDs families (Fig. 5). Therefore excitons recombine mostly trapped in one of the QD families.

Such interpretation is supported by temperature dependence of intensities of each of the peaks plotted in the Arrhenius form in Fig. 4(b). Here, the initial enhancement of PL intensity from the lower-energy PL bands (C–F) is observed up to intermediate temperature range. These QD families correspond to deeper confinement for carriers. On the other hand, the highest-energy peaks exhibit only (band A) or mostly (B) a single process of PL quenching. This combination of observations illustrates how carriers are, on average, moved from lower to higher QDs. We note that the significant enhancement of PL intensities for QD families emitting in the third telecom window (families D–F) at above-cryogenic temperatures (>77 K) is particularly advantageous from the point of view of possible applications as sources of single photons operating at elevated temperatures.

In Fig. 4(c), we show how the PL intensity enhancement and quenching are accompanied by partly suppressed thermal redshift of the low-energy peaks C–G, and by enhanced one for the highest-energy band A. Nominally, for emission from a bulk material, a thermal redshift following the trend approximated by the Varshni relation is expected [45],

$$E_g(T) = E_g(0) - \frac{\alpha T^2}{T + \beta}, \tag{2}$$

where E_g is the band-gap energy and parameters for InAs are $\alpha = 2.76 \times 10^{-4}$eV/K, $\beta = 93$ K. Corresponding curves are plotted with dashed lines. However, the Varshni formula takes into account only the thermal change of the semiconductor band gap. The minor blueshift from these predictions observed here is most probably related to the state filling effect: at higher temperature carriers are redistributed within each of the QD-family ensembles so that higher energy-emitting QDs get occupied, i. e., those smaller in-plane and thus characterized by weaker confinement. Therefore, the high-energy tails of QDs distributions become comparatively more optically active as the temperature increases.

For QDs with the shallowest confining potential (band A), emission energy initially follows the Varshni

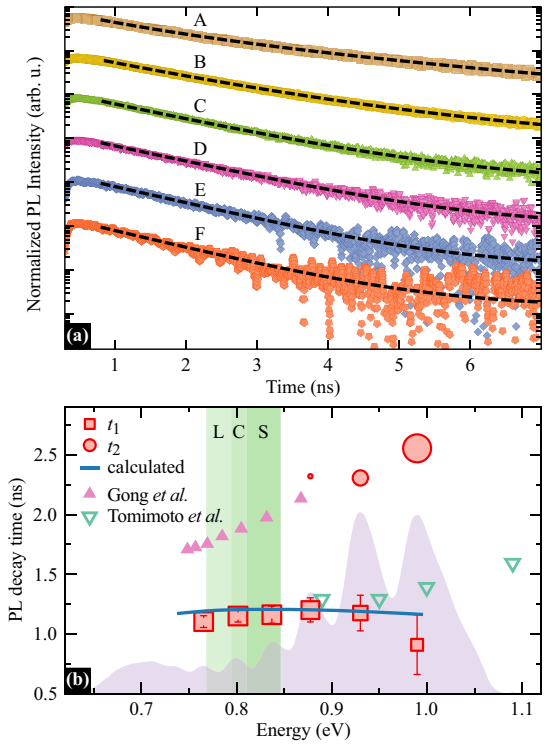

FIG. 5. (a) Time-resolved photoluminescence traces for all PL maxima (points) along with reconstructed curves (lines). (b) Experimentally obtained PL decay times (open symbols; values correspond to means of fitted lifetime distributions; point size marks the component amplitude) compared with calculated radiative exciton lifetimes (line) for QDs families. Triangles mark values obtained theoretically [51] (▲) and experimentally [52] (▽) for other InAs/InP QDs.

relation, but around 120 K it considerably deviates due to fast depletion of high-energy QDs associated with strong PL quenching. For families B–E, the emission energy follows Eq. (2) within the entire temperature range. The different behavior for maximum G exhibiting almost no energy shift may indicate that structures forming this peak do not form QD family analogous to QDs A–F, whose well-defined central emission energies shift spectrally. This interpretation is supported by very broad emission from this maximum (see Fig. 2). Instead, the maximum G may be attributed to large material islands where the size, and hence emission energy, change quasi-continuously. Additionally, we may expect there a high density of structural defects due to the onset of strain relaxation, resulting in dislocations [46].

To verify these initial qualitative speculations, PL intensity data for peaks A and B was fitted with a formula taking into account one activation process of energy E_q and relative rate B_q [47]:

$$I(T) = \frac{I_0}{1 + B_q \exp\left(-\frac{E_q}{k_B T}\right)}, \tag{3}$$

where I_0 is the PL intensity for $T \to 0$.

For emitters from families C–G, this analysis has to be extended to account for temperature-driven supply of carriers. Their recapturing and resulting PL enhancement is described by a characteristic energy E_e corresponding to release of carriers from their reservoir, and act as another source of occupation (apart from optical excitation) for the given bright state. Thus, we modify Eq. (3) in a straightforward manner by adding a state to the set of source kinetic equations from Ref. [47], on the same footage as the given emitting state has been introduced, but with different activation energy to the common higher state (here WL). With this a lengthy but simple to use formula accounting for exchange of carriers through the WL is obtained,

$$I(T) = \frac{U P\left[R + U \exp\left(-\frac{E_2}{k_B T}\right)\right]}{R U (U + R_2)\left[\exp\left(-\frac{E_1}{k_B T}\right) + \exp\left(-\frac{E_2}{k_B T}\right)\right] + U^2 R_2 \exp\left(-\frac{E_1+E_2}{k_B T}\right) + R^2(2U + R_2)}, \tag{4}$$

where P is the pumping rate, U is a common relaxation rate from the WL to both radiative states considered, R and R_2 are the radiative and nonradiative loss rates also assumed equal for both states, while E_1 and E_2 are their energy differences from the WL ground state. Note that arbitrary changes made via educated guess in Eq. (3) that may be found in literature may lead to spurious values of extracted activation energies, if the form of modification does not comply with the nature of reservoir and its coupling to the given state. Activation energies for PL quenching and enhancement extracted in the aforementioned way are presented in Fig. 4(d) (points) versus the height given in the number of monolayers assigned to each of the peaks. Additionally, we plot the theoretically calculated energies needed for excitation of the electron, the hole, and the whole exciton (all in their ground states, trapped in a QD) to the WL ground state, taking the Coulomb coupling energies into account (lines). The results are obtained for the set of modeled QDs described above that led to agreement of exciton energies with maxima of PL bands. Comparing values of E_q to theoretical lines, we notice that also in this aspect peaks A and B behave differently than the few next ones. For these two, the activation energy related to quenching fits well to the value needed for escape of the electron from QD ground state. Then, for peaks C–E, we rather deal with an escape of whole excitons to the WL ground state. Another change of behavior is present for the lowest-energy peaks, where a value between electron and hole escape is found, which possibly means that both these processes take place

with similar probability. To understand the source of carriers that feed the thermally enhanced emission in the moderate temperature regime, we plot the values of E_e extracted via fitting, but we shift them by one ML with respect to the value for which they were observed. This helps us to notice that possibly the most effective redistribution takes place between QDs with 1 ML difference in height, i. e., that N-ML-high QDs are fed mostly by carriers that escape from QDs that are $(N-1)$-ML-high. Additionally, according to theoretical curves, this process is dominated by holes, which means that, while both carriers escape QDs, it is more probable for holes to be recaptured by another QD. This is intuitively in line with their higher effective mass and lower mobility. Thus, the assumption about migration of carriers between QDs from different families through the WL proves to be reasonable.

The dominant PL quenching mechanisms assessed via fitting are also in agreement with those determined by calculation of the phenomenological parameter

$$\nu_i = \frac{E_q^{(i)}}{\Delta E_i}, \tag{5}$$

where i labels QD families, and ΔE_i stands for the difference between transition energies in the QDs and in the WL, E_{WL}. From PLE experiments we take $E_{WL} = 1.07$ eV and obtain values presented in Fig. 4(e). Generally, $\nu < 0.5$ indicates a dominant role of a single-carrier escape and in this case E_q corresponds to the lower of single-particle confinement energies (of either electron or hole) [48]. For $\nu = 0.5$, we expect correlated escape of electron-hole pairs [49] and, finally, for $\nu \approx 1$ escape of excitons takes place [50].

C. Photoluminescence dynamics

The emission from all maxima has been investigated in the time domain by means of TRPL. Then, recorded PL decays were analyzed employing the PTI FELIXGX software by Photon Technology International that utilizes the maximal entropy method (MEM) [53,54], which among many applications has proved effective in multiexponential luminescence decay reconstruction [55,56]. It allows one to extract photoluminescence lifetimes without initial knowledge on the number of underlying processes, and thus decay components. Additionally, it does not introduce artificial features into the distribution of lifetimes, which are not supported by the data, if a reliable model of experimental noise is used. The analysis yielded the most probable distributions of PL decay constants τ_i, which through the formula

$$I(t) = I(0) \times \sum_{i=1}^{N} A_i \exp\left(-\frac{t}{\tau_i}\right) \tag{6}$$

reconstruct the experimental curves with the level of uncertainty given by the amplitude of experimental noise. Here, N is the number of components in the quasi-continuous distribution of lifetimes describing the decay, and A_i are the corresponding amplitudes. The results of this analysis are presented in Fig. 5(a), where the TRPL traces collected for A–F luminescence peaks in the low excitation-power regime are shown along with the reconstructed curves. Via MEM reconstruction one obtains a distribution of times of nonzero width, which, if not really present in the system, represents the incomplete information carried by a noisy data. However, given a set of well-resolved peaks of amplitudes A_i, it is valid to treat their means as single representative values. Lifetimes presented with open squares and circles in Fig. 5(b) result from such an analysis. For the highest-energy peaks, we deal with two-exponential decays, where the shorter lifetime corresponds to recombination of excitons confined in a well-formed QD, while the longer one most probably comes from electron-hole pairs weakly bound on small WL width fluctuations. Amplitudes of each of decay components are marked with symbol size, and vanishing of the longer one with the number of MLs is present, which is reasonable, as no multiple-ML-wide fluctuations are expected.

Investigated QDs exhibit a dispersion of the t_1 PL lifetimes, which is different from what is expected and typically observed for more commonly studied InAs/GaAs QDs. In the latter, confinement characteristics for both types of carriers are comparable, with a weak tendency of hole wave function to leak into the barrier. Additionally, such QDs are typically of in-plane sizes not exceeding ~30 nm, which results in strong exciton confinement [57], characterized by a weak impact of electron-hole Coulomb interaction, energy of which is much smaller than single-particle level spacing. In this regime, the oscillator strength is simply defined by the overlap of electron and hole envelopes, which is close to 1 for a range of typical QD geometries. Thus, the observed dispersion of radiative lifetimes is caused mostly by the direct dependence of the latter on transition energy, which may be found in the dipole approximation as $\propto E^{-2}$.

Here we deal with radiative lifetimes of nearly no dispersion, which places investigated QDs in the middle between above-mentioned InAs/GaAs dots, and those grown in InP reported previously [51]. In the latter, the main source of radiative-lifetime dispersion for excitons has been found to come from the single-particle confinement characteristics, which are inversed in InP as compared to the GaAs matrix. In InP matrix, the electron is the particle that is more prone to leak into the barrier, as it experiences weaker confinement than holes, which is highly pronounced for flat QDs. The impact of electron leakage on exciton oscillator strength and lifetime in the InAs/InP QD system has been studied theoretically [51], and for completeness we plot the corresponding values with full triangles in Fig. 5(b). It was found that oscillator strength increases as electron wave function is increasingly better confined within the QD, i.e., for higher dots. For example, for a lens-shaped QD with diameter of 25 nm and height $H = 2.5$ nm only 53.5% probability of finding the electron inside the QD was reported, while for $H = 5.5$ nm this value increases to 81.2% [58]. Such decrease of lifetimes with decreasing energy was also observed experimentally [52] for InAs/InP QDs and is presented with open triangles in Fig. 5(b).

Due to very small height of QDs investigated here, especially those from families A and B, we also deal with the reduction of oscillator strength caused by the weakly localized electron wave function. Contrarily, the hole is strongly localized within the dot, which reduces the overlap of their envelopes. Within the strong confinement limit this would lead to a direct reduction of coupling to light. With increasing

QD height, the electron wave function tends to be more localized in the dot and its overlap with the hole becomes more complete, which reduces the observed PL lifetime. While this factor is common for all InAs/InP QDs, in the case of those studied here, it does not lead to expected inverted PL lifetime trend. Instead of this, a plateau is found, which means that another mechanism has to play a significant role.

We find it by investigating the details of exciton eigenstates comprised of Coulomb-correlated electron-hole configurations. Typically, any admixtures of higher bright single-particle configurations into the exciton ground state result in the increase of oscillator strength. This purely quantum effect can be intuitively understood as the ability of the exciton to recombine simultaneously via each of the superposed electron-hole pair states. For large QDs, in which level spacing for electrons and/or holes is low enough to be comparable with ∼20 meV energy of their Coulomb interaction, this is the main source of lifetime reduction. While the dots considered here are flat, they are also relatively large in-plane. Additionally, which may seem counterintuitive, we find that reduced height results in stronger electron-hole Coulomb correlations, and as a result in larger admixtures of higher-energy configurations to the exciton ground state. For a fixed in-plane size of $L =$ 45 nm, the admixture of higher electron-hole configurations is reduced from 16% to 5.5% when the height changes from 1 to 7 MLs. This may be understood, as the stronger the confinement along the growth axis, the more carrier wave functions are forced to penetrate the whole available in-plane area of the QD, which effectively increases the volume available for the exciton. This effect, pushing the dispersion of lifetimes in discussed QDs back towards the one known from InAs/GaAs dots underlies the observed approximately flat plot of lifetimes versus emission energy.

D. Emission from single QDs

To deepen the understanding of the system in question, and to check the applicability of QDs toward the single-photon emission from spatially well-resolved emitters, we have performed optical experiments on spatially and spectrally isolated QDs. For better spatial separation of single emitters, the sample was processed with electron-beam lithography and etched, leaving the array of mesa structures containing QDs. This enabled identification of exciton complexes and determination of their properties. An example of a single mesa is shown in the inset to Fig. 6.

We begin with presenting in Fig. 6 the results of μPL experiments performed on various mesas, which show intensive, well background-isolated emission lines. We attribute them to recombination of neutral exciton (X) and biexciton (XX) complexes as well as to charged excitons (CX), each coming from a single QD. Spectral positions of lines are compared with the PL spectrum from the ensemble of dots, showing that they belong to the D, E, and F families of QDs emitting in the L, C, and S telecom bands, respectively. We note that lines within L band are at the edge of efficiency for InGaAs-based multichannel array detector utilized here (∼1.6–1.65 μm), so single lines may also be present beyond this cut-off wavelength. Further identification of the emission lines shows that most of the dots emit due to recombination

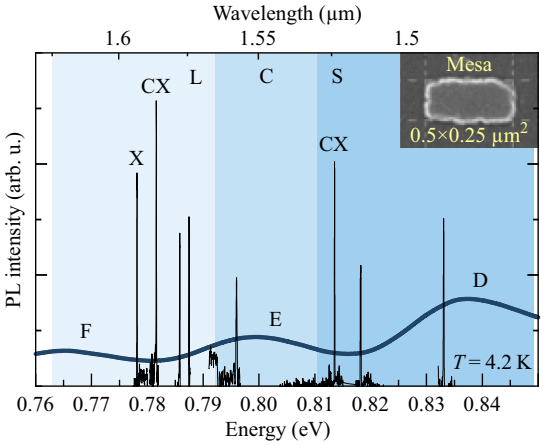

FIG. 6. Part of the μPL spectrum from a mesa with QDs showing single emission lines observed at the third telecom window.

of charged exciton complexes (trions), and only a few of them show characteristics of the X and XX recombination. In this section, we present examples of μPL investigations for both neutral and charged complexes.

A pair of lines identified as the XX-X recombination cascade is analyzed in Fig. 7. First, μPL spectra taken under various excitation powers are shown in Fig. 7(a). From spectral positions of lines we determine the biexciton binding energy

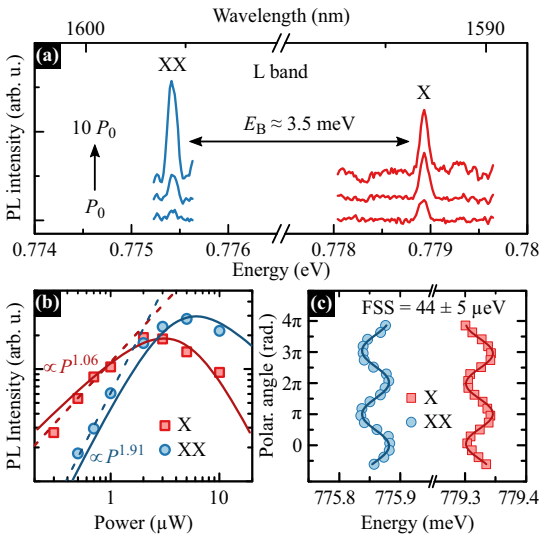

FIG. 7. Exciton (X) and biexciton (XX) emission at L band. Measured biexciton binding energy is ∼3.5 meV. $P_0 = 0.5$ μW (b) Power dependence of the μPL line intensities fitted with three-level rate-equation model showing a correlation between X and XX lines. (c) Polarization-resolved μPL revealing exciton fine structure splitting of $E_{FSS} = 44 \pm 5$ μeV.

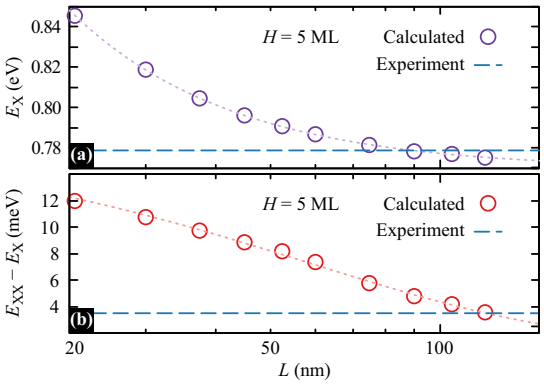

FIG. 8. (a) Dependence of calculated exciton energy on QD in-plane size L (circles) and the value of X line energy from experiment (dashed line). (b) Dependence of calculated biexciton binding energy on QD length (circles) and experimental value (dashed line). Dotted lines are to guide the eye.

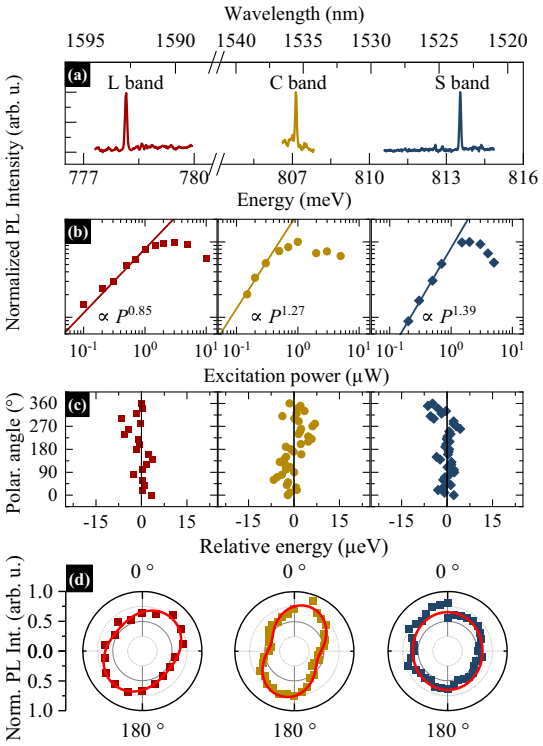

FIG. 9. Emission from charged excitons (CX) in the third telecom window. (a) μPL spectra. (b) μPL power dependence (points) with fitted power laws (lines). (c) Polarization-resolved μPL emission energy showing no fine structure splitting. (d) Anisotropy of polarization-resolved μPL intensity evidencing mixing of light-hole and heavy-hole states (lines are fits to the data).

of $E_{XX} - E_X \simeq 3.5$ meV. The XX-X cascade was identified based on the power-dependent μPL, shown in Fig. 7(b), and polarization-resolved μPL presented in Fig. 7(c). Both the three-level rate-equation model [59] [solid lines in Fig. 7(b)] and anti-phase of energy oscillations in Fig. 7(c) confirm correlation between observed lines. Additionally, in the low-power regime, the power dependence of X (I_X) and XX (I_{XX}) line intensities is well described with power laws: $I_X \propto P^{1.06}$ and $I_{XX} \propto P^{1.91}$, where P is the excitation power. This is in a good agreement with expected approximately linear power dependence for X and quadratic for XX. In the polarization-angle domain sinusoidal fits to the traces of emission energy yield the exciton fine structure splitting of $E_{FSS} = 44 \pm 5$ μeV.

The X-line energy places the emitting QD in the low-energy tail of the E family of QDs. Thus, properties different from those observed for the central part of the peak with the most typical QDs are expected. In particular, for a QD from this family to emit at such a long wavelength, the in-plane size has to be much larger than the average. To verify this, we use the results of a series of calculations for QDs with in-plane size varying up to $L = 120$ nm. The resulting trend is plotted in Fig. 8(a) along with the measured energy of the X line (dashed line). As anticipated, the line is likely to come from a QD with large in-plane size close to 100 nm. Next, we calculate also the biexciton biding energy in the same range of QD sizes, and plot the results in Fig. 8(b). Here, for $L = 100$ nm, a binding energy of ∼4 meV is found, which is close to the experimentally determined value. Thus, we conclude that the pair of lines is very likely to come from an atypically in-plane large QD.

Finally, in Fig. 9, we focus on charged complexes, optical signatures of which are found also within L, C, and S bands. Trions were identified based on close-to-linear power dependence of their intensity presented in Fig. 9(b), and the lack of any systematic variation in emission energy versus the angle of linear polarization of emission, as expected for spin singlet states [Fig. 9(c)]. Additionally, observed CX lines exhibit no phase correlation in polarization-resolved μPL to other nearby-lying lines within the biexciton binding energy range [such correlation is expected for neutral complexes, cf. Fig. 8(c)]. This spectral isolation strengthens their assignment as charged complexes.

In Fig. 9(d), we present the polarization-resolved μPL intensity plots for trions. The anisotropy is observed for all three CX lines as expected in asymmetric [60] and strained QDs [61] due to the mixing of light-hole and heavy-hole (LH-HH) subbands in these structures.

We estimate the degree of LH-HH mixing by fitting the function $I(\phi) = A(1 + \rho_L \cos[2(\phi - \theta)])$ [61] to the data in Fig. 9(d), where $I(\phi)$ is the PL intensity as a function of polarization angle, A is a scaling factor, ρ_L quantifies the degree of linear polarization, and θ is the offset from 0°, a value intrinsic for a given QD [61] and not necessarily corresponding to the elongation axis [60]. For investigated lines, we obtain values of $\rho_{L,L} = 0.154 \pm 0.020$, $\rho_{L,C} = 0.312 \pm 0.024$, and $\rho_{L,S} = 0.054 \pm 0.029$, for L-, C-, and S-band lines, respectively. The degree of linear polarization ρ_L can be traced back to

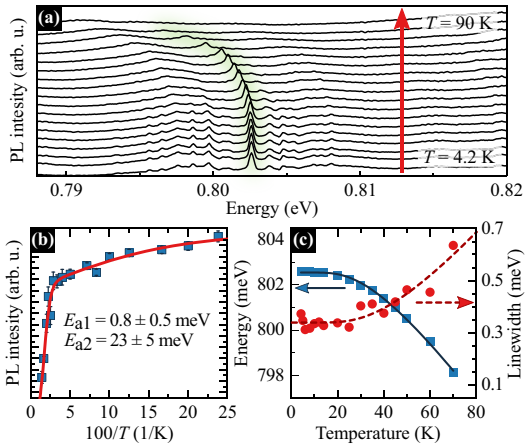

FIG. 10. Temperature dependence of emission for charged exciton from a 5-ML-high QD. (a) Stacked μPL spectra. (b) Temperature dependence of the μPL intensity (points) with a fit (line). (c) Energy shift (squares) and linewidth broadening (circles) with fits (lines).

the degree of LH-HH mixing. Here, different values of ρ_L evidence large dot-to-dot variation in this aspect.

For a CX line emitting in the C band we performed further μPL temperature-dependent studies reported in Fig. 10. The decreasing with temperature μPL signal was visible up to $T = 70$ K. The Arrhenius plot in Fig. 10(b) reveals two thermally activated processes. From fitting the data with Eq. (3) with two activation energies, we obtain values of $E_{a1} = 1.0 \pm 0.5$ meV and $E_{a2} = 23 \pm 5$ meV. To interpret this result, it is vital to underline the difference in possible sources of PL quenching for the ensemble and single emitters. In the former case, the main source is related to thermal escape of carriers from the localization centers, such as QDs. Other thermal effects, like excitation of complexes to their higher orbital levels do not impact the integrated intensity from a PL band, as those excited states also emit there. On the other hand, if a single line is studied, excitation of a carrier complex to its higher state results in the emission occurring at a different wavelength that is not accounted for during the analysis of the emission intensity. As a result, quenching of a single μPL line reveals the relative energy of the first considerably bright excited state. The line investigated in Fig. 10 lies in the high-energy tail of the ensemble, thus most probably comes from a QD with a relatively small in-plane size. Calculation for a QD with $H = 5$ ML and $L = 28$ nm yielded the lowest-energy bright excited CX states at $\Delta E = 18.5$ and 18.7 meV with radiative lifetimes of 2.7 and 2.1 ns, respectively. Thus the energy E_{a2} from experimental data may be attributed to the transfer of emission to a higher orbital state.

The thermal redshift of CX emission is presented with squares in Fig. 10(c) and fitted with formula accounting for phonon-mode occupation [62]. Increase of the latter enhances exciton-phonon interaction, influencing the chemical bonds and their energy and as a result it is the main factor leading to the band-gap renormalization [63,64]. Extracted average phonon energy is $E_{ph,E} = 9.24 \pm 0.39$ meV. We note that in contrast to Fig. 4(c), where we compared the thermal energy shifts of ensemble emission with Varshni curves, on the level of single emitters we can observe footprints of exciton-phonon interaction, therefore we use here more appropriate formula to explain the observed behavior.

The linewidth broadening $\Gamma(T)$ is presented in Fig. 10(c). The rather large initial value of $\Gamma(4.2\ \mathrm{K}) = 340$ μeV points at the crucial impact of defects or deep charge traps in the vicinity of a QD affecting significantly the emission properties. The broadening raises to 630 μeV at $T = 70$ K. The temperature dependence of linewidth was fitted with the formula that includes the contribution of thermally activated phonon sidebands to the zero-phonon line [65,66],

$$\Gamma(T) = \Gamma(4.2\ \mathrm{K}) + a\left[\exp\left(\frac{E_{ph,\Gamma}}{k_B T}\right) - 1\right]^{-1}, \qquad (7)$$

where k_B is the Boltzmann constant, $a = 1.5 \pm 1.1$ meV, and $E_{ph,\Gamma} = 11.5 \pm 3.4$ meV is the average phonon energy. We note that average energies of phonons obtained from energy shift $E_{ph,E} = 9.24 \pm 0.39$ meV and linewidth broadening $E_{ph,\Gamma} = 11.5 \pm 3.4$ meV agree well with one another and with previously reported value for InAs/InP stacked QDs [67].

V. SUMMARY

In conclusion, we have obtained InAs/InP QDs with low surface density grown by MOVPE and have studied their morphological and optical properties in detail, both experimentally and theoretically. The QDs are found to have families of different heights, from one to a few MLs of material above the WL, which is reflected in their emission with well-resolved multiple peaks covering a broad spectral range including the third window of silica-based optical fibers. In time-resolved spectroscopy, we observe dispersion of radiative lifetimes different from previously observed in InAs/InP QDs. While these typically show lifetimes increasing with emission energy in contrast to the opposite trend found in InAs/GaAs QDs, the dots under investigation show nearly no dispersion, which places them in between with respect to the electron-hole confinement parameters. With the aid of theoretical modeling, comprised of multiband $\boldsymbol{k}\cdot\boldsymbol{p}$ calculations of single-particle states and configuration-interaction method for neutral and charged excitons, we explain the observed dispersionless lifetimes as originating from the interplay of weak electron confinement (typical for InAs/InP) and strongly height-dependent exciton confinement regime. The latter is shown in the amount of higher single-particle eigenstates admixed to the exciton ground state, changing from 5.5% for 7 ML to 16% for 1 ML. Thus, the flatter the dot the weaker the exciton confinement regime, which may be understood in geometric terms as a result of higher effective in-plane size of a QD that is penetrated by carrier wave functions. At higher temperatures a redistribution of carriers among families of QDs takes place, in which we observe escape of both single particles and whole excitons resulting in PL quenching, as well as recapturing of holes by higher QDs leading to emission enhancement at moderate temperatures. Owing to the low surface density of QDs, we have observed XX-X cascade and charged-exciton emission from single emitters persisting up to $T = 70$ K. With theoretical

modeling, we have reproduced experimental findings such as emission energies, radiative lifetimes, thermal activation energies for PL quenching and enhancement, and biexciton binding energy, which allowed for a comprehensive and detailed study of the system.

ACKNOWLEDGMENTS

We acknowledge support from the Villum Fonden via the NATEC Centre (8692), and YIP QUEENs project (VKR023442). P.H. acknowledges financial support from the Polish budgetary funds for science in 2018-2020 via the "Diamond Grant" program (Ministry for Science and Higher Education, Grant No. DI 2017 011747). Numerical calculations have been carried out using resources provided by Wroclaw Centre for Networking and Supercomputing (http://wcss.pl), Grant No. 203. We would like to thank Christian Schneider for mesa fabrication as part of the collaboration between Wrocław University of Science and Technology and the University of Würzburg within the International Academic Partnership project funded by the Polish National Agency for Academic Exchange, which also supported this work. We thank Krzysztof Gawarecki for sharing his implementation of the $\boldsymbol{k}\cdot\boldsymbol{p}$ method, as well as Janusz Andrzejewski and Grzegorz Sęk for helpful discussions.

P.H. and M.G. contributed equally to this work.

[1] I. Aharonovich, D. Englund, and M. Toth, Solid-state single-photon emitters, Nat. Photonics **10**, 631 (2016).

[2] P. Senellart, G. Solomon, and A. White, High-performance semiconductor quantum-dot single-photon sources, Nat. Nanotechnol. **12**, 1026 (2017).

[3] L. Scarpelli, B. Lang, F. Masia, D. M. Beggs, E. A. Muljarov, A. B. Young, R. Oulton, M. Kamp, S. Höfling, C. Schneider, and W. Langbein, 99% beta factor and directional coupling of quantum dots to fast light in photonic crystal waveguides determined by spectral imaging, Phys. Rev. B **100**, 035311 (2019).

[4] E. S. Semenova, R. Hostein, G. Patriarche, O. Mauguin, L. Largeau, I. Robert-Philip, A. Beveratos, and A. Lemaître, Metamorphic approach to single quantum dot emission at 1.55 μm on GaAs substrate, J. Appl. Phys. **103**, 103533 (2008).

[5] F. Olbrich, J. Höschele, M. Müller, J. Kettler, S. L. Portalupi, M. Paul, M. Jetter, and P. Michler, Polarization-entangled photons from an InGaAs-based quantum dot emitting in the telecom C-band, Appl. Phys. Lett. **111**, 133106 (2017).

[6] L. Seravalli, G. Trevisi, P. Frigeri, D. Rivas, G. Muñoz-Matutano, I. Suárez, B. Alén, J. Canet-Ferrer, and J. P. Martínez-Pastor, Single quantum dot emission at telecom wavelengths from metamorphic InAs/InGaAs nanostructures grown on GaAs substrates, Appl. Phys. Lett. **98**, 173112 (2011).

[7] R. Kubota, T. Saiki, P. Regreny, A. Benamrouche, and M. Gendry, Low-density InAs quantum dots grown on InP(001) using solid-source molecular beam epitaxy with a post-growth annealing process, Jpn. J. Appl. Phys. **49**, 041201 (2010).

[8] M. Benyoucef, M. Yacob, J. P. Reithmaier, J. Kettler, and P. Michler, Telecom-wavelength (1.5μm) single-photon emission from InP-based quantum dots, Appl. Phys. Lett. **103**, 162101 (2013).

[9] M. Yacob, J. P. Reithmaier, and M. Benyoucef, Low-density InP-based quantum dots emitting around the 1.5μm telecom wavelength range, Appl. Phys. Lett. **104**, 022113 (2014).

[10] K. Takemoto, Y. Sakuma, S. Hirose, T. Usuki, and N. Yokoyama, Observation of exciton transition in 1.3-1.55 μm band from single InAs/InP quantum dots in mesa structure, Jpn. J. Appl. Phys **43**, L349 (2004).

[11] R. P. Leavitt and C. J. K. Richardson, Pathway to achieving circular InAs quantum dots directly on (100) InP and to tuning their emission wavelengths toward 1.55 μm, J. Vac. Sci. Technol. B **33**, 051202 (2015).

[12] A. Musiał, P. Holewa, P. Wyborski, M. Syperek, A. Kors, J. P. Reithmaier, G. Sęk, and M. Benyoucef, High-purity triggered single-photon emission from symmetric single InAs/InP quantum dots around the telecom c-band window, Adv. Quantum Technol. **3**, 1900082 (2019).

[13] T. Miyazawa, K. Takemoto, Y. Nambu, S. Miki, T. Yamashita, H. Terai, M. Fujiwara, M. Sasaki, Y. Sakuma, M. Takatsu, T. Yamamoto, and Y. Arakawa, Single-photon emission at 1.5μm from an InAs/InP quantum dot with highly suppressed multi-photon emission probabilities, Appl. Phys. Lett. **109**, 132106 (2016).

[14] A. Musiał, P. Kaczmarkiewicz, G. Sęk, P. Podemski, P. Machnikowski, J. Misiewicz, S. Hein, S. Höfling, and A. Forchel, Carrier trapping and luminescence polarization in quantum dashes, Phys. Rev. B **85**, 035314 (2012).

[15] M. Gawełczyk, M. Syperek, A. Maryński, P. Mrowiński, Ł. Dusanowski, K. Gawarecki, J. Misiewicz, A. Somers, J. P. Reithmaier, S. Höfling, and G. Sęk, Exciton lifetime and emission polarization dispersion in strongly in-plane asymmetric nanostructures, Phys. Rev. B **96**, 245425 (2017).

[16] M. Gawełczyk, P. Wyborski, P. Podemski, J. P. Reithmaier, S. Höfling, and G. Sęk, Excited states of neutral and charged excitons in single strongly asymmetric InP-based nanostructures emitting in the telecom C band, Phys. Rev. B **100**, 241304(R) (2019).

[17] M. Gawełczyk, Excitons in asymmetric nanostructures: Confinement regime, Acta Phys. Pol. A **134**, 930 (2018).

[18] Ł. Dusanowski, P. Mrowiński, M. Syperek, J. Misiewicz, A. Somers, S. Höfling, J. P. Reithmaier, and G. Sęk, Confinement regime in self-assembled InAs/InAlGaAs/InP quantum dashes determined from exciton and biexciton recombination kinetics, Appl. Phys. Lett. **111**, 253106 (2017).

[19] A. Sauerwald, T. Kümmell, G. Bacher, A. Somers, R. Schwertberger, J. P. Reithmaier, and A. Forchel, Size control of InAs quantum dashes, Appl. Phys. Lett. **86**, 253112 (2005).

[20] K. Karrai and R. J. Warburton, Optical transmission and reflection spectroscopy of single quantum dots, Superlattices Microstruct. **33**, 311 (2003).

[21] See Supplemental Material at http://link.aps.org/supplemental/10.1103/PhysRevB.101.195304 for the high-resolution STEM image with surface and buried QDs and for the map of fractional lattice-spacing changes, including Ref. [22].

[22] M. Hÿtch, E. Snoeck, and R. Kilaas, Quantitative measurement of displacement and strain fields from HREM micrographs, Ultramicroscopy **74**, 131 (1998).
[23] S. Kadkhodazadeh, High resolution STEM of quantum dots and quantum wires, Micron **44**, 75 (2013).
[24] S. Birner, T. Zibold, T. Andlauer, T. Kubis, M. Sabathil, A. Trellakis, and P. Vogl, nextnano: General purpose 3-D simulations, IEEE Trans. Electron Devices **54**, 2137 (2007).
[25] I. Vurgaftman, J. R. Meyer, and L. R. Ram-Mohan, Band parameters for III–V compound semiconductors and their alloys, J. Appl. Phys. **89**, 5815 (2001).
[26] R. Winkler, *Spin-orbit Coupling Effects in Two-dimensional Electron and Hole Systems* (Springer-Verlag GmbH, Berlin, Heidelberg, 2003).
[27] M. A. Caro, S. Schulz, and E. P. O'Reilly, Origin of nonlinear piezoelectricity in III-V semiconductors: Internal strain and bond ionicity from hybrid-functional density functional theory, Phys. Rev. B **91**, 075203 (2015).
[28] K. Gawarecki, P. Machnikowski, and T. Kuhn, Electron states in a double quantum dot with broken axial symmetry, Phys. Rev. B **90**, 085437 (2014).
[29] M. G. Burt, The justification for applying the effective-mass approximation to microstructures, J. Phys.: Condens. Matter **4**, 6651 (1992).
[30] B. A. Foreman, Effective-mass Hamiltonian and boundary conditions for the valence bands of semiconductor microstructures, Phys. Rev. B **48**, 4964 (1993).
[31] G. L. Bir, *Symmetry and Strain-induced Effects in Semiconductors* (Wiley, New York, 1974).
[32] K. Gawarecki, Spin-orbit coupling and magnetic-field dependence of carrier states in a self-assembled quantum dot, Phys. Rev. B **97**, 235408 (2018).
[33] A. Thränhardt, C. Ell, G. Khitrova, and H. M. Gibbs, Relation between dipole moment and radiative lifetime in interface fluctuation quantum dots, Phys. Rev. B **65**, 035327 (2002).
[34] A. Gustafsson, D. Hessman, L. Samuelson, J. F. Carlin, R. Houdré, and A. Rudra, Cathodoluminescence investigations of three-dimensional island formation in quantum wells, J. Cryst. Growth **147**, 27 (1995).
[35] P. J. Poole, J. McCaffrey, R. L. Williams, J. Lefebvre, and D. Chithrani, Chemical beam epitaxy growth of self-assembled InAs/InP quantum dots, J. Vac. Sci. Technol. B **19**, 1467 (2001).
[36] H. Folliot, S. Loualiche, B. Lambert, V. Drouot, and A. LeCorre, Effects of interface-layers composition and strain distribution on the optical transitions of InAs quantum dots on InP, Phys. Rev. B **58**, 10700 (1998).
[37] Y. Berhane, M. O. Manasreh, H. Yang, and G. J. Salamo, Thermal annealing effect on the intersublevel transitions in InAs quantum dots, Appl. Phys. Lett. **78**, 2196 (2001).
[38] Y. Sakuma, M. Takeguchi, K. Takemoto, S. Hirose, T. Usuki, and N. Yokoyama, Role of thin InP cap layer and anion exchange reaction on structural and optical properties of InAs quantum dots on InP (001), J. Vac. Sci. Technol. B **23**, 1741 (2005).
[39] A. Lanacer, N. Shtinkov, P. Desjardins, R. A. Masut, and R. Leonelli, Optical emission from InAs/InP self-assembled quantum dots: evidence for As/P intermixing, Semicond. Sci. Technol. **22**, 1282 (2007).
[40] F. Guffarth, R. Heitz, A. Schliwa, O. Stier, N. N. Ledentsov, A. R. Kovsh, V. M. Ustinov, and D. Bimberg, Strain engineering of self-organized InAs quantum dots, Phys. Rev. B **64**, 085305 (2001).
[41] M. Syperek, M. Baranowski, G. Sęk, J. Misiewicz, A. Löffler, S. Höfling, S. Reitzenstein, M. Kamp, and A. Forchel, Impact of wetting-layer density of states on the carrier relaxation process in low indium content self-assembled (In,Ga)As/GaAs quantum dots, Phys. Rev. B **87**, 125305 (2013).
[42] M. Bayer, P. Hawrylak, K. Hinzer, S. Fafard, M. Korkusiński, Z. R. Wasilewski, O. Stern, and A. Forchel, Coupling and entangling of quantum states in quantum dot molecules, Science **291**, 451 (2001).
[43] T. Förster, Zwischenmolekulare energiewanderung und fluoreszenz, Ann. Phys. **437**, 55 (1948).
[44] C. R. Kagan, C. B. Murray, and M. G. Bawendi, Long-range resonance transfer of electronic excitations in close-packed CdSe quantum-dot solids, Phys. Rev. B **54**, 8633 (1996).
[45] Y. Varshni, Temperature dependence of the energy gap in semiconductors, Physica **34**, 149 (1967).
[46] K. Yamaguchi, Self-formation of semiconductor quantum dots, in *Handbook of Nano-Optics and Nanophotonics*, edited by M. Ohtsu (Springer Berlin Heidelberg, Berlin, Heidelberg, 2013), pp. 809–843.
[47] J. D. Lambkin, D. J. Dunstan, K. P. Homewood, L. K. Howard, and M. T. Emeny, Thermal quenching of the photoluminescence of InGaAs/GaAs and InGaAs/AlGaAs strained-layer quantum wells, Appl. Phys. Lett. **57**, 1986 (1990).
[48] G. Gélinas, A. Lanacer, R. Leonelli, R. A. Masut, and P. J. Poole, Carrier thermal escape in families of InAs/InP self-assembled quantum dots, Phys. Rev. B **81**, 235426 (2010).
[49] W. Yang, R. R. Lowe-Webb, H. Lee, and P. C. Sercel, Effect of carrier emission and retrapping on luminescence time decays in InAs/GaAs quantum dots, Phys. Rev. B **56**, 13314 (1997).
[50] S. Khatsevich, D. H. Rich, E.-T. Kim, and A. Madhukar, Cathodoluminescence imaging and spectroscopy of excited states in InAs self-assembled quantum dots, J. Appl. Phys. **97**, 123520 (2005).
[51] M. Gong, W. Zhang, G. C. Guo, and L. He, Atomistic pseudopotential theory of optical properties of exciton complexes in InAs/InP quantum dots, Appl. Phys. Lett. **99**, 231106 (2011).
[52] S. Tomimoto, A. Kurokawa, Y. Sakuma, T. Usuki, and Y. Masumoto, Radiative recombination of excitons in disk-shaped InAs/InP quantum dots, Phys. Rev. B **76**, 205317 (2007).
[53] E. T. Jaynes, Information theory and statistical mechanics, Phys. Rev. **106**, 620 (1957).
[54] E. T. Jaynes, Information theory and statistical mechanics. II, Phys. Rev. **108**, 171 (1957).
[55] J. C. Brochon and A. K. Livesey, Analyzing the distribution of decay constants in pulse-fluorimetry using the maximum entropy method, Biophys. J. **52**, 693 (1987).
[56] A. T. N. Kumar, L. Zhu, J. F. Christian, A. A. Demidov, and P. M. Champion, On the rate distribution analysis of kinetic data using the maximum entropy method: applications to myoglobin relaxation on the nanosecond and femtosecond timescales, J. Phys. Chem. B **105**, 7847 (2001).
[57] Al. L. Éfros and A. L. Éfros, Interband absorption of light in a semiconductor sphere, Fiz. Tekh. Poluprovodn. **5**, 2191 (1982) [Sov. Phys. Semicond. **16**, 772 (1982)].

[58] M. Gong, K. Duan, C.-F. Li, R. Magri, G. A. Narvaez, and L. He, Electronic structure of self-assembled InAs/InP quantum dots: Comparison with self-assembled InAs/GaAs quantum dots, Phys. Rev. B **77**, 045326 (2008).

[59] G. Sęk, A. Musiał, P. Podemski, and J. Misiewicz, On the applicability of a few level rate equation model to the determination of exciton versus biexciton kinetics in quasi-zero-dimensional structures, J. Appl. Phys. **108**, 033507 (2010).

[60] T. Belhadj, T. Amand, A. Kunold, C.-M. Simon, T. Kuroda, M. Abbarchi, T. Mano, K. Sakoda, S. Kunz, X. Marie, and B. Urbaszek, Impact of heavy hole-light hole coupling on optical selection rules in GaAs quantum dots, Appl. Phys. Lett. **97**, 051111 (2010).

[61] A. V. Koudinov, I. A. Akimov, Y. G. Kusrayev, and F. Henneberger, Optical and magnetic anisotropies of the hole states in Stranski-Krastanov quantum dots, Phys. Rev. B **70**, 241305(R) (2004).

[62] K. P. O'Donnell and X. Chen, Temperature dependence of semiconductor band gaps, Appl. Phys. Lett. **58**, 2924 (1991).

[63] P. B. Allen and V. Heine, Theory of the temperature dependence of electronic band structures, J. Phys. C: Solid State Phys. **9**, 2305 (1976).

[64] P. B. Allen and M. Cardona, Temperature dependence of the direct gap of Si and Ge, Phys. Rev. B **27**, 4760 (1983).

[65] D. Gammon, E. S. Snow, B. V. Shanabrook, D. S. Katzer, and D. Park, Homogeneous linewidths in the optical spectrum of a single gallium arsenide quantum dot, Science **273**, 87 (1996).

[66] G. Moody, M. E. Siemens, A. D. Bristow, X. Dai, D. Karaiskaj, A. S. Bracker, D. Gammon, and S. T. Cundiff, Exciton-exciton and exciton-phonon interactions in an interfacial GaAs quantum dot ensemble, Phys. Rev. B **83**, 115324 (2011).

[67] J. Ishi-Hayase, K. Akahane, N. Yamamoto, M. Kujiraoka, K. Ema, and M. Sasaki, Negligible pure dephasing in InAs self-assembled quantum dots, Jpn. J. Appl. Phys. **46**, 6352 (2007).

ARTICLE 2

Symmetric InAs/(In,Al,Ga)As/InP quantum dots

PHYSICAL REVIEW APPLIED **14,** 064054 (2020)

Optical and Electronic Properties of Symmetric InAs/(In,Al,Ga)As/InP Quantum Dots Formed by Ripening in Molecular Beam Epitaxy: A Potential System for Broad-Range Single-Photon Telecom Emitters

P. Holewa,[1,*] M. Gawełczyk,[2,1,‡] A. Maryński,[1,§] P. Wyborski,[1] J.P. Reithmaier,[3] G. Sęk,[1] M. Benyoucef,[3,†] and M. Syperek[1]

[1] *Laboratory for Optical Spectroscopy of Nanostructures, Department of Experimental Physics, Faculty of Fundamental Problems of Technology, Wrocław University of Science and Technology, Wybrzeże Wyspiańskiego 27, Wrocław 50-370, Poland*

[2] *Department of Theoretical Physics, Faculty of Fundamental Problems of Technology, Wrocław University of Science and Technology, Wybrzeże Wyspiańskiego 27, Wrocław 50-370, Poland*

[3] *Institute of Nanostructure Technologies and Analytics (INA), Center for Interdisciplinary Nanostructure Science and Technology (CINSaT), University of Kassel, Heinrich-Plett-Str. 40, Kassel 34132, Germany*

(Received 14 October 2020; accepted 17 November 2020; published 17 December 2020)

We present a detailed experimental optical study supported by theoretical modeling of InAs quantum dots (QDs) embedded in an (In,Al,Ga)As barrier lattice matched to InP(001) grown with the use of a ripening step in molecular beam epitaxy. The method leads to the growth of in-plane symmetric QDs of low surface density, characterized by a multimodal size distribution resulting in a spectrally broad emission in the range of 1.4–2.0 μm, essential for many near-infrared photonic applications. We find that, in contrast to the InAs/InP system, the multimodal distribution results here from a two-monolayer difference in QD height between consecutive families of dots. This may stem from the long-range ordering in the quaternary barrier alloy that stabilizes QD nucleation. Measuring the photoluminescence (PL) lifetime of the spectrally broad emission, we find a nearly dispersionless value of 1.3 ± 0.3 ns. Finally, we examine the temperature dependence of emission characteristics. We underline the impact of localized states in the wetting layer playing the role of carrier reservoir during thermal carrier redistribution. We determine the hole escape to the (In,Al,Ga)As barrier to be a primary PL quenching mechanism in these QDs.

DOI: 10.1103/PhysRevApplied.14.064054

I. INTRODUCTION

Self-assembled InAs quantum dots (QDs) embedded between barriers lattice matched to InP remain attractive candidates for photon emitters in the near-infrared spectral range [1,2]. It is mostly due to vast possibilities to shape their properties and photonic environment to target specific applications ranging from low-threshold lasers to nonclassical photon sources for quantum communication protocols. The latter is especially difficult to achieve, since the typical growth of InAs QDs on the InP substrate by molecular beam epitaxy (MBE) leads to the formation of strongly in-plane asymmetric objects of a significant areal density reaching 10^{10}–10^{11} cm^{-2}. Such high surface coverage prevents sufficient spatial and spectral isolation of individual QDs, while large QD sizes result in an atypically rich and dense optical spectrum unfavorable for single-dot applications [3,4]. The growth process of InAs QDs on an InP(001) substrate and control of their parameters are still challenging and comprise many technological steps and details [5].

Recently, it has been proposed [6,7] to utilize an additional growth step in MBE of InAs QDs on InP(001) that mimics the Ostwald ripening known for the formation of colloidal microcrystals. During the ripening process initially formed QDs decompose, and the material is redistributed between other dots, which typically leads to splitting of the initial QDs size distribution into distinct families. The ripening technique has already been applied to other semiconductor QD systems, such as Ge/Si [8], PbSe/PbTe [9], and InAs/GaAs [10]. In the case of InAs/(In,Al,Ga)As/InP(001) QDs, it has been shown [7] that the mean size of the dots depends on the ripening temperature. These ripening-assisted grown InAs QDs on the InP substrate are particularly promising for quantum information processing as their

*pawel.holewa@pwr.edu.pl
†m.benyoucef@physik.uni-kassel.de
‡Present address: Institute of Physics, Faculty of Physics, Astronomy and Informatics, Nicolaus Copernicus University, Toruń 87-100, Poland.
§Present address: Currently at McKinsey Knowledge Center Poland, 50-141 Wrocław, Poland.

recent development led to demonstrations of single-photon emission at approximately 1.45 μm [6] (the *S* band), coupling to optical modes of photonic crystal microcavities [11], and triggered single-photon emission with high purity [12].

Although some optical experiments on these QDs have already been presented [6,7,11–13], we elaborate here on possible further benefits that come from a single-stage ripening process by pointing at their so-far unexplored and not described application-relevant properties. We focus on: (a) broad spectral coverage of QD emission superimposed with the *S* (1460–1530 nm), *C* (1530–1565 nm), *L* (1565–1625 nm), and *U* (1625–1675 nm) transmission bands of silica fibers, which can be useful for the multiband quantum-secured transmission protocols highly sought for overcrowded long-haul optical networks; (b) the multimodal QD size distribution, simultaneously allowing for better spectral isolation and filtering of single-dot emission, as well as for assuring spatial isolation of a spectrally chosen QD for site-selective engineering of the photonic environment [14] to control the QD emission properties in a future device; (c) thermal stability of emission from QDs, which is important for applications in devices operating at elevated temperatures.

The flexibility in the choice of a quantum emitter from a single wafer in a very broad spectral range covering all the high transmission telecommunication bands can be of practical relevance for certain future applications. It especially concerns all the concepts based on wavelength division multiplexing (WDM), allowing increases in the total transmission rate through the fibers or the optical system efficiency and functionality in analogy to such schemes known from classical communication. For instance, there exist both predictions and experimental demonstrations of the so-called multiuser quantum key distribution employing WDM for quantum networks [15] and showing recently a really impressive increase in the achievable secure key rates [16] and even a practical implementation in a node–free eight-user metropolitan quantum communication network [17]. WDM is also utilized in the on-chip operation using quantum light in photonic integrated circuits [18] for linear optics quantum computation, where the telecom wavelength range is demanded to combine the III-V single-photon emitters with a silicon technological platform. Another branch is gas spectroscopy or the LIDAR-like sensing systems with single-photon emitters in the near infrared considered as prospective and competitive in imaging of gas leaks and dangerous vapors or in performing quantified remote mapping of gases to monitor air quality in agricultural and metropolitan areas [19]. Here, the broad-range selection of the quantum emitters is also profitable to allow detection of many environmentally relevant gasses, such as, e.g., CO_2, N_2O, H_2O, CH_4, having their strong absorption lines in the 1400–1650 nm range. In that context more sophisticated single-photon-based gas detection solutions employing WDM or on-chip spectrometers for, e.g., astronomical observation, spectroscopic imaging, and quantum communications, are also reported [20].

Here, we report on the optical investigations of InAs/(In,Al,Ga)As/InP QDs, which we support by theoretical modeling. We observe the multimodal distribution of QD sizes and explain the emission-energy separation of consecutive QD families by their modeling. With this, we obtain a strong indication that their heights differ by two monolayers (MLs) of InAs. This in turn suggests the presence of long-range ordering of atoms in the barrier alloy that may enhance the reliability of future photonic devices, as it reduces the crystal-lattice free energy [21–23], stabilizing the entire strained QD system.

The detailed goals of this work are to: (i) find the links between QD parameters (height, in-plane size, and chemical composition) and the resulting broad spectral range and other characteristics of emission, (ii) study the character and importance of wetting layer (WL) states, (iii) assess the impact of exciton confinement in a QD on recombination dynamics, (iv) investigate the thermal carrier redistribution processes and optical response of the dots at elevated temperatures. These objectives are achieved by using several complementary spectroscopic tools: modulated reflectivity ($\Delta R/R$), excitation-power-, polarization-, and temperature-dependent photoluminescence (PL), and time-resolved photoluminescence (TRPL), all supported by numerical modeling of exciton states in QDs and WL within the multiband envelope-function $\mathbf{k}\cdot\mathbf{p}$ theory. The collected data and conclusions drawn can trigger the work on such ripening-assisted grown QDs towards unveiling their physical and chemical properties and their use in photonic applications in the near infrared.

II. EXPERIMENTAL AND THEORETICAL METHODOLOGY

In this section we provide details about sample growth, experimental setups, and theoretical framework used to study the optical and electronic properties of the structure.

A. Sample growth

The investigated sample is grown on a (001)-oriented InP substrate using a MBE reactor equipped with two-valved solid-source arsenic and phosphorus cracker cells. The growth sequence starts from a 100-nm-thick InP buffer layer directly deposited on the substrate at 465 °C and followed by a nominally 228-nm-thick $In_{0.53}Al_{0.24}Ga_{0.23}As$ layer lattice matched to InP. A growth interruption lasting for 35 s is introduced to allow for the group-V atoms exchange on the InP/(In,Al,Ga)As interface. Subsequently, the Stranski-Krastanov (SK) growth mode is used to form an initial layer of QDs by deposition of nominally two MLs of InAs at 514 °C with a growth rate of

0.4 ML/s. Following the SK QD formation, the ripening process starts during the reduction of the substrate temperature down to 413 °C with a cooling rate of 30 K/min under As_2 pressure of 6×10^{-6} Torr [7]. After the cooling process, the dots are capped by a nominally 228-nm-thick $In_{0.53}Al_{0.24}Ga_{0.23}As$ layer. During the growth of the cap layer, the substrate temperature is kept at 413 °C for the first 20 nm. Afterwards, it is increased with a rate of 30 K/min up to 514 °C and then kept constant for the remaining layer thickness. More details about the growth procedure can be found in Refs. [6,7].

B. Experimental details

For spectroscopic experiments, the structure is held in a helium closed-cycle refrigerator to allow for the control of the sample temperature in the range of 10–300 K. In the case of PL and TRPL experiments, the sample is excited by a train of approximately 2-ps-long pulses with about a 13.2 ns pulse-to-pulse interval and about a 1.48 eV photon energy. The laser spot is focused to approximately 150 μm in diameter. Emission from the structure is collected in a standard far-field optical setup and dispersed by a 0.3-m-focal-length monochromator. Time-integrated PL spectra are measured in a wide spectral range of 1.2–2.1 μm via the lock-in technique at the reference modulation frequency of 2 kHz, using a thermoelectrically cooled InAs-based single-channel detector. The high-resolution PL is measured in the same setup. However, in this case the excitation and collection of emission are performed through a microscope objective with high numerical aperture NA = 0.65. The laser spot is defined to approximately 2 μm in diameter. A liquid-nitrogen-cooled (In, Ga)As-based linear camera detector registered the high-resolution PL spectrum in the limited spectral range up to 1.65 μm. The TRPL is measured by a time-correlated single-photon counting method. Photons are spectrally filtered by a monochromator and subsequently collected by the NbN superconducting detector. The multichannel event timer is synchronized to the pulse train to produce photon event statistics. The overall temporal resolution of the TRPL setup is approximately 80 ps.

In the $\Delta R/R$ experiment, a halogen lamp is used as a broadband probe beam source. The 630 nm line from a semiconductor diode laser is employed for photomodulation purposes. The 0.3-m-focal-length monochromator dispersed the white light reflected from the sample, the normalized changes of which are measured via the lock-in technique similarly to the PL.

C. Theoretical framework

Initial calculations of single-particle states in the WL and QDs are performed with the commercially available NEXTNANO software [24,25], which utilizes the continuum elasticity model for the strain distribution, and afterwards calculates the electron eigenstates within the eight-band $\mathbf{k}\cdot\mathbf{p}$ method including the strain-driven piezoelectric field. Relevant material parameters are taken from Ref. [26]. The calculations allowed for establishing the bounds for QD parameters (height, lateral dimension, and chemical content) leading to the multimodal energy distribution, analysis of the WL states, and separation between relevant energy states in the investigated structure as an input for discussion on the PL quenching mechanisms.

We then extend the band-structure calculations using a state-of-the-art implementation of the multiband $\mathbf{k}\cdot\mathbf{p}$ method [27,28], including spin-orbit interactions, structural strain, and piezoelectric field up to second-order terms in the strain tensor. Next, exciton states are found within the configuration-interaction approach by diagonalizing the Coulomb and phenomenological electron-hole exchange interactions in the basis of 32×32 electron-hole state configurations, where hole states are obtained by time reversal of valence electron ones. The number of single-particle states included in the calculations is determined on the basis of convergence tests. Then, oscillator strengths and radiative lifetimes for exciton states are obtained within the dipole approximation by computation of matrix elements of the momentum operator $\mathbf{P} = (m_0/\hbar)(\partial H/\partial \mathbf{k})$, where m_0 is the electron mass. The oscillator strength for the ith exciton state composed of a number of electron-hole configurations (single-particle states are labeled by α and β) is then $f_i = 2/(m_0 E_i)|\sum_{\alpha\beta} c_{\alpha\beta}\langle \psi_v^{(\alpha)}|\mathbf{P}|\psi_c^{(\beta)}\rangle|^2$. Finally, we calculate radiative lifetimes, connected with the oscillator strength f by the relation that may be approximately written as $\tau[\mathrm{ns}] = 45(\lambda[\mu\mathrm{m}])^2/nf$, where λ is the emission wavelength and n is the refractive index. The derivation can be found in Ref. [29], while the details of modeling and the parameters taken for the InAs/(In,Al,Ga)As/InP material system can be found in Ref. [30].

III. RESULTS AND DISCUSSION

In this section, we show experimental results supported by theoretical calculations and provide discussion on the properties of the investigated QD structure.

A. Modulated reflectivity and photoluminescence

The measured modulated reflectivity spectrum is plotted with a solid red line in Fig. 1 and shows two noticeable $\Delta R/R$ features settled in the ranges 1.13–1.20 eV and 0.92–0.96 eV, respectively. While the former is attributed to optical absorption involving valence and conduction bands of the (In,Al,Ga)As barrier [31], the latter is tentatively assigned to absorption in the WL. The WL-related feature appears to be constituted of at least two transitions centered at approximately 0.93 and 0.94 eV. The PL spectrum presented as a gray shaded area in Fig. 1

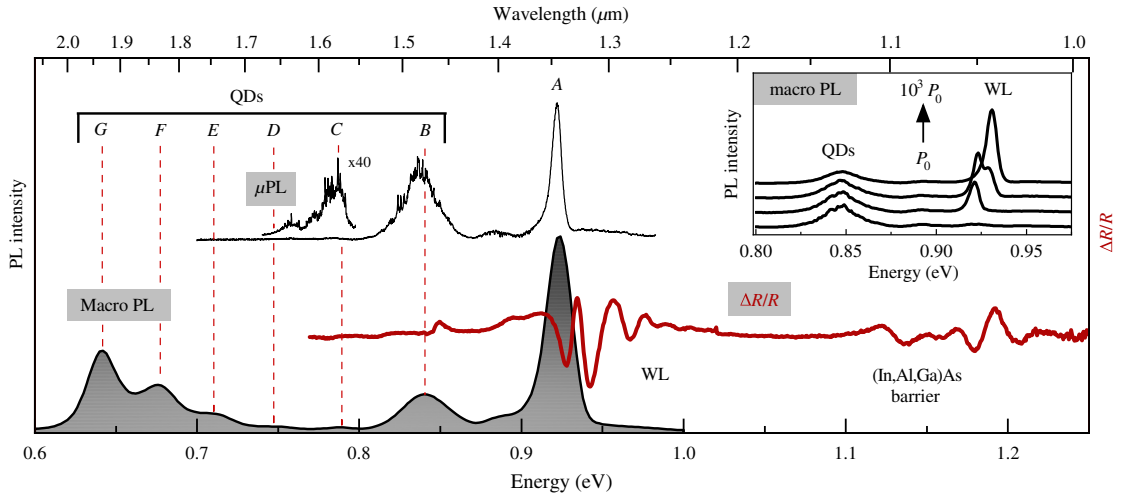

FIG. 1. Photoluminescence (macro PL, gray shaded area), high-resolution PL (μPL, solid black line), and modulated reflectivity ($\Delta R/R$, solid red line) from the structure with QDs at $T = 10$ K. QD-related PL emission bands are labeled B–G, where B denotes remnants of initially grown SK QDs and maxima C–G represent ripening-assisted grown QDs. Inset: power series of macro PL from the B family of QDs and WL.

helps to reveal the nature of both these features. It shows an intensive emission band labeled as A and centered at about 0.93 eV, which overlaps with the low-energy part of the $\Delta R/R$ feature. More interestingly, it changes with increasing optical-pumping power P, as shown in the inset of Fig. 1. For the low pumping power $P = P_0$, band A is centered between 0.92–0.93 eV and shifts towards higher energies with increasing P. We tentatively stated that PL band A and the low-energy $\Delta R/R$ feature are related to optical transitions among the zero-dimensional (0D) localized states in the WL [32–38], whereas the higher-energy $\Delta R/R$ transition involves its 2D band edges. Consequently, the observed evolution of the PL peak A with P can be related to gradual filling of the WL density of states (DOS) starting from its 0D-like tail (0D DOS) and ending in the 2D states. The 0D DOS may originate from an inhomogeneity of the WL due to fluctuation of its thickness and chemical composition, possibly introduced during the ripening stage of the MBE growth. Alternatively, the WL inhomogeneity could be triggered by chemical fluctuations in the (In,Al,Ga)As barrier, as suggested by the spectral smearing of the barrier-related $\Delta R/R$ feature.

The 2D band-edge-related transition in the WL at approximately 0.94 eV allows us to determine the range of possible WL characteristics (composition x of the $In_{0.47x+0.53}Al_{0.24(1-x)}Ga_{0.23(1-x)}As$ alloy and WL thickness d_{WL}). For this purpose, the electronic structure of the WL is calculated, using the NEXTNANO software [24], for d_{WL} varied from 0.9 to 1.5 nm and x from 0.85 to 1. The calculated transition energies are presented in Fig. 2 as a color map, where the two dotted lines distinguish the area of energies corresponding to the WL transition. As we do not expect very strong intermixing, this calculation allows us to determine that the average WL characteristics have to be between four MLs (approximately 1.2 nm) of pure InAs and five MLs (approximately 1.5 nm) of alloy with $x = 0.85$, which resembles the recent transmission electron microscope images of similar QDs [39]. In the latter a rather soft interface with a gradient of composition is

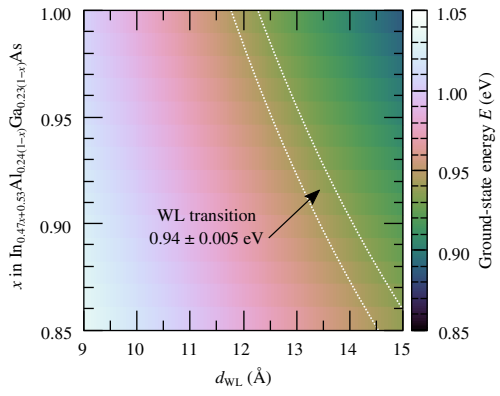

FIG. 2. Color map of the calculated wetting layer ground-state energy as a function of the WL width H (x axis) and material composition (y axis). Dotted white lines mark the energy of the WL transition observed in the $\Delta R/R$ signal.

found. Based on this, in further calculations done for QDs, we take a WL consisting of four MLs of pure InAs and perform Gaussian averaging to simulate the soft interface. Nonetheless, these subtle WL details have in fact only a very minor impact on the QD calculation results presented below.

In Fig. 1 we show also a series of PL peaks below the WL-assigned optical transitions with their positions extending down to approximately 0.6 eV. At least six such bands are resolved and labeled *B*–*G*. These are attributed to emission from QDs with multimodal size distribution formed during the ripening step in the MBE growth. Band *B* has a relatively high intensity compared to bands *C*–*G*, for which the intensity gradually increases. It is reasonable to assume that QDs from family *B* are the remnants of initially grown SK QDs. During the ripening stage, material from partially decomposed SK dots is transferred to other dots, forming the *C*–*G* families. This scenario is supported by previously published structural data [7], where the surface density of the remnants of the initially grown QDs (10^9–10^{10} cm^{-2}) can be comparable to that of newly formed QDs after the ripening stage. Interestingly, for QDs belonging to the *C* family emitting in the telecom spectral range of 1.53–1.63 μm, the surface density seems to be the lowest among all families. Indeed, the μPL spectrum presented in Fig. 1 obtained from the unprocessed sample (without any special patterning of the structure, e.g., mesa etching) shows a discrete spectrum, i.e., sharp and narrow PL lines originating from single QDs. The same is hardly resolvable for QDs in the band *B* and disappears completely for the band *A*, suggesting high areal density of the 0D potential traps in the WL, additionally confirmed by its high PL intensity dominating the emission spectrum.

Bands *B*–*G* originate mostly from ground-state recombination in QDs, rather than from excited states. This conclusion is drawn from the analysis of the pump-fluence-dependent PL presented in Fig. 3(b), which shows a nearly linear increase of the peak intensity with pump fluence across almost three decades. In further analysis of PL spectra we extracted the FWHM, peak position, and peak-to-peak distance (ΔE) between consecutive bands. These are obtained by fitting each PL peak with a Gaussian function. The relevant parameters are shown at the top of Fig. 3(a). PL bands *B*–*G* have the FWHM ranging from 24 to 36 meV, which reveals similar inhomogeneity within each of the QD families that could be in-plane size fluctuations, strain inhomogeneity, and chemical content variation. We observe an expected superlinear decrease in ΔE from approximately 54 meV between peaks *B* and *C* down to approximately 33 meV between *G* and *F* resulting from the quantum size effect. This issue will be further addressed in the theoretical considerations below.

In addition, the angle-resolved linear polarization of PL is presented in Fig. 3(c) for the selected PL bands *A*, *C*, *F*, and *G* to keep the subfigure clear. Surprisingly,

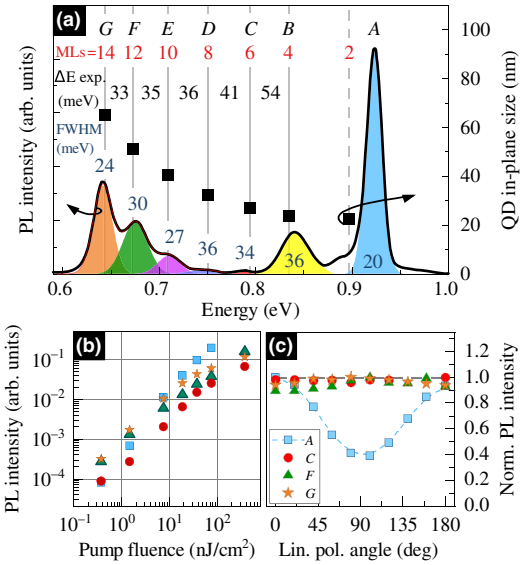

FIG. 3. (a) The PL spectrum (solid black line) at $T = 10$ K with Gaussian fits (color shaded areas for consecutive PL bands). Letters label the peaks; ΔE is the energetic distance between PL bands; FWHM is the full width at half maximum for the peaks. Vertical gray lines indicate energies obtained from numerical calculations for a given QD in-plane size. The dashed gray vertical line indicates potential remnants of initially grown SK QDs with two 2-ML height. Full squares represent the QD in-plane size, determined from the calculations of the ground-state energies. (b) Pump-fluence-dependent PL for selected PL bands: *A* (blue squares), *C* (red circles), *F* (green triangles), and *G* (orange stars). (c) Normalized PL intensity from the selected PL bands in (b), but as a function of the angle of linear polarization with respect to the laboratory frame.

an almost 40% degree of linear polarization (DOLP) is observed for band *A*, whereas for the QD-related bands *C*, *F*, and *G*, the DOLP is negligible, within an experimental accuracy of 5%. The lack of significant DOLP for the QDs can be linked to their high in-plane symmetry that for similar QDs was shown to lead to a negligible fine-structure splitting of the confined exciton states [11,12]. In contrast, high DOLP for band *A* may be related to the built-in optical anisotropy in the WL induced by local strain variations and its anisotropy or chemical disorder at the InAs/(In,Al,Ga)As or (In,Al,Ga)As/InP interfaces.

B. Long-range atom ordering and two-monolayer QD height steps

Previous observations of multimodally distributed InAs QDs embedded directly within the InP barrier were interpreted as resulting from the QD size variation in the form of 1-ML changes in their height between consecutive families [40–42]. A similar observation and interpretation

were also reported for InAs/GaAs QDs [10,43]. This does not seem to apply to the investigated QDs since the 1-ML (approximately 0.3 nm) change in QD height would lead to much smaller energy separation between PL bands than actually observed. Instead, we propose that the height of consecutive QD families changes by 2-ML steps. This hypothesis can find its justification in the expected long-range atom ordering that takes place in the quaternary barrier alloy. The ordering arises spontaneously for a multitude of III-V alloys as the coherent placing of atoms reduces the free energy of the crystal lattice in comparison to a disordered material or to a two-phase alloy [21].

The resulting structure has a modulation of composition along particular crystallographic directions where the elemental cell can be expanded as compared to, e.g., a binary alloy. Therefore, if the barrier above the investigated QD layer is organized in the direction [001] into In-rich and In-poor monolayers alternately then the effective height of a QD may be changed only by an even number of monolayers, i.e. by at least two MLs.

Previous observations of long-range ordering include (Al, Ga)As/GaAs [44], (In, Al)As/InP [45,46], (In, Ga)As/InP(110) [47,48], and (In, As)Sb/InSb(001) [49] heterointerfaces, which establish a background for our conclusion. The most common is the CuPt-type superlattice ($L1_1$ structure) resulting in ordering of cation lattices along the [111] direction [46]. Importantly, it was reported for the (In, Ga, As)P quaternary alloy lattice matched to InP(001) [48,50]. The CuPt-type structure ordering along the [001] direction relevant for this work was modeled [51] and observed for, e.g., bulk (In, Al)As grown on the InP(001) substrate [45,52]. Another, less frequently investigated ordering is the CuAu-I type, which also results in alternating layers along the [001] direction reported for MBE-grown strained (In, Ga)As/(In, Al)As multiple quantum wells on the InP(001) substrate [53]. The atomic ordering was also observed for various III-V and II-VI systems with epitaxial nanostructures [23,54]. For applications, the long-term stability of QDs and their properties is crucial. The size and composition of a highly strained QD after its growth significantly depend on the conditions in the barrier. Thermodynamic calculations suggest that QDs in atomically ordered alloys may be more stable than those grown in random lattices [23]. There are also, e.g., *ab initio* total energy [55,56] and strain energy calculations [23] showing that ordered structures are more stable than random alloys [22]. These results hold for systems with large differences in the lattice constants between the binary constituents; however, the ordering is also observed when this condition is not true. Therefore, other models (kinetic [51] and surface thermodynamic considerations) are proposed to understand this phenomenon for low-mismatch alloys, as in the case of alternating rows of large and small atoms building in along the growth steps (this is the proposed mechanism for the explanation of, e.g., the origin of the ordered CuPt-type structure [57]). These models help to explain the ordering observed for the (Al, Ga)As alloy [44], although AlAs and GaAs have very similar lattice constants.

Although the long-range ordering in III-V ternary and quaternary alloys has been confirmed by crystallographic methods, it has never been observed for the (In,Al,Ga)As quaternary alloy investigated here. Even though our research focuses only on optical properties and does not include the direct investigation of the structural properties, we deduce a similar ordering for (In,Al,Ga)As as has been observed for its constituents [45–48], (In, Ga)As and (In, Al)As, and there is no evident reason that their mixture should organize in a different way. Additionally, there are some premises, e.g., for (Ga, In)As(P) [48], under which ordering in quaternaries may be even more pronounced than in ternaries.

C. Modeling of QDs

The observed multimodal QD emission can be explained based on calculations of the QD ground state as a function of QD parameters (height, lateral dimensions, and chemical composition). The modeled QD geometry is a truncated pyramid with a square at the base and an angle between the side facets and the base of 25°, in accordance with the structural studies of QDs grown under similar conditions [39]. The dot is settled on a 4-ML-thick WL, and the barrier material is $In_{0.53}Ga_{0.23}Al_{0.24}As$.

We begin with two initial series of single-particle calculations, in which we take almost pure InAs ($In_{0.95}Al_{0.025}Ga_{0.025}As$) in the WL and a purely InAs QD with height varying by one ML and two fixed in-plane sizes, $L = 25$ nm and $L = 45$ nm, plotted in Fig. 4 with blue squares and diamonds, respectively. These results are compared with the experimental data plotted with black squares at 2-ML height steps and with gray squares at 1-ML steps. While the qualitative agreement is very weak, one may note that the assumption on the 2-ML QD height variation, and thus the presence of long-range ordering and the resulting enhanced stability of QDs, is correct here. Additionally, with a dotted green line we plot the ground-state energy for the limit of $L \to \infty$, i.e., for a quantum well (QW) as high as the studied QDs. The experimental data plotted assuming 1-ML steps (gray squares) is so steep that it even crosses this line, which makes it nonphysical, as it implies QDs having lower energy than for the QW. Thus, at this point we establish that the *G* family with emission around 0.65 eV is assigned as having $H = 14$ MLs, while $H = 4$ MLs characterizes the *B* family centered near 0.84 eV. Within this assumption, the smallest dots having 2-ML height should emit near 0.89 eV. Indeed, at this energy the PL spectra in Figs. 1 and 3 (vertical dashed gray line) reveal a PL band of low intensity overlapping with

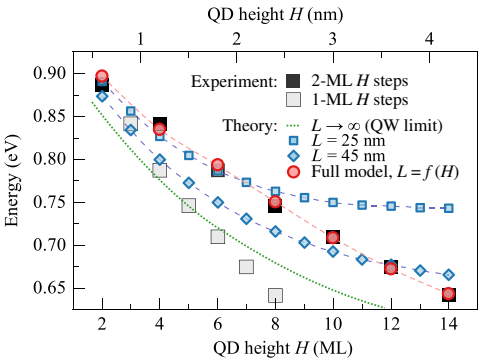

FIG. 4. Comparison of observed QD emission energies, plotted assuming 2-ML (black squares) and 1-ML (gray squares) steps in the QD heights, with trends calculated in a simple model for QDs with $L = 25$ nm (blue squares) and $L = 45$ nm (blue diamonds), as well as in the full model including the exciton binding energy and varying dependence $L = f(H)$. The dotted green line shows energy calculated for a quantum well. The height H is measured from the top of the WL.

tails of bands A and B, which thus comes from the 2-ML height QDs.

For two probe cases related to fixed L, the calculated ground-state energies as a function of H deviate from the postulated trend especially for larger heights. The obtained energy change saturates for large H, as predicted by the H^{-2} dependence. Therefore, to obtain agreement between the experimental and theoretical points, we need to introduce an additional, nonlinear dependence that relates H with L, which we presented in Fig. 3. It allowed us to achieve good qualitative agreement; the respective theoretical values are plotted with red circles. This final series of calculations is performed in an extended model taking into account the electron-hole Coulomb interaction and soft material interfaces. Starting with nominally clean InAs inside the WL and QDs, Gaussian averaging (with $\sigma = 0.3$ nm) of the material profile is used to simulate material intermixing at interfaces. QDs of height from 2 to 14 MLs are simulated, with the in-plane size varied in the range of $L = 25$–70 nm. The resultant dependence of the ground-state energy on these dimensions is very smooth, thus allowing for extraction of the $L = f(H)$ dependence that is then fit to the experimental values. Finally, this nonlinear dependence introduced into QD modeling resulted in very good agreement between the calculated energies and the positions of the PL peaks (see the red circles in Fig. 4).

The introduction of variable L might suggest that in principle the experimental data could also be reproduced assuming 1-ML height steps, by using a strong enough dependence of L on H. This is however not the case. As mentioned above, the 1-ML-stepped experimental data cross the theoretical result obtained for a quantum well, which means that the hypothetical $L(H)$ dependence is divergent. Thus, such a sequence of ground-state energies could not be obtained for QDs varying in height by a single ML.

D. Carrier dynamics

The theoretical calculation of excitonic states in QDs also allowed us to determine the exciton recombination dynamics, presented as a solid red line in Fig. 5. The result of the comparison with the experimental values may shed some light on the correctness of the assumptions made and the legitimacy of using a specific set of QD structural parameters.

The TRPL experiment is performed at $T = 10$ K. The PL decay curves measured at each of the respective PL peaks shown in Fig. 3(a) are analyzed using the PTI FelixGX software by Photon Technology International. Using the maximal entropy method (MEM) [58,59], the PL lifetimes are extracted without initial knowledge or assumptions on the number of underlying processes. Because of this, the MEM has proved effective in reconstructing decays consisting of several exponential components [60]. In this approach, we obtain a distribution of times of nonzero width, which results from the incomplete (noisy) information. The reconstruction formula is

$$I(t) = I(0) \sum_{i=1}^{N} A_i \exp\left(-\frac{t}{\tau_i}\right), \tag{1}$$

where N is the number of components in the quasicontinuous distribution of lifetimes describing the decay, and coefficients A_i are the corresponding amplitudes. If the distribution is a set of well-resolved peaks, it is valid to treat their means as single representative lifetimes. Such averages are plotted with circles in Fig. 5.

The PL lifetimes obtained for QD families B–F (1.4 ± 0.2, 1.5 ± 0.2, 1.2 ± 0.2, and 1.1 ± 0.2 ns, respectively) are similar and, as their variation is on the level of

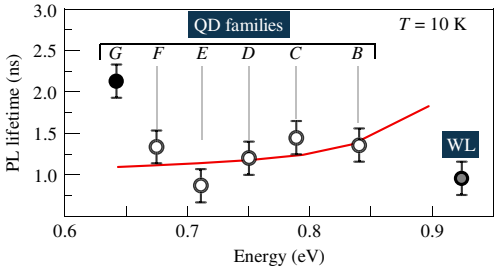

FIG. 5. PL lifetimes at $T = 10$ K for different families of ripening-assisted grown InAs/(In,Al,Ga)As/InP(001) QDs (PL bands B–G) and the WL (PL band A). The solid red line is a calculated trend for the PL lifetime.

the experimental uncertainty, no clear trend can be determined. These overall values that average to 1.3 ± 0.3 ns agree well with those obtained theoretically. In theory, a noticeable increasing trend is present, due to effectively weaker (relative to single-particle level spacing) electron-hole Coulomb interaction in smaller QDs. However, the uncertainty of experimental values does not allow this result to be verified. At the emission energy of 0.84 eV, a similar PL lifetime of approximately 1.65 ns has been obtained for slightly in-plane asymmetric SK InAs/(In,Al,Ga)As/InP(001) QDs [31]. For highly asymmetric confining potentials like those in InAs/(In,Al,Ga)As/InP(001) quantum dashes, the PL lifetime consists of two short and long components [30]. Nevertheless, the average PL lifetime of 1.45–1.8 ns is comparable to that obtained here, and indicates the main influence of the exciton confinement regime on the observed PL dynamics.

A significantly different value is obtained for family G, where the analysis yields a PL lifetime of 2.0 ± 0.2 ns. This family also shows a different PL quenching characteristic than other families, as discussed in the next section, which may suggest a much different exciton confinement nature reflected in a much longer PL decay time.

Finally, the observed long PL decay time of 0.9 ± 0.2 ns for the 0D WL states represented by PL band peak A at approximately 0.93 eV confirms the localized nature of the states [38] since the lifetime of excitons confined in the 2D WL is expected to be significantly shorter.

E. Temperature-dependent photoluminescence

In this section, we describe temperature-dependent PL that provides information on the carrier confinement parameters in the WL and QDs and the thermal carrier redistribution processes involving 0D and 2D states in this system.

First, the analysis focuses on the thermal shift of the PL peak energy presented in Fig. 6(a). The shift is compared to the well-known Varshni relation for the temperature dependence of the energy gap for a bulk InAs material [61]:

$$E_g(T) = E_g(0) - \frac{\alpha T^2}{T + \beta}. \tag{2}$$

Here $E_g(0)$ is the estimated transition energy at $T = 0$ K, with $\alpha = 2.76 \times 10^{-4}$ eV/K^2 and $\beta = 93$ K the parameters for InAs.

From Fig. 6(a) we infer that, for PL band A (blue circles), the peak energy follows the Varshni relation (solid blue line) only at elevated temperatures. At $T < 120$ K, the peak position remains nearly T independent or slightly drops when T decreases. The effect reminds the so-called "S-shape" function for a QW [62,63]. In this case, photoinjected carriers populate 0D-like states residing below the QW's mobility edge (2D states) and the resultant emission under low photoexcitation conditions involves the localized states only. The WL can be considered as a QW with additional localization potentials that come from, e.g., fluctuations of its width and chemical content, as well as variations of local strain. However, the optical response from the 2D WL states should be present: (i) in the PL spectrum, once the 0D states are fully occupied, preventing the carrier transfer process from 2D to 0D WL states, or (ii) in the $\Delta R/R$ trace, where all the 2D states with a large transition oscillator strength are accessible in the optical absorption process. Both are observed experimentally among the registered data set. The extrapolation of the Varshni trend to low temperatures predicts the optical response involving 2D WL states to be observed at approximately 0.94 eV. While the inset of Fig. 1 shows the shift of PL band A towards the predicted energy range with increasing excitation power, the $\Delta R/R$ experiment presented in Fig. 1 reveals the highly intensive feature at 0.94 eV, identified as the optical absorption process involving 2D WL states. The energy distance between PL band A and

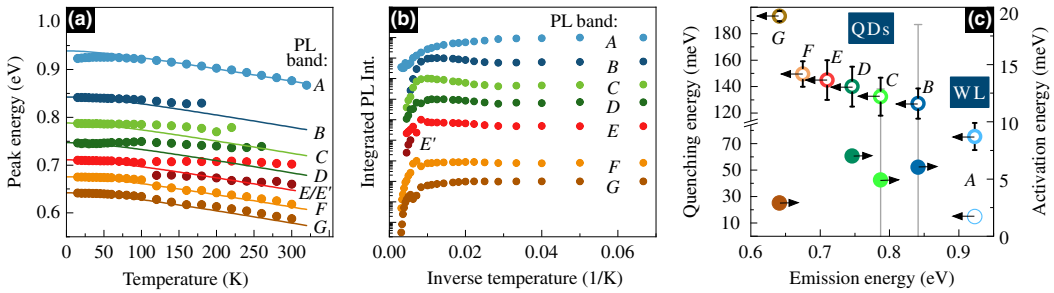

FIG. 6. Analysis of temperature-dependent PL spectra: (a) PL band peak energy, (b) integrated PL intensity, (c) activation (closed circles) and quenching (open circles) energies for the emission bands taken from the Arrhenius fit.

the 2D WL is approximately 10 meV at $T = 10$ K, which may serve as a rough estimate of the carrier localization energy. These observations confirm the existence of 0D WL states able to localize carriers at low T and suggest their impact on the thermal carrier redistribution process in the structure. A similar issue has previously been studied for (In,Ga)As/GaAs QDs [38].

The temperature dependence of QD-related PL bands *B*–*G* is different from that observed for the WL emission. At $T < 40$ K, the peak energy follows the Varshni trend. However, with increasing T, the redshift is either stopped (bands *B*–*E*) or weakened (bands *F* and *G*). This so-called anomalous energy shift is only partially caused by the bandgap reduction of the QD material [64]. It is predominantly related to the migration of carriers between different QD families and within each of them, as well as involving an exchange of carriers with the WL reservoir. During the thermally activated redistribution, carriers can be captured by QDs characterized by high emission energy. Therefore, the high-energy tails of QD size distributions in each of the families become optically active, shifting the PL-band peak energy towards higher energies, thus compensating for the effect of the thermal bandgap reduction [64].

The analysis of the temperature-dependent PL intensity presented in Fig. 6(b) provides further information about the carrier redistribution in the investigated structure. Each data set is fitted with the Arrhenius-type formula

$$I(T) = \frac{I_0}{1 + \sum_i B_i \exp(-E_i/k_B T)}, \tag{3}$$

where E_i is the average activation energy (or PL quenching energy) and B_i is the amplitude of the activation (PL quenching) process. The respective energies are summarized in Fig. 6(c).

For the already discussed PL band *A* originating from the 0D WL states overlapping with 2D WL states, the PL intensity is thermally quenched, characterized by two energies of 16 ± 2 and 75 ± 22 meV, represented by open blue circles in Fig. 6(c) at approximately 0.93 eV. The lower energy is close to the estimated energy of the additional localization in the WL, most probably caused by the fluctuations in the chemical content and/or the WL width variations. Note that these two do not have to match, as the latter is a difference between exciton levels in the WL and in an additional potential trap, while the former is composed of such a difference for just one of the carriers (most probably the hole) and exciton binding energy. Since the PL quenching is rather weak in the low-T range, most of the exciton population is trapped back to the 0D WL states and recombines there, while only a small exciton population feeds QDs. In the range of higher temperatures more complex PL quenching processes occur. When the thermal energy is larger, the WL reservoir is depopulated by the carrier capture in QDs, and at the same time, reactivated carriers from QDs supply the WL reservoir. Against this background, the escape of holes from the WL to the barrier seems to be the most important process, as the higher quenching-related energy corresponds well to the calculated difference in hole levels plus the exciton binding energy in the WL.

Prior to the discussion on the characteristic PL quenching and activation energies for QDs, it is justified to assume that in the low-T limit free carrier migration is negligible. This comes from the calculated electron-hole Coulomb correlation energy between approximately 9.5 meV for 14-ML-high QDs and approximately 20 meV for the flattest ones, which corresponds to $T \sim 110$–235 K. At higher temperatures, electrons and holes can escape from the confining potential with characteristic activation energies composed of the energy distance to WL states (δ_e, δ_h) or barrier band edges (Δ_e, Δ_h), in which we also include the exciton binding energy (E_b), as the exciton has to dissociate.

Let us now refocus on the T-dependent PL intensity from QDs. For families *B*–*D*, an enhancement is first observed, followed by a decrease of intensity at elevated temperatures. The extracted activation energy connected with this enhancement is approximately 6 meV with variation within the uncertainty bounds, as depicted with full circles in Fig. 6(c). This is close to the determined PL quenching energy for the 0D WL states, suggesting that QDs may acquire excitons released from the WL already at low T. However, this feeding process competes with the thermal escape of carriers at elevated temperatures. Energies connected with quenching of PL from QD families are depicted with open circles in Fig. 6(c), with values varying between 127 ± 11 and 150 ± 10 meV. As could be expected, a monotonic increase of quenching-related energies with rising QD size (families *B*–*F*) is present, as the localized states are sunk deeper into a wider potential.

To propose a scenario underlying the carrier activation process, one can compare the obtained PL quenching energies with calculated energy distances between the lowest single-particle electron (e_1) and hole (h_1) states confined in a dot and respective 2D WL ground states (e_{WL}, h_{WL}) or the (In,Al,Ga)As barrier (e_{bulk}, h_{bulk}). Results are presented in Fig. 7(a) together with a sketch of the confining potential in a QD and the WL in Fig. 7(b). Note that all the calculated energy differences $\delta_e = e_{\mathrm{WL}} - e_1 + E_b$, $\delta_h = h_1 - h_{\mathrm{WL}} + E_b$, $\Delta_e = e_{\mathrm{bulk}} - e_1 + E_b$, $\Delta_h = h_1 - h_{\mathrm{bulk}} + E_b$ include the electron-hole interaction energy, as discussed above. Additionally, with stars we also plot the calculated energy of exciton extraction to the WL, in which the difference between 0D and 2D exciton binding energies is taken into account.

From Fig. 7(a), note that extraction of a single electron from a dot to the barrier cannot be responsible for the PL quenching in the considered T range since the Δ_e (green

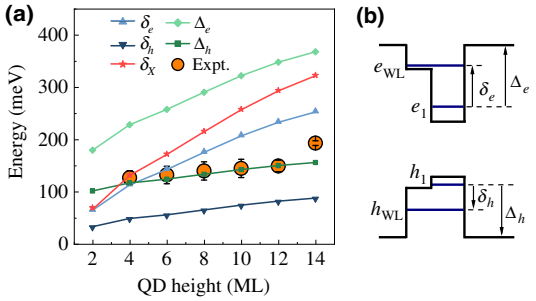

FIG. 7. (a) Comparison between experimentally obtained PL quenching energies (orange circles) and calculated energy distances between single-particle electron (e_1) and hole (h_1) ground states confined in a QD and (i) 2D WL electron (e_{WL}) and hole (h_{WL}) states, with $\delta_e = e_{WL} - e_1 + E_b$ and $\delta_h = h_1 - h_{WL} + E_b$, and (ii) the (In,Al,Ga)As barrier, where Δ_e and Δ_h are the distances from QD states to the conduction- and valence-band edges in the barrier, respectively. Here $\delta_X = \delta_e + \delta_h + E_b$ is sum of energy required to dissolve the exciton (E_b) and excite both carriers to the WL (δ_e, δ_h). (b) Energy diagram of the confinement potential for the system with a QD and the WL.

diamonds) is far above the obtained PL quenching energies (orange circles). From the primary PL quenching mechanism, we can also exclude hole escape from a dot to the WL. The calculated energy distance δ_h for the dots (blue down triangles) is too small to match the PL quenching energy. Note, however, that despite the relatively small energy necessary to eject a hole to the WL, the inverse process of fast hole relaxation mechanisms back to a QD at low T may lead to the absence of quenching related to such energies.

For small QDs, with $H \leq 6$ MLs, at least three PL quenching mechanisms can be considered: (i) the one related to single-electron escape to the WL [blue up triangles in Fig. 7(a)], (ii) single-hole escape to the barrier (green squares), and (iii) whole exciton extraction to the WL (red stars). In all these cases the calculated energy distances closely or perfectly fit the respective PL quenching energies.

For large QDs, with $H > 6$ MLs, the dominant PL quenching mechanism seems to be related to single-hole escape to the barrier as the calculated energy distance Δ_h perfectly matches the quenching energy. Since the hole extraction to the barrier is also present for small QDs, we can conclude that it can be the primary mechanism for the PL quenching in the investigated QDs.

Finally, we comment on the observed anomalies in the temperature dependence of PL from the investigated structure. At $T > 125$ K, the PL spectrum is enriched by the appearance of the PL band labeled E' between previously identified bands E and F. Temperature dependence of the E' band is presented in Fig. 6(a); however, the fitting procedure did not allow for a precise determination of changes in the band intensity due to its substantial overlap with bands E and F. The origin of the band is unknown; it could be related to another family of QDs that is split off from families E and F. Another anomaly is related to the observation of two quenching energies for band G. While the higher one, 193 ± 5 meV, is in agreement with the abovementioned general scenario for QDs, the lower one, 25 ± 5 meV, suggests the existence of another nonradiative relaxation channel that we could not identify.

IV. SUMMARY

In conclusion, we perform detailed optical studies of InAs/(In,Al,Ga)As/InP(001) QDs grown by MBE employing the ripening-assisted scheme. QDs emit in the 1.4–2 μm spectral range, which places them among attractive solutions for photonic applications in the near infrared. We study a multimodal emission from QDs, which reveals their grouping into at least six families according to their height. Based on the quantitative agreement between our theoretical calculations and experimental data, we show that the dots belonging to the consecutive families differ by two material monolayers in QD height, contrarily to 1-ML steps typically observed for InAs/InP QDs made of binary alloys. We suggest that this may stem from crystallographic long-range ordering in the quaternary (In,Al,Ga)As barrier alloy that stabilises the growth of InAs QDs. Because of the minimization of the crystal lattice free energy by atomic ordering, QDs in such systems should be characterized by higher long-term stability in comparison to those embedded in alloys without ordering, which is also beneficial for future applications. We also find that QDs from consecutive families differ significantly in lateral dimensions spanning the 24–65 nm range of in-plane sizes. Such geometries allow us to calculate the relatively short PL lifetimes monotonically decreasing from approximately 1.4 ns for flat dots to approximately 1.1 ns for higher ones, which agrees with the mean trend from experimental data. Observation of a single-exponential decay and negligible linear polarization of PL from QDs suggest their high in-plane symmetry. Finally, we observe a thermal carrier redistribution process, in which localized states in the WL play the role of carrier reservoir, feeding the QDs at elevated temperatures. Based on the comparison of calculated energy splittings between carrier states in the dots, the wetting layer, and in the barrier with the experimental data, we determine that the dominant PL quenching mechanism is the escape of holes to the barrier.

ACKNOWLEDGMENTS

M.G., G.S., and M.S. acknowledge financial support from the National Science Centre (Poland) under Grant

No. 2014/14/M/ST3/00821. P.H. acknowledges financial support from the Polish budgetary funds for science in 2018–2020 via the "Diamond Grant" program (Ministry for Science and Higher Education, Grant No. DI 2017 011747) and from the National Science Centre (Poland) under the Etiuda 8 Grant No. 2020/36/T/ST5/00511. A.M. acknowledges financial support from the National Science Centre (Poland) grant Preludium 8 (project No. 2014/15/N/ST7/04708). This work is also financially supported by the BMBF Project (Q.Link.X) and DFG (DeLiCom). We thank Krzysztof Gawarecki for sharing his implementation of the $\mathbf{k}\cdot\mathbf{p}$ method, Janusz Andrzejewski for discussions of the calculation results, and Matusala Yacob for his assistance in the MBE growth process.

[1] P. Senellart, G. Solomon, and A. White, High-performance semiconductor quantum-dot single-photon sources, Nat. Nanotechnol. **12**, 1026 (2017).

[2] S. Buckley, K. Rivoire, and J. Vučković, Engineered quantum dot single-photon sources, Rep. Prog. Phys. **75**, 126503 (2012).

[3] M. Gawełczyk, Excitons in asymmetric nanostructures: Confinement regime, Acta Phys. Pol. A **134**, 930 (2018).

[4] M. Gawełczyk, P. Wyborski, P. Podemski, J. P. Reithmaier, S. Höfling, and G. Sęk, Excited states of neutral and charged excitons in single strongly asymmetric InP-based nanostructures emitting in the telecom C band, Phys. Rev. B **100**, 241304 (2019).

[5] M. Z. M. Khan, T. K. Ng, and B. S. Ooi, Self-assembled InAs/InP quantum dots and quantum dashes: Material structures and devices, Prog. Quantum. Electron. **38**, 237 (2014).

[6] M. Benyoucef, M. Yacob, J. P. Reithmaier, J. Kettler, and P. Michler, Telecom-wavelength (1.5 μm) single-photon emission from InP-based quantum dots, Appl. Phys. Lett. **103**, 162101 (2013).

[7] M. Yacob, J. P. Reithmaier, and M. Benyoucef, Low-density InP-based quantum dots emitting around the 1.5 μm telecom wavelength range, Appl. Phys. Lett. **104**, 022113 (2014).

[8] F. M. Ross, J. Tersoff, and R. M. Tromp, Coarsening of Self-Assembled Ge Quantum Dots on Si(001), Phys. Rev. Lett. **80**, 984 (1998).

[9] A. Raab and G. Springholz, Oswald ripening and shape transitions of self-assembled PbSe quantum dots on PbTe (111) during annealing, Appl. Phys. Lett. **77**, 2991 (2000).

[10] K. Pötschke, L. Müller-Kirsch, R. Heitz, R. L. Sellin, U. W. Pohl, D. Bimberg, N. Zakharov, and P. Werner, Ripening of self-organized InAs quantum dots, Phys. E Low-Dimens. Syst. Nanostruct. **21**, 606 (2004).

[11] A. Kors, K. Fuchs, M. Yacob, J. P. Reithmaier, and M. Benyoucef, Telecom wavelength emitting single quantum dots coupled to InP-based photonic crystal microcavities, Appl. Phys. Lett. **110**, 031101 (2017).

[12] A. Musiał, P. Holewa, P. Wyborski, M. Syperek, A. Kors, J. P. Reithmaier, G. Sęk, and M. Benyoucef, High-purity triggered single-photon emission from symmetric single InAs/InP quantum dots around the telecom C-band window, Adv. Quantum Technol. **3**, 1900082 (2019).

[13] A. Kors, J. P. Reithmaier, and M. Benyoucef, Telecom wavelength single quantum dots with very small excitonic fine-structure splitting, Appl. Phys. Lett. **112**, 172102 (2018).

[14] L. Sapienza, M. Davanço, A. Badolato, and K. Srinivasan, Nanoscale optical positioning of single quantum dots for bright and pure single-photon emission, Nat. Commun. **6**, 7833 (2015).

[15] G. Brassard, F. Bussieres, N. Godbout, and S. Lacroix, in *Applications of Photonic Technology 6*, edited by R. A. Lessard and G. A. Lampropoulos (SPIE, Quebec City, Québec, Canada, 2003).

[16] T. A. Eriksson, T. Hirano, B. J. Puttnam, G. Rademacher, R. S. Luís, M. Fujiwara, R. Namiki, Y. Awaji, M. Takeoka, N. Wada, and M. Sasaki, Wavelength division multiplexing of continuous variable quantum key distribution and 18.3 Tbit/s data channels, Commun. Phys. **2**, 9 (2019).

[17] S. K. Joshi, D. Aktas, S. Wengerowsky, M. Lončarić, S. P. Neumann, B. Liu, T. Scheidl, G. C. Lorenzo, Ž. Samec, L. Kling, A. Qiu, M. Razavi, M. Stipčević, J. G. Rarity, and R. Ursin, A trusted node–free eight-user metropolitan quantum communication network, Sci. Adv. **6**, eaba0959 (2020).

[18] A. W. Elshaari, I. E. Zadeh, A. Fognini, M. E. Reimer, D. Dalacu, P. J. Poole, V. Zwiller, and K. D. Jöns, On-chip single photon filtering and multiplexing in hybrid quantum photonic circuits, Nat. Commun. **8**, 379 (2017).

[19] https://www.idquantique.com/.

[20] R. Cheng, C.-L. Zou, X. Guo, S. Wang, X. Han, and H. X. Tang, Broadband on-chip single-photon spectrometer, Nat. Commun. **10**, 4104 (2019).

[21] G. B. Stringfellow, Atomic ordering in III/V semiconductor alloys, J. Vac. Sci. Technol. B **9**, 2182 (1991).

[22] G. Stringfellow, Ordered structures and metastable alloys grown by OMVPE, J. Cryst. Growth **98**, 108 (1989).

[23] P. Moeck, Epitaxial and endotaxial semiconductor quantum dots: A brief review on atomic ordering and the void-mediated formation mechanism, Nonlinear Anal. Theory Methods Appl. **63**, e1311 (2005).

[24] The release date is October 31, 2018.

[25] S. Birner, T. Zibold, T. Andlauer, T. Kubis, M. Sabathil, A. Trellakis, and P. Vogl, nextnano: General purpose 3-D simulations, IEEE Trans. Electron Devices **54**, 2137 (2007).

[26] I. Vurgaftman, J. R. Meyer, and L. R. Ram-Mohan, Band parameters for III–V compound semiconductors and their alloys, J. Appl. Phys. **89**, 5815 (2001).

[27] K. Gawarecki, P. Machnikowski, and T. Kuhn, Electron states in a double quantum dot with broken axial symmetry, Phys. Rev. B **90**, 085437 (2014).

[28] K. Gawarecki, Spin-orbit coupling and magnetic-field dependence of carrier states in a self-assembled quantum dot, Phys. Rev. B **97**, 235408 (2018).

[29] K. Karrai and R. J. Warburton, Optical transmission and reflection spectroscopy of single quantum dots, Superlattices Microstruct. **33**, 311 (2003).

[30] M. Gawełczyk, M. Syperek, A. Maryński, P. Mrowiński, Ł. Dusanowski, K. Gawarecki, J. Misiewicz, A. Somers,

J. P. Reithmaier, S. Höfling, and G. Sęk, Exciton lifetime and emission polarization dispersion in strongly in-plane asymmetric nanostructures, Phys. Rev. B **96**, 245425 (2017).

[31] M. Syperek, J. Andrzejewski, E. Rogowicz, J. Misiewicz, S. Bauer, V. I. Sichkovskyi, J. P. Reithmaier, and G. Sęk, Carrier relaxation bottleneck in type-II InAs/InGaAlAs/InP(001) coupled quantum dots-quantum well structure emitting at 1.55 μm, Appl. Phys. Lett. **112**, 221901 (2018).

[32] D. Gammon, E. S. Snow, B. V. Shanabrook, D. S. Katzer, and D. Park, Homogeneous linewidths in the optical spectrum of a single gallium arsenide quantum dot, Science **273**, 87 (1996).

[33] K. Leosson, J. R. Jensen, W. Langbein, and J. M. Hvam, Exciton localization and interface roughness in growth-interrupted GaAs/AlAs quantum wells, Phys. Rev. B **61**, 10322 (2000).

[34] H. D. Robinson, B. B. Goldberg, and J. L. Merz, Observation of excitation transfer among neighboring quantum dots, Phys. Rev. B **64**, 075308 (2001).

[35] A. Babiński, J. Borysiuk, S. Kret, M. Czyż, A. Golnik, S. Raymond, and Z. R. Wasilewski, Natural quantum dots in the InAs/GaAs wetting layer, Appl. Phys. Lett. **92**, 171104 (2008).

[36] G. Sęk, A. Musiał, P. Podemski, M. Syperek, J. Misiewicz, A. Löffler, S. Höfling, L. Worschech, and A. Forchel, Exciton kinetics and few particle effects in self-assembled GaAs-based quantum dashes, J. Appl. Phys. **107**, 096106 (2010).

[37] J. Q. Ning, S. J. Xu, X. Z. Ruan, Y. Ji, H. Z. Zheng, W. D. Sheng, and H. C. Liu, Electronic band structures and electron spins of InAs/GaAs quantum dots induced by wetting-layer fluctuation, J. Appl. Phys. **110**, 054320 (2011).

[38] M. Syperek, M. Baranowski, G. Sęk, J. Misiewicz, A. Löffler, S. Höfling, S. Reitzenstein, M. Kamp, and A. Forchel, Impact of wetting-layer density of states on the carrier relaxation process in low indium content self-assembled (In, Ga)As/GaAs quantum dots, Phys. Rev. B **87**, 125305 (2013).

[39] C. Carmesin, M. Schowalter, M. Lorke, D. Mourad, T. Grieb, K. Müller-Caspary, M. Yacob, J. P. Reithmaier, M. Benyoucef, A. Rosenauer, and F. Jahnke, Interplay of morphology, composition, and optical properties of InP-based quantum dots emitting at the 1.55 μm telecom wavelength, Phys. Rev. B **96**, 235309 (2017).

[40] S. Raymond, S. Studenikin, S.-J. Cheng, M. Pioro-Ladriere, M. Ciorga, P. J. Poole, and M. D. Robertson, Families of islands in InAs/InP self-assembled quantum dots: A census obtained from magneto-photoluminescence, Semicond. Sci. Technol. **18**, 385 (2003).

[41] S. Tomimoto, A. Kurokawa, Y. Sakuma, T. Usuki, and Y. Masumoto, Radiative recombination of excitons in disk-shaped inas/inp quantum dots, Phys. Rev. B **76**, 205317 (2007).

[42] G. Gélinas, A. Lanacer, R. Leonelli, R. A. Masut, and P. J. Poole, Carrier thermal escape in families of InAs/InP self-assembled quantum dots, Phys. Rev. B **81**, 235426 (2010).

[43] F. Guffarth, R. Heitz, A. Schliwa, K. Pötschke, and D. Bimberg, Observation of monolayer-splitting for InAs/GaAs quantum dots, Phys. E Low-Dimens. Syst. Nanostruct. **21**, 326 (2004).

[44] T. S. Kuan, T. F. Kuech, W. I. Wang, and E. L. Wilkie, Long-Range Order in $Al_xGa_{1-x}As$, Phys. Rev. Lett. **54**, 201 (1985).

[45] O. Ueda, T. Fujii, Y. Nakada, H. Yamada, and I. Umebu, TEM investigation of modulated structures and ordered structures in InAlAs crystals grown on (001) InP substrates by molecular beam epitaxy, J. Cryst. Growth **95**, 38 (1989).

[46] W. S. Han, B. Lee, J. H. Baek, J.-H. Lee, B. S. Jung, E.-H. Lee, and O. Byungsung, Ordering effect on band-gap lowering in lattice-matched InAlAs epilayers grown on InP by metal–organic chemical-vapor deposition, Appl. Phys. Lett. **72**, 1905 (1998).

[47] T. S. Kuan, W. I. Wang, and E. L. Wilkie, Long-range order in $In_xGa_{1-x}As$, Appl. Phys. Lett. **51**, 51 (1987).

[48] M. A. Shahid, S. Mahajan, D. E. Laughlin, and H. M. Cox, Atomic Ordering in $Ga_{0.47}In_{0.53}As$ and $Ga_xIn_{1-x}As_yP_{1-y}$ Alloy Semiconductors, Phys. Rev. Lett. **58**, 2567 (1987).

[49] H. R. Jen, K. Y. Ma, and G. B. Stringfellow, Long-range order in InAsSb, Appl. Phys. Lett. **54**, 1154 (1989).

[50] M. A. Shahid and S. Mahajan, Long-range atomic order in $Ga_xIn_{1-x}As_yP_{1-y}$ epitaxial layers [(x, y) = (0.47, 1), (0.37, 0.82), (0.34, 0.71), and (0.27, 0.64)], Phys. Rev. B **38**, 1344 (1988).

[51] M. Ishimaru, S. Matsumura, N. Kuwano, and K. Oki, Kinetics of CuPt-type ordered phase formation in III-V semiconductor alloys during (001) epitaxial growth due to step flow, Phys. Rev. B **51**, 9707 (1995).

[52] K. Kurihara, H. Namita, R. Ueda, M. Takashima, K. Akimoto, K. Sakata, T. Takahashi, T. Nakamura, and K. Shimoyama, Ordering structure along the direction of InAlAs, J. Cryst. Growth **272**, 9 (2004).

[53] D. U. Lee, J. Y. Jin, T. Y. Yun, T. W. Kim, H. S. Lee, M. S. Kwon, and J. Y. Lee, Atomic arrangements of a CuAu-I type ordered structure in strained $In_xGa_{1-x}As/In_yAl_{1-y}As$ multiple quantum wells, J. Mater. Sci. **40**, 3843 (2005).

[54] P. Möck, T. Topuria, N. D. Browning, G. R. Booker, N. J. Mason, R. J. Nicholas, M. Dobrowolska, S. Lee, and J. K. Furdyna, Internal self-ordering in In(Sb, As), (In, Ga)Sb, and (Cd, Zn, Mn)Se nano-agglomerates/quantum dots, Appl. Phys. Lett. **79**, 946 (2001).

[55] A. A. Mbaye, L. G. Ferreira, and A. Zunger, First-Principles Calculation of Semiconductor-Alloy Phase Diagrams, Phys. Rev. Lett. **58**, 49 (1987).

[56] G. P. Srivastava, J. L. Martins, and A. Zunger, Atomic structure and ordering in semiconductor alloys, Phys. Rev. B **31**, 2561 (1985).

[57] T. Suzuki, A. Gomyo, and S. Iijima, Strong ordering in GaInP alloy semiconductors formation mechanism for the ordered phase, J. Cryst. Growth **93**, 396 (1988).

[58] E. T. Jaynes, Information theory and statistical mechanics, Phys. Rev. **106**, 620 (1957).

[59] E. T. Jaynes, Information theory and statistical mechanics. II, Phys. Rev. **108**, 171 (1957).

[60] A. K. Livesey and J. C. Brochon, Analyzing the distribution of decay constants in pulse-fluorimetry using the maximum entropy method, Biophys. J. **52**, 693 (1987).

[61] Y. Varshni, Temperature dependence of the energy gap in semiconductors, Physica **34**, 149 (1967).

[62] M. Baranowski, M. Syperek, R. Kudrawiec, J. Misiewicz, J. A. Gupta, X. Wu, and R. Wang, Carrier dynamics between delocalized and localized states in type-II GaAsSb/GaAs quantum wells, Appl. Phys. Lett. **98**, 061910 (2011).

[63] M. Baranowski, R. Kudrawiec, M. Latkowska, M. Syperek, J. Misiewicz, and J. A. Gupta, Dynamics of localized excitons in $Ga_{0.69}In_{0.31}N_{0.015}As_{0.985}$/GaAs quantum well: Experimental studies and monte-carlo simulations, Appl. Phys. Lett. **100**, 202105 (2012).

[64] W. Lei, Y. Chen, B. Xu, P. Jin, Y. Wang, C. Zhao, and Z. Wang, Anomalous temperature dependence of photoluminescence peak energy in InAs/InAlAs/InP quantum dots, Solid State Commun. **137**, 606 (2006).

ARTICLE 3

Droplet epitaxy symmetric InAs/InP quantum dots

DE GRUYTER Nanophotonics 2022; aop

Research Article

Paweł Holewa*, Shima Kadkhodazadeh, Michał Gawełczyk, Paweł Baluta, Anna Musiał, Vladimir G. Dubrovskii, Marcin Syperek and Elizaveta Semenova

Droplet epitaxy symmetric InAs/InP quantum dots for quantum emission in the third telecom window: morphology, optical and electronic properties

https://doi.org/10.1515/nanoph-2021-0482
Received August 25, 2021; accepted January 13, 2022;
published online January 28, 2022

***Corresponding author**: **Paweł Holewa**, DTU Fotonik, Technical University of Denmark, Kongens Lyngby DK-2800, Denmark; and Laboratory for Optical Spectroscopy of Nanostructures, Department of Experimental Physics, Faculty of Fundamental Problems of Technology, Wrocław University of Science and Technology, Wybrzeże Wyspiańskiego 27, 50-370 Wrocław, Poland,
E-mail: pawel.holewa@pwr.edu.pl. https://orcid.org/0000-0002-2154-896X
Shima Kadkhodazadeh, DTU Nanolab-National Centre for Nano Fabrication and Characterization, Technical University of Denmark, Kongens Lyngby DK-2800, Denmark; and NanoPhoton-Center for Nanophotonics, Technical University of Denmark, DK-2800 Kongens Lyngby, Denmark, E-mail: shka@dtu.dk. https://orcid.org/0000-0003-3606-8851
Michał Gawełczyk, Department of Theoretical Physics, Faculty of Fundamental Problems of Technology, Wrocław University of Science and Technology, 50-370 Wrocław, Poland; and Institute of Physics, Faculty of Physics, Astronomy and Informatics, Nicolaus Copernicus University in Toruń, ul. Grudziądzka 5, Toruń 87-100, Poland,
E-mail: michal.gawelczyk@pwr.edu.pl. https://orcid.org/0000-0003-2299-140X
Paweł Baluta, **Anna Musiał and Marcin Syperek**, Laboratory for Optical Spectroscopy of Nanostructures, Department of Experimental Physics, Faculty of Fundamental Problems of Technology, Wrocław University of Science and Technology, Wybrzeże Wyspiańskiego 27, 50-370 Wrocław, Poland, E-mail: 250164@student.pwr.edu.pl (P. Baluta), anna.musial@pwr.edu.pl (A. Musiał), marcin.syperek@pwr.edu.pl (M. Syperek). https://orcid.org/0000-0001-9602-8929 (A. Musiał). https://orcid.org/0000-0002-5260-7360 (M. Syperek)
Vladimir G. Dubrovskii, Faculty of Physics, St. Petersburg State University, Universitetskaya Embankment 13B, 199034, St. Petersburg, Russia, E-mail: dubrovskii.ioffe@mail.ru. https://orcid.org/0000-0003-2088-7158
Elizaveta Semenova, DTU Fotonik, Technical University of Denmark, Kongens Lyngby DK-2800, Denmark; and NanoPhoton-Center for Nanophotonics, Technical University of Denmark, DK-2800 Kongens Lyngby, Denmark, E-mail: esem@fotonik.dtu.dk. https://orcid.org/0000-0002-5856-4461

Abstract: The rapidly developing quantum communication technology requires deterministic quantum emitters that can generate single photons and entangled photon pairs in the third telecom window, in order to be compatible with existing optical fiber networks and on-chip silicon photonic processors. InAs/InP quantum dots (QDs) are among the leading candidates for this purpose, due to their high emission efficiency in the required spectral range. However, fabricating versatile InAs/InP QD-based quantum emitters is challenging, especially as these QDs typically have asymmetric profiles in the growth plane, resulting in a substantial bright-exciton fine structure splitting (FSS). This hinders the generation of entangled photon pairs and thus, compromises the versatility of InAs/InP QDs. We overcome this by implementing droplet epitaxy (DE) synthesis of low surface density (2.8×10^8 cm^{-2}) $InAs_xP_{1-x}$ QDs with $x = (80 \pm 15)\%$ on an (001)-oriented InP substrate. The resulting QDs are located in etched pits, have concave bases, and most importantly, have symmetric in-plane profiles. We provide an analytical model to explain the kinetics of pit formation and QD base shape modification. Our theoretical calculations of electronic states reveal the properties of neutral and charged excitons and biexcitons confined in such QDs, which agree with the optical investigations of individual QDs. The optical response of QDs' ensemble suggests that FSS may indeed be negligible, as reflected in the vanishing degree of linear polarization. However, single QD spectrum gathered from an etched mesa shows moderate FSS of (50 ± 5) μeV that we link to destructive changes made in the QD environment during the post-growth processing. Finally, we show that the studied DE QDs provide a close-to-ideal single-photon emission purity of $(92.5 \pm 7.5)\%$ in the third telecom window.

Keywords: near-infrared spectroscopy; quantum dots; quantum telecommunication; single-photon sources.

1 Introduction

Epitaxially-grown semiconductor quantum dots (QDs), among other applications [1], are considered as nearly perfect quantum emitters [2, 3] for applications in quantum communication [4] and quantum computation [1, 5] technologies. QDs emitting in the long-wavelength third telecom band centered at 1550 nm are of special interest for these applications [6], as they offer ultra-low-loss single-photon-encoded data transmission between quantum nodes, both in distributed silica-fiber-based optical networks [7, 8] and on-chip optical circuits [9–13]. Two main material systems have been identified for long-wavelength QD-based single-photon emission: InAs/GaAs [14–17] and InAs/InP [18–24]. InAs/GaAs QDs show excellent single-photon emission properties [25], including high single-photon emission purity [15, 17], and high degree of photon indistinguishability [16]. This, however, is at the cost of complicated strain engineering epitaxial processes to red-shift the emission [6, 26]. In comparison, InAs/InP QDs naturally emit at longer wavelengths, while also offering high photon emission purity [18, 26] and indistinguishability [27]. However, controlling their growth kinetics and the resulting morphology with respect to size, shape anisotropy, and surface density is complicated. Therefore, establishing an epitaxial method that allows tailoring the aforementioned properties independently will make InAs/InP QDs highly attractive as solid-state single-photon quantum emitters in the long-wavelength telecom range.

There are two main epitaxial techniques for synthesizing InAs/InP QDs: Stranski–Krastanov (SK) [18, 21, 28], and droplet epitaxy (DE) [19, 20, 29]. SK InAs/InP QDs hold the record for single-photon purity in the long-wavelength spectral range [18], whereas DE InAs/InP QDs have the lead in entangled photon pair emission [30] due to their more symmetric shape compared to SK QDs [19]. The high symmetry of QD confining potential is important for efficient generation of entangled photon pairs, as it directly impacts the bright-exciton fine structure splitting (FSS) [2]. Symmetry can be inherited from the substrate by employing high-Miller-index planes, such as (111)A- [31] and (111)B-oriented GaAs [32] for the emission in the visible range, or InP(111)A with C_{3v} symmetry [33, 34] in the near-infrared spectral range. These high-Miller-index planes substrates are difficult to process and are thus unpractical for device applications. Moreover, despite the promising prospects of this approach [35], the FSS of the resulting QDs has not been below (60 ± 38) μeV [36]. Therefore, it is important to develop new methods that allow synthesis of symmetric QDs on the industry-compatible (001)-oriented InP substrate. Inspiring results have been achieved in the GaAs-based material system using the DE approach [37, 38]. The obtained DE QDs have been shown to possess high in-plane symmetry and hence, exhibit very low FSS values [39, 40], allowing them to be employed in quantum communication schemes utilizing entangled photon pairs [4]. For (001) InP substrates, a modified DE method, where the QD crystallization from an In droplet is followed by the annealing in AsH_3 ambient, was recently suggested by Sala et al. [41]. The resulting QDs were shown to have high in-plane symmetry and are located at the center of etched pits, formed during the annealing step.

In this work, we present a detailed investigation of the morphology, chemical composition, electronic structure and optical properties of ensemble, and individual DE InAs(P)/InP QDs grown in metalorganic vapor-phase epitaxy (MOVPE). By optimizing the growth process, we could achieve an array of low surface density QDs (2.8×10^8 cm^{-2}), with highly in-plane symmetric profiles located in etched pits. The QD emission covers the range of interest centered around 1500 nm. We have examined in detail the morphology and chemical composition of surface and buried QD-in-pit structures using atomic force microscopy (AFM) imaging, scanning transmission microscopy (STEM) and energy dispersive X-ray spectroscopy (EDX). Based on the insight gained, we propose a kinetic model to explain the formation of asymmetric pits etched around the QDs and the QD base shape modification. Moreover, we have performed theoretical calculation of electronic and optical properties within the eight-band $\boldsymbol{k} \cdot \boldsymbol{p}$ method combined with the configuration–interaction approach for states of carrier complexes. Together with the morphological investigations they support the interpretation of properties of ensemble and individual QDs revealed by the low-temperature photoluminescence (PL) measurements. Excitonic complexes in individual QDs were studied by the micro-PL (μPL) and time-resolved μPL experiments. We show that the fabricated QDs are promising candidates for single-photon sources emitting at 1500 nm, supported by their high purity single-photon emission with an as-measured value of $\mathcal{P} = 92.5\%$ and fitted $g^{(2)}_{\mathrm{fit}} = 0$ with a standard error of $\sigma = 0.10$ associated with the fitting procedure. In addition, the high lateral symmetry of the QDs makes them interesting for entangled photon pair generation for quantum communication applications. Although we measure an exciton FSS value on the level of (50 ± 5) μeV, this is likely related to the post-growth processing of the QD structure and requires further optimization.

2 Results and discussion

2.1 Description of the structure

Each of two studied samples contains two QD arrays grown under the same conditions by low-pressure MOVPE on an (001)-oriented InP substrate. The first QD array is covered by a 30 nm-thick InP layer and was used for STEM and optical studies. The second QD array is deposited on the top InP surface and is left uncovered for AFM investigation.

The QDs were synthesized in a two-step process. First, an array of In droplets was deposited on the InP surface at 360 °C under a trimethylindium (TMIn) flux and in the absence of Vth group flux. Afterward, the In droplets were annealed under an arsine (AsH_3) ambient as the temperature was being ramped up to 550 °C, followed by 180 s-long waiting time (annealing). For comparison, a reference structure was grown without the high-temperature annealing. Instead, after the In droplet deposition at 360 °C, the temperature was raised only to 475 °C in AsH_3 ambient and no waiting followed. A detailed description of the growth procedure can be found in the Methods section.

2.2 QD morphology investigations

The surface morphology of the QDs was investigated by AFM. Figure 1a and b present typical AFM images of the surface QDs in the annealed, and the un-annealed reference samples, respectively. The density of the surface QDs is similar in the two samples, since this parameter is determined by the initial stage of DE QD growth, i.e., the In droplet deposition [29]. The difference between the two samples arises from the annealing conditions under AsH_3. It can be seen that for the sample annealed at an elevated temperature, every QD is located in a pit formed by local etching of the surrounding material on the perimeter of the InAs DE QD [41]. The exemplary cross-sectional profiles of the AFM scans through the QD centers for the annealed sample shown in Figure 1c reveal the typical shape of the pits in two orthogonal directions. The pits are asymmetric, with a typical width of ∼ 470 nm and ∼ 310 nm along the [110] and [$\bar{1}$10] directions, respectively. The high-resolution QD AFM profiles in Figure 1d reveal the high symmetry of the annealed QDs (top panel) in comparison to the reference QDs (bottom panel). Statistical analysis of the QD profiles presented in Figure 1e shows that the in-plane aspect ratio of the annealed QDs, defined as the ratio of the QD base median length along [110] and [$\bar{1}$10] directions, is 1.09 compared to 1.75 for the reference QDs. We also observe a significant decrease of the QD height due to annealing, from $H_s \approx 4.8$ nm for the reference sample to $H_s \approx 1.9$ nm for the annealed QDs [bottom panel in Figure 1e]. For the annealed QDs, we defined H_s as the height of a surface QD measured from the bottom of the pit to the QD apex.

Since surface QDs are optically inactive, buried QDs need to be examined with respect to photon generation processes. Detailed investigation of the shape and composition of annealed buried QDs and their environment was carried out here by high resolution STEM [42] and EDX in cross-section geometry. The results are summarized in Figure 2, where we show cross-sections of QDs

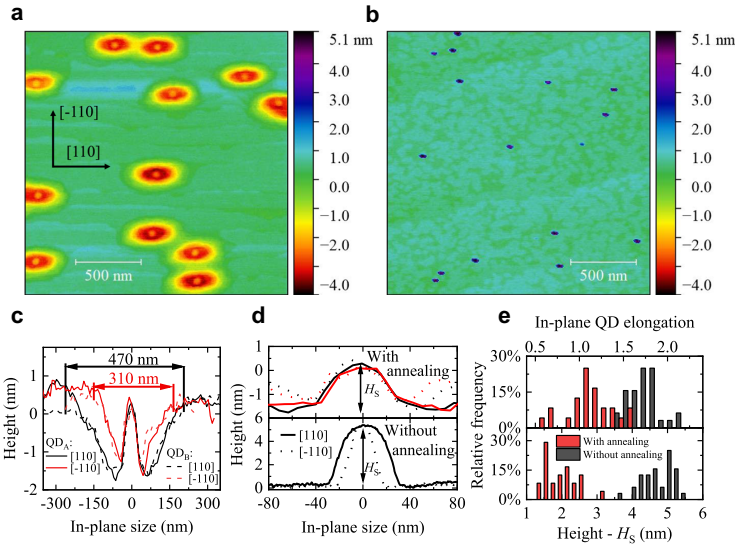

Figure 1: Morphological investigation of surface DE QDs by atomic force microscopy, $(2 \times 2)\ \mu m^2$ scans.
(a) Annealed QDs in etched pits. (b) QDs before annealing. (c) Cross-section scans of QDs and the pits around annealed QDs. (d) Comparison of the QD cross-sections: after annealing [top panel, close-up of (c)] and before annealing (bottom). (e) Statistics of the QD in-plane elongation (top) and height (bottom).

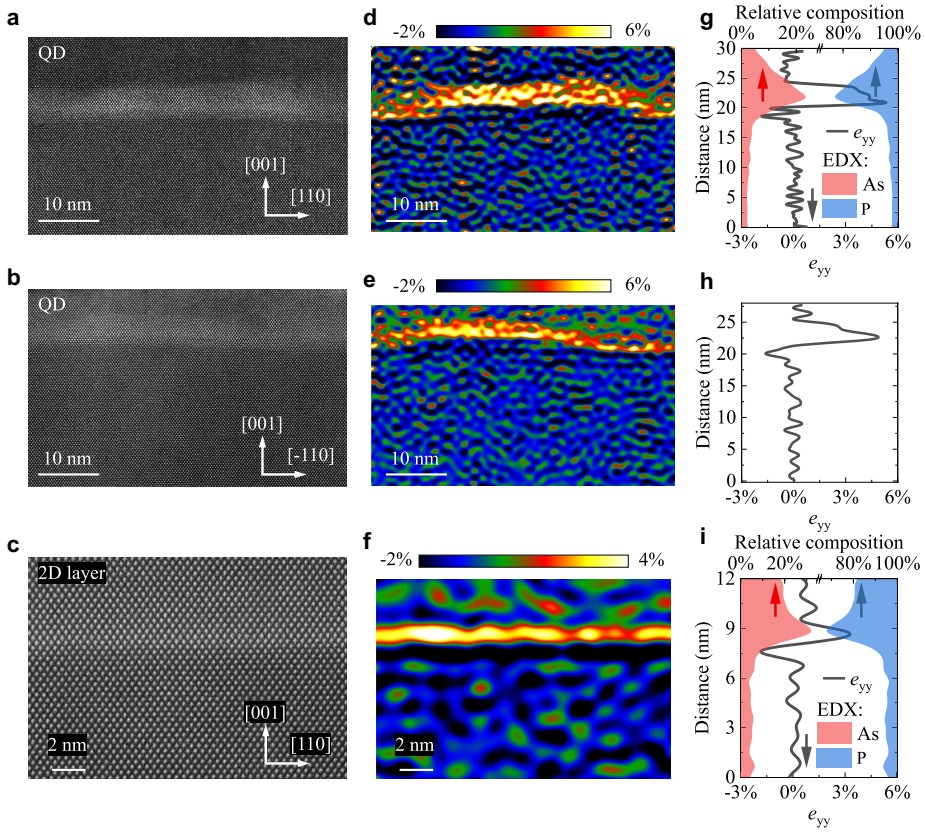

Figure 2: Morphological investigation of the buried annealed DE QDs by STEM and EDX. QDs in cross-section geometry viewed along the (a) [$\bar{1}$10] and (b) [110] directions, and (c) the 2D InAs(P) layer. (d)–(f) Maps representing the fractional change in lattice spacing along the [001] direction (relative to the InP lattice), e_{yy}, for each of the images in (a)–(c). (g)–(i) Line scan profiles of P (blue) and As (red) concentrations measured by EDX, and the lattice displacement values e_{yy} (black lines) along the [001] direction.

viewed along the [$\bar{1}$10] (top row) and [110] directions (middle row), and on the 2D layer (bottom row). While the base length of the buried QDs seems to be very similar to the surface QDs, we measure larger heights for the buried QDs compared to the surface ones. Based on the images shown in Figure 2a and b, the buried QDs can be approximated as truncated cones with arched bases and almost symmetric in-plane dimensions. We measure a base diameter of $B = (45 \pm 2)$ nm, top diameter of $D = (33 \pm 1.7)$ nm and height of $H = (5.2 \pm 0.3)$ nm for the buried QDs in the annealed sample. The chemical composition of these QDs is found to be $InAs_xP_{1-x}$ with $x = (80 \pm 15)\%$, measured both by EDX and by analyzing the change in the lattice parameter along the [001] direction from the atomic resolution STEM images (for details, see Methods). The color-coded maps of changes in lattice spacing along the [001] direction relative to the InP substrate (e_{yy}) are shown in Figure 2d–f. Line scans of e_{yy} across the QDs and As and P composition profiles obtained from EDX measurements are plotted in Figure 2g–i. Additional EDX data is shown in Figure S1.

The formation of a 2D $InAs_xP_{1-x}$ layer, shown in Figure 2c, is a self-limited process of P atoms substitution by As, taking place at the InP surface during its annealing in the AsH_3 ambient. In contrast to SK QDs, DE QDs are formed without a wetting layer, due to the entirely different nature of their nucleation [19]. In the case of InAs/GaAs QDs, the dot and the barrier share the Vth group atoms, while in the case of our studied InAs/InP material system, the Vth group fluxes are switched at the QD interface. This means that the InP surface is exposed to the AsH_3 ambient during the QD crystallization step. In such conditions, the As–P exchange starts with the desorption of the P atoms from the III–V surface. At standard growth conditions, when the InP surface is exposed to the PH_3 ambient, the vacant positions are immediately refilled with

new P atoms. However, if the InP surface is annealed in the AsH_3 ambience, the As atoms are more likely to bind to available In atoms left vacant after the P desorption. The kinetics of As–P exchange is temperature-dependent and the process is reversible [43, 44]. The thickness of this layer in our sample is $h \approx 3$ MLs, estimated from the STEM images [see Figure 2c, f and i]. A chemical composition of $x = (50 \pm 15)\%$ is estimated for this layer from both atomic resolution STEM images and EDX profiles as shown in Figure 2f and i. For EDX data of the 2D layer, see Figure S2. Moreover, we consistently observe a region about 15 nm-thick above the 2D layer containing up to $\sim 20\%$ As. Based on our AFM and STEM observations of DE QDs and their environment, we reconstruct the model presented in Figure 3a for buried DE InAs/InP QDs located in etched pits and connected by a 2D InP(As) layer.

In the following section, we focus on an analytical description of the local etching mechanism during the DE QD annealing step. We assume a symmetric QD with dimensions inferred from the STEM measurements (QD1). We assume the bottom base diameter of $B \sim 43$ nm and top diameter of $D \sim 33$ nm. We then include a small QD elongation of ~ 1.09 to the model, as measured by AFM for surface QDs. This resizes the dimensions to $B_{[\bar{1}10]} \sim 41.1$ nm and $D_{[\bar{1}10]} \sim 31.6$ nm along the $[\bar{1}10]$ direction, and $B_{[110]} \sim 44.9$ nm and $D_{[110]} \sim 34.4$ nm along the [110] direction (QD2).

Interestingly, STEM images show that the bottom base of the QD is arched upwards, where the sides are at the same level as the etched pits around the QDs and the central part of QD base is approximately at the same level as the 2D layer outside the pits. Therefore, in our model, we keep the pit's depth and the central part of the QD base level equal [marked with d in Figure 3a]. For QD1, we take $d =$ 1.9 nm in both directions, and for QD2 $d = 2.6$ nm and $d = 2$ nm along the [110] and $[\bar{1}10]$ directions, respectively. For both QDs, we keep the same in-plane distance λ between the QD base and the substrate outside the pit: $\lambda = 213$ nm along [110] and $\lambda = 133$ nm along the $[\bar{1}10]$ direction.

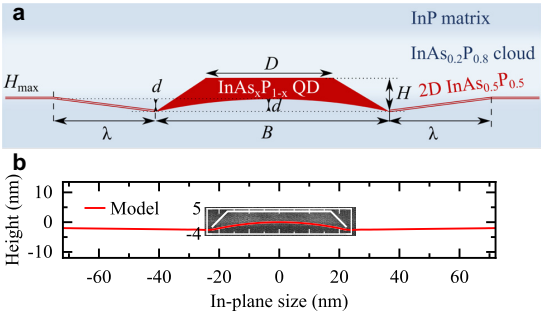

Figure 3: Scheme of a QD geometry.
(a) Model of a QD and surrounding pit inferred from the STEM scans. (b) The modeled profile of the bottom base of the QD and the 2D InP(As) layer surrounding it (red line) overlaid on the STEM image in Figure 2a. The white eye-guiding line indicates the QD top interfaces.

2.3 Formation of pits around QDs

Annealing takes place under the As supplying ambient, while P is available from the InP substrate. We need, however, an In supply to form additional InAs(P) material in the island during annealing, most probably followed by InAs(P) evaporation from the QD apex, leading to the observed decrease in the height of the annealed QDs. The material exchange between the substrate and the island is In-limited. We assume that the In diffusion occurs preferentially through the perimeter of the island base in contact with a 2D InP(As) layer, where the elastic stress induced by the lattice mismatch is highest, similar to InAs/InGaAs system [45, 46]. Coordinate-dependent coverage of the substrate with In atoms θ can be described using the steady-state diffusion equation

$$\frac{\mathrm{d}^2\theta}{\mathrm{d}x^2} = -I_k\Omega/D_k h, \tag{1}$$

with $k = 0$ or 1. Here, x is the coordinate along a given crystallographic direction (either $[\bar{1}10]$ or [110]), Ω is the elementary volume per one III–V pair, h is the height of InAs(P) ML, I_0 and D_0 are the In fluxes [$\mathrm{nm}^{-2}\ \mathrm{s}^{-1}$] and diffusion coefficient for In migration from the substrate to area around the island, while I_1 and D_1 describe In diffusion from the substrate into the island through the interface beneath the QD. The diffusion process is driven by the elastic stress field [45, 46], which depends on the position around the island and the shape of the QD itself.

The relevant boundary conditions are given by

$$\theta(x = B/2) = \theta_{\min}, \quad \theta(x = B/2 + \lambda) = \theta_{\max} \tag{2}$$

for $B/2 \le x \le B/2 + \lambda$ and

$$\left(\frac{\mathrm{d}\theta}{\mathrm{d}x}\right)_{x=0} = 0, \quad \theta(x = B/2) = \theta_{\min} \tag{3}$$

for $0 \le x \le B/2$. Here, B is a QD base diameter along a given direction and λ is the effective diffusion length of In atoms in this direction. The height profile of the surface around a QD is then obtained as $H - H_{\max} = -I_k\Omega t(\theta_{\max} - \theta)$, with $H_{\max}$ as the height outside the pit (the zero level) and t as the annealing time. According to Eq. (2), the profile depth is maximum at the island boundary and zero outside the pit. According to Eq. (3), the height of the surface layer in the growth direction reaches its maximum at $x = 0$ by symmetry. Our measurements show that this maximum is

very close to the surface height outside the pit, meaning that the etching does not occur under the QD, e.g., in the center of the pit. Solutions for the pit cross-sections along the $[\bar{1}10]$ and [110] directions are given by

$$H - H_{\max} = -I_0\Omega\Delta\theta t\left[1 - \frac{x - B/2}{\lambda} - \frac{(B+\lambda)(x-B/2) + B^2/4 - x^2}{r_0^2}\right] \quad (4)$$

for $B/2 \le x \le B/2 + \lambda$ around the QD and

$$H - H_{\max} = -I_1\Omega\Delta\theta t\left[1 - \frac{B^2/4 - x^2}{r_1^2}\right] \quad (5)$$

for $0 \le x \le B/2$ beneath the QD, with $r_i^2 = 2D_i h\Delta\theta/(I_i\Omega)$ $(i = 0, 1)$, and $\Delta\theta = \theta_{\max} - \theta_{\min}$. According to the measurements, the height profiles of the pits around the QD are linear within the AFM experimental accuracy (the slope d/λ is only 1–2%), corresponding to $r_0 \to \infty$ in Eq. (4). This should be due to a high diffusivity of In through 2D layer relative to the diffusivity of In at the island–substrate interface ($D_0 \ll D_1$). The calculated profile in Figure S3 shows the excellent fits to the measured cross-sections of the pits around symmetric QD1 and asymmetric QD2, as well as the concave-shaped cross-sections of the QD base. The fits are obtained with $I_0\Omega\Delta\theta t = I_1\Omega\Delta\theta t = 1.9$ nm, $B = 43$ nm, $r_1 = 21.5$ nm, $\lambda = 132.5$ nm in the $[\bar{1}10]$ direction and 213 nm in the [110] direction for symmetric QD1. For asymmetric QD2, we use the same λ, $I_0\Omega\Delta\theta t = I_1\Omega\Delta\theta t = 2.0$ nm, $B = 41.12$ nm, $r_1 = 20.58$ nm in the $[\bar{1}10]$ direction, and $I_0\Omega\Delta\theta t = I_1\Omega\Delta\theta t = 2.6$ nm, $B = 44.88$ nm, $r_1 = 22.4$ nm in the [110] direction. In all cases, the values of r_1 are very close to $B/2$, which explains an absence of etching in the center of the pit. The fitting values of $I_0\Omega\Delta\theta t$ and $I_1\Omega\Delta\theta t$ appear identical, showing that the supply of In from the substrate to the QD volume is the same around and underneath the QDs, while different shapes of the cross sections are due to different diffusion coefficients of In atoms. The effective diffusion length of In atoms is larger along the [110] direction thus the etching process occurs at different rates along different crystallographic directions and results in the elongated pit profiles. Overall, the fact that QDs become almost symmetric after annealing should be due to a more homogeneous solid diffusion of In atoms compared to its surface diffusion leading to elongated shapes of the initial islands.

2.4 Electronic and optical properties of QDs

2.4.1 Optical properties of the QD ensemble

Optical properties of an ensemble of buried QDs were investigated by low-temperature ($T = 12$ K) PL, time-resolved PL and polarization dependence of QD PL response, and the results are summarized in Figure 4. The optical response of the QD ensemble reflects the statistical properties of the investigated QDs. The PL spectrum of the sample is shown in Figure 4a. The emission is centered at ~ 0.85 eV, showing spectral broadening mainly related to the QD size and chemical composition distribution.

To link the optical and morphological investigations of the QDs, we calculate the electron and hole eigenstates within the multiband envelope-function $\boldsymbol{k}\cdot\boldsymbol{p}$ theory, based on the QD geometry presented in Figure 3a, and then include Coulomb and anisotropic electron–hole exchange interactions within the configuration–interaction approach. Details of the numerical calculations and the parameters used are given in the Methods section. We probe a range of parameters within the uncertainty window provided by the morphological studies of buried annealed QDs. The exciton ground-state energy for a series of calculations for QDs with As composition x in the range 72–88% and height H varied between 3.6 and 6.0 nm, is plotted with symbols in Figure 4a for comparison with the PL spectrum. The position of the PL peak fits to an exciton transition calculated for an $InAs_xP_{1-x}$ QD with $x \sim 80\%$ and $H \sim 5$ nm, thus confirming a good agreement between the QD model constructed from the STEM and EDX measurements and the optical response.

The degree of linear polarization (DOLP) for the ensemble emission, presented in Figure 4b, is experimentally estimated to be on the low level of ~ 3.5% (see Methods for the definition of DOLP). Such a low value can be linked to a very small in-plane asymmetry of the confining potential. This parameter is influenced by strain fields, local atomic disorder, the electric field, and more importantly, the QD shape [47]. High in-plane symmetry of QDs revealed from the morphological investigation is expected to provide a highly symmetric QD potential and,

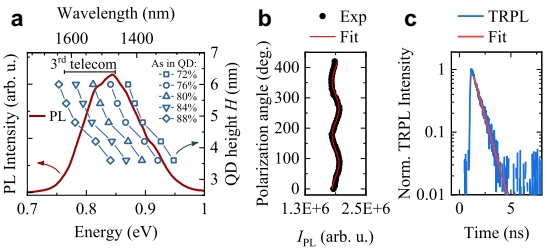

Figure 4: Optical properties of the QD ensemble emission. (a) PL spectrum (left axis) with the calculated X emission energy as a function of QD height and As content (right axis). (b) Integrated PL intensity of QD ensemble as a function of the polarization angle. (c) Time-resolved photoluminescence for the peak of the QD ensemble.

consequently, lead to vanishing FSS for confined exciton and biexciton states. This satisfies the general requirement for a source of polarization-entangled photon pairs.

We also carried out time-resolved PL measurements of QD ensemble to estimate the recombination time at the PL peak energy. The obtained PL trace shows a mono-exponential decay characterized by a time constant $\tau_{PL} = (0.75 \pm 0.01)$ ns (Figure 4c). In the case of QD confining potential asymmetry, two PL decay components in the PL trace should be observed due to two different oscillator strengths for the doublet of fundamental exciton transitions [47]. This in turn would result in a significant DOLP. Thus, the results of optical investigations of the QD ensemble are in line with the expected relatively small FSS in the investigated QDs.

2.4.2 Single QD emission properties

In this section, we present a detailed investigation of the optical properties of individual QDs. To spatially isolate individual QDs, the structure was processed into large mesas 2–3 µm in size (for details see Methods). The µPL spectra for the buried annealed QDs are presented in Figure 5a, comprising a handful of well-isolated emission lines, indicating the presence of only a few QDs within the excitation spot.

A zoomed-in plot of the group of µPL lines at ~0.83 eV is presented in Figure 5b. The excitonic complexes are identified by measuring the excitation power (P) dependence of the line intensity (I). While for the µPL line at ~0.8324 eV we have $I_X \sim P^{1.01}$, for the line at ~0.8303 eV the intensity changes quadratically with power ($I_{XX} \sim P^{1.95}$). These dependencies, displayed in Figure 5c, allowed for a tentative assignment of the lines as exciton (X) and biexciton (XX) transitions in the same QD. The µPL spectrum also contains another line at ~0.8334 eV, for which $I_{CX} \sim P^{1.27}$. Therefore, the line is tentatively identified as a charged exciton transition (CX) [48, 49], without clear assignment to a particular QD.

We carry out theoretical calculations of a QD having the ground state near the observed X transition. The geometry of simulated QDs is based on our morphological investigations (see Figure 3) with $H = 4.8$ nm and $x = 80\%$, while for the in-plane size we calculate both an ideally symmetric (labeled QD1) and a slightly asymmetric dot (QD2), which includes minor deviations from the perfect symmetry: slight elongation and a difference in the concave QD base arcs in the [110] and [$\bar{1}$10] directions. All the relevant computed parameters are summarized in Table 1. The only parameter with a noticeable, yet still insignificant, difference between the ideally symmetric QD1 and the realistic QD2 is the electron single-particle excitation energy. Thus, we can consider that the slight asymmetry present in the investigated QDs should have very small effects on optical properties.

The calculated binding energies for the biexciton, the positively-charged exciton (X^+), and the negatively-charged exciton (X^-) are negative with magnitudes of

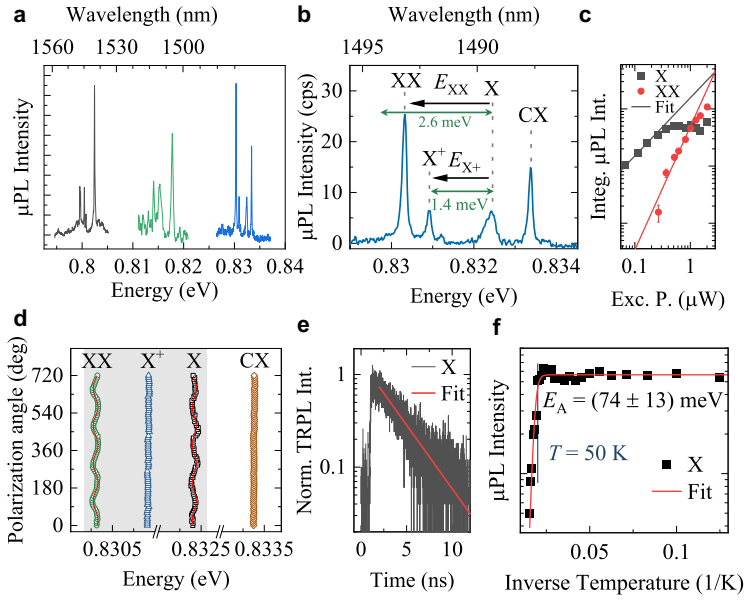

Figure 5: Single QD emission.
(a) Exemplary high-resolution low-temperature (T = 4.2 K) µPL spectra measured in three different mesas containing QDs. (b) µPL spectrum of an individual QD with identified excitonic complexes (exciton, X, positive trion, X^+, and biexciton, XX), as well as a trion line from a neighboring QD (CX). The corresponding calculated binding energies for trion and biexciton are written and shown with green arrows (see QD2 in Table 1). (c) Integrated µPL intensity for XX and X lines with fit lines. (d) Polarization-resolved µPL for the lines shown in panel (b). (e) Time-resolved photoluminescence for the X line. (f) Temperature dependence of the X line µPL intensity with the Arrhenius fit line.

Table 1: Results of calculation for the idealized (QD1) and realistic (QD2) models of a QD: first excited level splitting for the electron and the hole, light-hole admixture, X ground state energy, DOLP, X lifetime, carrier-complex binding energies with respect to X energy.

	$e_2 - e_1$ (meV)	$h_2 - h_1$ (meV)	lh admixture (%)	E_X (meV)	DOLP (%)	τ_X (ns)	Δ_{X^-} (meV)	Δ_{X^+} (meV)	Δ_{XX} (meV)
QD1	10.18	7.64	0.056	823.82	0.32	0.87	3.01	1.64	2.78
QD2	7.60	7.77	0.06	818.75	1.42	0.84	2.99	1.43	2.63

$\Delta_{XX} = 2.63$ meV, $\Delta_{X^+} = 1.43$ meV, and $\Delta_{X^-} = 2.9$ meV, respectively (see Figure S4 for the binding energies for all calculated QD2 geometries). The calculated Δ_{XX} value fits very well to the experimentally obtained XX binding energy, whereas another line in the QD spectrum fits to the X^+ binding energy. For comparison, the calculated binding energies are shown in Figure 5b with green arrows. Therefore, the respective exciton complexes presumably belong to the same QD. However, the CX line at emission energy above X is attributed to a different QD as the existence of a negative trion with a positive binding energy may be excluded based on the theoretical calculations.

The results of polarization-resolved μPL investigation are presented in Figure 5d. Since the identified X^+ and CX lines come from recombination of spin-singlet states, one can expect zero FSS, and hence no doublet in the linear polarization-resolved spectrum. However, such doublets are present for the X and XX emission lines. The extracted exciton FSS is $\sim (50 \pm 5)$ μeV, which is comparable to the average values in symmetric GaAs-based QDs [36]. However, it is much higher than expected for the studied DE QDs as suggested by the ensemble emission properties described above. Moreover, the minor deviation from rotational symmetry found in the QD morphology, according to the calculation summarized in Table 1, could not explain the appearance of considerable FSS, since it results in negligible light-hole admixture to the hole ground state (see Table 1). Such admixture is typically the main source of FSS in QDs [50]. Additionally, time-resolved μPL investigations of the exciton line, shown in Figure 5e, reveal $\tau = (3.16 \pm 0.04)$ ns. This is in stark contrast to the ensemble measurements, (0.75 ± 0.01) ns, and to the theoretically predicted value of 0.84 ns, which indicates the presence of other factors involved in carrier states and dynamics in the processed sample. The measured FSS and increased QD lifetime can be attributed to, e.g., the presence of crystal point defects and/or electric charges in the vicinity of QDs as a consequence of the dry etching process for mesa fabrication. Such a nearby electric charge acts as a source of an electric field that partially separates the electron and the hole in a QD leading to slower recombination, an effect observed also in other systems [51]. The increase in exciton lifetime in etched mesas is universal. However, its extent is random without any noticeable correlation with other QD properties, which is in line with irregular charge locations. This effective degradation of the initial in-plane rotational symmetry of the QD confining potential (exhibited in FSS and recombination time) requires further investigation.

The temperature-dependent μPL intensity of the X line is used to evaluate the prospect of single-photon applications at elevated temperatures, which require just Stirling-compatible cryocooler [52] (Figure 5d). Quenching of the μPL intensity is observable at relatively high temperatures as for pure InP barriers, starting from $T = 50$ K. This temperature is prospective for applications of our QDs in the quantum technology industry as it is easily achievable with a cryogenic-free Stirling cooler [52]. The activation energy, E_A, of (74 ± 13) meV (see Methods for the fitting formula), is larger than typically observed for telecommunication-relevant SK InAs/InP QDs [23] or InAs/InAlGaAs quantum dashes [53], and proves a good carrier localization in the QDs under investigation.

Finally, we investigate the single-photon emission purity $\mathcal{P}$ by the autocorrelation spectroscopy of the charged-exciton line in Figure 6a, having one of the largest emission intensities. For that, we record the second-order correlation function $g^{(2)}(\tau)$, exploiting the off-resonant continuous wave (cw) excitation scheme. The obtained histogram $C(\tau)$ without normalization is presented in

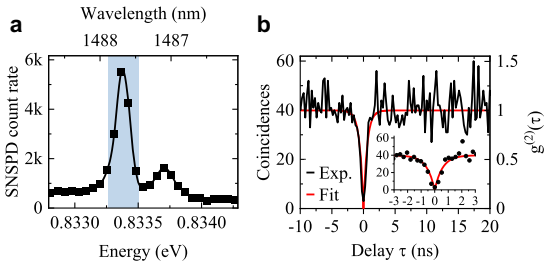

Figure 6: QD single-photon emission.
(a) The μPL spectrum for the CX line recorded on superconducting nanowire single-photon detectors with (b) CX autocorrelation histogram. Shaded area in (a) marks the monochromator band-pass.

Figure 6b which we fit [54] (see Methods) and obtain the $g^{(2)}(\tau)$ function by normalizing $C(\tau)$ with the average level A of coincidences per channel for $|\tau| \gg 0$. We obtain the fitted value of $g^{(2)}(\tau = 0) = 0$ and the standard error of the fitting procedure $\sigma = 0.10$ (without background correction or other data post-processing and with $A = 40$). The raw data-estimated purity is $\mathcal{P} = 1 - C(0)/A = 92.5\%$, and with the moderate level of A, we use a conservative estimation of the single-photon purity $\mathcal{P} = (92.5 \pm 7.5)\%$. The obtained high purity of the single-photon emission is comparable to the previous reports for DE QDs of higher density emitting in the third telecom window [30] and indicates the potential of the investigated QDs in quantum information processing as single-photon emitters operating in this spectral range.

3 Conclusions

We have synthesized InAs/InP QDs with low-surface density on (001)-oriented InP substrate by DE in the MOVPE process. By implementing an additional annealing step under AsH_3 ambient after QD formation, we induced modifications to the QD shape, as well as local etching of pits around the QD's perimeter.

The morphology of resulting DE QDs was investigated in detail by atomic force microscopy, scanning transmission electron microscopy and energy dispersive X-ray spectroscopy. The resulting DE QDs were found to have close to symmetric in-plane profiles and concave bases. Based on our morphological investigations, we proposed a kinetic model describing the formation of the pits surrounding QDs and the modification of the QD base shape.

The optical properties of a DE QDs ensemble revealed low DOLP, supporting the observation of high in-plane symmetry of the dots based on our structural characterizations.

The electronic and optical properties of carrier complexes confined in the QDs were calculated within the eight-band $\boldsymbol{k} \cdot \boldsymbol{p}$ and configuration–interaction methods, including the expected range of energies for the neutral exciton and binding energies for the biexciton and charged exciton. The optical properties of individual QDs were studied by high-spatially-resolution PL in mesa-processed structures. The experimentally obtained binding energies for the exciton and the biexciton were in a good agreement with the theoretically calculated values. The close to symmetric shape of the QDs should result in near zero FSS. However, the measurements revealed FSS $\sim (50 \pm 5)$ μeV. This, together with the increased carrier lifetime in mesa-processed structures compared to the planar structure, suggests that the defects introduced during the dry etching process can distort the QD electronic and optical properties from the average picture derived from the ensemble studies. Thus, further investigation and optimization of the processing are required.

Finally, the QDs show excellent single-photon emission properties: the Hanbury-Brown and Twiss-type interferometric experiment on a charged exciton revealed high purity of single-photon emission at ~ 1500 nm of $\mathcal{P} = (92.5 \pm 7.5)\%$, showing that these dots are promising candidates for single-photon emitters at the third telecom window.

4 Methods

4.1 Fabrication

The QDs were grown in the low-pressure MOVPE TurboDisc reactor using arsine (AsH_3), phosphine (PH_3), tertiarybutylphosphine (TBP) and trimethylindium (TMIn) precursors with H_2 as a carrier gas. The growth sequence began with a 0.5 μm-thick InP buffer layer deposited on an (001)-oriented InP substrate at 610 °C. Then, the temperature was decreased to 360 °C and stabilized under TBP. The deposition of indium droplets occurred under the TMIn flow rate of 13 μmol/min with nominally 1.8 ML-thick indium layer. The indium droplets were annealed for 60 s and the temperature was being raised to 550 °C during 130 s under AsH_3 with the flow rate of 52.2 μmol/min. Afterward, the temperature and AsH_3 flow were kept constant for 180 s and finally the 30 nm-thick InP was deposited. We repeated the indium droplet deposition and the annealing sequence for the surface QDs. For the reference structure, without annealing, after the 60 s-long waiting time, the temperature was raised to 475 °C during 70 s under AsH_3 ambient followed by the immediate InP layer deposition and the same sequence for the surface QD array finished the structure. Such structure was used for the QD ensemble investigation (time-dependent and polarization-resolved PL studies). For the μPL studies, the annealed structure was additionally processed to fabricate large mesa structures (size of 2–3 μm) in electron cyclotron resonance-reactive ion etching (RIE) in an Ar^+/Cl^- plasma.

4.2 Scanning transmission electron microscopy

Electron transparent lamellas of the cross-sections of the samples were prepared by focused ion beam milling (FIB) using a Helios Nanolab dual beam instrument. The FIB milling and polishing was carried out using a Ga^+ beam at 30 kV and with currents ranging from 2 nA −20 pA. The samples were then further polished in an Ar^+ Nanomill instrument at 700 V in order to remove FIB induced damage. High-angle annular dark-field STEM images of the samples were acquired using an FEI Titan 80-300 instrument fitted with a field emission gun and with an aberration-corrector on the probe forming lenses, operated at 300 kV. The electron probe had a convergence semi-angle of 18 mrad and the images were recorded on an annular detector with an inner collection semi-angle of 50 mrad. Geometric phase analysis was applied to the images to obtain lattice displacement maps along the [001] direction using the freely

available FRWRtools script [55]. The obtained changes in the lattice spacing along the growth direction and the Poisson ratio of InAs were then used to estimate the As content of the examined regions. The uncertainty of the composition estimation is determined by the measurement accuracy.

4.3 Optical experiments

During the optical experiments, the structures were held in a helium-flow cryostat allowing for the sample's temperature control in the range of 4.2–300 K. For the μPL studies, the structures were excited by a 640 nm line from a cw semiconductor laser diode through a high-numerical-aperture (NA = 0.4) microscope objective with 20× magnification. The same objective was used to collect the μPL signal and to direct it for the spectral analysis with a 1 m-focal-length monochromator equipped with a liquid-nitrogen-cooled InGaAs multichannel array detector, providing spatial and spectral resolution of ∼ 2 μm and ∼ 25 μeV, respectively. For the QD ensemble investigations, we used an optical lens instead of the microscope objective to probe a larger sample area of (150 × 150) μm^2. Polarization properties of emitted light were analyzed by rotating the half-wave retarder mounted before a fixed high-contrast-ratio (10^6:1) linear polarizer placed in front of the monochromator's entrance. Autocorrelation histograms and TRPL were measured in a similar setup. However, the structure was excited by a 787 nm cw laser line for the correlation spectroscopy, and by a train of ∼ 50 ps-long pulses at the frequency of 80 MHz, and the central photon wavelength of 805 nm. In this case, the collected photons were dispersed by a 0.3 m-focal-length monochromator equipped either with the InGaAs multichannel array detector or NbN-based superconducting nanowire single-photon detectors with ∼ 90% efficiency in the 1.5–1.6 μm range and ∼ 200 dark counts per second. A multichannel picosecond event timer analyzed the single photon counts as the time-to-amplitude converter with the 256 ps channel time bin width. The overall temporal resolution of the setup is ∼ 80 ps.

The DOLP is defined as

$$\mathrm{DOLP} = \frac{I_{\max} - I_{\min}}{I_{\max} + I_{\min}}, \tag{6}$$

where $I_{\max}$ ($I_{\min}$) is the maximal (minimal) PL intensity. The quenching of the integrated μPL intensity was fitted with the standard formula with a single activation processes related to excitation of carriers to higher-energy states or their escape from a QD:

$$I(T) = I_0 / \left[1 + B \exp\left(-E_A / k_B T\right)\right], \tag{7}$$

where I_0 is the μPL intensity for $T \to 0$, E_A is the activation energy, and B is the quenching rate. The autocorrelation histogram is fitted with the function of the form

$$C(\tau) = A\left[1 - \left(1 - g^{(2)}_{\mathrm{fit}}(0)\right)\exp\left(-|\tau|/t_r\right)\right], \tag{8}$$

where $g^{(2)}_{\mathrm{fit}}(0)$ is the single-photon emission purity, A in an average coincidence level, and $t_r = 1/(\Gamma + W_P)$ is the antibunching time constant with Γ being the electron–hole radiative recombination rate, and W_P – the effective pump rate.

4.4 Calculation of electronic and optical properties

The material composition profiles of simulated QDs, as presented in Figure 3a, were discretized and represented on a numerical grid. The strain field was calculated within the standard continuum elasticity theory, such that it minimizes the total elastic energy of the system. As the materials are noncentrosymmetric, the shear components of the strain tensor lead to a nonuniform piezoelectric field [56], which was calculated taking into account up to second-order terms in strain. Next, electron and hole (time-reversed valence-band electron) eigenstates were calculated using a numerical implementation [57] of the eight-band envelope-function $\boldsymbol{k}\cdot\boldsymbol{p}$ method [58, 59] including the calculated strain and piezoelectric fields as well as spin–orbit effects (for the explicit form of the Hamiltonian and details of numerical implementation, see Ref. [60]; for material parameters used for the InAs/InP material system see Ref. [23] and references therein). Calculated eigenstates have the form of discretized envelope functions for each of the eight bands included in the model, which allows us to determine, e.g., the light-hole admixture to the hole ground state. For each of simulated QDs a 40 × 40 electron–hole single-particle basis was computed and used to calculate the eigenstates of excitons, charged excitons and biexcitons within the configuration–interaction method by exact diagonalization of the electron–hole Coulomb and phenomenological anisotropic exchange interactions expanded in the configuration basis. Using the light–matter coupling Hamiltonian in the dipole approximation [61], optical transition dipole moments and resultant radiative lifetime and degree of polarization were calculated for each of the carrier-complex states.

Acknowledgments: We are grateful to Krzysztof Gawarecki for sharing his implementation of the $\boldsymbol{k}\cdot\boldsymbol{p}$ method. Numerical calculations have been carried out using resources provided by Wroclaw Centre for Networking and Supercomputing (https://wcss.pl).

Author contribution: All the authors have accepted responsibility for the entire content of this submitted manuscript and approved submission.

Research funding: We acknowledge support from the Danish National Research Foundation via Research Centre of Excellence NanoPhoton (ref. DNRF147). P. H. was funded by the Polish National Science Center within the Etiuda 8 scholarship (Grant No. 2020/36/T/ST5/00511) and by the European Union under the European Social Fund. V. G. D. gratefully acknowledges financial support of St. Petersburg State University under the research grant 75746688.

Conflict of interest statement: The authors declare no conflicts of interest regarding this article.

References

[1] I. Aharonovich, D. Englund, and M. Toth, "Solid-state single-photon emitters," *Nat. Photonics*, vol. 10, p. 631, 2016.

[2] P. Senellart, G. Solomon, and A. White, "High-performance semiconductor quantum-dot single-photon sources," *Nat. Nanotechnol.*, vol. 12, p. 1026, 2017.

[3] L. Schweickert, K. D. Jöns, K. D. Zeuner, et al., "On-demand generation of background-free single photons from a solid-state source," *Appl. Phys. Lett.*, vol. 112, 2018, Art no. 093106.

[4] F. B. Basset, M. Valeri, E. Roccia, et al., "Quantum key distribution with entangled photons generated on demand by a quantum dot," *Sci. Adv.*, vol. 7, 2021, Art no. eabe6379.
[5] J. Wang, F. Sciarrino, A. Laing, and M. G. Thompson, "Integrated photonic quantum technologies," *Nat. Photonics*, vol. 14, p. 273, 2019.
[6] X. Cao, M. Zopf, and F. Ding, "Telecom wavelength single photon sources," *J. Semiconduct.*, vol. 40, 2019, Art no. 071901.
[7] S. Wehner, D. Elkouss, and R. Hanson, "Quantum internet: a vision for the road ahead," *Science*, vol. 362, 2018, Art no. eaam9288.
[8] D. Cuomo, M. Caleffi, and A. S. Cacciapuoti, "Towards a distributed quantum computing ecosystem," *IET Quant. Commun.*, vol. 1, p. 3, 2020.
[9] Y. A. Vlasov and S. J. McNab, "Losses in single-mode silicon-on-insulator strip waveguides and bends," *Opt. Express*, vol. 12, p. 1622, 2004.
[10] J.-H. Kim, S. Aghaeimeibodi, C. J. K. Richardson, R. P. Leavitt, D. Englund, and E. Waks, "Hybrid integration of solid-state quantum emitters on a silicon photonic chip," *Nano Lett.*, vol. 17, p. 7394, 2017.
[11] M. Tran, D. Huang, T. Komljenovic, J. Peters, A. Malik, and J. Bowers, "Ultra-low-loss silicon waveguides for heterogeneously integrated silicon/III-V photonics," *Appl. Sci.*, vol. 8, p. 1139, 2018.
[12] S. Hepp, M. Jetter, S. L. Portalupi, and P. Michler, "Semiconductor quantum dots for integrated quantum photonics," *Adv. Quant. Tech.*, vol. 2, p. 1900020, 2019.
[13] A. W. Elshaari, W. Pernice, K. Srinivasan, O. Benson, and V. Zwiller, "Hybrid integrated quantum photonic circuits," *Nat. Photonics*, vol. 14, p. 285, 2020.
[14] E. S. Semenova, R. Hostein, G. Patriarche, et al., "Metamorphic approach to single quantum dot emission at 1.55μm on GaAs substrate," *J. Appl. Phys.*, vol. 103, p. 103533, 2008.
[15] M. Paul, F. Olbrich, J. Höschele, et al., "Single-photon emission at 1.55 μm from MOVPE-grown InAs quantum dots on InGaAs/GaAs metamorphic buffers," *Appl. Phys. Lett.*, vol. 111, 2017, Art no. 033102.
[16] C. Nawrath, F. Olbrich, M. Paul, S. L. Portalupi, M. Jetter, and P. Michler, "Coherence and indistinguishability of highly pure single photons from non-resonantly and resonantly excited telecom C-band quantum dots," *Appl. Phys. Lett.*, vol. 115, 2019, Art no. 023103.
[17] K. D. Zeuner, K. D. Jöns, L. Schweickert, et al., "On-Demand generation of entangled photon pairs in the telecom C-band with InAs quantum dots," *ACS Photonics*, vol. 8, p. 2337, 2021.
[18] T. Miyazawa, K. Takemoto, Y. Nambu, et al., "Single-photon emission at 1.5 μm from an InAs/InP quantum dot with highly suppressed multi-photon emission probabilities," *Appl. Phys. Lett.*, vol. 109, p. 132106, 2016.
[19] J. Skiba-Szymanska, R. M. Stevenson, C. Varnava, et al., "Universal growth scheme for quantum dots with low fine-structure splitting at various emission wavelengths," *Phys. Rev. Appl.*, vol. 8, 2017, Art no. 014013.
[20] N. Ha, T. Mano, S. Dubos, T. Kuroda, Y. Sakuma, and K. Sakoda, "Single photon emission from droplet epitaxial quantum dots in the standard telecom window around a wavelength of 1.55 μm," *Appl. Phys. Express*, vol. 13, 2020, Art no. 025002.
[21] A. Musiał, P. Holewa, P. Wyborski, et al., "High-purity triggered single-photon emission from symmetric single InAs/InP quantum dots around the telecom C-band window," *Adv. Quantum Technol.*, vol. 3, p. 1900082, 2019.
[22] A. Shikin, E. Lebedkina, C. Ciostek, et al., "Synthesis and systematic optical investigation of selective area droplet epitaxy of InAs/InP quantum dots assisted by block copolymer lithography," *Opt. Mater. Express*, vol. 9, p. 1738, 2019.
[23] P. Holewa, M. Gawełczyk, C. Ciostek, et al., "Optical and electronic properties of low-density InAs/InP quantum-dot-like structures designed for single-photon emitters at telecom wavelengths," *Phys. Rev. B*, vol. 101, p. 195304, 2020.
[24] P. Holewa, M. Gawełczyk, A. Maryński, et al., "Optical and electronic properties of symmetric InAs/(In,Al,Ga)As/InP quantum dots formed by ripening in molecular beam epitaxy: a potential system for broad-range single-photon telecom emitters," *Phys. Rev. Appl.*, vol. 14, 2020, Art no. 064054.
[25] S. L. Portalupi, M. Jetter, and P. Michler, "InAs quantum dots grown on metamorphic buffers as non-classical light sources at telecom C-band: a review," *Semicond. Sci. Technol.*, vol. 34, 2019, Art no. 053001.
[26] Y. Arakawa and M. J. Holmes, "Progress in quantum-dot single photon sources for quantum information technologies: a broad spectrum overview," *Appl. Phys. Rev.*, vol. 7, 2020, Art no. 021309.
[27] M. Anderson, T. Müller, J. Skiba-Szymanska, et al., "Coherence in single photon emission from droplet epitaxy and Stranski-Krastanov quantum dots in the telecom C-band," *Appl. Phys. Lett.*, vol. 118, 2021, Art no. 014003.
[28] P. Holewa, A. Sakanas, U. M. Gür, et al., *Bright Quantum Dot Single-Photon Emitters at Telecom Bands Heterogeneously Integrated on Si*, 2021, arXiv:2104.07589.
[29] M. Gurioli, Z. Wang, A. Rastelli, T. Kuroda, and S. Sanguinetti, "Droplet epitaxy of semiconductor nanostructures for quantum photonic devices," *Nat. Mater.*, vol. 18, p. 799, 2019.
[30] T. Müller, J. Skiba-Szymanska, A. B. Krysa, et al., "A quantum light-emitting diode for the standard telecom window around 1,550 nm," *Nat. Commun.*, vol. 9, p. 862, 2018.
[31] T. Kuroda, T. Mano, N. Ha, et al., "Symmetric quantum dots as efficient sources of highly entangled photons: violation of Bell's inequality without spectral and temporal filtering," *Phys. Rev. B*, vol. 88, 2013, Art no. 041306.
[32] G. Juska, V. Dimastrodonato, L. O. Mereni, A. Gocalinska, and E. Pelucchi, "Towards quantum-dot arrays of entangled photon emitters," *Nat. Photonics*, vol. 7, p. 527, 2013.
[33] X. Liu, N. Ha, H. Nakajima, et al., "Vanishing fine-structure splittings in telecommunication-wavelength quantum dots grown on (111)A surfaces by droplet epitaxy," *Phys. Rev. B*, vol. 90, 2014, Art no. 081301.
[34] N. Ha, T. Mano, Y.-N. Wu, et al., "Wavelength extension beyond 1.5 µm in symmetric InAs quantum dots grown on InP(111)A using droplet epitaxy," *Appl. Phys. Express*, vol. 9, p. 101201, 2016.
[35] A. Schliwa, M. Winkelnkemper, A. Lochmann, E. Stock, and D. Bimberg, "In(Ga)As/GaAs quantum dots grown on a (111) surface as ideal sources of entangled photon pairs," *Phys. Rev. B*, vol. 80, p. 161307, 2009.

[36] I. Ranjbar Jahromi, G. Juska, S. Varo, et al., "Optical properties and symmetry optimization of spectrally (excitonically) uniform site-controlled GaAs pyramidal quantum dots," *Appl. Phys. Lett.*, vol. 118, 2021, Art no. 073103.

[37] Z. M. Wang, K. Holmes, Y. I. Mazur, K. A. Ramsey, and G. J. Salamo, "Self-organization of quantum-dot pairs by high-temperature droplet epitaxy," *Nanoscale Res. Lett.*, vol. 1, p. 57, 2006.

[38] Z. M. Wang, B. L. Liang, K. A. Sablon, and G. J. Salamo, "Nanoholes fabricated by self-assembled gallium nanodrill on GaAs(100)," *Appl. Phys. Lett.*, vol. 90, p. 113120, 2007.

[39] Y. H. Huo, A. Rastelli, and O. G. Schmidt, "Ultra-small excitonic fine structure splitting in highly symmetric quantum dots on GaAs (001) substrate," *Appl. Phys. Lett.*, vol. 102, p. 152105, 2013.

[40] C. Heyn, A. Stemmann, T. Köppen, et al., "Highly uniform and strain-free GaAs quantum dots fabricated by filling of self-assembled nanoholes," *Appl. Phys. Lett.*, vol. 94, p. 183113, 2009.

[41] E. M. Sala, Y. I. Na, M. Godsland, A. Trapalis, and J. Heffernan, "InAs/InP quantum dots in etched pits by droplet epitaxy in metalorganic vapor phase epitaxy," *Phys. Status Solidi RRL*, vol. 14, p. 2000173, 2020.

[42] S. Kadkhodazadeh, "High resolution STEM of quantum dots and quantum wires," *Micron*, vol. 44, p. 75, 2013.

[43] M. González, J. Garcia, L. González, et al., "In situ measurements of As/P exchange during InAs/InP(0 0 1) quantum wires growth," *Appl. Surf. Sci.*, vol. 188, p. 188, 2002.

[44] N. Carlsson, T. Junno, L. Montelius, M.-E. Pistol, L. Samuelson, and W. Seifert, "Growth of self-assembled InAs and InAsxP1−x dots on InP by metalorganic vapour phase epitaxy," *J. Cryst. Growth*, vol. 191, p. 347, 1998.

[45] A. V. Osipov, F. Schmitt, S. A. Kukushkin, and P. Hess, "Stress-driven nucleation of coherent islands: theory and experiment," *Appl. Surf. Sci.*, vol. 188, p. 156, 2002.

[46] V. G. Dubrovskii, G. E. Cirlin, and V. M. Ustinov, "Kinetics of the initial stage of coherent island formation in heteroepitaxial systems," *Phys. Rev. B*, vol. 68, 2003, Art no. 075409.

[47] M. Gawełczyk, M. Syperek, A. Maryński, et al., "Exciton lifetime and emission polarization dispersion in strongly in-plane asymmetric nanostructures," *Phys. Rev. B*, vol. 96, p. 245425, 2017.

[48] M. Abbarchi, C. Mastrandrea, T. Kuroda, et al., "Poissonian statistics of excitonic complexes in quantum dots," *J. Appl. Phys.*, vol. 106, 2009, Art no. 053504.

[49] M. H. Baier, A. Malko, E. Pelucchi, D. Y. Oberli, and E. Kapon, "Quantum-dot exciton dynamics probed by photon-correlation spectroscopy," *Phys. Rev. B*, vol. 73, p. 205321, 2006.

[50] E. Tsitsishvili, "Impact of heavy hole-light hole coupling on the exciton fine structure in quantum dots," *Phys. E Low-dimens. Syst. Nanostruct.*, vol. 87, p. 161, 2017.

[51] R. Ivanov, S. Marcinkevičius, T. K. Uždavinys, L. Y. Kuritzky, S. Nakamura, and J. S. Speck, "Scanning near-field microscopy of carrier lifetimes in m-plane InGaN quantum wells," *Appl. Phys. Lett.*, vol. 110, 2017, Art no. 031109.

[52] A. Musiał, K. Żołnacz, N. Srocka, et al. *Adv. Quantum Technol.*, vol. 3, p. 2000018, 2020.

[53] Ł. Dusanowski, M. Syperek, J. Misiewicz, et al., "Single-photon emission of InAs/InP quantum dashes at 1.55 μm and temperatures up to 80 K," *Appl. Phys. Lett.*, vol. 108, p. 163108, 2016.

[54] P. Michler, A. Imamoğlu, M. D. Mason, P. J. Carson, G. F. Strouse, and S. K. Buratto, "Quantum correlation among photons from a single quantum dot at room temperature," *Nature*, vol. 406, p. 968, 2000.

[55] *FRWRtools Script*, Available at: https://www.physics.hu-berlin.de/en/sem/software [accessed: Jan. 19, 2022].

[56] M. A. Caro, S. Schulz, and E. P. O'Reilly, "Origin of nonlinear piezoelectricity in III−V semiconductors: internal strain and bond ionicity from hybrid-functional density functional theory," *Phys. Rev. B*, vol. 91, 2015, Art no. 075203.

[57] K. Gawarecki, P. Machnikowski, and T. Kuhn, "Electron states in a double quantum dot with broken axial symmetry," *Phys. Rev. B*, vol. 90, 2014, Art no. 085437.

[58] M. G. Burt, "The justification for applying the effective-mass approximation to microstructures," *J. Phys.: Condens. Matter*, vol. 4, p. 6651, 1992.

[59] B. A. Foreman, "Effective-mass Hamiltonian and boundary conditions for the valence bands of semiconductor microstructures," *Phys. Rev. B*, vol. 48, p. 4964, 1993.

[60] K. Gawarecki, "Spin-orbit coupling and magnetic-field dependence of carrier states in a self-assembled quantum dot," *Phys. Rev. B*, vol. 97, p. 235408, 2018.

[61] A. Thränhardt, C. Ell, G. Khitrova, and H. M. Gibbs, "Relation between dipole moment and radiative lifetime in interface fluctuation quantum dots," *Phys. Rev. B*, vol. 65, 2002, Art no. 035327.

Supplementary Material: The online version of this article offers supplementary material (https://doi.org/10.1515/nanoph-2021-0482).

ARTICLE 4

Bright quantum dot single-photon emitters heterogeneously integrated on Si

ACS Photonics

pubs.acs.org/journal/apchd5 Article

Bright Quantum Dot Single-Photon Emitters at Telecom Bands Heterogeneously Integrated on Si

Paweł Holewa,* Aurimas Sakanas, Ugur M. Gür, Paweł Mrowiński, Alexander Huck, Bi-Ying Wang, Anna Musiał, Kresten Yvind, Niels Gregersen, Marcin Syperek,* and Elizaveta Semenova*

Cite This: *ACS Photonics* 2022, 9, 2273−2279 Read Online

ACCESS | Metrics & More | Article Recommendations | Supporting Information

ABSTRACT: Whereas the Si photonic platform is highly attractive for scalable optical quantum information processing, it lacks practical solutions for efficient photon generation. Self-assembled semiconductor quantum dots (QDs) efficiently emit photons in the telecom bands (1460−1625 nm) and allow for heterogeneous integration with Si. In this work, we report on a novel, robust, and industry-compatible approach for achieving single-photon emission from InAs/InP QDs heterogeneously integrated with a Si substrate. As a proof of concept, we demonstrate a simple vertical emitting device, employing a metallic mirror beneath the QD emitter, and experimentally obtained photon extraction efficiencies of ∼10%. Nevertheless, the figures of merit of our structures are comparable with values previously only achieved for QDs emitting at shorter wavelength or by applying technically demanding fabrication processes. Our architecture and the simple fabrication procedure allows for the demonstration of high-purity single-photon generation with a second-order correlation function at zero time delay, $g^{(2)}(\tau = 0) < 0.02$, without any corrections at continuous wave excitation at the liquid helium temperature and preserved up to 50 K. For pulsed excitation, we achieve the as-measured $g^{(2)}(0)$ down to 0.205 ± 0.020 (0.114 ± 0.020 with background coincidences subtracted).

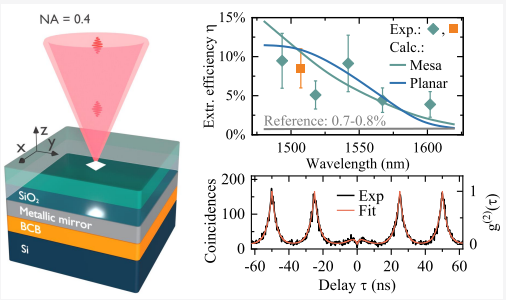

KEYWORDS: *semiconductor quantum dots, InAs/InP, heterogeneous integration, telecom spectral range, single-photon sources, photon extraction efficiency*

INTRODUCTION

Exploiting single photons as a resource is a powerful approach for quantum information processing (QIP).[1−4] Photons have long coherences and efficiently propagate over macroscopic distances, which enabled the demonstration of a computational advantage with a quantum photonic processor,[5] loophole-free tests of Bell's theorem,[6,7] and long-distance quantum key distribution.[8,9] Scalability of optical QIP requires the miniaturization, coupling, and integration of active and passive photonic components into quantum photonic integrated circuits (QPICs).[10] The Si-based photonic platform is a leading candidate for integration with transparency wavelengths greater than 1.1 μm and mature manufacturing processes.[4,11] QPICs supporting multidimensional entanglement[11] and quantum processors with hundreds of elements[11,12] have been demonstrated. Si however does not allow for efficient light generation. Spontaneous four-wave mixing is the commonly employed approach for single-photon generation on Si and realized with Si-on-insulator integration.[11−13] This process is probabilistic with few-percent efficiency,[10] thus limiting scalability. Hybrid approaches combining solid-state single-photon emitters (SPEs) with Si have instead been investigated,[14] but so far requiring technically demanding fabrication. The reliable realization of SPEs monolithically integrated with Si and allowing for the deterministic emission of pure single photons remains challenging.

Among different candidates,[15,16] epitaxially grown self-assembled semiconductor quantum dots (QDs)[17] emitting in the long-wavelength telecom bands (1460−1625 nm)[18] are suitable for integration with Si.[11,19,20] The telecom wavelength promises very low Si-waveguide propagation losses[19] and allows for interconnecting distant QIPCs using optical fiber networks and for distributed quantum computing.[21,22] Photon emission in the telecom bands has been achieved with QDs based on either InAs/GaAs[23−27] or InAs/InP[28−36] material composition, and excellent quantum light sources with high purity[29] were demonstrated, fulfilling the requirements for QIP.[17,18,37]

Received: January 5, 2022
Published: June 22, 2022

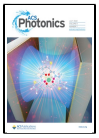

https://doi.org/10.1021/acsphotonics.2c00027
ACS Photonics 2022, 9, 2273−2279

ACS Photonics pubs.acs.org/journal/apchd5 Article

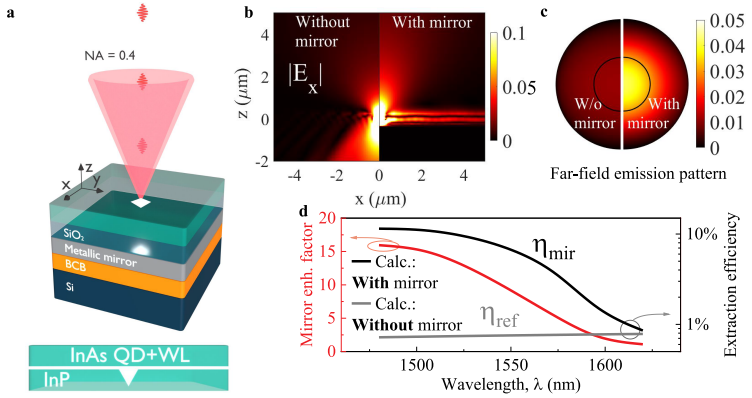

Figure 1. Design of our structures and theoretically estimated performance. (a) Investigated structure scheme, consisting of InAs/InP quantum dots (QDs) with a metallic reflector integrated on a Si substrate. WL, wetting layer. (b) The electric field component $|E_x|$ for λ = 1550 nm for the structure without (left) and with (right) a metallic reflector made of aluminum (Al). (c) Calculated far field emission ($P_{lens,NA}$) for the reference (left) and the device with an Al mirror (right). The half-circle marks the collection cone of a 0.4 NA objective. (d) Calculated broadband mirror enhancement factor (left axis) and photon extraction efficiency for the QD device with a mirror (η_{mir}) and the reference structure without a mirror (η_{ref}) as a function of emitter wavelength.

The photon extraction efficiency η for as-grown QD-based SPEs is typically <1%[17] due to the large semiconductor−air refractive index contrast, but can be increased by tailoring the local optical environment.[38−40] Common approaches for increasing η include placing a QD in a monolithic cavity defined by distributed Bragg reflectors (DBRs),[33] in an optical horn structure,[28] or atop a single DBR reflector.[24,25,31,41] DBR-based approaches are scalable and η up to 13% was achieved in a narrow spectral window,[41] following demanding fabrication in the InAs/InP material system due to the layers' low refractive index contrast. With the horn structure, $\eta \approx 11\%$ at 1560 nm (numerical aperture NA = 0.55) was shown,[28] requiring complex fabrication. These approaches however are not suitable for the monolithic integration of QD-based SPEs with Si.

In this work, we propose and demonstrate efficient single-photon emission with $\eta > 10\%$ (NA = 0.4) and wavelength in the telecom bands. Our photon sources are based on InAs QDs epitaxially grown on InP and heterogeneously integrated on a Si substrate via chemical bonding. We achieve triggered single-photon emission with $g^{(2)}(0) < 0.02$ up to 50 K. A further increase of η is possible employing a higher NA objective and tailoring the QD optical environment. Our approach promises localizing individual QDs via optical imaging[42] and subsequent processing of photonic components with deterministic spatial alignment. Moreover, our QD integration method on the Si platform provides a broad range of device architecture possibilities, in particular the in-plane emission into planar waveguides as required for on-chip integration.

RESULTS

Structure Design. The schematic design of our structures together with calculated device performances are presented in Figure 1. Self-assembled InAs QDs are placed in a weak planar cavity system formed between a bottom metallic mirror and a top InP/air interface, as illustrated in Figure 1a. We determine the achievable photon extraction efficiency using numerical simulations of the electromagnetic (EM) field (Figure 1a) generated by the InAs QD modeled as a classical point dipole with in-plane dipole orientation. The EM field distribution ($|E_x|$) is presented in Figure 1b for a reference structure (as-grown InAs/InP QDs) without (left panel) and with a metal mirror (right panel). We observe that the effect of the mirror is to suppress leakage of light into the substrate and instead direct light in the vertical direction. While additional in-plane guiding of light in the slab waveguide formed by the air−semiconductor−metal interfaces is visible, the out-of-plane field pattern is significantly enhanced compared to the structure without a reflector. Furthermore, the enhancement is observed in the far field emission pattern presented in Figure 1c, highlighting the role of the metallic mirror for the directional emission. The black circle represents the collection aperture of a typical, long-working-distance microscope objective with a 0.4 NA used for light collection in the experiment, and the extraction efficiency η is then defined as the ratio of the power collected within the NA of the objective ($P_{lens,NA}$) to the total power emitted by the dipole. The computed extraction efficiency is presented in Figure 1d as a function of wavelength. We define the mirror enhancement factor as the ratio between the extraction efficiency for the planar structure with a mirror (η_{mir}) and the reference structure (η_{ref}). The presence of the metallic reflector leads to a broadband enhancement of the extraction efficiency (left axis), with the 9.2-fold increase at 1550 nm and $\eta \approx 7\%$ and nearly 16-fold increase at 1500 nm and $\eta \approx 11\%$. This expected performance is competitive with state-of-the-art extraction efficiencies[28,41] for single-photon sources operating in the long-wavelength telecom bands.

The device fabrication begins with the epitaxy of an InGaAs sacrificial layer lattice-matched to a standard (001)-oriented InP substrate, followed by the growth of an InP λ−cavity with an array of low surface density ($\sim 2.8 \times 10^9$ cm^{-2}) InAs QDs placed in the center for quantum confinement. In the next step, the top InP surface is covered by 100 nm of SiO_2 followed by a 100-nm-thick metallic reflector (Al in our case). Subsequently, the chip is flipped and bonded to a Si substrate using benzocyclobutene (BCB), and finally, the thick InP substrate,

https://doi.org/10.1021/acsphotonics.2c00027
ACS Photonics 2022, 9, 2273−2279

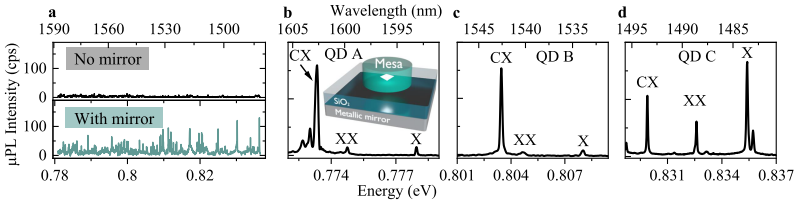

Figure 2. Excitonic complexes in InAs/InP QDs. (a) Representative high spatially resolved photoluminescence (μPL) spectra recorded for the reference structure without a mirror (top panel) and the structure with a mirror (bottom panel) with identical pulsed laser excitation at T = 4.2 K. (b–d) μPL spectra of the investigated InAs/InP QDs (labeled A, B, and C) with identified excitonic emission complexes: neutral exciton (X), biexciton (XX), and charged exciton (CX). Inset in (b): mesa structure.

now on top, and the InGaAs sacrificial layer are removed. We emphasize that this approach and the dimensions are suitable for in-plane photon emission into a Si photonic circuit, although not explicitly pursued in this work.

We applied a 2-fold experimental evaluation strategy to verify the significant robustness of the structure design with respect to the level of η and the related broadband performance and to present bright SPEs heterogeneously integrated on a Si substrate. In Figure 2a, we present typical emission spectra obtained from a reference structure without a metallic reflector and the planar structure containing the metallic mirror, both recorded with the same high spatial resolution photoluminescence setup (μPL) from a diffraction-limited spot. The spectra consist of multiple sharp emission lines distributed over a broad spectral range, originating from QDs of mainly different sizes within the optical excitation spot and various emission complexes including neutral exciton (X), charged exciton (CX), and biexciton (XX) transitions. For the structure containing the mirror and compared to the reference structure, we observe a clear intensity enhancement of the emission lines. The quantitative analysis of photon extraction efficiency η from SPEs requires the isolation of single QDs and identification of their respective spectral features. We therefore proceeded with the processing of the mirror-containing planar structure to fabricate cylindrical mesas with diameters of D_1 = 2 μm and D_2 = 3 μm, respectively, as schematically illustrated in the inset of Figure 2b. The finite size of the mesas allows for the spatial isolation of single QDs, a vital element in single-photon source engineering, and leads to modifications of the calculated EM field pattern and extraction efficiencies. In Figures 2b–2d, we present the μPL spectra of three representative and isolated QD emitters, which in the following we refer to as QD A, B, and C, with their emission spectrum located in the telecom L-, C-, and S-band, respectively. The indicated excitonic complexes (X, CX, XX) are identified based on a series of excitation power-dependent and polarization-resolved μPL measurements and confirmed by the cross-correlation of the XX–X and CX–X complexes.

Brightness of SPEs. We employ two approaches to compare the calculated with the experimentally obtained photon extraction efficiency η. In the first approach, we consider the broadband enhancement of the photon extraction for planar structures due to the mirror. The approach is based on the statistical analysis of correlated and uncorrelated emission processes, from where we derive a rough estimate of η. We thus compare the intensity of nearly 50 spectral lines recorded from the mirror-containing and the reference structure, respectively, and the results are plotted in Figure 3a. The spectrally averaged enhancement factor of $7.4^{+1.6}_{-1.3}$ is

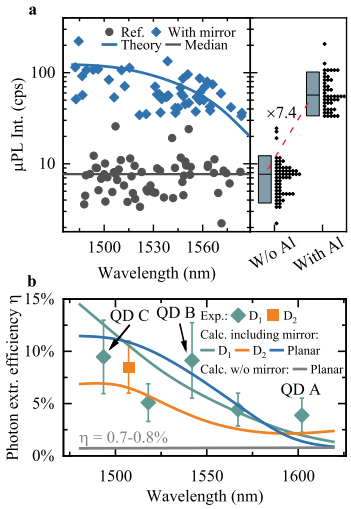

Figure 3. Photon extraction efficiency for the investigated structures. (a) Left panel: comparison of the μPL intensity of ~50 of the brightest emission lines (points) for the planar mirror-containing (blue diamonds) and the reference (black circles) structures, respectively. The solid blue line is the expected μPL intensity for the mirror-containing structure obtained by multiplying the median μPL intensity of the reference structure (solid black line) by the mirror enhancement factor (cf. red line in Figure 1d). Right panel: statistical analysis of measured intensities. Boxes illustrate one standard deviation; the line inside the box is the median value of each distribution shown as points. (b) Photon extraction efficiency η for the mesa-processed structure with a metallic mirror. Green diamonds show recorded η values for mesas with D_1 = 2 μm including QDs A–C. The result shown as an orange square is obtained for an emitter in a mesa with D_2 = 3 μm. The solid lines represent calculated η values obtained with the modal method for mesas with D_1 = 2 μm (green) and D_2 = 3 μm (orange). Solid blue and gray lines show the calculated η for a planar structure with a mirror and a reference structure without a mirror, respectively.

obtained by comparing the median values for the distributions of emission intensity, which can be converted to a mean photon extraction efficiency $\eta \approx 6\%$ for the device containing the metallic mirror. The 95% confidence levels for the enhancement factor are calculated according to ref 43. In the second approach, we adopt the method described by M. Gschrey et al.[44] and directly measure η for individual QDs in mesa-processed structures. The results for η from in total six QDs (including QDs A–C) are presented in Figure 3b

https://doi.org/10.1021/acsphotonics.2c00027
ACS Photonics 2022, 9, 2273–2279

ACS Photonics pubs.acs.org/journal/apchd5 Article

together with the numerically calculated values. For these mesa structures, we experimentally determine photon extraction efficiencies η above 4.4% and as high as η_B = 9.1% and η_C = 9.5% for QDs B and C, respectively. Those values demonstrate a 1 order of magnitude improvement compared to the efficiency of 0.7−0.8% estimated for the reference structure without the metallic mirror. Importantly, we obtain good agreement between the experimentally determined extraction efficiency and the theoretical prediction, for both the broadband approach (Figure 3a) and the individually investigated six QDs in mesas (Figure 3b). We attribute the small deviations between simulation and experimental values to possible nonradiative recombination channels in the QD vicinity, changes in the mesa geometry due to fabrication imperfections, and nondeterministic positioning of the QD within the mesa. These effects generally result in a lower recorded photon flux compared to the theoretical prediction, as well as in a limited probability of finding a mesa characterized by the η value as high as presented in Figure 3b in our sample. Additionally, we note that a ∼200 nm displacement of a QD from the mesa center results in an increase in the extraction efficiency as compared to a QD placed in the center. Such a displacement may explain the high η value obtained for QD B.

Evaluation of the Photon Purity. The order of magnitude improvement in photon extraction efficiency from InAs/InP QDs renders our structures an attractive source of single photons heterogeneously integrated with the Si platform. We evaluate in the following the quality of single-photon emission from the QDs in mesa structures by investigating the purity of single photons emitted from QDs A−C. For that purpose, we recorded the second-order correlation function $g^{(2)}(\tau)$ exploiting off-resonant continuous wave (cw) and pulsed excitation schemes, and the obtained histograms without normalization are presented in Figure 4. For pulsed excitation (Figure 4a), we observe that the coincidences $\tau \approx 0$ are strongly suppressed compared to the coincidence peaks at multiples of the inverse laser repetition rate (τ_0 = 25 ns). Furthermore, we record a significant dip in the histogram counts at short time delays $|\tau| < 5$ ns (insets to Figure 4a). This feature indicates the capture of more than one carrier by the QD and cascaded photon emission within a single excitation, effectively resulting in multiphoton events[45] within $|\tau| < 5$ ns. We explain this observation with the off-resonant excitation scheme applied in our experiment, where a substantial amount of carriers are excited and trapped in the wetting layer or in other charge trap states.[45−47] After release, those carriers are captured by the QD within the characteristic capture time τ_{cap} and produce secondary photons[48] via exciton recombination with the time constant τ_{dec}.

We fit the correlation histograms obtained with pulsed laser excitation with the function[29,49]

$$C(\tau) = B + A[\exp(-|\tau|/\tau_{dec}) - \exp(-|\tau|/\tau_{cap})] + H\sum_{n\neq 0}\exp(-|\tau - n\tau_0|/\tau_{dec}) \quad (1)$$

where B is the level of background coincidences, A is a scaling parameter related to secondary photon emission, $n \neq 0$ is the peak number, and H is the average height of the peaks at $\tau_n = n\tau_0$. The second-order correlation function $g^{(2)}(\tau)$ is then obtained by normalizing $C(\tau)$ with H. Evaluating $g^{(2)}(\tau)$ at τ = 0, we obtain $g^{(2)}(0)$ values of 0.023 ± 0.010, 0.087 ± 0.017, and 0.018 ± 0.012 for QDs A−C, respectively. This estimation ignores coincidences produced by secondary photon emission events, which may be avoided asymptotically employing an on-resonance excitation scheme. Comparing the integrated peak area of $g^{(2)}(\tau = 0)$ with the average peak area at τ_n, as it is relevant for applications of our single-photon sources in QIP, yields values for $g^{(2)}(0)_{area}$ of 0.371 ± 0.020, 0.433 ± 0.018, and 0.205 ± 0.020 for QDs A−C, respectively (see the SI). Detector dark counts and uncorrelated photons also contribute to the registered histograms, where they cause a buildup of a time-independent level of coincidences B. We estimate this influence using eq 1 and calculate the $g^{(2)}(0)_{area,cor}$ values that can be associated with coincidences caused only by the QD signal. By doing so, we obtain values of $g^{(2)}(0)_{area,cor}$ = 0.276 ± 0.002, 0.209 ± 0.018, and 0.114 ± 0.020 for QDs A−C. The emission purity recorded in the pulsed regime is mainly limited by the capture of secondary carriers and subsequent photon emission. We note that the data are well described by our model and do not consider the capture of secondary carriers at τ_n. Furthermore, with the modeling routine we determine τ_{dec} in the range 1.9−2.8 ns, which is in accordance with the CX decay time measured in time-resolved μPL (see the SI). Importantly, the obtained single-photon purity of the investigated structures is very robust for a wide range of temperatures and excitation powers. In Figure 4b,c we present

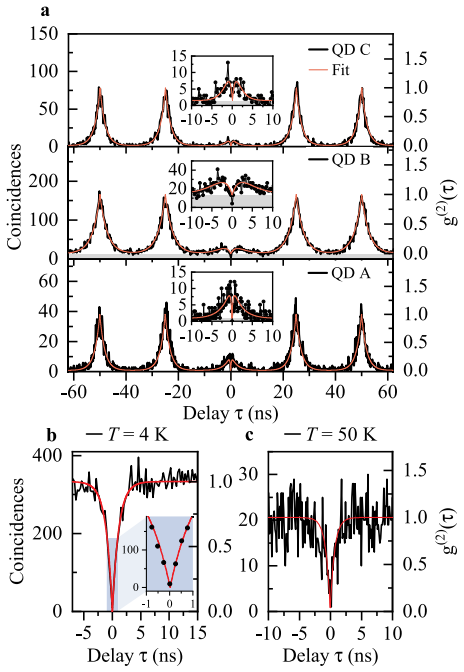

Figure 4. Autocorrelation histograms for CX lines. (a) Triggered single-photon emission for investigated QDs: C (top), B (center), A (bottom). Insets: Close-ups of the histograms showing coincidences around zero delay. (b, c) Single-photon emission under cw excitation for the CX in QD B, recorded (b) under the laser excitation power corresponding to the saturation of the CX μPL intensity (inset: zoom around τ = 0), and (c) at T = 50 K. Red lines are fits to the experimental data. Gray area in (a) shows the level of background coincidences B obtained by the fit with eq 1.

https://doi.org/10.1021/acsphotonics.2c00027
ACS Photonics 2022, 9, 2273−2279

correlation histograms recorded in cw excitation mode from the CX line of QD B at sample temperatures of 4 and 50 K, respectively, while optically pumping at the saturation power P_{sat} (see the SI for correlation histograms taken at T = 30 and 80 K, at 0.3 × P_{sat} and 0.7 × P_{sat}, and for the summary of the obtained $g^{(2)}(0)$ values). We fitted the normalized histograms recorded in cw mode with a standard single-exponential function[50] (see the SI) to extract the single-photon emission purity from the measurements. The raw data estimated $g^{(2)}(0)_{raw}$ value from the histogram recorded at P_{sat} and at T = 4.2 K is $g^{(2)}(0)_{raw} = 0.027^{+0.011}_{-0.027}$ (see the SI) limited by the finite time resolution of our setup. The best fit to our data thus suggests even higher values of photon purity with $g^{(2)}(0)_{fit} = 0$, with a standard error σ = 0.038, and without background correction. Such high purity of the single-photon flux in the high-excitation power regime ($P \geq P_{sat}$) has previously been observed only for InAs/GaAs QDs emitting at λ = (910−920 nm).[38,44] In contrast to these sources, the structure investigated here demonstrates high brightness and close-to-ideal single-photon purity while emitting in the telecom C-band. At 50 K sample temperature, which easily can be reached with a cryogen-free Stirling cooler,[27] a significant feature at τ = 0 is visible in the histogram, quantifying the robustness of this source of single photons. Although the emission line visibility is reduced at this temperature (see the SI for the analysis of temperature-dependent μPL of QD B), we obtain a high purity of single-photon emission with the fitted value of $g^{(2)}(0)_{fit,50\ K} = 0.017$ (σ = 0.096, without background correction; see also the SI for the histogram recorded at T = 80 K with $g^{(2)}(0) < 0.5$).

CONCLUSIONS

The demonstrated design of the structure with InAs/InP QDs on a metallic mirror integrated on a Si substrate paves the way toward a simplified, small-footprint, cost-effective, and scalable manufacturing process of triggered single-photon emitters operating in the telecom S-, C-, and L-bands, suitable for Si-based on-chip photonic quantum information processing. The spectral range of the InAs/InP single-photon emitters investigated here eliminates the necessity for frequency conversion to the telecom bands, potentially allowing for the implementation of distributed schemes for information processing and computation using low-loss fiber-based optical networks. Combining the robust design of our structures and the manufacturing process compatible with the existing industry standards establishes single-photon sources with high photon extraction efficiency in the broader telecom spectral range, with performance properties comparable to the DBR-based solutions but with significantly reduced fabrication-related technological demands.

The presented robust architecture, offering spectrally broad high photon extraction efficiency, is beneficial for further processing steps tailoring the photonic environment of a deterministically localized emitter. The high emitter brightness allows for its fast spatial positioning utilizing the emission imaging method successfully employed for short-wavelength (<1000 nm) QDs.[42] However, at telecom wavelengths, the imaging relies on 2D state-of-the-art InGaAs-based matrices with yet poor efficiencies and high noise levels compared to Si-based arrays desired for shorter wavelengths. Therefore, the simplified architecture of a QD on a metal mirror can open the route toward fabrication of fully deterministic, scalable QPICs at telecom wavelengths.

ASSOCIATED CONTENT

Supporting Information

The Supporting Information is available free of charge at https://pubs.acs.org/doi/10.1021/acsphotonics.2c00027.

Description of methods, extended data for optical characterization of the device, numerical simulations, and evaluation of single-photon purity (PDF)

AUTHOR INFORMATION

Corresponding Authors

Paweł Holewa − *Laboratory for Optical Spectroscopy of Nanostructures, Faculty of Fundamental Problems of Technology, Department of Experimental Physics, Wrocław University of Science and Technology, 50-370 Wrocław, Poland; DTU Fotonik, Technical University of Denmark, Lyngby 2800, Denmark;* orcid.org/0000-0002-2154-896X; Email: pawel.holewa@pwr.edu.pl

Marcin Syperek − *Laboratory for Optical Spectroscopy of Nanostructures, Faculty of Fundamental Problems of Technology, Department of Experimental Physics, Wrocław University of Science and Technology, 50-370 Wrocław, Poland;* orcid.org/0000-0002-5260-7360; Email: marcin.syperek@pwr.edu.pl

Elizaveta Semenova − *DTU Fotonik, Technical University of Denmark, Lyngby 2800, Denmark; NanoPhoton-Center for Nanophotonics, Technical University of Denmark, Lyngby 2800, Denmark;* orcid.org/0000-0002-5856-4461; Email: esem@fotonik.dtu.dk

Authors

Aurimas Sakanas − *DTU Fotonik, Technical University of Denmark, Lyngby 2800, Denmark;* orcid.org/0000-0001-5155-5557

Ugur M. Gür − *DTU Electrical Engineering, Technical University of Denmark, Lyngby 2800, Denmark*

Paweł Mrowiński − *Laboratory for Optical Spectroscopy of Nanostructures, Faculty of Fundamental Problems of Technology, Department of Experimental Physics, Wrocław University of Science and Technology, 50-370 Wrocław, Poland;* orcid.org/0000-0001-9931-7523

Alexander Huck − *Center for Macroscopic Quantum States (bigQ), Department of Physics, Technical University of Denmark, Lyngby 2800, Denmark;* orcid.org/0000-0002-2354-5922

Bi-Ying Wang − *Hefei National Laboratory for Physical Sciences at Microscale, University of Science and Technology of China, Hefei, Anhui 230026, China; DTU Fotonik, Technical University of Denmark, Lyngby 2800, Denmark;* orcid.org/0000-0003-1325-3261

Anna Musiał − *Laboratory for Optical Spectroscopy of Nanostructures, Faculty of Fundamental Problems of Technology, Department of Experimental Physics, Wrocław University of Science and Technology, 50-370 Wrocław, Poland;* orcid.org/0000-0001-9602-8929

Kresten Yvind − *DTU Fotonik, Technical University of Denmark, Lyngby 2800, Denmark; NanoPhoton-Center for Nanophotonics, Technical University of Denmark, Lyngby 2800, Denmark;* orcid.org/0000-0001-8013-1606

Niels Gregersen − *DTU Fotonik, Technical University of Denmark, Lyngby 2800, Denmark;* orcid.org/0000-0002-8252-8989

Complete contact information is available at:

https://doi.org/10.1021/acsphotonics.2c00027
ACS Photonics 2022, 9, 2273−2279

ACS Photonics pubs.acs.org/journal/apchd5 Article

https://pubs.acs.org/10.1021/acsphotonics.2c00027

Notes

The authors declare no competing financial interest.

■ ACKNOWLEDGMENTS

We acknowledge financial support from the Danish National Research Foundation via the Research Centers of Excellence NanoPhoton (DNRF147) and the Center for Macroscopic Quantum States bigQ (DNRF142). P.H. was funded by the Polish National Science Center within the Etiuda 8 scholarship (Grant No. 2020/36/T/ST5/00511) and by the European Union under the European Social Fund. P.M. acknowledges the financial support from the Polish National Science Center (Grant No. 2020/39/D/ST5/02952). N.G. acknowledges support from the European Research Council (ERC-CoG "UNITY", Grant No. 865230) and from the Independent Research Fund Denmark (Grant No. DFF-9041-00046B).

■ REFERENCES

(1) Knill, E.; Laflamme, R.; Milburn, G. J. A scheme for efficient quantum computation with linear optics. *Nature* **2001**, *409*, 46−52.
(2) Kok, P.; Munro, W. J.; Nemoto, K.; Ralph, T. C.; Dowling, J. P.; Milburn, G. J. Linear optical quantum computing with photonic qubits. *Rev. Mod. Phys.* **2007**, *79*, 135−174.
(3) Wang, Z. M.; Qin, J.; Ding, Y.; Chen, Z.-s.; You, X.; He, Y. M.; Jiang, X.; You, L.; Schneider, C.; Renema, J. J.; Höfling, S.; Lu, C. Y.; Pan, J. W. Boson Sampling with 20 Input Photons and a 60-Mode Interferometer in a 1014 -Dimensional Hilbert Space. *Phys. Rev. Lett.* **2019**, *123*, 250503.
(4) Elshaari, A. W.; Pernice, W.; Srinivasan, K.; Benson, O.; Zwiller, V. Hybrid integrated quantum photonic circuits. *Nat. Photonics* **2020**, *14*, 285−298.
(5) Zhong, H.-S.; et al. Quantum computational advantage using photons. *Science* **2020**, *370*, 1460−1463.
(6) Shalm, L. K.; et al. Strong Loophole-Free Test of Local Realism. *Phys. Rev. Lett.* **2015**, *115*, 250402.
(7) Giustina, M.; et al. Significant-Loophole-Free Test of Bell's Theorem with Entangled Photons. *Phys. Rev. Lett.* **2015**, *115*, 250401.
(8) Takemoto, K.; Nambu, Y.; Miyazawa, T.; Sakuma, Y.; Yamamoto, T.; Yorozu, S.; Arakawa, Y. Quantum key distribution over 120 km using ultrahigh purity single-photon source and superconducting single-photon detectors. *Sci. Rep.* **2015**, *5*, 14383.
(9) Yin, J.; et al. Entanglement-based secure quantum cryptography over 1,120 kilometres. *Nature* **2020**, *582*, 501−505.
(10) Wang, J.; Sciarrino, F.; Laing, A.; Thompson, M. G. Integrated photonic quantum technologies. *Nat. Photonics* **2020**, *14*, 273−284.
(11) Wang, J.; et al. Multidimensional quantum entanglement with large-scale integrated optics. *Science* **2018**, *360*, 285−291.
(12) Qiang, X.; Zhou, X.; Wang, J.; Wilkes, C. M.; Loke, T.; O'Gara, S.; Kling, L.; Marshall, G. D.; Santagati, R.; Ralph, T. C.; Wang, J. B.; O'Brien, J. L.; Thompson, M. G.; Matthews, J. C. F. Large-scale silicon quantum photonics implementing arbitrary two-qubit processing. *Nat. Photonics* **2018**, *12*, 534−539.
(13) Paesani, S.; Ding, Y.; Santagati, R.; Chakhmakhchyan, L.; Vigliar, C.; Rottwitt, K.; Oxenløwe, L. K.; Wang, J.; Thompson, M. G.; Laing, A. Generation and sampling of quantum states of light in a silicon chip. *Nat. Phys.* **2019**, *15*, 925−929.
(14) Kim, J.-H.; Aghaeimeibodi, S.; Richardson, C. J. K.; Leavitt, R. P.; Englund, D.; Waks, E. Hybrid Integration of Solid-State Quantum Emitters on a Silicon Photonic Chip. *Nano Lett.* **2017**, *17*, 7394−7400.
(15) Eisaman, M. D.; Fan, J.; Migdall, A.; Polyakov, S. V. Invited Review Article: Single-photon sources and detectors. *Rev. Sci. Instrum.* **2011**, *82*, 071101.
(16) Aharonovich, I.; Englund, D.; Toth, M. Solid-state single-photon emitters. *Nat. Photonics* **2016**, *10*, 631−641.
(17) Senellart, P.; Solomon, G.; White, A. High-performance semiconductor quantum-dot single-photon sources. *Nat. Nanotechnol.* **2017**, *12*, 1026−1039.
(18) Arakawa, Y.; Holmes, M. J. Progress in quantum-dot single photon sources for quantum information technologies: A broad spectrum overview. *Appl. Phys. Rev.* **2020**, *7*, 021309.
(19) Tran, M. A.; Huang, D.; Komljenovic, T.; Peters, J.; Malik, A.; Bowers, J. E. Ultra-Low-Loss Silicon Waveguides for Heterogeneously Integrated Silicon/III-V Photonics. *Appl. Sci.* **2018**, *8*, 1139.
(20) Vlasov, Y. A.; McNab, S. J. Losses in single-mode silicon-on-insulator strip waveguides and bends. *Opt. Express* **2004**, *12*, 1622.
(21) Wehner, S.; Elkouss, D.; Hanson, R. Quantum internet: A vision for the road ahead. *Science* **2018**, *362*, No. eaam9288.
(22) Cuomo, D.; Caleffi, M.; Cacciapuoti, A. S. Towards a distributed quantum computing ecosystem. *IET Quantum Communication* **2020**, *1*, 3−8.
(23) Semenova, E. S.; Hostein, R.; Patriarche, G.; Mauguin, O.; Largeau, L.; Robert-Philip, I.; Beveratos, A.; Lemaître, A. Metamorphic approach to single quantum dot emission at 1.55 μm on GaAs substrate. *J. Appl. Phys.* **2008**, *103*, 103533.
(24) Paul, M.; Olbrich, F.; Höschele, J.; Schreier, S.; Kettler, J.; Portalupi, S. L.; Jetter, M.; Michler, P. Single-photon emission at 1.55 μm from MOVPE-grown InAs quantum dots on InGaAs/GaAs metamorphic buffers. *Appl. Phys. Lett.* **2017**, *111*, 033102.
(25) Zeuner, K. D.; Jöns, K. D.; Schweickert, L.; Hedlund, C. R.; Lobato, C. N.; Lettner, T.; Wang, K.; Gyger, S.; Schöll, E.; Steinhauer, S.; Hammar, M.; Zwiller, V. On-Demand Generation of Entangled Photon Pairs in the Telecom C-Band with InAs Quantum Dots. *ACS Photonics* **2021**, *8*, 2337−2344.
(26) Nawrath, C.; Olbrich, F.; Paul, M.; Portalupi, S. L.; Jetter, M.; Michler, P. Coherence and indistinguishability of highly pure single photons from non-resonantly and resonantly excited telecom C-band quantum dots. *Appl. Phys. Lett.* **2019**, *115*, 023103.
(27) Musiał, A.; et al. Plug&Play Fiber-Coupled 73 kHz Single-Photon Source Operating in the Telecom O-Band. *Adv. Quantum Technol.* **2020**, *3*, 2000018.
(28) Takemoto, K.; Takatsu, M.; Hirose, S.; Yokoyama, N.; Sakuma, Y.; Usuki, T.; Miyazawa, T.; Arakawa, Y. An optical horn structure for single-photon source using quantum dots at telecommunication wavelength. *J. Appl. Phys.* **2007**, *101*, 081720.
(29) Miyazawa, T.; Takemoto, K.; Nambu, Y.; Miki, S.; Yamashita, T.; Terai, H.; Fujiwara, M.; Sasaki, M.; Sakuma, Y.; Takatsu, M.; Yamamoto, T.; Arakawa, Y. Single-photon emission at 1.5 μm from an InAs/InP quantum dot with highly suppressed multi-photon emission probabilities. *Appl. Phys. Lett.* **2016**, *109*, 132106.
(30) Birowosuto, M. D.; Sumikura, H.; Matsuo, S.; Taniyama, H.; van Veldhoven, P. J.; Nötzel, R.; Notomi, M. Fast Purcell-enhanced single photon source in 1,550-nm telecom band from a resonant quantum dot-cavity coupling. *Sci. Rep.* **2012**, *2*, 321.
(31) Benyoucef, M.; Yacob, M.; Reithmaier, J. P.; Kettler, J.; Michler, P. Telecom-wavelength (1.5 μm) single-photon emission from InP-based quantum dots. *Appl. Phys. Lett.* **2013**, *103*, 162101.
(32) Skiba-Szymanska, J.; Stevenson, R. M.; Varnava, C.; Felle, M.; Huwer, J.; Müller, T.; Bennett, A. J.; Lee, J. P.; Farrer, I.; Krysa, A. B.; Spencer, P.; Goff, L. E.; Ritchie, D. A.; Heffernan, J.; Shields, A. J. Universal Growth Scheme for Quantum Dots with Low Fine-Structure Splitting at Various Emission Wavelengths. *Phys. Rev. Appl.* **2017**, *8*, 014013.
(33) Müller, T.; Skiba-Szymanska, J.; Krysa, A. B.; Huwer, J.; Felle, M.; Anderson, M.; Stevenson, R. M.; Heffernan, J.; Ritchie, D. A.; Shields, A. J. A quantum light-emitting diode for the standard telecom window around 1,550 nm. *Nat. Commun.* **2018**, *9*, 862.
(34) Anderson, M.; Müller, T.; Huwer, J.; Skiba-Szymanska, J.; Krysa, A. B.; Stevenson, R. M.; Heffernan, J.; Ritchie, D. A.; Shields, A. J. Quantum teleportation using highly coherent emission from telecom C-band quantum dots. *npj Quantum Inf* **2020**, *6*, 14.
(35) Anderson, M.; Müller, T.; Skiba-Szymanska, J.; Krysa, A. B.; Huwer, J.; Stevenson, R. M.; Heffernan, J.; Ritchie, D. A.; Shields, A. J. Gigahertz-Clocked Teleportation of Time-Bin Qubits with a

Quantum Dot in the Telecommunication C Band. *Phys. Rev. Appl.* **2020**, *13*, 1.
(36) Holewa, P.; Gawełczyk, M.; Ciostek, C.; Wyborski, P.; Kadkhodazadeh, S.; Semenova, E.; Syperek, M. Optical and electronic properties of low-density InAs/InP quantum-dot-like structures designed for single-photon emitters at telecom wavelengths. *Phys. Rev. B* **2020**, *101*, 195304.
(37) Cao, X.; Zopf, M.; Ding, F. Telecom wavelength single photon sources. *J. Semicond.* **2019**, *40*, 071901.
(38) Claudon, J.; Bleuse, J.; Malik, N. S.; Bazin, M.; Jaffrennou, P.; Gregersen, N.; Sauvan, C.; Lalanne, P.; Gérard, J.-M. A highly efficient single-photon source based on a quantum dot in a photonic nanowire. *Nat. Photonics* **2010**, *4*, 174−177.
(39) Stepanov, P.; Delga, A.; Gregersen, N.; Peinke, E.; Munsch, M.; Teissier, J.; Mørk, J.; Richard, M.; Bleuse, J.; Gerard, J.-M.; Claudon, J.; et al. Highly directive and Gaussian far-field emission from "giant" photonic trumpets. *Appl. Phys. Lett.* **2015**, *107*, 141106.
(40) Liu, J.; Su, R.; Wei, Y.; Yao, B.; da Silva, S. F. C.; Yu, Y.; Iles-Smith, J.; Srinivasan, K.; Rastelli, A.; Li, J.; Wang, X. A solid-state source of strongly entangled photon pairs with high brightness and indistinguishability. *Nat. Nanotechnol.* **2019**, *14*, 586−593.
(41) Musiał, A.; Mikulicz, M.; Mrowiński, P.; Zielińska, A.; Sitarek, P.; Wyborski, P.; Kuniej, M.; Reithmaier, J. P.; Sęk, G.; Benyoucef, M. InP-based single-photon sources operating at telecom C-band with increased extraction efficiency. *Appl. Phys. Lett.* **2021**, *118*, 221101.
(42) Sapienza, L.; Davanço, M.; Badolato, A.; Srinivasan, K. Nanoscale optical positioning of single quantum dots for bright and pure single-photon emission. *Nat. Commun.* **2015**, *6*, 7833.
(43) Bonett, D. G.; Price, R. M. Confidence Intervals for Ratios of Means and Medians. *Journal of Educational and Behavioral Statistics* **2020**, *45*, 750−770.
(44) Gschrey, M.; Thoma, A.; Schnauber, P.; Seifried, M.; Schmidt, R.; Wohlfeil, B.; Krüger, L.; Schulze, J. H.; Heindel, T.; Burger, S.; Schmidt, F.; Strittmatter, A.; Rodt, S.; Reitzenstein, S. Highly indistinguishable photons from deterministic quantum-dot microlenses utilizing three-dimensional in situ electron-beam lithography. *Nat. Commun.* **2015**, *6*, 7662.
(45) Fischbach, S.; Schlehahn, A.; Thoma, A.; Srocka, N.; Gissibl, T.; Ristok, S.; Thiele, S.; Kaganskiy, A.; Strittmatter, A.; Heindel, T.; Rodt, S.; Herkommer, A.; Giessen, H.; Reitzenstein, S.; et al. Single Quantum Dot with Microlens and 3D-Printed Micro-objective as Integrated Bright Single-Photon Source. *ACS Photonics* **2017**, *4*, 1327−1332.
(46) Peter, E.; Laurent, S.; Bloch, J.; Hours, J.; Varoutsis, S.; Robert-Philip, I.; Beveratos, A.; Lemaître, A.; Cavanna, A.; Patriarche, G.; Senellart, P.; Martrou, D. Fast radiative quantum dots: From single to multiple photon emission. *Appl. Phys. Lett.* **2007**, *90*, 223118.
(47) Kumano, H.; Harada, T.; Suemune, I.; Nakajima, H.; Kuroda, T.; Mano, T.; Sakoda, K.; Odashima, S.; Sasakura, H. Stable and efficient collection of single photons emitted from a semiconductor quantum dot into a single-mode optical fiber. *Appl. Phys. Express* **2016**, *9*, 032801.
(48) Chang, H.-S.; Chen, W.-Y.; Hsu, T.-M.; Hsieh, T.-P.; Chyi, J.-I.; Chang, W.-H. Origins of nonzero multiple photon emission probability from single quantum dots embedded in photonic crystal nanocavities. *Appl. Phys. Lett.* **2009**, *94*, 163111.
(49) Dalgarno, P. A.; McFarlane, J.; Brunner, D.; Lambert, R. W.; Gerardot, B. D.; Warburton, R. J.; Karrai, K.; Badolato, A.; Petroff, P. M. Hole recapture limited single photon generation from a single n-type charge-tunable quantum dot. *Appl. Phys. Lett.* **2008**, *92*, 193103.
(50) Michler, P.; Imamoğlu, A.; Mason, M.; Carson, P.; Strouse, G.; Buratto, S. Quantum correlation among photons from a single quantum dot at room temperature. *Nature* **2000**, *406*, 968.

https://doi.org/10.1021/acsphotonics.2c00027
ACS Photonics 2022, 9, 2273−2279

ARTICLE 5

Quantum dots in nanocavities resulting from deterministic processing

Scalable quantum photonic devices emitting indistinguishable photons in the telecom C-band

Paweł Holewa,[1,2,3,a] Emilia Zięba-Ostój,[1] Daniel A. Vajner,[4] Maja Wasiluk,[1] Benedek Gaál,[2] Aurimas Sakanas,[2] Marek Burakowski,[1] Paweł Mrowiński,[1] Bartosz Krajnik,[1] Meng Xiong,[2,3] Alexander Huck,[5] Kresten Yvind,[2,3] Niels Gregersen,[2] Anna Musiał,[1] Tobias Heindel,[4] Marcin Syperek,[1,b] and Elizaveta Semenova[2,3,c]

[1)] *Department of Experimental Physics, Faculty of Fundamental Problems of Technology, Wrocław University of Science and Technology, Wyb. Wyspiańskiego 27, 50-370 Wrocław, Poland*

[2)] *DTU Electro, Department of Electrical and Photonics Engineering, Technical University of Denmark, Kongens Lyngby 2800, Denmark*

[3)] *NanoPhoton-Center for Nanophotonics, Technical University of Denmark, 2800 Kongens Lyngby, Denmark*

[4)] *Institute of Solid State Physics, Technische Universität Berlin, 10623 Berlin, Germany*

[5)] *Center for Macroscopic Quantum States (bigQ), Department of Physics, Technical University of Denmark, 2800 Kongens Lyngby, Denmark*

Epitaxial semiconductor quantum dots (QDs) are a promising resource for quantum light generation and the realization of non-linear quantum photonic elements operating at the single-photon level. Their random spatial distribution resulting from their self-organized nature, however, restrains the fabrication yield of quantum devices with the desired functionality. As a solution, the QDs can be imaged and localized, enabling a deterministic device fabrication. Due to the significant electronic noise of camera sensors operating in the telecommunication C-band, 1530-1560 nm, this technique remained challenging. In this work, we report on the imaging of QDs epitaxially grown on InP with emission wavelengths in the telecom C-band demonstrating a localization accuracy of 80 nm. This is enabled by the hybrid integration of QDs in a planar sample geometry with a bottom metallic reflector to enhance the out-of-plane emission. To exemplify our approach, we successfully fabricate circular Bragg grating cavities around single pre-selected QDs with an overall cavity placement uncertainty of 90 nm. QD-cavity coupling is demonstrated by a Purcell enhancement up to ~ 5 with an estimated photon extraction efficiency of $(16.6 \pm 2.7)\,\%$ into a numerical aperture of 0.4. We demonstrate triggered single-photon emission with $g^{(2)}(0) = (3.2 \pm 0.6) \times 10^{-3}$ and record-high photon indistinguishability associated with two-photon interference visibilities of $V = (19.3 \pm 2.6)\,\%$ and $V_{\mathrm{PS}} = 99.8^{+0.2}_{-2.6}\,\%$ without and with temporal postselection, respectively. While the performance of our devices readily enables proof-of-principle experiments in quantum information, further improvements in the yield and coherence may enable the realization of non-linear devices at the single photon level and advanced quantum networks at the telecom wavelength.

Keywords: semiconductor quantum dots, circular Bragg gratings, InAs/InP, deterministic fabrication, telecom spectral range, single-photon sources;

INTRODUCTION

A quantum network[1] based on remote nodes interconnected via fiber-optical links and capable of transferring quantum information using flying qubits will provide the backbone for the implementation of protocols for secure communication[2,3] and distributed quantum computing[4]. Notably, the network can rely on the existing silica-fiber-based infrastructure, utilizing a low-loss channel for the transmission of photons with a wavelength in the telecom C-band around 1550 nm[5]. These quantum network architectures can benefit from existing components and classical signal management protocols, hence making it feasible to transfer quantum information over large distances[5].

In recent years, the technology for the epitaxial growth of self-assembled quantum dots (QDs) has rapidly advanced, resulting in the demonstration of QD-based single-photon sources (SPSs) with outstanding characteristics. These include high photon extraction efficiencies ($\sim 79\,\%$)[6], high single photon generation rates ($\sim 1\,$GHz)[7], and near unity photon indistinguishability ($> 96\,\%$)[7,8], however, all achieved outside the telecom-relevant C-band. Besides the extraordinary material quality, these characteristics are achieved owing to efficient light-matter coupling between a QD and a suitable photonic element. For efficient coupling, spectral and spatial matching is required between the quantum emitter and the engineered photonic mode, which is challenging due to the spatial and spectral distribution of epitaxial QDs. Until now, the QD coupling to photonic cavities operating around 1550 nm has only been realized using non-deterministic fabrication processes, limiting device yield and scalability[9].

In this article, we report on the scalable fabrication of nanophotonic elements around pre-selected individual QDs emitting single and indistinguishable photons in the telecom C-band. For this purpose, we developed a near-infrared (NIR) imaging technique for self-assembled InAs/InP QDs utilizing a hybrid sample geometry with enhanced out-of-plane emission from single QDs[10] and a thermo-electrically cooled InGaAs camera in a wide-field imaging configuration. In combination with two electron-beam lithography (EBL) steps, our method

[a)] Electronic mail: pawel.holewa@pwr.edu.pl
[b)] Electronic mail: marcin.syperek@pwr.edu.pl
[c)] Electronic mail: esem@fotonik.dtu.dk

enables an overall positioning accuracy of 90 nm of the QD with respect to the photonic element and allows for rapid data collection as compared to competing techniques based on scanning *in-situ* imaging[11].

We applied our technique for the deterministic integration of pre-selected QDs into circular Bragg grating (CBG) cavities. The proposed technological workflow allows us to greatly enhance the device fabrication yield reaching $\sim 30\,\%$, which is a significant improvement compared to $< 1\,\%$ that would typically be achieved with a random placement approach. The QD-CBG coupling is evidenced by a Purcell factor ~ 5, and our devices demonstrate a state-of-the-art photon extraction efficiency of $\eta = (16.6 \pm 2.7)\,\%$ into the first lens with a numerical aperture (NA) of 0.4, a high single-photon purity associated with $g^{(2)}(0) = (3.2 \pm 0.6) \times 10^{-3}$, and a record-high photon-indistinguishability of $V = (19.3 \pm 2.6)\,\%$ for QD-based SPSs at C-band wavelengths.

RESULTS

Design of a QD structure for wide-field imaging

Imaging at extremely low light levels at wavelengths $>1\,\mu$m is challenging due to the high level of electronic noise of respective camera systems. Although cameras based on InGaAs achieve quantum efficiencies $> 80\%$, they are characterized by a factor of $> 10^4$ higher dark currents compared to Si-based devices. The photon emission rate from the sample is therefore of key importance for the ability to image and localize single QDs. Following our previous work[10], we have designed a planar sample geometry that significantly enhances the photon extraction efficiency, allowing to localize single QDs and the subsequent fabrication of photonic elements.

The planar QD structure consists of an epitaxially grown 312 nm-thick InP slab containing a single layer of InAs QDs. The InP slab is atop a 359 nm-thick SiO_2 layer with a bottom Al mirror bonded to a Si wafer carrier (Fig. 1a, see **Methods**)[10]. Overall, this geometry enhances the QD emission in the out-of-plane direction by a factor > 7 as compared to bulk InP samples, reaching a total photon extraction efficiency of $> 10\,\%$ from a single QD for NA $= 0.4$. For QD localization later in the experiment, we structure the top InP layer in a mesh with fields of size $(50 \times 50)\ \mu m^2$ separated by $10\,\mu$m-wide ridges (see **Methods**), where the field edges are used as alignment marks (AMs) for imaging. The fields are furthermore organized in blocks accompanied by InP crosses that allow us to align the electron beam to specific target QDs during the EBL process (see **Supplemental Material** for the optical microscope image of the sample surface with fabricated cavities).

For the self-assembled Stranski-Krastanov QD epitaxy, we employed the near-critical growth regime in metalorganic vapor-phase epitaxy (MOVPE)[12] (see **Supplemental Material**) and obtained a QD surface density of $3.1 \times 10^8/\mathrm{cm}^2$ corresponding to an average QD separation of $1.5\,\mu$m. Since QDs exhibit a size, shape, and strain distribution, only a fraction of the QDs have their ground-state optical transition in the C-band. With a (1550 ± 8) nm bandpass filter, we find on average $N_F = 10$ QDs per field, which translates to an effective QD density of $4 \times 10^5/\mathrm{cm}^2$ and an average QD separation of $\sim 16\,\mu$m.

Design of circular Bragg grating cavities

The CBG geometry is optimized using the modal method (see **Supplemental Material**) to enhance the cavity figures of merit at 1550 nm, namely the collection efficiency at the first lens and the Purcell factor (F_P). As opposed to other implementations[9], we consider a simplified CBG geometry consisting of a central mesa and only four external rings. According to our calculations, this number is sufficient for high η and F_P, providing a smaller footprint and less complexity in the fabrication process. The in-plane cavity dimensions include the central mesa radius of $R_0 = 648$ nm, the grating period of 747 nm, and the separation between InP rings (air gap) of 346 nm. For these geometrical parameters, Fig. 1b shows the calculated broadband η that amounts to nearly 62 % and 82 % at 1550 nm for a NA of 0.4 and 0.65, respectively, which is similar to other state-of-the-art CBG designs[13–15]. The wavelength dependence of the Purcell factor, presented in Fig. 1b, mimics the CBG cavity mode centered at 1550 nm and reaches a maximum value $F_P = 18.1$ with a quality factor of 110. The influence of the cavity geometry on the dispersion of η and F_P suggests that the cavity grating together with the Al mirror creates a photonic bandgap that governs the η-dependence and enhances the emission directionality, while the InP membrane thickness and central mesa diameter crucially affect the center wavelength of the F_P-dependence. A scanning electron microscopy (SEM) image of a fabricated CBG cavity is shown in Fig. 1c.

Optical imaging and QD localization

The NIR imaging setup utilizes a wide-field bright microscope configuration as shown in Fig. 2a. The structure with QDs above the Al reflector is mounted in an optical cryostat at $T = 4.2$ K movable by a *x*-*y*-*z* stage for targeting fabricated fields that are imaged consecutively. For sample illumination, we use a 660 nm continuous-wave semiconductor laser diode, spatially shaped with a beam expander, and focused on the backside of a commercially-available microscope objective (NA $= 0.65$) with $50\times$ magnification, 57 % transmission in the NIR, and 10 mm working distance. This configuration provides nearly homogeneous surface illumination across a $(50 \times 50)\ \mu m^2$ field and high photon collection efficiency. The spatially-distributed QD microphotoluminescence (μPL) and scattered light from the field edges (here used as AMs) are collected by the same objective and pass through a cold mirror cutting off the laser light. Finally, the emission is projected onto a thermo-electrically cooled InGaAs-based camera with a $(12.8 \times 10.24)\ mm^2$ chip and a pixel size of $(20 \times 20)\ \mu m^2$. With the $4\times$ magnification lens in front of the camera, the setup has a $200\times$ magnification, enabling the optimal filling of the entire camera chip with a single field (Fig. 2b). The

3

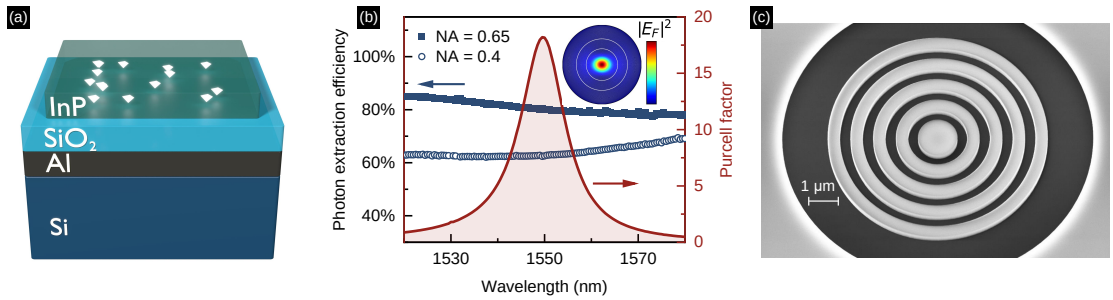

FIG. 1. Structure with QDs for imaging and optimized CBGs. **a**, The layer stack for efficient localization of single InAs/InP QDs emitting at C-band, **b**, calculated CBG Purcell factor (dark red line, right axis) and photon extraction efficiency (blue points, left axis). Inset: far-field emission pattern with rings marking NA = 0.4 and NA = 0.65. **c**, SEM image of a CBG cavity etched in InP on top of SiO_2.

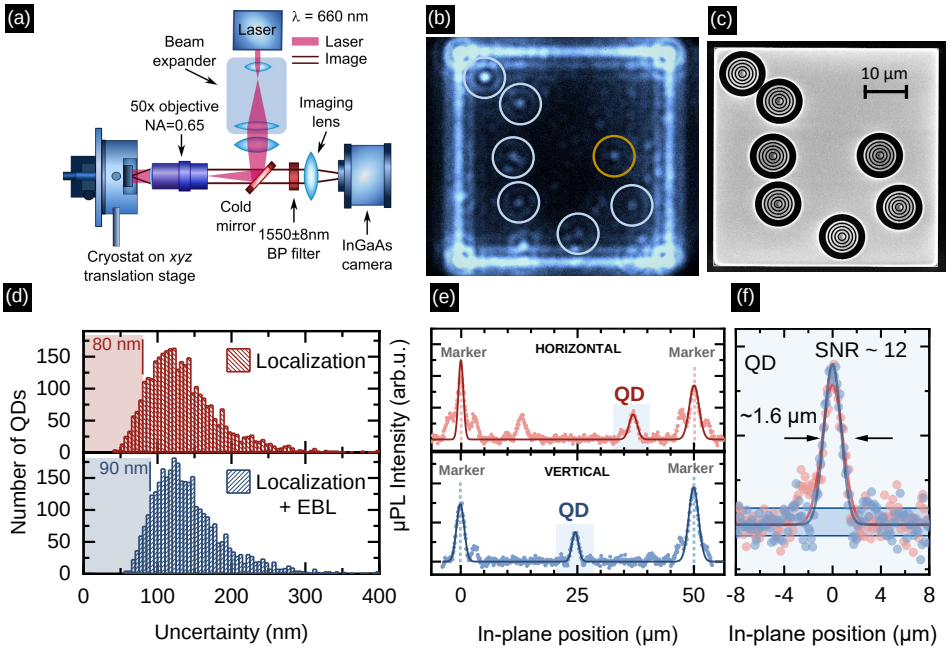

FIG. 2. µPL imaging of the QDs. **a**, The optical setup used for imaging, **b**, a µPL map of a (50×50) µm^2 InP field containing seven localized InAs QDs emitting at C-band, **c**, SEM image of CBGs fabricated atop the localized and preselected QDs, **d**, histograms of QD localization accuracy (top) and overall cavity placement accuracy (bottom) for all detected spots, with markers for 10th distribution percentiles, **e**, exemplary µPL map cross-sections showing the signal of the QD labeled with the orange circle in **b** and alignment marks together with Gaussian fits used for the QD localization, **f**, close-up of the QD signal from **e**, centered to 0 µm. The FWHM of the fitted Gaussian profiles is ∼1.6 µm and the signal-to-noise ratio (SNR) is 12.

1550 nm band-pass filter with 8 nm full-width half-maximum (FWHM) placed in front of the imaging lens selects QDs with emission in the C-band.

Figure 2b shows a representative image of a field recorded with a camera integration time of 2.5 s. The QDs can clearly be recognized as individual bright spots with FWHM ≈ 1.6 µm (see Fig. 2f and **Supplemental Material**) and Airy rings around. The square-shaped outline of the field scatters light and is used as AM for QD localization.

The localization of QDs is performed by taking vertical and horizontal cross-sections both crossing at a QD emission spot in the µPL intensity map. Each cross-section thus contains the position of the target QD relative to two AMs (Fig. 2e). Gaussian profiles fitted to the QD and the AM signals are sub-

sequently used to determine the QD peak position relative to the AMs. The average signal-to-noise ratio for QD emission spots is 10.6, emphasizing the importance of the 7× emission enhancement in the planar structure as compared to bulk InP. We find that for the brightest 10 % of all QDs with SNR > 15.5, the position is fitted with an uncertainty of < 54 nm in 1D and with an uncertainty of the AM position of < 36 nm, resulting in a total uncertainty of QD position in 1D of < 62 nm. In 2D, this translates to 80 nm accuracy for the QD localization. Finally, taking into account the EBL alignment accuracy of 40 nm as measured in our previous work[16], we estimate the overall accuracy of 2D CBG placement to $\Delta R = 90$ nm. The histograms of QD localization accuracy and overall cavity placement accuracy for all detected spots are shown in Fig. 2d in the upper and lower panel, respectively, and the 80 nm and 90 nm levels are marked for reference. Medians for the distributions are slightly larger, 127 nm and 133 nm, due to processing of all detected spots, irrespective of their brightness and expected cavity fabrication precision. Details on the localization algorithm, derivation and discussion of the uncertainties, and data on the accuracy of cavity positioning are given in the **Supplemental Material**. Following the localization of suitable QDs, CBGs are fabricated using EBL with proximity error correction and an optimized inductively coupled plasma-reactive ion etching (ICP-RIE) process (see **Methods**). The SEM image presented in Fig. 2c is taken from the same field after fabricating the CBG cavities around pre-selected QDs indicated by the circles in Fig. 2b.

Characteristics of the fabricated devices

Process yield

We use a μPL setup to quantify the process yield that we define as the ratio between the number of QD-CBG devices with QD emission spectra matching the CBG mode and the number of all CBGs investigated, and we obtain $Y = 30\,\%$. This value should be compared with the yield that would be obtained in a statistical QD-CBG fabrication process. As we estimate the average number of QDs per field of size $F = 50\,\mu$m to $N_F = 10$, the probability of covering one of them with the central mesa of diameter $2R_0$ is $Y_{\text{random}} \sim N_F \times (2R_0/F)^2 = 0.67\,\% \ll Y$. Some of the QD (inside a CBG) emission spectra are significantly broadened (median linewidth of 0.76 nm, see **Supplemental Material**) as compared to the narrowest recorded linewidth of 0.14 nm (identical to the spectrometer resolution). We attribute the broadening to the impact of surface states and point defects caused by the cavity fabrication, effectively resulting in the spectral wandering of the QD emission line[17]. Such defects can as well introduce non-radiative recombination centers in the close vicinity of or even into the QD, quench the optical emission, and effectively reduce the process yield. Using the temperature-dependent μPL studies, we make sure that even the broadened emission lines follow the expected Varshni trend, ensuring that these spectral lines can indeed be associated with the QD emission as the temperature dependence of the cavity mode energy is much weaker.

Purcell enhancement

In the following, we discuss the optical properties of two exemplary devices, QD-CBG #1 and QD-CBG #2, each containing a single pre-selected QD coupled to the CBG cavity mode (see **Supplemental Material** for the properties of a third device QD-CBG #3). Figure 3a shows the narrow QD emission lines overlaid on the cavity mode with $Q = 194$, the latter obtained under high power cavity excitation, evidencing good spectral overlap between the cavity mode and the QD emission. We interpret the dominant QD emission lines in both devices as trions (CX), due to their linear intensity dependence on excitation power, and the lack of fine-structure splitting. This is in line with typical spectra for our InAs/InP QDs with preferential CX recombination where the average CX binding energy was measured to be 4.7 meV[10].

The coupling between the QD and the CBG cavity is evidenced by the observation of a reduced emission decay time as compared to the decay of QDs in the planar reference structure. For the CX line in QD-CBG #1 and #2 we record decay times of $\tau_{\#1} = (0.40 \pm 0.01)$ ns and $\tau_{\#2} = (0.53 \pm 0.01)$ ns, respectively (Fig. 3b). To take statistical QD-to-QD fluctuations for the reference decay time into account, we estimate the average decay time of 8 uncoupled QD CX lines and obtain $\tau_{\text{ref}} = (1.99 \pm 0.16)$ ns, while the single reference shown in Fig. 3b has a decay time of (2.01 ± 0.02) ns. Therefore, the measured Purcell factor for QD-CBG #1 is $F_P = 5.0 \pm 0.4$ and $F_P = 3.8 \pm 0.3$ for QD-CBG #2. Although the obtained Purcell factors are comparable with $F_P = 3$ obtained in the non-deterministic fabrication approach[9], we expect it to be much higher if the QD would perfectly match the cavity mode both spectrally and spatially. However, the expected Purcell factor decays rapidly with the dipole displacement $\mathbf{r}_0$ from the cavity center (decreases by half for $|\mathbf{r}_0| = 100$ nm), as the fabricated CBG is optimized for a higher-order mode that exhibits electric field minima along the cavity radial direction (see **Supplemental Material**). Hence, the relatively large total positioning uncertainty for QD-CBGs #1-#3 ($\Delta R \sim$ 140-150 nm) and the non-ideal spectral emitter-cavity overlap explain the reduced F_P as compared to the model.

Photon extraction efficiency

We evaluate the photon extraction efficiency by recording the power-dependent μPL signal with a superconducting nanowire single-photon detector (SNSPD) in a calibrated optical setup (see Fig. 3c). The setup has a total transmission of $(1.1 \pm 0.2)\,\%$ (see **Supplemental Material**). The measured η values are corrected by the factor $\sqrt{1 - g^{(2)}(0)}$, to account for the detection of secondary photons due to the refilling of QD states[18,19]. Here, the $g^{(2)}(0)$ value is obtained under the excitation power P_{sat} corresponding to saturation of the CX line. Evaluating the CX emission, we obtain an extraction efficiency $\eta_{\#1} = (16.6 \pm 2.7)\,\%$ for QD-CBG #1 and $\eta_{\#2} = (13.3 \pm 2.2)\,\%$ for QD-CBG #2 using an objective with NA = 0.4.

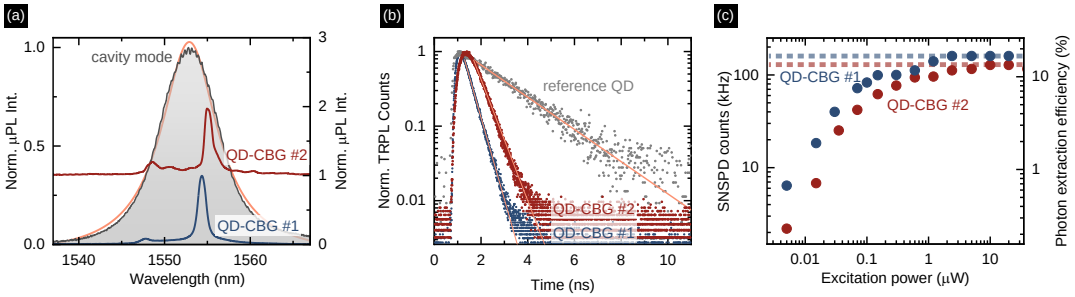

FIG. 3. Characteristics of exemplary fabricated devices, QD-CBGs #1 and #2. **a**, µPL spectra for QDs in devices #1 and #2 overlaid on the cavity mode of device #2 (grey) and fitted with a Lorentzian profile (orange), stacked for clarity, **b**, time-resolved µPL traces for these QDs with the reference QD decay, **c**, power-dependent count rates registered on the SNSPD detector. Horizontal lines mark the line µPL signal saturation level used for the determination of photon extraction efficiency.

Single-photon emission purity

The photon statistics of a quantum light source are of fundamental importance for applications in photonic quantum technologies. In the following, we investigate the single-photon purity of the emission from QD-CBG #2 by analyzing the photon autocorrelation function $g^{(2)}(\tau)$ (cf. **Supplemental Material** for details on the data analysis and complementary $g^{(2)}(\tau)$ measurements).

Fig. 4a depicts the measured $g^{(2)}(\tau)$ histograms obtained under pulsed off-resonant excitation at a power $0.5 \times P_{\mathrm{sat}}$ and LO-phonon-assisted, quasi-resonant excitation at $0.04 \times P_{\mathrm{sat}}$ in the upper and lower panel, respectively. Under off-resonant excitation, the single-photon purity is limited by recapture processes resulting in $g^{(2)}(0)_{\mathrm{fit}} = 0.05 \pm 0.02$, where the uncertainty is mainly determined by the background level B. From the fit, we determine a decay time of $\tau_{\mathrm{dec}} = (0.67 \pm 0.03)\,\mathrm{ns}$, in good agreement with the spontaneous emission decay time observed in Fig. 3b ($\tau_{\#2} = (0.53 \pm 0.01)\,\mathrm{ns}$).

Under weak quasi-resonant excitation at $P \ll P_{\mathrm{sat}}$, the probability for charge-carrier recapture is strongly reduced, resulting in almost negligible background contributions ($B = 0$) (Fig. 4a, lower panel) and a fitted value of $g^{(2)}(0)_{\mathrm{fit}} = (4.7 \pm 2.6) \times 10^{-3}$ at $P = 0.04 \times P_{\mathrm{sat}}$. Additionally, we evaluated the raw antibunching value by integrating the raw coincidences around $\tau = 0$ over a full repetition period normalized by the Poisson level of the side peaks. This results in $g^{(2)}(0)_{\mathrm{raw}} = (3.2 \pm 0.6) \times 10^{-3}$, with the error deduced from the standard deviation of the distribution of counts in the side peaks. As discussed later, this result compares favorably with previous reports on non-deterministically fabricated QD-CBGs.

Photon indistinguishability

Finally, we explore the photon indistinguishability of QD-CBG #2 by Hong-Ou-Mandel (HOM)-type two-photon interference (TPI) experiments[20] (see **Methods** and **Supplemental Material** for details on the experimental setup, data analysis, and complementary TPI measurements). The HOM histograms recorded for co- and cross-polarized measurement configurations are presented in Fig. 4b, and were obtained under pulsed quasi-resonant excitation with identical experimental conditions as the $g^{(2)}(\tau)$ measurement presented in the previous section (at $0.04 \times P_{\mathrm{sat}}$). The data shown in Fig. 4b is not corrected for multi-photon events or contributions from residual laser light.

The HOM histograms feature a characteristic pattern that we analyze following the methodology described in Ref. 21. The reduced area of the central peak in the co-polarized measurement as compared to the maximally distinguishable cross-polarized measurement is a distinct signature of the two-photon coalescence due to a significant degree of photon-indistinguishability. From the width of the central dip we extract a photon coherence time of $T_2 = (103 \pm 13)\,\mathrm{ps}$. The visibility of the TPI is calculated from the ratio of the fitted central peak area in the co- and cross-polarized measurements as $V = 1 - A_{\mathrm{Co}}/A_{\mathrm{Cross}}$. We obtain a TPI visibility of $V = (19.3 \pm 2.6)\,\%$ with the accuracy being the propagated fitting errors reflecting the statistics of the experimental data. The temporally post-selected visibility at zero delay time ($\tau = 0$) is $V_{\mathrm{PS}} = 99.8^{+0.2}_{-2.6}\,\%$, limited only by the system temporal response.

DISCUSSION

The scalable fabrication of active quantum photonic devices operating in the telecom C-band has been a long-standing challenge. This is mainly due to the random size and strain distribution of epitaxially grown QDs causing an inhomogeneous broadening of the emission and difficulties in localizing suitable QDs due to the high electronic noise level of detector arrays sensitive around 1.55 µm wavelength. In this work, we present a solution to this problem based on a hybrid sample design. We fabricate an InP layer containing epitaxial QDs on

6

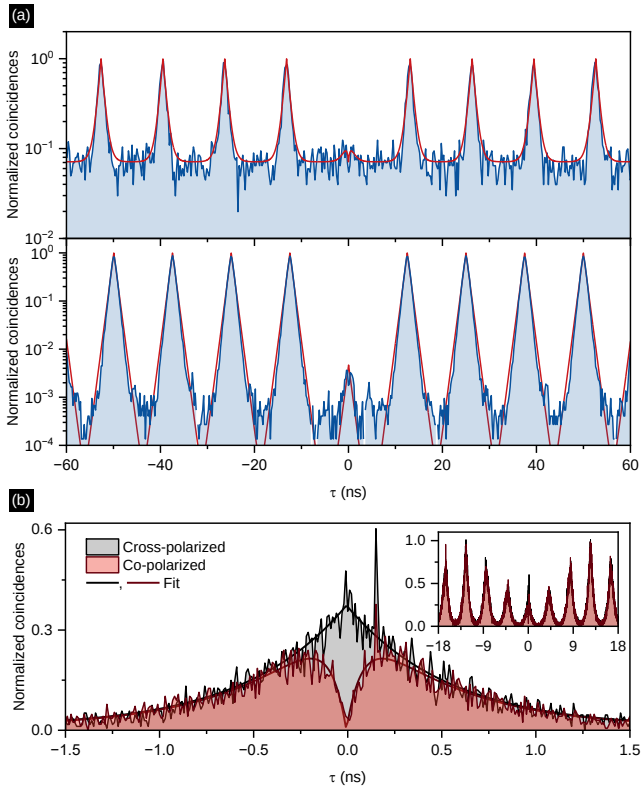

FIG. 4. Quantum optical experiments on QD-CBG #2. **a**, The second-order autocorrelation function $g^{(2)}(\tau)$ of the triggered photons for the above-band excitation (top), and LO-phonon-assisted quasi-resonant excitation (bottom), **b**, HOM histogram for cross- and co-polarized photons evidencing the indistinguishability by the two-photon interference visibility of $V = (19.3 \pm 2.6)\,\%$, and the post-selected value of $V_{\mathrm{PS}} = 99.8^{+0.2}_{-2.6}\%$.

top of a Al reflector placed on a Si wafer carrier. This geometry significantly enhances the photon extraction efficiency from the QDs by a factor > 7 enabling the localization of single QDs in a wide-field imaging setup with a thermo-electrically cooled InGaAs camera. For the 10 % brightest QDs our setup achieves an imaging SNR > 15.5 and a localization uncertainty of ~ 80 nm with respect to alignment marks. After final EBL processing, we achieve an overall uncertainty of ~ 90 nm for fabricating a nano-photonic device around pre-selected QDs. The localization accuracy of our setup is comparable to setups operating in the 770-950 nm range (48 nm[22], 30 nm[23]) where Si-based sensors with four orders of magnitude lower electronic noise can be used. The accuracy in our setup can be further improved by using higher-NA objectives inside the cryostat together with an overall increased microscope magnification, which was reported to reduce the localization accuracy down to 5 nm[24]. Alternatively, *in-situ* EBL[25] or photolithography[26] scanning techniques provide a similar accuracy down to ~ 35 nm, but are comparably slow, require cathodoluminescence signal for QD localization or, in case of photolithography, are not suitable to define reliably sub-µm features.

To exemplify our approach, we fabricate CBG cavities with a resonance wavelength of 1.55 µm around some of the pre-selected QDs. The QD-to-CBG coupling is evidenced by a Purcell factor of $F_{\mathrm{P}} = 5.0 \pm 0.4$, further increasing the single-photon emission rate and final source brightness. Using our approach, we obtain a total process yield of 30 % for finding a pre-selected QD spectrally matching the CBG cavity, which is a significant improvement compared to the yield achievable with a random placement approach ($\sim 0.7\,\%$). For our QD-CBG device, we measure a photon extraction efficiency of $(16.6 \pm 2.7)\,\%$ with a NA $= 0.4$ objective, which is comparable to previously reported devices probabilistically-fabricated and operating at C-band wavelengths[9].

Our QD-CBG devices feature excellent single-photon emission purities with raw values down to $g^{(2)}(0) = (3.2 \pm 0.6) \times 10^{-3}$, beating previous records for non-deterministically fabricated QD-CBGs[9], as well as most QDs

operating in the C-band[27,28], while being not yet competitive with the state-of-the-art[29].

Importantly, we report for the first time triggered TPI experiments for InP-based cavity-coupled QDs with emission wavelengths in the telecom C-band, which is crucial for applications in quantum information processing (QIP). We generate indistinguishable photons with a TPI visibility up to $V = (19.3 \pm 2.6)\,\%$ and a post-selected value of $V_{\mathrm{PS}} = 99.8^{+0.2}_{-2.6}\,\%$ at zero time delay, setting a new record for QDs emitting in the C-band. Previous results in the C-band were based either on droplet epitaxy InAs/InP QDs in planar structures[30,31] or InAs QDs grown on GaAs followed by an InGaAs metamorphic buffer, also located in planar structures[32,33] or embedded in randomly placed CBGs[9].

Further improvement in the photon indistinguishability is of utmost importance for applications in QIP. This is challenged by the strong coupling of QDs to their semiconductor environment via charge and spin noise, both causing QD decoherence[21,34]. It is thus important to stabilize the QD environment, e. g. via electrical gates. In combination with coherent pumping schemes, such as two-photon resonant excitation, we expect a further improvement of the photon coherence time and hence indistinguishability[35].

Moreover, the InP material system used in our work appears to be advantageous for QD-based quantum photonic devices operating in the C-band and compared to GaAs-based devices. Despite the careful strain engineering involved in the epitaxy of QDs on GaAs[36], the metamorphic buffer complicates the device engineering and QD growth. In contrast, an unstrained InP system is free from threading dislocations that would be a source of dangling bonds causing non-radiative recombination, thus lowering the efficiency[37].

In conclusion, our work opens the route for the scalable fabrication of telecom C-band wavelength quantum photonic devices with QDs delivering flying qubits, i.e. single or entangled photons[38], or acting as a non-linear element for QIP[39]. Improvements in our optical imaging setup will further increase the device yield and positioning accuracy, while the electric control and coherent excitation of QD emitters will further push the achievable photon-indistinguishability.

Methods

Epitaxial growth and fabrication of planar structure with QDs– The fabrication of the QD-CBG devices starts with the MOVPE growth of low-density Stranski-Krastanov InAs/InP QDs emitting in the C-band[12]. Then, the applied process analogous to the one described in Ref. 10 results in the structure consisting of a thin InP layer with QDs over SiO_2 and Al, heterogeneously integrated with a Si carrier wafer using BCB and ready for imaging. Further details are given in **Supplemental Material**.

Modeling of the CBG– The QD is modeled as a classical dipole[40], and the numerical simulations of the CBG geometry are performed using a modal method employing a true open boundary condition[41]. See the **Supplemental Material** for further details.

Deterministic fabrication of QD-CBG devices– After the μPL imaging step, introduced in the Results section and elaborated in **Supplemental Material**, the CBG cavities are fabricated via e-beam lithography using high-precision alignment based on the InP mark detection in JEOL JBX-9500FSZ e-beam writer. This step is followed by HBr-based ICP-RIE etching, using CSAR resist and a PECVD-deposited SiN_x hard mask. The calculated design is first scaled and fabricated using a nominally identical heterostructure to investigate the mode energy vs. size dependence and to account for the fabrication imperfections. Additionally, we experimentally determine the $\sim$ 15 nm temperature-induced blueshift of the mode energy between a room and low temperature resulting from the contraction of the structure (introducing size and strain changes), as well as from the change of the refractive indices of the layers.

Optical characterization of devices– The structure with QD-CBG devices is held in a helium-flow cryostat allowing for control of the sample temperature in the range of 4.2-300 K. For our standard μPL studies, the structures are optically excited through a microscope objective with NA = 0.4 or 0.65 and 20× magnification using 660 nm or 805 nm light generated with semiconductor laser diodes. The same objective is used to collect the μPL signal and to direct it for spectral analysis into a 1 m-focal-length monochromator equipped with a liquid-nitrogen-cooled InGaAs multichannel array detector, providing spatial and spectral resolution of $\sim$2 μm and $\sim$25 μeV, respectively.

The photon extraction efficiency and time-resolved μPL are measured in the same setup. Here, QDs are excited by $\sim$50 ps-long pulses with a repetition rate of 80 MHz and a central wavelength of 805 nm. At the same time, the second monochromator output port is equipped with the fiber coupling system, transmitting the signal to an NbN-based SNSPD (Scontel) with $\sim$87 % quantum efficiency in the range 1.5-1.6 μm and $\sim$ 200 dark counts per second. A multichannel picosecond event timer (PicoHarp 300 by PicoQuant GmbH) analyzes the single photon counts as a time-to-amplitude converter. The overall time resolution of the setup is $\sim$80 ps. Experimental setups, and data on the setup transmission efficiency used for determining the photon extraction efficiency are given in **Supplemental Material**.

Photon autocorrelation measurements– For the photon-autocorrelation measurements, QD-CBG devices were optically excited using a Ti:Sapphire (Ti:Sa) laser (Coherent Mira-HP) or a widely tunable ps-pulsed laser system based on an optical parametric oscillator (OPO) (picoEmerald by APE GmbH) with repetition rates of 76 MHz and 80 MHz, respectively. We use a fiber-coupled bandpass filter (FWHM = $\sim$0.4 nm) for spectrally selecting the QD emission, followed by a 50:50 fiber beam splitter. For the off-resonant excitation, we use a microscope objective with NA = 0.7 and 100× magnification and excite the QD emission with $\sim$2 ps-long pulses at 830 nm from the Ti:Sa. The signal is detected with a pair of SNSPDs with $\sim$87 % and $\sim$92 % quantum efficiency at 1550 nm. For the quasi-resonant excitation, we use an aspheric lens (NA = 0.6) mounted inside a low-vibration closed-cycle cryostat (attoDRY800 by Attocube Systems AG) cooled to 4.5 K. Here, the OPO-laser is used and adjusted to a pulse length of 5 ps. Single photons are detected via SNSPDs with 80 % detection efficiency at 1550 nm and 57 ps timing jitter (complete system temporal response). The excitation energy was determined in photoluminescence excitation experiments to be 0.83537 eV (37.57 meV above the QD emission energy, cf. **Supplemental Material**), which was also used for following TPI experiments.

Photon-indistinguishability measurements– In the TPI experiments, an additional 4 ns delay was introduced between consecutive laser pulses by adding an imbalanced free-space Mach-Zehnder interferometer (MZI) in the excitation path, which was compensated in the HOM setup on the detection side. Hence, the excitation sequence is composed of pairs of pulses separated by 4 ns, every 12.5 ns corresponding to 80 MHz laser repetition rate. Free-space waveplates were used to match the polarization for the TPI inside the fiber beam splitter. The exact polarization was set by using a polarimeter at the beam splitter output in combination with a laser tuned to the QD emission wavelength. Fine-tuning the relative delay between both MZI arms was used to precisely match the detection and excitation delay, respectively. The contrast of classical Michelson interference of the laser with itself was used for optimization. See **Supplemental Material** for the scheme of the experimental setup and the details of the HOM data analysis.

Acknowledgements

The authors acknowledge financial support from the Danish National Research Foundation via the Research Centers of Excellence NanoPhoton (DNRF147) and the Center for Macroscopic Quantum States bigQ (DNRF142). P. H. was funded by the Polish National Science Center within the Etiuda 8 scholarship (Grant No. 2020/36/T/ST5/00511) and by the European Union under the European Social Fund. D. A. V. and T. H. acknowledge financial support by the German Federal Ministry of Education and Research (BMBF) via the project "QuSecure" (Grant No. 13N14876) within the funding program Photonic Research Germany, the BMBF joint project "tubLAN Q.0" (Grant No. 16KISQ087K), and by the Einstein Foundation via the Einstein Research Unit "Quantum Devices". P. M. acknowledges the financial support from the Polish National Science Center (Grant No. 2020/39/D/ST5/02952). N. G. acknowledges support from the European Research Council (ERC-CoG "UNITY", Grant No. 865230), and from the Independent Research Fund Denmark (Grant No. DFF-9041-00046B).

Funding Sources

Danish National Research Foundation: DNRF147, DNRF142; Polish National Science Center: 2020/36/T/ST5/00511; 2020/39/D/ST5/02952 European Union: European Social Fund; European Research Council: 865230; Independent Research Fund Denmark: DFF-9041-00046B German Federal Ministry of Education and Research: 13N14876, 16KISQ087K; Einstein Foundation: Einstein Research Unit "Quantum Devices".

Supplemental Material

The description of device fabrication, numerical simulations, extended data for QD localization algorithm and uncertainty analysis, optical characterization of the devices, evaluation of single-photon purity, and the analysis of the two-photon-interference measurements.

[1] H. J. Kimble, "The quantum internet," Nature **453**, 1023–1030 (2008).
[2] N. Gisin, G. Ribordy, W. Tittel, and H. Zbinden, "Quantum cryptography," Rev. Modern Phys. **74**, 145–195 (2002).

[3] D. A. Vajner, L. Rickert, T. Gao, K. Kaymazlar, and T. Heindel, "Quantum communication using semiconductor quantum dots," Adv. Quantum Technol. **5**, 2100116 (2022).
[4] A. Serafini, S. Mancini, and S. Bose, "Distributed quantum computation via optical fibers," Phys. Rev. Lett. **96**, 010503 (2006).
[5] Y. Cao, Y. Zhao, Q. Wang, J. Zhang, S. X. Ng, and L. Hanzo, "The Evolution of Quantum Key Distribution Networks: On the Road to the Qinternet," IEEE Communications Surveys & Tutorials **24**, 839–894 (2022).
[6] O. Gazzano, S. M. de Vasconcellos, C. Arnold, A. Nowak, E. Galopin, I. Sagnes, L. Lanco, A. Lemaître, and P. Senellart, "Bright solid-state sources of indistinguishable single photons," Nat. Commun. **4**, 1425 (2013).
[7] N. Tomm, A. Javadi, N. O. Antoniadis, D. Najer, M. C. Löbl, A. R. Korsch, R. Schott, S. R. Valentin, A. D. Wieck, A. Ludwig, and R. J. Warburton, "A bright and fast source of coherent single photons," Nat. Nanotechnol. **16**, 399–403 (2021).
[8] H. Wang, Z.-C. Duan, Y.-H. Li, S. Chen, J.-P. Li, Y.-M. He, M.-C. Chen, Y. He, X. Ding, C.-Z. Peng, C. Schneider, M. Kamp, S. Höfling, C.-Y. Lu, and J.-W. Pan, "Near-transform-limited single photons from an efficient solid-state quantum emitter," Phys. Rev. Lett. **116**, 213601 (2016).
[9] C. Nawrath, R. Joos, S. Kolatschek, S. Bauer, P. Pruy, F. Hornung, J. Fischer, J. Huang, P. Vijayan, R. Sittig, M. Jetter, S. L. Portalupi, and P. Michler, "High emission rate from a Purcell-enhanced, triggered source of pure single photons in the telecom C-band," (2022), arXiv:2207.12898 [quant-ph].
[10] P. Holewa, A. Sakanas, U. M. Gür, P. Mrowiński, A. Huck, B.-Y. Wang, A. Musiał, K. Yvind, N. Gregersen, M. Syperek, and E. Semenova, "Bright Quantum Dot Single-Photon Emitters at Telecom Bands Heterogeneously Integrated on Si," ACS Photonics **9**, 2273–2279 (2022).
[11] S. Liu, K. Srinivasan, and J. Liu, "Nanoscale positioning approaches for integrating single solid-state quantum emitters with photonic nanostructures," Laser Photonics Rev. **15**, 2100223 (2021).
[12] Y. Berdnikov, P. Holewa, S. Kadkhodazadeh, J. M. Śmigiel, A. Frąckowiak, A. Sakanas, K. Yvind, M. Syperek, and E. Semenova, "Fine-tunable near-critical Stranski-Krastanov growth of InAs/InP quantum dots," (2023), arXiv:2301.11008 [cond-mat.mes-hall].
[13] A. Barbiero, J. Huwer, J. Skiba-Szymanska, T. Müller, R. M. Stevenson, and A. J. Shields, "Design study for an efficient semiconductor quantum light source operating in the telecom C-band based on an electrically-driven circular Bragg grating," Opt. Express **30**, 10919 (2022).
[14] L. Bremer, C. Jimenez, S. Thiele, K. Weber, T. Huber, S. Rodt, A. Herkommer, S. Burger, S. Höfling, H. Giessen, and S. Reitzenstein, "Numerical optimization of single-mode fiber-coupled single-photon sources based on semiconductor quantum dots," Opt. Express **30**, 15913 (2022).
[15] L. Rickert, F. Betz, M. Plock, S. Burger, and T. Heindel, "High-performance designs for fiber-pigtailed quantum-light sources based on quantum dots in electrically-controlled circular Bragg gratings," Opt. Express (2023), 10.1364/oe.486060.
[16] A. Sakanas, E. Semenova, L. Ottaviano, J. Mørk, and K. Yvind, "Comparison of processing-induced deformations of InP bonded to Si determined by e-beam metrology: Direct vs. adhesive bonding," Microelectron. Eng. **214**, 93–99 (2019).
[17] J. Liu, K. Konthasinghe, M. Davanço, J. Lawall, V. Anant, V. Verma, R. Mirin, S. W. Nam, J. D. Song, B. Ma, Z. S. Chen, H. Q. Ni, Z. C. Niu, and K. Srinivasan, "Single self-assembled InAs/GaAs quantum dots in photonic nanostructures: The role of nanofabrication," Phys. Rev. Applied **9**, 064019 (2018).
[18] J. Yang, C. Nawrath, R. Keil, R. Joos, X. Zhang, B. Höfer, Y. Chen, M. Zopf, M. Jetter, S. L. Portalupi, F. Ding, P. Michler, and O. G. Schmidt, "Quantum dot-based broadband optical antenna for efficient extraction of single photons in the telecom O-band," Opt. Express **28**, 19457 (2020).
[19] H. Kumano, T. Harada, I. Suemune, H. Nakajima, T. Kuroda, T. Mano, K. Sakoda, S. Odashima, and H. Sasakura, "Stable and efficient collection of single photons emitted from a semiconductor quantum dot into a single-mode optical fiber," Appl. Phys. Express **9**, 032801 (2016).
[20] C. K. Hong, Z. Y. Ou, and L. Mandel, "Measurement of subpicosecond time intervals between two photons by interference," Phys. Rev. Lett. **59**, 2044–2046 (1987).
[21] A. Thoma, P. Schnauber, M. Gschrey, M. Seifried, J. Wolters, J. H. Schulze, A. Strittmatter, S. Rodt, A. Carmele, A. Knorr, T. Heindel, and S. Reitzenstein, "Exploring dephasing of a solid-state quantum emitter via time- and temperature-dependent Hong-Ou-Mandel experiments," Phys. Rev. Lett. **116**, 1–5 (2016).
[22] T. Kojima, K. Kojima, T. Asano, and S. Noda, "Accurate alignment of a photonic crystal nanocavity with an embedded quantum dot based on optical microscopic photoluminescence imaging," Appl. Phys. Lett. **102**, 011110 (2013).
[23] L. Sapienza, M. Davanço, A. Badolato, and K. Srinivasan, "Nanoscale optical positioning of single quantum dots for bright and pure single-photon emission," Nat. Commun. **6**, 7833 (2015).
[24] J. Liu, M. I. Davanço, L. Sapienza, K. Konthasinghe, J. V. D. M. Cardoso, J. D. Song, A. Badolato, and K. Srinivasan, "Cryogenic photoluminescence imaging system for nanoscale positioning of single quantum emitters," Rev. Sci. Instrum. **88**, 023116 (2017).
[25] M. Gschrey, A. Thoma, P. Schnauber, M. Seifried, R. Schmidt, B. Wohlfeil, L. Krüger, J.-H. Schulze, T. Heindel, S. Burger, F. Schmidt, A. Strittmatter, S. Rodt, and S. Reitzenstein, "Highly indistinguishable photons from deterministic quantum-dot microlenses utilizing three-dimensional in situ electron-beam lithography," Nat. Commun. **6**, 7662 (2015).
[26] A. Dousse, L. Lanco, J. Suffczyński, E. Semenova, A. Miard, A. Lemaître, I. Sagnes, C. Roblin, J. Bloch, and P. Senellart, "Controlled light-matter coupling for a single quantum dot embedded in a pillar microcavity using far-field optical lithography," Phys. Rev. Lett. **101**, 30–33 (2008).
[27] K. Takemoto, Y. Nambu, T. Miyazawa, Y. Sakuma, T. Yamamoto, S. Yorozu, and Y. Arakawa, "Quantum key distribution over 120 km using ultrahigh purity single-photon source and superconducting single-photon detectors," Sci. Rep. **5**, 14383 (2015).
[28] K. D. Zeuner, K. D. Jöns, L. Schweickert, C. R. Hedlund, C. N. Lobato, T. Lettner, K. Wang, S. Gyger, E. Schöll, S. Steinhauer, M. Hammar, and V. Zwiller, "On-Demand Generation of Entangled Photon Pairs in the Telecom C-Band with InAs Quantum Dots," ACS Photonics **8**, 2337–2344 (2021).
[29] T. Miyazawa, K. Takemoto, Y. Nambu, S. Miki, T. Yamashita, H. Terai, M. Fujiwara, M. Sasaki, Y. Sakuma, M. Takatsu, T. Yamamoto, and Y. Arakawa, "Single-photon emission at 1.5 µm from an InAs/InP quantum dot with highly suppressed multi-photon emission probabilities," Appl. Phys. Lett. **109**, 132106 (2016).
[30] M. Anderson, T. Müller, J. Skiba-Szymanska, A. B. Krysa, J. Huwer, R. M. Stevenson, J. Heffernan, D. A. Ritchie, and A. J. Shields, "Coherence in single photon emission from droplet epitaxy and Stranski–Krastanov quantum dots in the telecom C-band," Appl. Phys. Lett. **118**, 014003 (2021).
[31] L. Wells, T. Müller, R. M. Stevenson, J. Skiba-Szymanska, D. A. Ritchie, and A. J. Shields, "Coherent light scattering from a telecom C-band quantum dot," (2022), arXiv:2205.07997 [quant-ph].
[32] C. Nawrath, F. Olbrich, M. Paul, S. L. Portalupi, M. Jetter, and P. Michler, "Coherence and indistinguishability of highly pure single photons from non-resonantly and resonantly excited telecom C-band quantum dots," Appl. Phys. Lett. **115**, 023103 (2019).
[33] C. Nawrath, H. Vural, J. Fischer, R. Schaber, S. L. Portalupi, M. Jetter, and P. Michler, "Resonance fluorescence of single In(Ga)As quantum dots emitting in the telecom C-band," Appl. Phys. Lett. **118**, 244002 (2021).
[34] A. V. Kuhlmann, J. Houel, A. Ludwig, L. Greuter, D. Reuter, A. D. Wieck, M. Poggio, and R. J. Warburton, "Charge noise and spin noise in a semiconductor quantum device," Nature Physics **9**, 570–575 (2013).
[35] A. Reigue, R. Hostein, and V. Voliotis, "Resonance fluorescence of a single semiconductor quantum dot: the impact of a fluctuating electrostatic environment," Semicond. Sci. Technol. **34**, 113001 (2019).
[36] R. Sittig, C. Nawrath, S. Kolatschek, S. Bauer, R. Schaber, J. Huang, P. Vijayan, P. Pruy, S. L. Portalupi, M. Jetter, and P. Michler, "Thin-film InGaAs metamorphic buffer for telecom C-band InAs quantum dots and optical resonators on GaAs platform," Nanophotonics **11**, 1109–1116 (2022).
[37] L. Seravalli, G. Trevisi, P. Frigeri, D. Rivas, G. Muñoz-Matutano, I. Suárez, B. Alén, J. Canet-Ferrer, and J. P. Martínez-Pastor, "Single quantum dot emission at telecom wavelengths from metamorphic InAs/InGaAs nanostructures grown on GaAs substrates," Appl. Phys. Lett. **98**, 173112 (2011).
[38] C.-Y. Lu and J.-W. Pan, "Quantum-dot single-photon sources for the quantum internet," Nat. Nanotechnol. **16**, 1294–1296 (2021).
[39] A. Javadi, I. Söllner, M. Arcari, S. L. Hansen, L. Midolo, S. Mahmoodian, G. Kiršanskė, T. Pregnolato, E. H. Lee, J. D. Song, S. Stobbe, and P. Lodahl, "Single-photon non-linear optics with a quantum dot in a waveguide," Nat. Commun. **6**, 8655 (2015).
[40] L. Novotny and B. Hecht, *Principles of Nano-Optics*, 2nd ed. (Cambridge

University Press, 2012).
[41] U. M. Gür, S. Arslanagić, M. Mattes, and N. Gregersen, "Open-geometry modal method based on transverse electric and transverse magnetic mode expansion for orthogonal curvilinear coordinates," Phys. Rev. E **103**, 033301 (2021).

APPENDIX A

Supplemental Materials

A.1 SM for *Bright quantum dot single-photon emitters heterogeneously integrated on Si*

Supplemental Material

—

Bright Quantum Dot Single-Photon Emitters at Telecom Bands Heterogeneously Integrated on Si

CONTENTS

Number of pages in this file: 21, number of figures: 7, number of tables: 4.

S-I. METHODS

A. QD fabrication

The QDs are grown in the low-pressure MOVPE TurboDisc® reactor using arsine (AsH_3), phosphine (PH_3), tertiarybutylphosphine (TBP) and trimethylindium (TMIn) precursors with H_2 as a carrier gas. The growth sequence starts with the deposition of a 0.5 µm-thick InP buffer layer on a (001)-oriented InP substrate at 610 °C subsequently epitaxially covered by a 200 nm-thick $In_{0.53}Ga_{0.47}As$ sacrificial layer lattice-matched to InP and a 244 nm-thick InP layer. Then, the temperature is decreased to 483 °C, stabilized under TBP for 180 s and AsH_3 for 27 s. Finally, nucleation of QDs occurs in the Stranski-Krastanov growth mode after deposition of nominally 0.93 mono-layer thick InAs under TMIn and AsH_3 flow rates of 11.8 µmol/min and 52.2 µmol/min, respectively. Nucleated QDs are annealed for 60 s at the growth temperature in AsH_3 ambient, before the temperature is increased for 30 s to 515 °C and the annealing continues for another 30 s. Deposition of a 244 nm-thick InP capping layer (12 nm at 515 °C, and the remaining 232 nm after increasing the temperature up to 610 °C) finishes the growth sequence.

The reference structure contains the same InAs/InP quantum dots without InGaAs sacrificial layer and metallic mirror (no processing was done on this structure).

B. QD integration on Si substrate

To integrate the QD structure on Si, a 100 nm-thick layer of SiO_2 is deposited on top of the InP-based structure using plasma-enhanced chemical vapor deposition (PECVD) with the rate of 0.99 nm/s, and subsequently covered by a 100 nm-thick Al layer deposited via electron-beam evaporation with the rate of 90 Å/s. After flipping the structure bottom-up, it is bonded to the Si substrate. The bonding procedure includes, first, spin coating of the AP3000 adhesion promoter and benzocyclobutene (BCB) on Si and AP3000 on the InP wafer, and second, both structures are bonded at 250 °C in vacuum under an applied force of $\sim$ 2 kN. Plasma ashing disposes superfluous BCB from the back-side of the InP wafer. Afterward, the InP substrate is removed in HCl and the InGaAs etch stop layer in H_2SO_4:H_2O_2:H_2O=1:8:80 mixture. For the sample with mesas, HSQ resist (a high purity silsesquioxane-based semiconductor grade polymer) is spin-coated and exposed using electron-beam lithography and developed in water-diluted AZ400K. The mesa pattern is then transferred to the InP by inductively coupled plasma-reactive ion etching (ICP-RIE) followed by HSQ removal in a buffered oxide etch (BHF). The mesa height is 300 nm as measured with an atomic force microscope.

C. Optical experiments

For the optical experiments, the structure is hold in a helium-flow cryostat allowing for controlled sample temperatures in the range of 4.2 K to 300 K. For our standard µPL studies, the structures are optically excited through a high numerical aperture (NA = 0.4) microscope objective with 20× magnification with 660 nm or 787 nm light generated with semiconductor laser diodes, respectively. The same objective is used to collect the PL and direct it for spectral analysis to a 1 m-focal-length monochromator equipped with a liquid-nitrogen-cooled InGaAs multichannel array detector, providing spatial and spectral resolution of $\approx$ 2 µm and $\approx$ 25 µeV, respectively. Polarization properties of emitted light are analyzed by rotating a half-wave plate mounted before a fixed high-contrast-ratio (10^6:1) linear polarizer, both placed in front of the monochromator entrance.

Autocorrelation histograms, photon extraction efficiency, and TRPL are measured in a similar setup. In this setup, the structures are excited by a train of $\sim$ 50 ps-long pulses with a repetition frequency of 40 MHz or 80 MHz, and the central photon wavelength of 805 nm. The collected photons are dispersed by a 0.32 m-focal-length monochromator equipped either with a InGaAs multichannel array detector or NbN-based superconducting nanowire single-photon detectors (, Scontel) with $\sim$85 % quantum efficiency in the 1.5 µm to 1.6 µm range and $\sim$ 200 dark counts per second. A multichannel picosecond event timer (PicoHarp 300 by PicoQuant) analyzes the single photon counts as time-to-amplitude converter with 256 ps channel time bin width. The overall time resolution of the setup is $\sim$80 ps.

D. Determination of the photon extraction efficiency

To determine the value of photon extraction efficiency η_{QD}, we follow the method described in Ref. [1]. First, we estimate the efficiency of the setup η_{Setup} by reflecting a laser tuned to the investigated QD emission range off a silver mirror placed in the setup instead of the structure. The laser beam is attenuated with neutral density filters to achieve the count rate in the

S-3

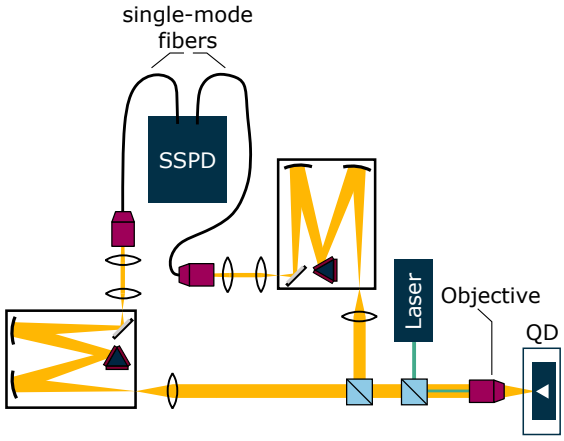

Supplementary Fig. S1. Scheme of the experimental setup used for correlation spectroscopy and determination of the extraction efficiency.

MHz range. This number is corrected by the measured mirror reflectivity, attenuation of filters, transmission of the cryostat window and the microscope objective. Based on the laser power coming on the silver mirror, the estimated setup efficiency is $\eta_{\text{Setup}} = (0.18 \pm 0.06)\,\%$, with the uncertainty being the standard deviation $\sigma(\eta)$ of $\eta_{\text{Setup}}(\lambda)$, mainly steming from the slight discrepancies in the fiber in-coupling efficiencies for different wavelengths. We performed the extraction efficiency experiments in the correlation spectroscopy setup, presented in Supplementary Fig. S1. The signal emitted from the sample passes through the following elements of the setup on the way to the detector: cryostat window (spectrally averaged transmission $T \approx 90\,\%$), microscope objective ($T \approx 55\,\%$), two beam splitters (introducing the optical excitation and splitting the QD signal, $T \approx 40\,\%$ each), monochromator ($T \approx 15\,\%$), fiber in-coupling (efficiency $\sim$18 %) and (efficiency $\sim$85 %). The multiplication of these values leads to the same η_{Setup} as determined using the described method, adopted from Ref. [1].

Then, we excite the QDs non-resonantly with a pulsed laser diode with $f_{\text{rep}} = 80\,\text{MHz}$ repetition rate at the saturation power for each QD. We collect the emission with the microscope objective (NA = 0.4), sum the count rates for CX and X lines (n_{QD}), as only one excitonic complex can radiatively decay at a time, and correct them by η_{Setup}. Taking into account the laser repetition f, we estimate the photon extraction efficiency $\eta_{\text{QD}} = n_{\text{QD}}/(f \times \eta_{\text{Setup}})$. The error bars for photon extraction efficiencies are calculated by propagating the $\sigma(\eta)$ uncertainty. This method assumes unity internal quantum efficiency of QDs ($\eta_{\text{int}} = 100\,\%$), respectively the QD photon repetition rate equals f_{rep}. It is however difficult to determine experimentally the contribution of non-radiative recombination and hence the real value of η_{int}. The assumption of $\eta_{\text{int}} = 100\,\%$ thus determines a lower limit of η_{QD} due to a possible overestimation of the total number of photons emitted by the QD (n_{QD}). Finally, we correct the measured η values for the QDs A-C by the factor $\sqrt{1 - g^{(2)}(0)_{\text{area}}}$ to account for the secondary photons due to the refilling of QD states that contribute to the measured photon flux [2, 3]. This procedure only slightly reduces the η values by 16 %, 11 %, and 5 % for QDs A, B, and C, respectively. With this correction, the highest η values are 9.5 % and 9.1 % for QDs C and B, respectively.

E. Determining the single-photon purity

For the pulsed QD excitation, we calculate the $g^{(2)}(0)$ value including the histogram background contribution B:

$$g^{(2)}(0)_{\text{area}} = \int_{-T_0/2}^{T_0/2} \left[B + A\left[\exp\left(-|\tau|/\tau_{\text{dec}}\right) - \exp\left(-|\tau|/\tau_{\text{cap}}\right)\right]\right] \mathrm{d}\tau \Big/ \int_{-T_0/2}^{T_0/2} \left[B + H\exp\left(-|\tau|/\tau_{\text{dec}}\right)\right] \mathrm{d}\tau, \tag{S1}$$

and with the background contribution subtracted:

$$g^{(2)}(0)_{\text{area}} = \int_{-T_0/2}^{T_0/2} A\left[\exp\left(-|\tau|/\tau_{\text{dec}}\right) - \exp\left(-|\tau|/\tau_{\text{cap}}\right)\right] \mathrm{d}\tau \Big/ \int_{-T_0/2}^{T_0/2} H\exp\left(-|\tau|/\tau_{\text{dec}}\right) \mathrm{d}\tau. \tag{S2}$$

For the histograms recorded in cw mode we use the standard equation

$$C(\tau) = N\left[1 - \left(1 - g^{(2)}_{\text{fit}}(0)\right)\exp\left(-|\tau|/t_{\text{r}}\right)\right], \tag{S3}$$

where N is the average coincidence level at $|\tau| \gg 0$. The purity is extracted as $\mathscr{P} = 1 - g^{(2)}(0)$, in particular, for the raw-data estimated purity $\mathscr{P}_{\text{raw}} = C(0)/N$.

F. Numerical calculations

The structure is modeled with a modal method (MM) employing a true open geometry boundary condition [4]. Here, the geometry is divided into uniform layers along a propagation z axis, and the field is expanded on eigenmodes of each uniform layer. The eigenmode expansion coefficients in the QD layer are computed using the reciprocity theorem [5], and the fields are connected at each layer interface using the S matrix formalism [5, 6]. The far field is then determined using the field equivalence principle and radiation integrals [7]. The extraction efficiency is defined as $\eta = P_{\text{lens, NA}}/P_{\text{in}}$, where $P_{\text{lens, NA}}$ is the power detected by the lens with NA $= 0.4$ in the far field, and P_{in} is the total power emitted from the dipole.

S-II. IDENTIFICATION OF EXCITONIC COMPLEXES

To demonstrate the optical properties of the QDs, three exemplary emitters representing the L- (QD A), C- (QD B), and S- (QD C) telecom bands are chosen, with their μPL spectra presented in Figs. 2b-2d. The excitonic complexes are identified based on the excitation power-dependent μPL intensity $I_{\mu\text{PL}}$ [shown in Supplementary Figs. S2a-S2c], and polarization-resolved μPL investigations [results shown in Supplementary Figs. S2d-S2e]. We obtain the expected [8, 9] linear, superlinear and almost quadratic power dependences for excitons, trions, and biexcitons, respectively, with the following exponents b from fitting the power dependence $I_{\mu\text{PL}} = aP^b$ to the line intensities: $b_{\text{X}} = 0.98 \pm 0.08$, $b_{\text{XX}} = 1.77 \pm 0.11$, $b_{\text{CX}} = 1.04 \pm 0.04$ (QD A), $b_{\text{X}} = 1.00 \pm 0.15$, $b_{\text{XX}} = 1.75 \pm 0.15$, $b_{\text{CX}} = 1.12 \pm 0.18$ (QD B), and $b_{\text{X}} = 1.02 \pm 0.02$, $b_{\text{XX}} = 1.67 \pm 0.10$, $b_{\text{CX}} = 1.15 \pm 0.05$ (QD C), where b_{X}, b_{XX}, b_{CX} are exponents for the X, XX, and CX lines, respectively.

An exemplary polarization-resolved μPL map is shown in Supplementary Fig. S2d with the traces that help to unambiguously ascribe the lines, with X and XX oscillating in anti-phase (right and center panel, respectively), revealing the exciton fine structure splitting with the energy $E_{\text{FSS}} = 91\,\mu\text{eV}$. The slight non-orthogonality of X states, visible in the intensities of both bright exciton (X_A and X_B) and biexciton (XX_A and XX_B) states (Supplementary Fig. S2e), as well as CX intensity modulation, evidences the valence-band mixing between heavy- and light-hole states due to in-plane QD shape asymmetry and anisotropic strain effects [10–12] what has also been observed for trions in similar InP-based QDs [13]. Based on the polarization dependence of the X line μPL intensity, we determine the degree of linear polarization $\text{DOLP}_\text{X} = (42.8 \pm 3.2)$ % and the amplitude of the hole states mixing [12] $\beta_\text{X} = (36.3 \pm 2.7)$ %. For the CX, we observe the lack of the emission energy dependence on the linear polarization angle (Supplementary Fig. S2d, left panel), as expected for the trion spin-singlet state, and based on its intensity we calculate the parameters $\text{DOLP}_\text{CX} = (36.4 \pm 3.2)$ % and $\beta_\text{CX} = (31.1 \pm 2.7)$ %.

We perform in an similar manner the identification of complexes for other QDs in the investigated structures. Based on polarization-resolved and excitation power-dependent μPL spectra of InAs/InP QDs in the structure with mirror which emit in the range of 1.48 μm to 1.6 μm, we determine the binding energies for trions ($E_{\text{X}-\text{CX}}$) and for biexcitons ($E_{\text{X}-\text{XX}}$). The summary of determined binding energies for biexcitons and trions, and the E_{FSS} values are shown in Supplementary Figs. S2f-S2g. We find that the distributions of biexciton and trion binding energies are narrow and the values for QDs A-C are close to their typical values (see the diamonds marking values for QDs A, B, and C). We calculate the average values of $\langle E_{\text{X}-\text{CX}}\rangle = 4.84\,\text{meV}$ and $\langle E_{\text{X}-\text{XX}}\rangle = 3.25\,\text{meV}$. The obtained values are spectrally-independent and only slightly spread around the average values, therefore they help in the identification of excitonic complexes in the investigated QDs A-C. For the fine structure splitting energy, we calculate the average value of $\langle E_{\text{FSS}}\rangle = 123\,\mu\text{eV}$.

Finally, for QD C we present the cross-correlation between XX-X and CX-X lines to unambiguously prove the identification of excitonic lines and the fact that they origin from the same QD. Here, X emission events are registered by the stopping detector. The histograms are shown in Supplementary Fig. S2g for XX-X and Supplementary Fig. S2h for CX-X cross-correlation measurements. In the case of XX-X, we find a strong bunching for positive delays, evidencing the cascaded XX-X emission, while for the CX-X case we see an asymmetric dip which we fit with the function of the form $g^{(2)}_{\text{CX}-\text{X}}(\tau) = A\left[1 - \exp\left(\tau/t_\text{r}\right)\right]$ separately for $\tau < 0$ and $\tau > 0$, where A is a scaling factor, τ is the time delay, and t_r is the antibunching time constant. We find that the t_r is different for positive and negative delays: $t_\text{r} = 1.25 \pm 0.08$ ns and $t_\text{r} = 1.06 \pm 0.08$ ns, respectively, corresponding with the CX and X emission.

S-5

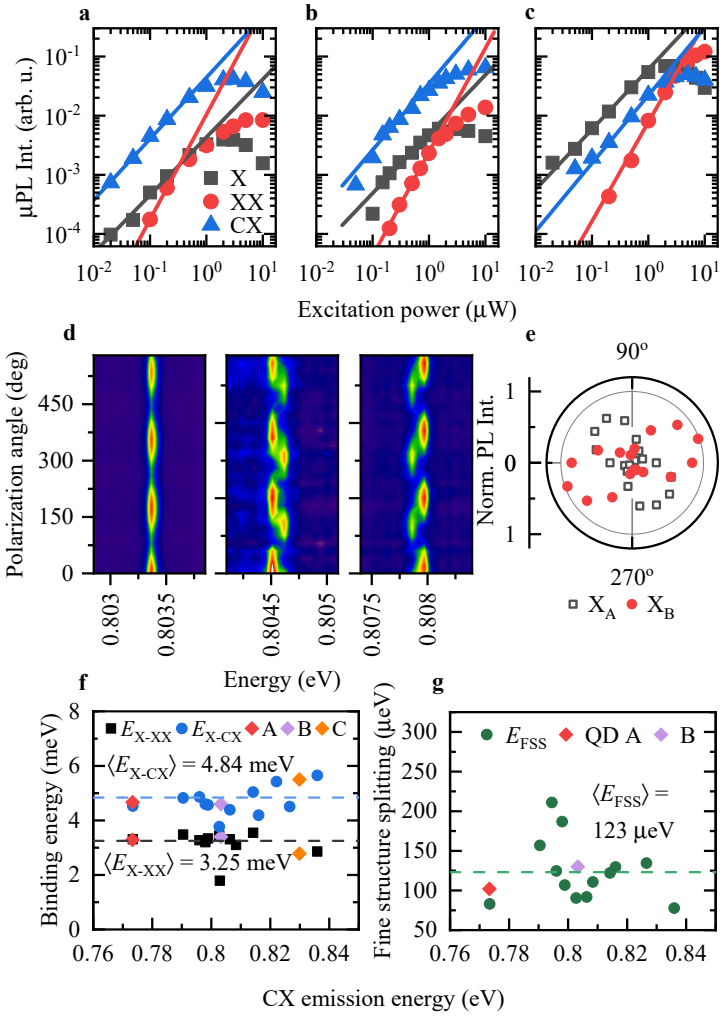

Supplementary Fig. S2. Excitonic complexes in InAs/InP QDs. **a-c**, Excitation power-dependent μPL intensity of identified lines in QDs: **a** A, **b** B, **c** C. **d**, Polarization-resolved μPL signal for excitonic complexes in QD B. **e**, Normalized polarization-resolved μPL intensity for X and XX in QD B. **f**, Binding energies for trions (E_{X-CX}) and for biexcitons (E_{X-XX}), with values for QDs A, B, and C marked with diamonds. **g**, Exciton fine structure splitting (E_{FSS}).

S-III. FDTD CALCULATIONS

In this section we investigate the influence of the QD position displacement in the mesa structure on the extraction efficiency. For that purpose, we employ finite-difference time-domain (FDTD) 3D Electromagnetic Simulator provided by Lumerical Inc. [14], as a complementary tool to the previous one based on the modal method (MM) [4]. More details of the employed FDTD method can be found elsewhere [15]. In order to establish convergence between the two numerical methods we first compare the results for the identical photonic mesa structures with D = 2 μm containing a point dipole at the central position $\Delta x = 0$ nm. Then, the FDTD approach was tuned to minimize deviation with respect to the modal method by slight change of the numerical aperture of the collected emission or the position of the 2D field-power monitor located above the mesa structure. Such tuning mechanism is visualized in Supplementary Fig. S4a as the black shaded area which overall is qualitatively similar to the results obtained by the modal method.

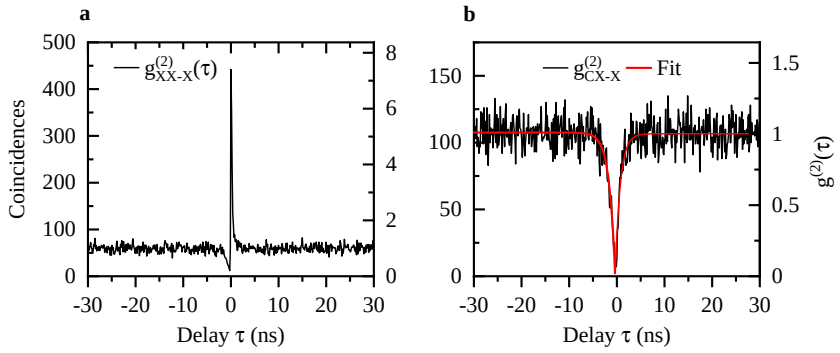

Supplementary Fig. S3. **a**, Cross-correlation of XX and X lines of QD C. **b**, Cross-correlation of CX and X lines of QD C with fit line (red).

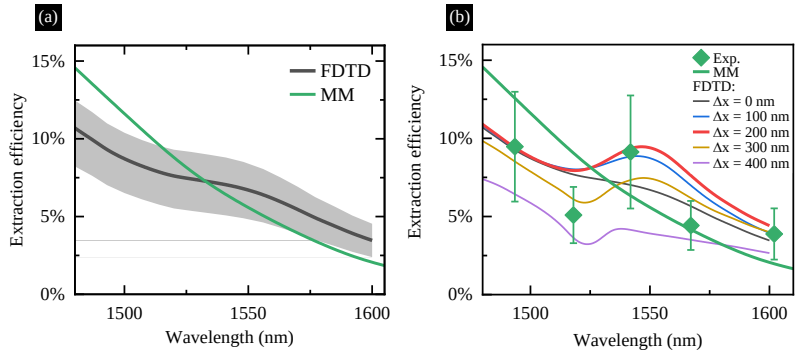

Supplementary Fig. S4. Analysis of the influence of the QD position in the mesa on the extraction efficiency. **a**, Comparison of calculated extraction efficiency between the FDTD and MM methods for the QD in the center of the mesa ($\Delta x = 0$ nm). The shaded uncertainty range results from different vertical screen positions (0.8 µm to 2.4 µm above the mesa surface) **b**, Dispersion of the extraction efficiency for different QD displacement from the center of the mesa (Δx).

Next, such consistent FDTD model was used to calculate the dispersion of extraction efficiency for a variety of the dipole displacements in the range of $\Delta x = 0$ nm to 400 nm. Starting from $\Delta x = 100$ nm, a local enhancement of extraction efficiency around 1.55 µm is already observable and this effect is further strengthened for $\Delta x = 200$ nm displacement, as it is shown in Supplementary Fig. S4b. Further shift of the dipole position causes decrease of the extraction efficiency values, and taking into account the experimental results we observe the best match for QD B at $\Delta x = 200$ nm, suggesting that the QDs are placed in between $\Delta x \approx 0$ nm to 200 nm.

S-IV. TIME-RESOLVED MICROPHOTOLUMINESCENCE FOR CX LINES IN QDS A-C

Low-temperature ($T = 4.2$ K) time-resolved µPL (TRPL) traces registered for QDs A, B, and C are presented in Supplementary Fig. S5 with solid black lines. Each trace is best fitted with a single-exponential decay function (red solid lines) to extract decay time constant τ_{PL}. We use the function of the form:

$$I(t) = A \exp(-t/\tau_{PL}), \tag{S4}$$

where $I(t)$ is the TRPL intensity at time t, and A is the amplitude of the signal. The extracted τ_{PL} values are 1.69 ± 0.01 ns (QD A), 2.61 ± 0.01 ns (QD B), and 1.92 ± 0.01 ns (QD C). The τ_{PL} times are rather typical for single InAs/InP QDs, independently of their exact size and symmetry [16–19] and agree with the τ_{dec} values (see comparison in Supplementary Tab. S2).

S-7

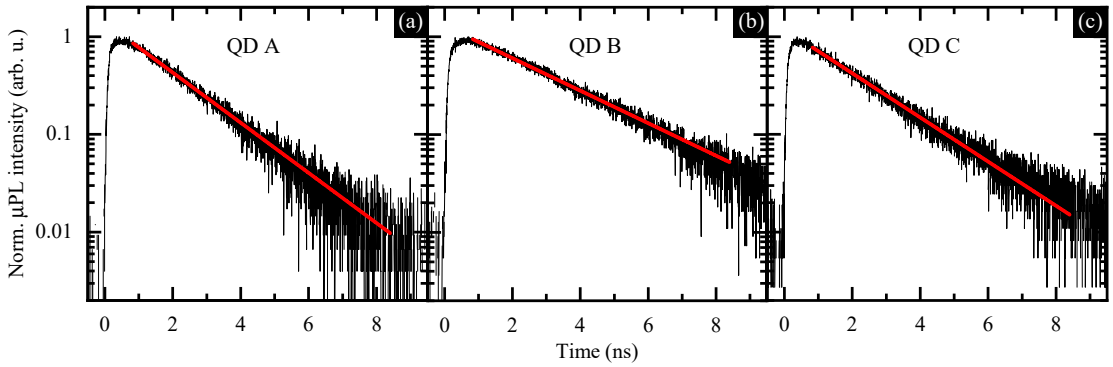

Supplementary Fig. S5. Time-resolved µPL traces for trions in QDs A-C: **a**, QD A, **b**, QD B, **c**, QD C. Red solid lines are fit lines to the experimental data (black lines), according to Eq. (S4).

S-V. CW AUTOCORRELATION HISTOGRAMS

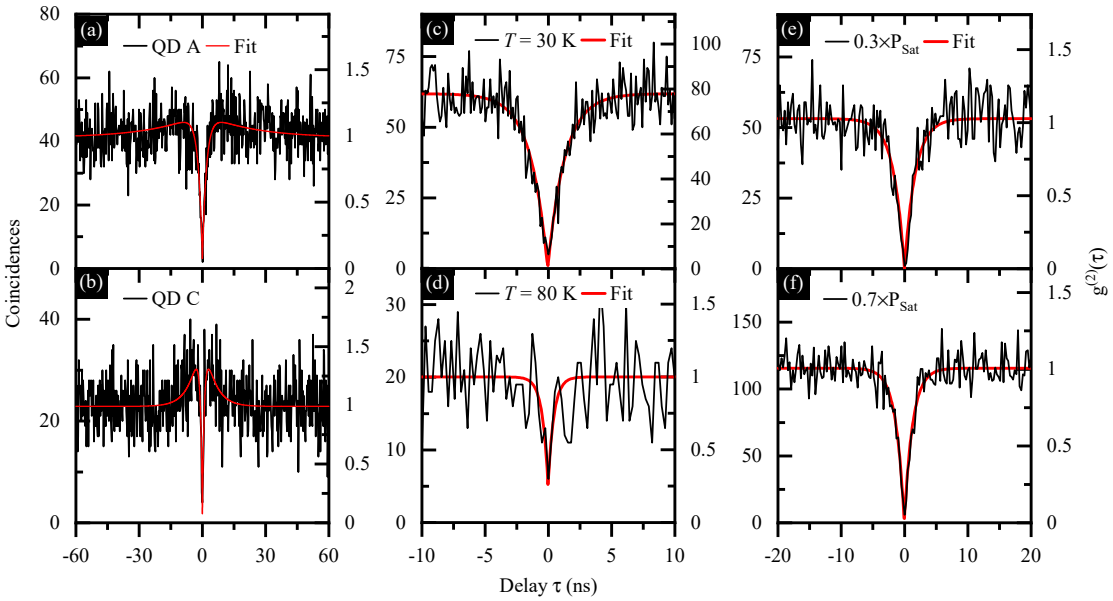

Supplementary Fig. S6. Evaluation of the single-photon emission purity for CX lines under cw excitation in QD **a**, A and **b**, C, and for CX line in QD B at elevated temperatures: recorded and C QD B, at **c**, $T = 30\,\mathrm{K}$, **d**, $T = 80\,\mathrm{K}$, and for **e**, $0.3 \times P_{\mathrm{Sat}}$ and **f**, $0.7 \times P_{\mathrm{Sat}}$.

In this section we present the histograms that broaden the discussion of the single-photon emission quality for investigated SPEs, presented in Fig. 4 in the article. Here, we focus on the cw excitation of the CX lines, and we show the autocorrelation histograms for QDs A and C in Supplementary Fig. S6a and Supplementary Fig. S6b, respectively, together with fit lines. The histograms were recorded for the laser excitation power corresponding to the $0.7 \times P_{\mathrm{Sat}}$ of the respective lines. We observe an additional weak bunching effect which we attribute to the blinking caused by the interaction with carrier traps in the QD vicinity or background doping [3, 20], and we fit the normalized histograms with the function [21]

$$g^{(2)}(\tau) = 1 - A\exp(-|\tau|/\tau_1) + B\exp(-|\tau|/\tau_2), \tag{S5}$$

where A and B are fit parameters, while τ_1 and τ_2 are antibunching and bunching time constants, respectively. The $g^{(2)}(0)$

value is obtained as $g^{(2)}(0) = 1 - A + B$. Determined parameters are $g^{(2)}(0) = 0.074$ ($\sigma = 0.062$), $\tau_1 = 1.93 \pm 0.15$ ns, and $\tau_2 = 22.7 \pm 3.0$ ns for QD A, and $g^{(2)}(0) = 0.07$ ($\sigma = 0.11$), $\tau_1 = 0.97 \pm 0.09$ ns, and $\tau_2 = 4.81 \pm 0.45$ ns for QD C. These $g^{(2)}(0)$ values are displayed in Supplementary Tab. S3 for their easier comparison.

Then, we show the histograms for CX in QD B registered under the same excitation conditions as in Figs. 4b-c, except for the temperature of the structure (Supplementary Figs. S6c-S6d) and excitation power (Supplementary Figs. S6e-S6f). We fit the normalized histograms with the standard function shown in Eq. (**??**). For the Stirling-compatible temperature of $T = 30$ K we obtain almost perfect single-photon emission with the purity of $g^{(2)}(0)_{30\,\mathrm{K}} = 0$ ($\sigma = 0.054$, Supplementary Fig. S6c). Moreover, we record the histogram at 80 K sample temperature, achievable with a liquid nitrogen dewar. Although the reduction of the signal-to-noise ratio for investigated line results in a pronounced noise in the recorded histogram, the dip at zero delay is still visible and the single photon purity can be estimated. We obtain $g^{(2)}(0)_{\mathrm{fit},80\,\mathrm{K}} = 0.25(\sigma = 0.19)$. We note that the achieved purity at $T = 80$ K is higher than the record values of $g^{(2)}(0) = 0.34$ and $g^{(2)}(0) = 0.33$ previously reported at this temperature and at 1.55 µm emission wavelength achieved with InAs/InAlGaAs/InP quantum dashes [22, 23] and InAs/GaAs QDs grown with the metamorphic approach [24], respectively. Importantly, both these previous approaches are obtained in different carrier confinement conditions, InAlGaAs or GaAs barriers respectively, and thus cannot be directly compared with the pure InAs/InP system investigated here.

Next, for the C-band QD B we study the quantum nature of the emission in the excitation power-dependent photon autocorrelation measurements under cw non-resonant excitation. Supplementary Figs. S6e-S6f present the autocorrelation histograms corresponding to the excitation of the CX line under $0.3 \times P_{\mathrm{Sat}}$ (Supplementary Fig. S6e), and $0.7 \times P_{\mathrm{Sat}}$ (Supplementary Fig. S6f), where P_{Sat} is the laser excitation power corresponding to the saturation of the line's µPL intensity. We fit the histograms using Eq. (**??**), and achieve the values of $g^{(2)}(0) = 0$ for all probed excitation powers, with $\sigma = 0.075, 0.056, 0.038$ for $0.3 \times P_{\mathrm{Sat}}$, $0.7 \times P_{\mathrm{Sat}}$, and P_{Sat}[25], respectively. The increasing pump rate W_p results in the decrease of t_r so that $t_r = (1.70 \pm 0.19)$ ns, $t_r = (1.31 \pm 0.11)$ ns, and $t_r = (1.12 \pm 0.06)$ ns for $0.3 \times P_{\mathrm{Sat}}$, $0.7 \times P_{\mathrm{Sat}}$, and P_{Sat}, respectively.

The obtained $g^{(2)}(0)$ for CX in the QD B are repeated in Supplementary Tab. S4.

S-VI. TEMPERATURE-DEPENDENT PHOTOLUMINESCENCE OF QD B

The temperature-dependent µPL of the QD B is recorded in the temperature range of $T = 5$ K to 120 K and analyzed before recording the autocorrelation histograms at elevated temperatures, shown in Fig. 4c. The spectra, the temperature-dependent quench of CX and X lines, and the linewidth broadening of the CX line are presented in Supplementary Fig. S7.

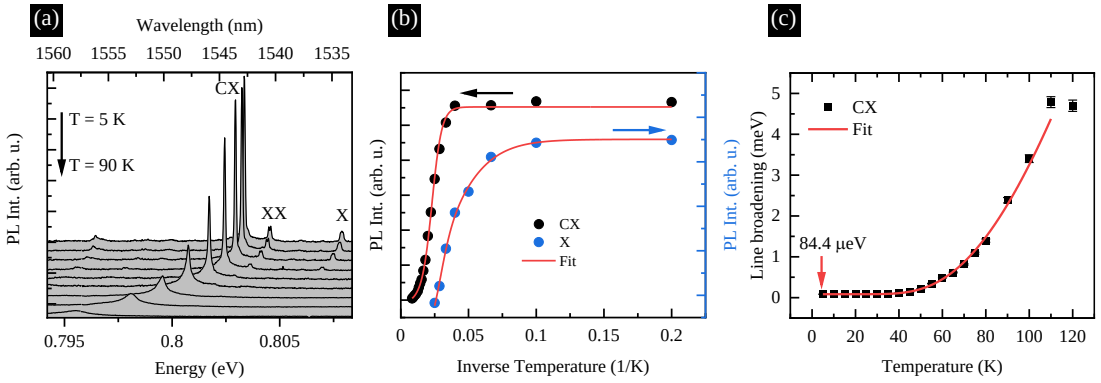

Supplementary Fig. S7. Analysis of the temperature-dependent µPL spectra for QD B. **a**, µPL spectra taken at different temperatures in the range of $T = 5$ K to 90 K. **b**, µPL intensity for X and CX lines fitted with the Arrhenius formula (red lines), according to Eq. (S6). **c**, Broadening of the CX line with the fitted temperature dependence of Eq. (S7).

To identify the most efficient carrier excitation channels, the temperature-dependent µPL intensity is fitted with a standard formula assuming two activation processes [26]:

$$I(T) = \frac{I_0}{1 + B_1 \exp(-E_{\mathrm{a},1}/k_{\mathrm{B}}T) + B_2 \exp(-E_{\mathrm{a},2}/k_{\mathrm{B}}T)}, \tag{S6}$$

where I_0 is the PL intensity for $T \to 0$, $E_{\mathrm{a},1}$ and $E_{\mathrm{a},2}$ are activation energies, and B_1 and B_2 are relative rates corresponding to the efficiency of involved processes. We achieve the activation energies of $E_{\mathrm{a},1} = 23.6 \pm 0.8$ meV and $E_{\mathrm{a},2} = 81.1 \pm 15$ meV for CX

and $E_{a,1} = 5.0 \pm 1.5$ meV and $E_{a,2} = 22.2 \pm 7.3$ meV for X. We find that for both lines the dominant process responsible for the μPL intensity quench is the one corresponding to the $E_{a,2}$ energy, as the rates ratio $B_1 : B_2$ is 1 : 264 and 1 : 402 for CX and X lines, respectively. Interestingly, both complexes share the activation energy in the range of ∼22 meV to 24 meV, in agreement with the value obtained for the CX line in similar QDs [13], where the values of $E_{a,1} = 0.8 \pm 0.5$meV and $E_{a,2} = 23 \pm 5$meV were reported for a CX. There, the process corresponding to the $E_{a,2}$ activation energy was attributed as the charge transfer to higher orbital states, based on the band structure calculations within the 8-band $k \cdot p$ framework. Furthermore, for a QD emitting around the 1.55 μm spectral range, the calculated energy distance for holes between their QD and WL ground states is in the range of 70 meV to 90 meV [13], therefore we attribute the $E_{a,2} = 81.1 \pm 15$meV estimated for the CX as the excitation of the hole from the QD B to the WL ground state.

The temperature dependence of linewidth was fitted with the formula that includes the contribution of thermally-activated phonon sidebands to the zero-phonon line [27, 28],

$$\Gamma(T) = \Gamma(4.2\,\mathrm{K}) + a\left[\exp\left(\frac{E_{\mathrm{ph},\Gamma}}{k_B T}\right) - 1\right]^{-1}, \tag{S7}$$

where k_B is the Boltzmann constant, parameter $a = 72.8 \pm 6.8$ meV and $E_{\mathrm{ph},\Gamma} = 27.39 \pm 0.55$ meV is an average energy of phonons. From the fitting we obtain the initial CX line broadening of $\Gamma(4.2\,\mathrm{K}) = 84.4 \pm 1.2$ μeV what is above the lifetime-limited linewidth (0.5 μeV to 0.8 μeV, according to TRPL data in Supplementary Fig. S5) as well as above the spectral resolution of the μPL setup (∼25 μeV) and so points to the presence of spectral diffusion due to the deep charge traps in the QD vicinity, also on the etched mesa walls [29]. On the other hand, the initial broadening is much lower than in the previously fabricated structure with InAs/InP QDs in mesas of 340 μeV [13].

S-VII. SUMMARY OF DERIVED PARAMETERS

In Supplementary Tab. S1 we provide the fit parameters for the histograms obtained under cw laser excitation for QDs A, B, and C. The purity $\mathscr{P}$ is defined as $\mathscr{P} = 1 - g^{(2)}(0)$. For the purity determination we take the fitted values of $g^{(2)}(0)_{\mathrm{fit}}$ unless $g^{(2)}(0)_{\mathrm{fit}} = 0$. In such cases, we employ the more conservative estimation of purity, utilizing the $g^{(2)}(0)_{\mathrm{raw}} = C(0)/N$ value (Eq. (**??**)).

Supplementary Table S1. Fit parameters of single-photon emission under cw excitation (Supplementary Figs. S6a-S6b for QDs A and C, Supplementary Fig. S6f for QD B).

Different QDs, cw excitation			
QD	$g^{(2)}(0)_{\mathrm{fit}}$	$g^{(2)}(0)_{\mathrm{raw}}$	$\mathscr{P}$
A	0 ($\sigma = 0.11$)	0.0480	$\left(95.2^{+4.8}_{-6.2}\right)$ %
B	0 ($\sigma = 0.056$)*	0.0519	$\left(94.8^{+5.2}_{-0.4}\right)$ %
C	0.07 ($\sigma = 0.11$)	0.173	$\left(93^{+7}_{-11}\right)$ %

* At $0.7 \times P_{\mathrm{Sat}}$.

In Supplementary Tab. S2 we give the fit parameters for histograms obtained for the pulsed laser excitation (see Methods section for the fitting formula). B is the level of background coincidences, A is a scaling parameter related to secondary photon emission, H is an average non-zero peak height, τ_{dec} and τ_{cap} are the decay and capture time constants, respectively. The corresponding histograms are shown in Fig. 4 and Supplementary Figs. S6a-S6b. We give also the μPL decay time τ_{PL} recorded in time-resolved μPL experiment (the corresponding μPL decay traces are presented in Supplementary Fig. S5). The uncertainties given in Supplementary Tab. S2 are standard errors of the fitting procedure (σ).

Supplementary Table S2. Fit parameters of single-photon emission under CW and pulsed excitation for QDs A-C (Fig. 4a) with PL decay times (Fig. S5).

	Different QDs, pulsed excitation					TRPL
QD	B	A	H	τ_{cap}	τ_{dec}	τ_{PL}
A	0.86 ± 0.05	12.49 ± 0.90	37.30 ± 0.16	0.34 ± 0.07 ns	1.91 ± 0.02 ns	1.69 ± 0.01 ns
B	13.32 ± 0.16	176 ± 15	152.35 ± 0.47	2.28 ± 0.05 ns	2.80 ± 0.02 ns	2.61 ± 0.01 ns
C	1.41 ± 0.15	11.2 ± 2.0	76.82 ± 0.58	0.44 ± 0.17 ns	1.99 ± 0.02 ns	1.92 ± 0.01 ns

* At $0.7 \times P_{\mathrm{Sat}}$.

Supplementary Tab. S3 gives the derived $g^{(2)}(0)$ function values for pulsed excitation together with corresponding purity. We give both the $g^{(2)}(0)$ value based on the level of coincidences at $\tau = 0$ compared with H, and based on the area under the zero histogram peak. See Methods section for the applied formulas with and without the background correction. The uncertainties given in Supplementary Tab. S3 are combined standard uncertainties based on A and H standard fitting errors.

Supplementary Table S3. $g^{(2)}(0)$ values and corresponding purity $\mathscr{P}$ of the single-photon emission under pulsed excitation (Fig. 4a) derived based on the fit parameters given in Supplementary Tab. S2.

Different QDs, pulsed excitation						
	Function value approach		Peak area approach			
	Fit value at $\tau = 0$		Histogram background included		Histogram background subtracted	
QD	$g^{(2)}(0) = B/H$	$\mathscr{P} = 1 - g^{(2)}(0)$	$g^{(2)}(0)_{\text{area}}$	$\mathscr{P}_{\text{area}}$	$g^{(2)}(0)_{\text{area}}$	$\mathscr{P}_{\text{area}}$
A	0.023 ± 0.010	97.7 ± 1.0 %	0.371 ± 0.020	62.9 ± 2.0 %	0.276 ± 0.002	72.4 ± 2.0 %
B	0.087 ± 0.017	91.3 ± 1.7 %	0.433 ± 0.018	56.7 ± 1.8 %	0.209 ± 0.018	79.1 ± 1.8 %
C	0.018 ± 0.012	98.2 ± 1.2 %	0.205 ± 0.02	79.5 ± 2.0 %	0.114 ± 0.02	88.6 ± 2.0 %

* At $0.7 \times P_{\text{Sat}}$.

Supplementary Tab. S4 displays the fit parameters obtained for CX in QD B, for the excitation-power- and temperature-dependent autocorrelation histograms. Again, for the determination of $\mathscr{P}$ we use the fitted values of $g^{(2)}(0)_{\text{fit}}$ unless $g^{(2)}(0)_{\text{fit}} = 0$. In such cases, we utilize the $g^{(2)}(0)_{\text{raw}} = C(0)/N$ value.

Supplementary Table S4. The histogram fit parameters obtained for CX in QD B, for excitation power- and temperature-dependent autocorrelation histograms [see Figs. 4b-c and Supplementary Figs. S6c-S6f].

QD B, cw excitation							
Excitation power series				Temperature series			
Laser power	$g^{(2)}(0)_{\text{fit}}$	$g^{(2)}(0)_{\text{raw}}$	$\mathscr{P}$	Temperature	$g^{(2)}(0)_{\text{fit}}$	$g^{(2)}(0)_{\text{raw}}$	$\mathscr{P}$
$0.3 \times P_{\text{Sat}}$	0 ($\sigma = 0.075$)	0.0188	$\left(98.1^{+1.9}_{-5.6}\right)$ %	30 K	0 ($\sigma = 0.054$)	0.0808	91.9 ± 5.4%
$0.7 \times P_{\text{Sat}}$	0 ($\sigma = 0.056$)	0.0519	$\left(94.8^{+5.2}_{-0.4}\right)$ %	50 K	0.017 ($\sigma = 0.096$)	0.0486	$\left(98.3^{+1.7}_{-7.9}\right)$ %
P_{Sat}	0 ($\sigma = 0.038$)	0.0272	$\left(97.3^{+2.7}_{-1.1}\%\right)$	80 K	0.25 ($\sigma = 0.19$)	0.299	75 ± 19%

[1] M. Gschrey, A. Thoma, P. Schnauber, M. Seifried, R. Schmidt, B. Wohlfeil, L. Krüger, J. H. Schulze, T. Heindel, S. Burger, F. Schmidt, A. Strittmatter, S. Rodt, and S. Reitzenstein, Highly indistinguishable photons from deterministic quantum-dot microlenses utilizing three-dimensional in situ electron-beam lithography, Nat. Commun. **6**, 7662 (2015).

[2] J. Yang, C. Nawrath, R. Keil, R. Joos, X. Zhang, B. Höfer, Y. Chen, M. Zopf, M. Jetter, S. L. Portalupi, F. Ding, P. Michler, and O. G. Schmidt, Quantum dot-based broadband optical antenna for efficient extraction of single photons in the telecom O-band, Opt. Express **28**, 19457 (2020).

[3] H. Kumano, T. Harada, I. Suemune, H. Nakajima, T. Kuroda, T. Mano, K. Sakoda, S. Odashima, and H. Sasakura, Stable and efficient collection of single photons emitted from a semiconductor quantum dot into a single-mode optical fiber, Appl. Phys. Express **9**, 032801 (2016).

[4] U. M. Gür, S. Arslanagić, M. Mattes, and N. Gregersen, Open-geometry modal method based on transverse electric and transverse magnetic mode expansion for orthogonal curvilinear coordinates, Phys. Rev. E **103**, 033301 (2021).

[5] A. V. Lavrinenko, J. Lgsgaard, and N. Gregersen, *Numerical Methods in Photonics* (CRC PR INC, 2014).

[6] L. Li, Formulation and comparison of two recursive matrix algorithms for modeling layered diffraction gratings, J. Opt. Soc. Amer. A **13**, 1024 (1996).

[7] C. A. Balanis, *Antenna Theory: Analysis and Design* (Wiley John + Sons, 2016).

[8] M. Abbarchi, C. Mastrandrea, T. Kuroda, T. Mano, A. Vinattieri, K. Sakoda, and M. Gurioli, Poissonian statistics of excitonic complexes in quantum dots, J. Appl. Phys. **106**, 053504 (2009).

[9] M. H. Baier, A. Malko, E. Pelucchi, D. Y. Oberli, and E. Kapon, Quantum-dot exciton dynamics probed by photon-correlation spectroscopy, Phys. Rev. B **73**, 205321 (2006).

[10] Y. Léger, L. Besombes, L. Maingault, and H. Mariette, Valence-band mixing in neutral, charged, and Mn-doped self-assembled quantum dots, Phys. Rev. B **76**, 045331 (2007).

[11] T. Belhadj, T. Amand, A. Kunold, C.-M. Simon, T. Kuroda, M. Abbarchi, T. Mano, K. Sakoda, S. Kunz, X. Marie, and B. Urbaszek, Impact of heavy hole-light hole coupling on optical selection rules in GaAs quantum dots, Appl. Phys. Lett. **97**, 051111 (2010).

[12] C. Tonin, R. Hostein, V. Voliotis, R. Grousson, A. Lemaitre, and A. Martinez, Polarization properties of excitonic qubits in single self-assembled quantum dots, Phys. Rev. B **85**, 155303 (2012).

S-11

[13] P. Holewa, M. Gawełczyk, C. Ciostek, P. Wyborski, S. Kadkhodazadeh, E. Semenova, and M. Syperek, Optical and electronic properties of low-density InAs/InP quantum-dot-like structures designed for single-photon emitters at telecom wavelengths, Phys. Rev. B **101**, 195304 (2020).
[14] Https://www.lumerical.com/products/.
[15] P. Mrowiński and G. Sęk, Modelling the enhancement of spectrally broadband extraction efficiency of emission from single InAs/InP quantum dots at telecommunication wavelengths, Phys. B **562**, 141 (2019).
[16] K. Takemoto, M. Takatsu, S. Hirose, N. Yokoyama, Y. Sakuma, T. Usuki, T. Miyazawa, and Y. Arakawa, An optical horn structure for single-photon source using quantum dots at telecommunication wavelength, J. Appl. Phys. **101**, 081720 (2007).
[17] Ł. Dusanowski, M. Gawełczyk, J. Misiewicz, S. Höfling, J. P. Reithmaier, and G. Sęk, Strongly temperature-dependent recombination kinetics of a negatively charged exciton in asymmetric quantum dots at 1.55 µm, Appl. Phys. Lett. **113**, 043103 (2018), 1807.02836.
[18] M. Syperek, Ł. Dusanowski, J. Andrzejewski, W. Rudno-Rudziński, G. Sęk, J. Misiewicz, and F. Lelarge, Carrier relaxation dynamics in InAs/GaInAsP/InP(001) quantum dashes emitting near 1.55 µm, Appl. Phys. Lett. **103**, 083104 (2013).
[19] A. Musiał, P. Holewa, P. Wyborski, M. Syperek, A. Kors, J. P. Reithmaier, G. Sęk, and M. Benyoucef, High-Purity Triggered Single-Photon Emission from Symmetric Single InAs/InP Quantum Dots around the Telecom C-Band Window, Adv. Quantum Technol. **3**, 1900082 (2019).
[20] P. A. Dalgarno, J. McFarlane, D. Brunner, R. W. Lambert, B. D. Gerardot, R. J. Warburton, K. Karrai, A. Badolato, and P. M. Petroff, Hole recapture limited single photon generation from a single n-type charge-tunable quantum dot, Appl. Phys. Lett. **92**, 193103 (2008).
[21] M. Benyoucef, M. Yacob, J. P. Reithmaier, J. Kettler, and P. Michler, Telecom-wavelength (1.5 µm) single-photon emission from InP-based quantum dots, Appl. Phys. Lett. **103**, 162101 (2013).
[22] Ł. Dusanowski, M. Syperek, J. Misiewicz, A. Somers, S. Höfling, M. Kamp, J. P. Reithmaier, and G. Sęk, Single-photon emission of InAs/InP quantum dashes at 1.55 µm and temperatures up to 80 K, Appl. Phys. Lett. **108**, 163108 (2016).
[23] Y. Arakawa and M. J. Holmes, Progress in quantum-dot single photon sources for quantum information technologies: A broad spectrum overview, Appl. Phys. Rev. **7**, 021309 (2020).
[24] C. Carmesin, F. Olbrich, T. Mehrtens, M. Florian, S. Michael, S. Schreier, C. Nawrath, M. Paul, J. Höschele, B. Gerken, J. Kettler, S. L. Portalupi, M. Jetter, P. Michler, A. Rosenauer, and F. Jahnke, Structural and optical properties of InAs/(In)GaAs/GaAs quantum dots with single-photon emission in the telecom C-band up to 77 K, Phys. Rev. B **98**, 125407 (2018).
[25] The histogram recorded for P_{Sat} is shown in Fig. 4b.
[26] J. D. Lambkin, D. J. Dunstan, K. P. Homewood, L. K. Howard, and M. T. Emeny, Thermal quenching of the photoluminescence of InGaAs/GaAs and InGaAs/AlGaAs strained-layer quantum wells, Appl. Phys. Lett. **57**, 1986 (1990).
[27] D. Gammon, E. S. Snow, B. V. Shanabrook, D. S. Katzer, and D. Park, Homogeneous linewidths in the optical spectrum of a single gallium arsenide quantum dot, Science **273**, 87 (1996), https://science.sciencemag.org/content/273/5271/87.full.pdf.
[28] G. Moody, M. E. Siemens, A. D. Bristow, X. Dai, D. Karaiskaj, A. S. Bracker, D. Gammon, and S. T. Cundiff, Exciton-exciton and exciton-phonon interactions in an interfacial GaAs quantum dot ensemble, Phys. Rev. B **83**, 115324 (2011).
[29] G. Ortner, D. R. Yakovlev, M. Bayer, S. Rudin, T. L. Reinecke, S. Fafard, Z. Wasilewski, and A. Forchel, Temperature dependence of the zero-phonon linewidth in InAs/GaAs quantum dots, Phys. Rev. B **70**, 201301 (2004).

A.2 SM for *Quantum dots in nanocavities resulting from deterministic processing*

Supplemental Material

—

Scalable quantum photonic devices emitting indistinguishable photons in the telecom C-band

Paweł Holewa,[1,2,3,*] Emilia Zięba-Ostój,[1] Daniel A. Vajner,[4] Maja Wasiluk,[1] Benedek Gaál,[2] Aurimas Sakanas,[2] Marek Burakowski,[1] Paweł Mrowiński,[1] Bartosz Krajnik,[1] Meng Xiong,[2,3] Alexander Huck,[5] Kresten Yvind,[2,3] Niels Gregersen,[2] Anna Musiał,[1] Tobias Heindel,[4] Marcin Syperek,[1,†] and Elizaveta Semenova[2,3,‡]

[1]*Department of Experimental Physics, Faculty of Fundamental Problems of Technology, Wrocław University of Science and Technology, Wyb. Wyspiańskiego 27, 50-370 Wrocław, Poland*
[2]*DTU Electro, Department of Electrical and Photonics Engineering, Technical University of Denmark, Kongens Lyngby 2800, Denmark*
[3]*NanoPhoton-Center for Nanophotonics, Technical University of Denmark, 2800 Kongens Lyngby, Denmark*
[4]*Institute of Solid State Physics, Technische Universität Berlin, 10623 Berlin, Germany*
[5]*Center for Macroscopic Quantum States (bigQ), Department of Physics, Technical University of Denmark, 2800 Kongens Lyngby, Denmark*

CONTENTS

* pawel.holewa@pwr.edu.pl
† marcin.syperek@pwr.edu.pl
‡ esem@fotonik.dtu.dk

S-I. OPTICAL SIMULATIONS OF THE CAVITY GEOMETRY

The CBG geometry is modeled using a modal method employing a true open geometry boundary condition [1]. Here, the geometry is divided into uniform layers along a propagation z axis, and the field is expanded in eigenmodes of each uniform layer. The QD is modeled as a classical dipole emitter using the equivalence principle [2]. The eigenmode expansion coefficients in the QD layer are computed using the reciprocity theorem [3], and the fields are connected at each layer interface using the S matrix formalism [3, 4].

We model the Purcell factor $F_\mathrm{P} = P/P_0$ as the power P emitted by the classical dipole relative to the power P_0 in a bulk medium. The power P and the electric near field $\mathbf{E}(\mathbf{r})$ generated by a dipole $\mathbf{d}$ with frequency ω_0 at the position $\mathbf{r}_0$ can be written in terms of the optical Green's function $\overleftrightarrow{\mathbf{G}}(\mathbf{r},\mathbf{r}')$ as [2]

$$P(\mathbf{r}_0) = \frac{\omega_0^3 \mu_0 |\mathbf{d}|^2}{2} \mathrm{Im}\left(\mathbf{n}_\mathrm{d}^* \cdot \overleftrightarrow{\mathbf{G}}(\mathbf{r}_0,\mathbf{r}_0) \cdot \mathbf{n}_\mathrm{d}\right) \tag{S1}$$

$$\mathbf{E}(\mathbf{r}) = \omega_0^2 \mu_0 \overleftrightarrow{\mathbf{G}}(\mathbf{r},\mathbf{r}_0)\mathbf{d}, \tag{S2}$$

where $\mathbf{n}_\mathrm{d} = \mathbf{d}/|\mathbf{d}|$ is the dipole orientation. The corresponding far field $P_\mathrm{FF}(\theta,\varphi,\mathbf{r}_0)$ is then determined from Eq. (S2) using a standard near field to far field transformation [5]. The total collected power P_Lens detected by the lens with a given numerical aperture (NA) is obtained by integration of $P_\mathrm{FF}(\theta,\varphi,\mathbf{r}_0)$ over the unit solid angle Ω as

$$P_\mathrm{Lens}(\mathbf{r}_0) = \int_{\theta<\theta_\mathrm{NA}} P_\mathrm{FF}(\theta,\varphi,\mathbf{r}_0)\,\mathrm{d}\Omega, \tag{S3}$$

where θ_NA is defined by the NA of the lens. Finally, the extraction efficiency is defined as $\eta = P_\mathrm{Lens}/P$.

The dominant lines in all investigated QD-CBG devices are trions (CX) which emit circularly polarized photons ($\sigma^\pm$). We thus model the trion state dipole orientation as

$$\mathbf{n}_\mathrm{d} = \mathbf{n}_\mathrm{CX} = \frac{1}{\sqrt{2}}(\mathbf{r} \pm i\boldsymbol{\varphi}), \tag{S4}$$

where $\mathbf{r}$ and $\boldsymbol{\varphi}$ are unit vectors of the cylindrical coordinate system. Inserting Eq. (S4) into Eq. (S1), we obtain the power P_CX emitted by the trion given by

$$P_\mathrm{CX}(\mathbf{r}_0) = \frac{P_r(\mathbf{r}_0) + P_\varphi(\mathbf{r}_0)}{2}, \tag{S5}$$

where P_r (P_φ) is the power emitted by a dipole at position $\mathbf{r}_0$ oriented along the r (φ) axis. Similarly, the far field generated by the trion becomes

$$P_\mathrm{FF,CX}(\theta,\varphi,\mathbf{r}_0) = \frac{1}{2}\left(P_\mathrm{FF},_r(\theta,\varphi,\mathbf{r}_0) + P_\mathrm{FF},_\varphi(\theta,\varphi,\mathbf{r}_0)\right), \tag{S6}$$

where r and φ again refer to far fields generated by the two dipole orientations. Finally, the total photon extraction efficiency for the trion at the position $\mathbf{r}_0$ becomes

$$\eta_\mathrm{CX}(\mathbf{r}_0) = \frac{P_\mathrm{Lens,CX}(\mathbf{r}_0)}{P_\mathrm{CX}(\mathbf{r}_0)} = \frac{P_\mathrm{Lens},_r(\mathbf{r}_0) + P_\mathrm{Lens},_\varphi(\mathbf{r}_0)}{P_r(\mathbf{r}_0) + P_\varphi(\mathbf{r}_0)}. \tag{S7}$$

The near and far fields for the cavity mode are presented in Supplementary Fig. S1. The near-field profile shown in Supplementary Fig. S1a evidences the higher-order nature of the optimized cavity mode characteristic of the bullseye design [6].

The extraction efficiency η and Purcell factor F_P computed using Eq. (S5) and Eq. (S7) as a function of spatial misalignment ρ of the QD is presented in Supplementary Fig. S2. Whereas the photon extraction efficiency overall displays robustness towards misalignment, the decay of the Purcell factor with ρ is much more pronounced. The variations of F_P along the r and φ axes are quite different and result from the different variations of the field profile shown in Supplementary Fig. S1 along the x and y axes.

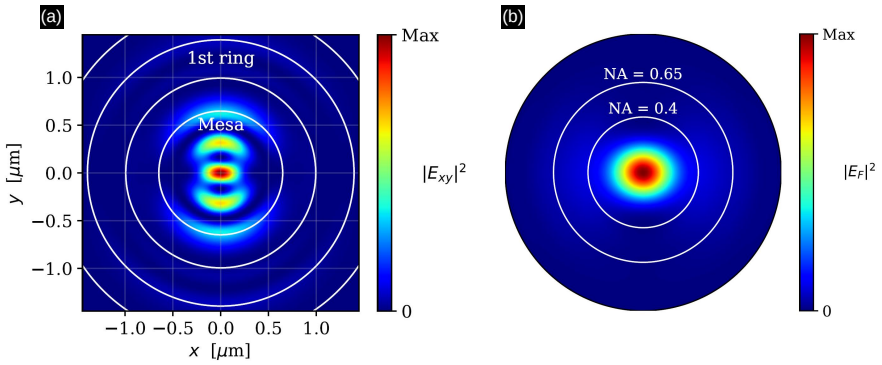

Supplementary Fig. S1. **a**, Near field and **b**, far field mode profiles of the CBG with 4 rings generated by a linear dipole $\mathbf{n}_d = \mathbf{r}$.

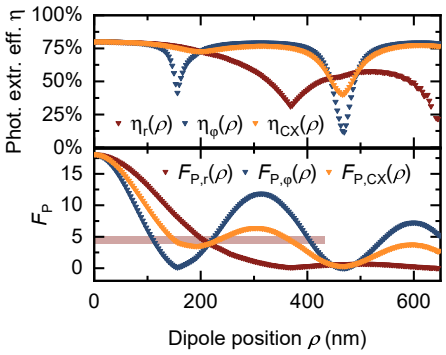

Supplementary Fig. S2. QD displacement tolerance: The photon extraction efficiency $\eta(\rho)$ (top) and Purcell factor $F_P(\rho)$ (bottom) as a function of the dipole-center separation ρ computed for the r, φ and CX dipole orientations.

S-II. NANOFABRICATION OF THE DEVICES

In this section, we present the details of the fabrication flow applied to realize the circular Bragg gratings with quantum dots. The fabrication of the structure is similar to the one presented in Ref. [7].

A. MOVPE growth of InAs/InP quantum dots

We start with the epi-ready InP wafer and grow the InGaAs etch stop and InP layers on a (001)-oriented InP substrate in the low-pressure metalorganic vapor-phase epitaxy (MOVPE) TurboDisc® reactor using arsine (AsH_3), phosphine (PH_3), tertiarybutylphosphine (TBP) and trimethylindium (TMIn) precursors with H_2 as a carrier gas. We grow the 0.5 µm-thick InP buffer and 200 nm-thick $In_{0.53}Ga_{0.47}As$ lattice-matched to InP at 610 °C and a 156 nm-thick InP layer. Then, the temperature is decreased to 493 °C, stabilized under TBP for 180 s and AsH_3 for 27 s. The nucleation of QDs occurs in the Stranski-Krastanov growth mode after deposition of nominally 1.22 ML-thick InAs at growth rate 0.53 ML/s under TMIn and AsH_3 flow rates of 11.8 µmol/min and 590 µmol/min, respectively (V/III ratio of 50). Nucleated QDs are annealed for 3.5 s at the growth temperature in AsH_3 ambient before the deposition of a 156 nm-thick InP capping layer (12 nm at 493 °C, and the remaining 144 nm after increasing the temperature up to 610 °C) what finishes the growth sequence.

Supplementary Figure S3 presents the atomic force microscopy (AFM) image of a reference structure that has the same InAs/InP quantum dots (grown under nominally same conditions) without InGaAs sacrificial layer and metallic mirror (no processing was done on this structure). We estimate the density of QDs to be $3.1 \times 10^8/\mathrm{cm}^2$ at the center of the wafer where the

S-4

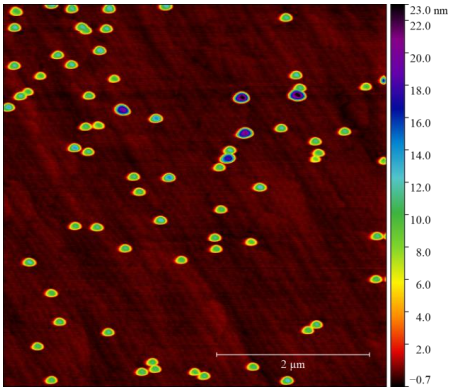

Supplementary Fig. S3. AFM image of the InP surface with InAs QDs grown in MOVPE under nominally the same conditions as those used for the imaging.

imaging fields are fabricated.

B. Fabrication of the sample for µPL imaging

Afterwards, SiO_2 is deposited in plasma-enhanced chemical vapor deposition (PECVD). This layer is intended to be 358.6 nm-thick. We cover it with a 120 nm-thick Al layer deposited via electron-beam evaporation. We bond the flipped structure to the Si chip carrier utilizing spin-coated AP3000 adhesion promoter and benzocyclobutene (BCB) on Si and AP3000 on the InP wafer. The bonding is done by applying the force of ~ 2 kN in vacuum at 250 °C. The substrate removal step is done by ~ 60 min dip in HCl and the InGaAs etch-stop layer is subsequently removed in H_2SO_4:H_2O_2:H_2O=1:8:80 mixture.

Next, by employing electron-beam lithography (EBL) followed by inductively coupled plasma-reactive ion etching (ICP-RIE) to etch InP down to SiO_2, we fabricate square imaging fields with 50 µm side-length and alignment marks (AMs) dedicated to EBL outside the fields. Therefore, we have different AMs for optical imaging (edges of the imaging fields) and for EBL alignment marks detection (InP crosses). This approach is justified by the simplification of the fabrication flow, as we do not deposit metallic AMs, relying instead on the outline of the field visible due to the µPL signal scattering from its edges. We check also that the material contrast between InP and SiO_2/Al regions is sufficient for the AM detection during the EBL alignment step.

C. Deterministic fabrication of the cavities

After determining the positions of QDs with respect to the AMs, we continue the deterministic workflow by the nanofabrication of the cavities. We deposit a 110 nm-thick SiN_x layer in PECVD on top of the InP membrane as a hard-mask and spin-coat CSAR e-beam resist on top of it. We expose the resist by the EBL, using the AMs outside the imaging fields in the form of InP crosses remaining on SiO_2. We develop the resist and transfer the cavities to the SiN_x hard-mask by employing ICP-RIE with SF_6-based etch recipe. Residual CSAR is stripped in Remover 1165 followed by 10 min descum in the barrel-type plasma asher. Subsequently, the pattern is transferred into the InP layer in ICP-RIE by HBr-based etch.

Supplementary Fig. S4 shows the optical microscope image of the sample's surface taken at 20× magnification with the cavities transferred to InP. The imaged fragment of the chip shows a 5×5 pattern of the imaging fields with four InP crosses at the corners of the pattern. Also visible are additional, 2 µm side-length square mesas.

S-III. ACCURACY OF DETERMINATION OF QD POSITIONS FROM µPL MAPS AND FINAL CAVITY POSITIONING

A. Signal-to-noise ratio

Supplementary Fig. S5 shows the histogram of signal-to-noise ratio (SNR) for the mapped QDs. The average SNR is 10.6 which underlines the crucial role of the 7-fold enhancement of the signal intensity for the planar structure by application of the

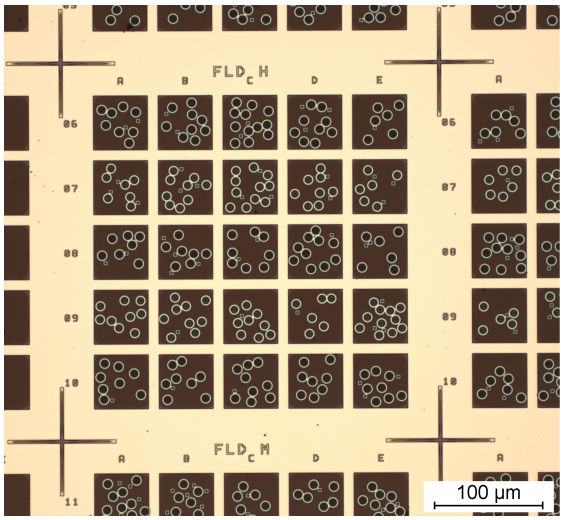

Supplementary Fig. S4. The optical microscope image of the sample's surface taken at 20× magnification with the cavities transferred to InP.

metallic mirror [7]. Based on this result, we deduce that for a sample without such a mirror, the SNR would be roughly 7 times lower (SNR of about 1.5), which would make the optical localization of QDs impossible (compare with the noise level in Figs. 2e and 2f in the main text).

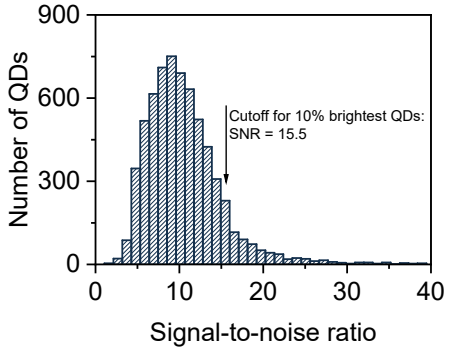

Supplementary Fig. S5. Histogram of signal-to-noise ratio for the recorded QD spots.

B. Localization algorithm

Our algorithm calculates the scaling factor $P\,[\mathrm{px}/\mu\mathrm{m}]$ to change the map unit from pixels (px) to µm. For a given µPL map, we identify n QD spots and take $2n$ cross-sections of the map (each QD is sectioned in two directions). The width of each cross-section is taken to equal a few pixels centered at the QD spot maximum to increase the signal-to-noise ratio (SNR). We found the best SNR for 10 pixels and used this value consistently.

For the i-th cross-section, we determine the positions $\mathbb{M}_{i,l}\,[\mathrm{px}]$, $\mathbb{M}_{i,u}\,[\mathrm{px}]$[1] of the field boundaries (acting as reference/alignment marks, AMs; indices l and u stand for lower and upper field boundaries, the same indices are applied also for left and right field

[1] For clarity, we use the blackboard-bold font for quantities given in pixels, e. g. $\mathbb{M}$, $\mathbb{Q}$. The normal font is used for the same dimensions given in µm, e. g. Q.

edges) and $\mathbb{Q}_i$ [px] for the QD spot position. All values $\mathbb{M}_{i,l}$, $\mathbb{M}_{i,u}$, and $\mathbb{Q}_i$ are the centers of the Gaussian peaks, fitted to respective maxima on the μPL map cross-section. Additionally, we assume that each field is a square of size $F = 50\,\mu$m.

P is calculated by averaging over all cross-section-related coefficients P_i recorded for a given field ($P = \bar{P}_i$) to ensure its highest accuracy, according to the formula

$$P = \frac{1}{2n}\sum_{i=1}^{2n} P_i = \frac{1}{2n}\sum_{i=1}^{2n} \frac{|\mathbb{M}_{i,u} - \mathbb{M}_{i,l}|}{F}. \tag{S8}$$

Calculating P separately for each map accounts for possible slight changes in the magnification due to defocusing of the sample surface during the cryostat translation, however, we find very low dispersion of P coefficients for different μPL maps (see the following section and Supplementary Fig. S6).

Then, the i-th QD position Q_i [μm] (vertical or horizontal) is calculated as

$$Q_i = \frac{\mathbb{Q}_i - \mathbb{M}_{i,l}}{P}. \tag{S9}$$

C. Uncertainty of scaling the μPL maps

The accuracy of the scaling factor ΔP_i for a single (i-th) μPL map cross-section can be calculated by propagating the uncertainties in Eq. (S8):

$$\Delta P_i = \sqrt{\left(\frac{\Delta\mathbb{M}_{i,u}}{F}\right)^2 + \left(\frac{\Delta\mathbb{M}_{i,l}}{F}\right)^2 + \left(\frac{\Delta F}{F^2}\right)^2}.$$

The uncertainty of the field size ΔF has two contributions, the uncertainty of the electron beam lithography alignment, estimated to $\Delta C = 40\,$nm [8] and the over-etching Δx during the ICP-RIE step (estimated to be up to $\Delta x = 40\,$nm), potentially influencing F by $2\Delta x = 80\,$nm. $\Delta\mathbb{M}_{i,u}$ and $\Delta\mathbb{M}_{i,l}$ are standard errors of the numerical fitting.

However, to increase the accuracy of the determination of the scaling factor, we average the P_i values for all cross-sections taken in a particular μPL map, as can be seen in Eq. (S8), so as the uncertainty ΔP we adopt the estimator of the standard error of mean $\hat{\sigma}_{\bar{P}_i}$ for the sample defined as a set of all $2n$ factors $P_i = |\mathbb{M}_{i,u} - \mathbb{M}_{i,l}|/F$ determined for a given μPL map:

$$\Delta P = \hat{\sigma}_{\bar{P}_i} = \frac{\sigma_{P_i}}{\sqrt{2n}}, \tag{S10}$$

where σ_{P_i} is the sample standard deviation.

According to calculated statistics for $m = 84$ exemplary μPL maps, we can compare the estimators of the standard error of mean $\hat{\sigma}_{\bar{P}_i}$ determined separately for each μPL map and reach the following conclusions:

1. We find that the coefficients P_i are very close to each other, evidencing no perceptible elongation or distortion of the registered images. This can be evaluated by the analysis of the set of calculated (for all m maps) uncertainties $\Delta P = \hat{\sigma}_{\bar{P}_i}$ scaled by the determined P factors: $\delta P = \Delta P/P$. We plot the histogram of δP in Supplementary Fig. S6 and find the median value of δP-distribution of 0.06 %. In other words, for half of the analyzed maps, the distribution of P_i factors is sufficiently narrow to determine the P factor with relative uncertainty $\delta P < 0.06\,\%$. This value includes the potential elongation of the image (difference in vertically and horizontally determined P_i factors).

2. The stability of the setup and overall repetitivity of the imaging process is high as the image magnification varies very little between maps. This can be evaluated by the estimator of the standard error of mean $\hat{\sigma}_{\bar{P}}$ calculated not for different cross-sections [averaging P_i values for a given map, as in Eq. (S8)] but for different maps (averaging P values for all maps). We obtain $\hat{\sigma}_{\bar{P}}/\bar{P} = 0.013\,\%$. We take this value as the estimation of variation of the setup magnification during the imaging process.

Then, the accuracy of cavity positioning ΔR depends primarily on the accuracy of the QD localization (ΔQ) and EBL alignment uncertainty ΔC. The ΔQ itself depends on the fit standard errors ($\Delta\mathbb{M}$, $\Delta\mathbb{Q}$), and scaling factor uncertainty ΔP.

D. Image rotation φ

Although we carefully align the image of the field with the horizontal and vertical axes of the detector array, we assume that there can be some indiscernible rotation of the image φ on the level of up to a few degrees. Even if this is the case, the rotation

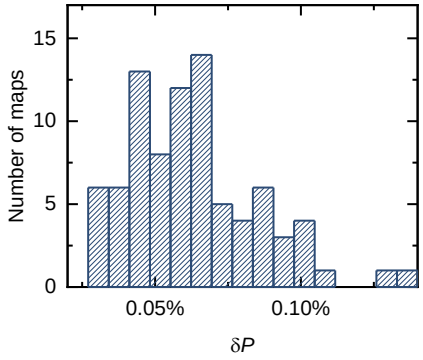

Supplementary Fig. S6. The histogram of relative μPL map scaling uncertainty $\delta P = \Delta P/P$ for the set of analyzed $m = 84$ exemplary μPL maps.

results first in the larger separation between AM peaks in the cross-sections ($|\mathbb{M}_{i,u} - \mathbb{M}_{i,l}|/\cos\varphi$ instead of $|\mathbb{M}_{i,u} - \mathbb{M}_{i,l}|$) and this is translated to scaled P: $P \to P/\cos\varphi$, according to Eq. (S8). The distance between lower AM and QD is however also elongated, $\left(\mathbb{Q}_i - \mathbb{M}_{i,l}\right)/\cos\varphi$ instead of $\left(\mathbb{Q}_i - \mathbb{M}_{i,l}\right)$. According to Eq. (S9), the new QD position is:

$$Q_{i,\mathrm{new}} = \frac{\left(\mathbb{Q}_i - \mathbb{M}_{i,l}\right)/\cos\varphi}{P/\cos\varphi} = Q_i,$$

so that the slight image rotation has no influence on the determination of QD position Q_i in our approach.

E. One-dimensional QD position ΔQ_i

The determination of i-th QD position Q_i is influenced by the scaling factor uncertainty ΔP, as well as QD ($\Delta\mathbb{Q}_i$) and lower AM ($\Delta\mathbb{M}_{i,l}$) fit uncertainties (standard errors of the numerical fitting), and is calculated by propagating the uncertainties, according to Eq. (S9):

$$\Delta Q_i = \sqrt{\left(\frac{\Delta\mathbb{Q}_i}{P}\right)^2 + \left(\frac{\Delta\mathbb{M}_{i,l}}{P}\right)^2 + \left(\frac{\left(\mathbb{Q}_i - \mathbb{M}_{i,l}\right)\Delta P}{P^2}\right)^2}. \tag{S11}$$

F. Two-dimensional QD position ΔQ

We combine the one-dimensional QD position uncertainties ΔQ_i into the two-dimensional uncertainty using the formula

$$\Delta Q = \sqrt{(\Delta Q_h)^2 + (\Delta Q_v)^2}, \tag{S12}$$

where ΔQ_h, ΔQ_v are ΔQ_i values calculated according to Eq. (S11) for horizontal and vertical cross-sections. We use the ΔQ value to determine the accuracy of our μPL imaging method.

G. Distance between QD position and cavity center R – accuracy of cavity positioning ΔR

We express the uncertainty ΔR of the expected distance $R = 0$ between the QD position and the cavity center as

$$\Delta R = \sqrt{(\Delta Q)^2 + (\Delta C)^2}. \tag{S13}$$

H. Example calculations for QD-CBGs #1–#3

Finally, in Supplementary Tab. S1 we show the uncertainties involved in the determination of the QD position ΔQ_i accordingly to Eq. (S11) and of the accuracy of cavity positioning ΔR accordingly to Eq. (S13) for three exemplary QD-CBGs #1–#3, described in the article (QD-CBG #1 and QD-CBG #2) and in the following part of the **Supplemental Material** (QD-CBG #3).

Supplementary Table S1. Uncertainties involved in the determination of accuracy of cavity positioning ΔR for exemplary devices QD-CBGs #1–#3.

Device	Orientation	$\Delta\mathbb{Q}_i/P$	$\Delta\mathbb{M}_i/P$	$(\mathbb{Q}_i-\mathbb{M}_{i,l})\,\Delta P/P^2$	ΔQ_i	ΔQ	ΔR
QD-CBG #1	Vertical	61.0 nm	14.4 nm	19.9 nm	65.8 nm	141.9 nm	147.4 nm
	Horizontal	120.0 nm	29.0 nm	23.5 nm	125.7 nm		
QD-CBG #2	Vertical	61.9 nm	12.7 nm	20.1 nm	66.3 nm	137.3 nm	143.0 nm
	Horizontal	115.7 nm	26.1 nm	20.2 nm	120.2 nm		
QD-CBG #3	Vertical	112.2 nm	20.7 nm	12.0 nm	114.7 nm	132.9 nm	138.8 nm
	Horizontal	59.5 nm	19.5 nm	24.6 nm	67.2 nm		

I. Calculation of the diffraction-limited spot size

In this and the following subsections, we consider a QD as a point light source and calculate the expected observed width of such a source in our imaging setup shown in Fig. 2a of the main text. Its emission can be described by the point spread function (PSF) of the setup, which for the approximation of 2D paraxial wide-field fluorescence microscope forms an Airy disc (first-order Bessel function of the first kind) [9].

Our QD localization algorithm uses the approximation of the Bessel function by the Gaussian profile, which we use for fitting the QD- and AM-related signal in the cross-sections of μPL maps.

First, we calculate the standard deviation σ_{diff} of the Gaussian curve that best approximates the PSF of our setup according to the formula [9]:

$$\sigma_{\text{diff}} \approx 0.21\frac{\lambda_{\text{QD}}}{\text{NA}} = 0.501\,\mu\text{m} \tag{S14}$$

with employed NA = 0.65 and $\lambda_{\text{QD}} = 1.55\,\mu$m. Then, we translate σ_{diff} to full width at half-maximum (FWHM) as

$$\text{FWHM}_{\text{diff}} = 2\sqrt{2\ln 2}\times\sigma_{\text{diff}} \approx 1.18\,\mu\text{m}. \tag{S15}$$

J. Statistics on QD spot size and the accuracy of QD positioning

We take the calculated $\text{FWHM}_{\text{diff}} = 1.18\,\mu$m (see previous section) as the diffraction-limited spot size and compare it with the histogram of all FWHM values for registered QD spots in Supplementary Fig. S7a. The medians for the registered FWHM values are similar for horizontal and vertical cross-sections, 1.62 μm and 1.58 μm, respectively, which is ∼35 % more than the calculated $\text{FWHM}_{\text{diff}}$. Almost all registered FWHM values are lower than $2\times\text{FWHM}_{\text{diff}}$. Therefore, our imaging setup operates close to the diffraction limit with residual broadening originating most probably from the cryostat window between the QDs and microscope objective [10]. The similarity between horizontal and vertical spot widths is evidenced by the histograms of ratios between the widths of the fitted horizontal and vertical cross-sections of the QD Gaussian profiles ("Vertical-to-horizontal spot width"), presented in Fig. S7b. The average ratio is determined as 99.78 %, in other words, it differs only by 0.22 % from the ideal case unity ratio. The standard sample deviation for the ratio values distribution is calculated to be $\sigma = 19.24\,\%$.

As expected, the fitting uncertainty $\Delta\mathbb{Q}_i/P$ is correlated with the QD brightness, here estimated by the Gaussian fit area, and the corresponding plot is shown in Supplementary Fig. S7c. We find a strong negative correlation between considered fit parameters (Pearson correlation coefficient of -0.68 and -0.73 for horizontal and vertical cross-sections, respectively).

Supplementary Figure S7d presents the fitting uncertainty for QD positions $\Delta\mathbb{Q}_i/P$, separately for horizontal and vertical cross-sections. The uncertainty is defined as the standard error of the fitting procedure for estimation of the center of the Gaussian profile and in all analyzed cases, the obtained values form positively skewed distributions that follow the log-normal distribution,

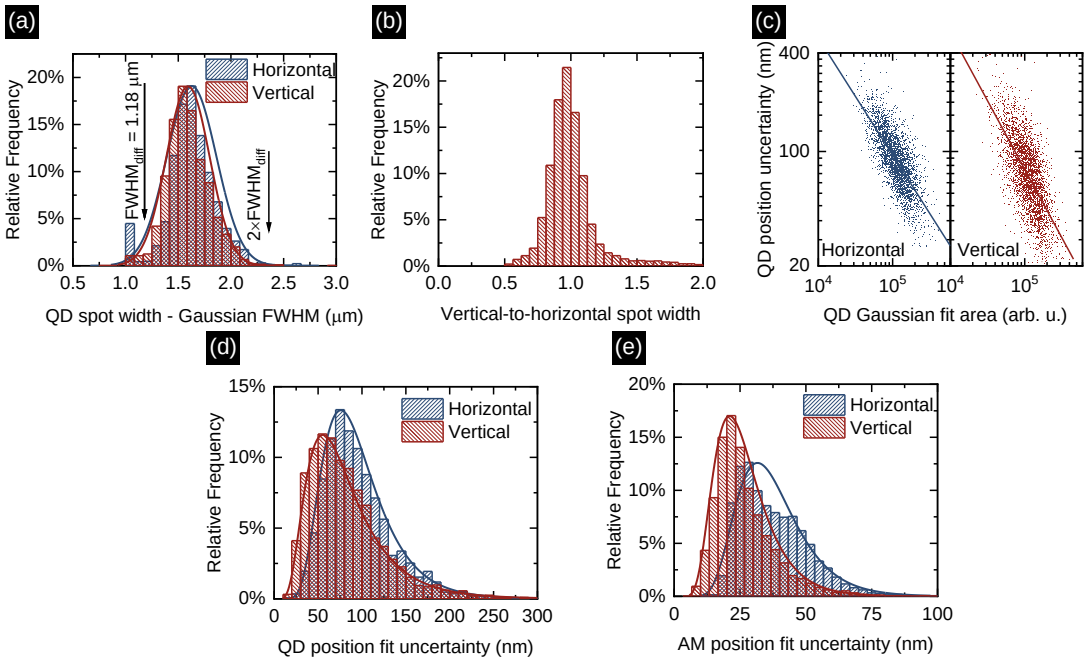

Supplementary Fig. S7. Parameters of fitting the µPL map cross-sections, shown separately for horizontal and vertical directions. **a**, the histogram of FWHM values for the fits used for the determination of QD position Q compared with the calculated diffraction-limited value $\mathrm{FWHM}_{\mathrm{diff}} = 1.18\,\mu\mathrm{m}$ [Eq. (S15)] and fitted with the normal distribution curves, **b**, histogram of the ratio between the widths of the fitted horizontal and vertical cross-sections of the QD Gaussian profiles, based on the panel (a), **c**, QD position fit uncertainty $\Delta\mathbb{Q}/P$ as a function of the QD fit area, **d**, histogram of the QD position fit uncertainty $\Delta\mathbb{Q}/P$, **e**, AM position fit uncertainty $\Delta\mathbb{M}/P$. Histograms in panels (d) and (e) are fitted with log-normal distributions.

as shown with fit curves. The medians for $\Delta\mathbb{Q}_i/P$ are 88.6 nm and 73.6 nm for horizontal and vertical cross-sections, with 24 % of vertical uncertainties being below 50 nm.

Finally, we analyze the fitting uncertainty for AMs positions $\Delta\mathbb{M}_i/P$, as it influences the uncertainty of QD position ΔQ_i determination via Eq. (S11). The medians for $\Delta\mathbb{M}_i/P$ distributions, shown in Supplementary Fig. S7e, are 24.1 nm and 35.1 nm for horizontal and vertical cross-sections. Importantly, 83 % of horizontal and 95 % of vertical cross-section uncertainties $\Delta\mathbb{M}_i/P$ are below 50 nm.

Based on these considerations and the correlation between QD spot brightness and uncertainty of QD position fit $\Delta\mathbb{Q}_i/P$, we estimate that working with only the brightest QD spot in each imaging field (due to the average number of $N_{\mathrm{F}} \approx 10$ spots detected per field, this amounts to limiting cavity fabrication to 10 % of the registered spots), our fitting accuracy would be $\Delta\mathbb{Q}_i/P < 53.2\,\mathrm{nm}$ and $\Delta\mathbb{Q}_i/P < 37\,\mathrm{nm}$ for horizontal and vertical cross-sections (10th percentiles for the uncertainties distributions). Taking medians for the fitting uncertainty of AMs positions $\Delta\mathbb{M}_i/P$, we find the uncertainty of QD localization $\Delta Q < 80.1\,\mathrm{nm}$, cf. Eq. (S12). Including the electron beam lithography uncertainty $\Delta C = 40\,\mathrm{nm}$, we find the total uncertainty of cavity placement $\Delta R < 90.3\,\mathrm{nm}$, according to Eq. (S13) (see Supplementary Tab. S2). Here, we assume $\left(Q_i - M_{i,l}\right) = 25\,\mu\mathrm{m}$ (center of the field) and for ΔP we take the median value of standard error of mean $\hat{\sigma}_{\bar{P}_i}$ calculated for 84 exemplary µPL maps.

Supplementary Table S2. Uncertainties involved in the determination of the accuracy of cavity positioning ΔR for an example of a QD with low uncertainty of fitting the QD positions $\Delta\mathbb{Q}_i/P$ – corresponding to a QD being in the 10 % of the brightest spots.

Orientation	$\Delta\mathbb{Q}_i/P$	$\Delta\mathbb{M}_i/P$	$\left(\mathbb{Q}_i - \mathbb{M}_{i,l}\right)\Delta P/P^2$	ΔQ_i	ΔQ	ΔR
Horizontal	$\leq 53.2\,\mathrm{nm}$	24.1 nm	15.1 nm	$< 61.1\,\mathrm{nm}$	$< 80.1\,\mathrm{nm}$	$< 90.3\,\mathrm{nm}$
Vertical	$\leq 37\,\mathrm{nm}$	35.1 nm		$< 53.2\,\mathrm{nm}$		

S-IV. OPTICAL SETUPS

Supplementary Fig. S8a presents the setup used for spectroscopy studies of fabricated devices (μPL, extraction efficiency determination, time-resolved μPL), while the above-band autocorrelation histograms are recorded in a setup shown in Supplementary Fig. S8b. Details of the equipment used are given in the **Methods** section.

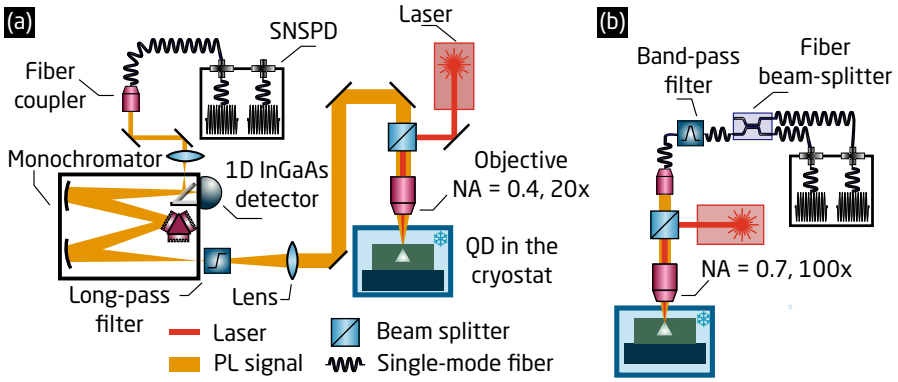

Supplementary Fig. S8. Simplified schemes of the experimental setups used for the device characterization. **a**, the optical setup used for the determination of the photon extraction efficiency and time-resolved μPL, **b**, setup used for autocorrelation experiments. SNSPD – superconducting nanowire single-photon detector.

S-V. DETERMINATION OF THE PHOTON EXTRACTION EFFICIENCY

To determine the value of photon extraction efficiency η, we calibrate the optical setup shown in Supplementary Fig. S8a and calculate its efficiency η_{Setup} as a multiplication of the transmission of all optical elements and of the efficiency of fiber in-coupling and superconducting nanowire single-photon detector (SNSPD) quantum efficiency. We start with reflecting the laser tuned to 1.55 μm off a silver mirror placed in the setup instead of the structure. The signal emitted from the sample passes through the elements enumerated in Supplementary Tab. S3, given with their measured transmission efficiencies. For SNSPD, we take nominal efficiency. We obtain $\eta_{\text{Setup}} = (1.10 \pm 0.17)\,\%$, where the uncertainty is calculated by propagating the assumed uncertainties of transmission of the consecutive elements.

Supplementary Table S3. The transmission of the optical components in the setup used for determination of photon extraction efficiency, as shown in Supplementary Fig. S8a.

Element	Transmission/Efficiency
cryostat window	$(90 \pm 2)\,\%$
microscope objective	$(55 \pm 3)\,\%$
beam splitter	$(38 \pm 2)\,\%$
a set of mirrors	$(85 \pm 5)\,\%$
focusing lens and long-pass filter	$(93 \pm 2)\,\%$
monochromator	$(27 \pm 5)\,\%$
mirrors for signal coupling	$(96 \pm 2)\,\%$
fiber in-coupling	$(41 \pm 10)\,\%$
fibers and their connections	$(80 \pm 10)\,\%$
SNSPD efficiency	$(87 \pm 3)\,\%$
Total setup efficiency η_{Setup}	$(1.10 \pm 0.17)\,\%$

Then, we excite the QDs off-resonantly with a pulsed laser diode with $f_{\mathrm{rep}} = 80\,\mathrm{MHz}$ repetition rate at the saturation power for each QD. We collect the emission with the microscope objective (NA = 0.4) and take the SNSPD count rate n_{QD} for the most intense QD lines, and correct them by η_{Setup} and f_{rep} according to the formula

$$\eta = \frac{n_{\mathrm{QD}}}{f_{\mathrm{rep}} \times \eta_{\mathrm{Setup}}}. \tag{S16}$$

The uncertainty of the photon extraction efficiency for QD-CBG #1 and #2 are calculated by propagating the uncertainties as

$$\Delta\eta = \sqrt{\left(\frac{\Delta n_{\mathrm{QD}}}{\eta_{\mathrm{Setup}}}\right)^2 + \left(\frac{n_{\mathrm{QD}}\Delta\eta_{\mathrm{Setup}}}{\eta_{\mathrm{Setup}}^2}\right)^2}, \tag{S17}$$

with $\Delta n_{\mathrm{QD}} = 1000$ and $\Delta\eta_{\mathrm{Setup}} = 0.17\,\%$. This method assumes unity internal quantum efficiency of QDs ($\eta_{\mathrm{int}} = 100\,\%$), so that the QD photon emission rate equals f_{rep}. It is however difficult to determine experimentally the contribution of non-radiative recombination and hence the real value of η_{int}. The assumption of $\eta_{\mathrm{int}} = 100\,\%$ thus sets a lower limit of η due to a possible overestimation of the total number of photons emitted by the QD.

S-VI. SUPPORTING μPL DATA FOR QD-CBG DEVICES

A. QD linewidths

Supplementary Figure S9 presents the histogram of linewidths for all 102 found QDs emitting in the CBGs. We use the FWHM of the fitted Gaussian profiles to describe the linewidth and find that the median linewidth is 0.76 nm, 1st quartile 0.52 nm, and the minimal value 0.14 nm. Additionally, the linewidths for QD-CBGs #1–#3 are shown in Supplementary Tab. S4.

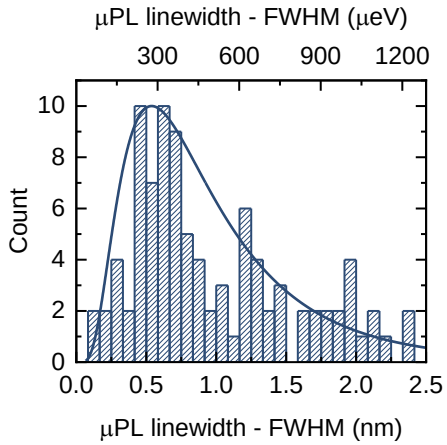

Supplementary Fig. S9. The histogram of linewidths for QDs in CBGs (FWHM of fitted Gaussian profiles).

Supplementary Table S4. μPL linewidths of QD-CBGs #1–#3.

QD	QD linewidth in μPL
QD-CBG #1	0.47 nm
QD-CBG #2	0.17 nm
QD-CBG #3	0.19 nm

S-12

B. Time-resolved μPL

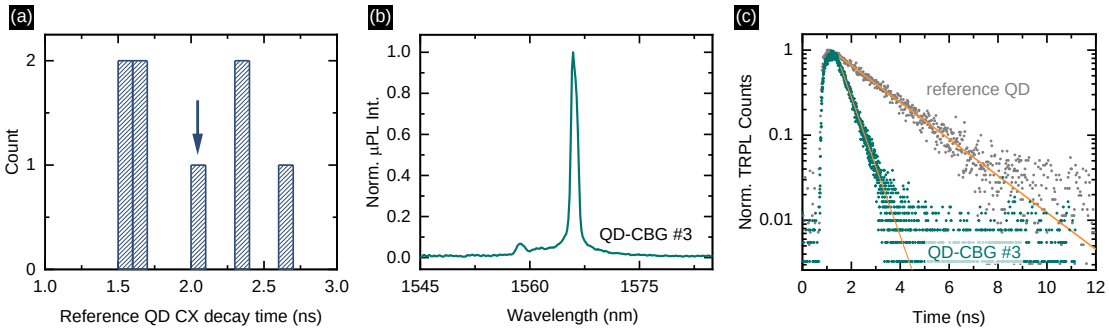

Supplementary Fig. S10. Additional μPL data. **a**, Histogram of recorded decay times for reference QD trion lines; arrow points to the QD shown in Fig. 3b in the article and in panel (c), **b**, μPL spectrum for QD-CBG #3, **c**, time-resolved μPL time traces for QD-CBG #3 and the reference QD.

Supplementary Figure S10 shows the μPL data supporting the determination of F_P. We focus on an additional QD-CBG #3 with a well-isolated transition line, analogous to QD-CBGs #1 and #2 presented in the article, Fig. 3.

Fig. S10a shows a histogram of recorded decay times for the reference QD trion lines. The time-resolved μPL results for eight QDs found in the area outside the fabricated cavities with intense trion lines indicate a considerable scattering of the decay times, with minimal and maximal registered times 1.59 ns and 2.69 ns and the average decay time $\tau_{ref} = 1.99$ ns. The standard deviation of the fitted normal distribution is 0.44 ns and the standard error of mean is 0.16 ns. We take the average decay time $\tau_{ref} = (1.99 \pm 0.16)$ ns to calculate the F_P according to formula $F_P = \tau_{ref}/\tau_{cav}$.

Fig. S10b shows the spectrum of QD-CBG #3, and Fig. S10c presents time-resolved μPL decay traces in analogy to Fig. 3b of the article, where the same reference time trace is presented. Decay time for QD-CBG #3 is the same as for QD-CBG #2 within the fitting accuracy, $\tau_{\#3} = \tau_{\#2} = (0.53 \pm 0.01)$ ns, what translates to $F_P = 3.75 \pm 0.30$.

C. Temperature-dependent μPL

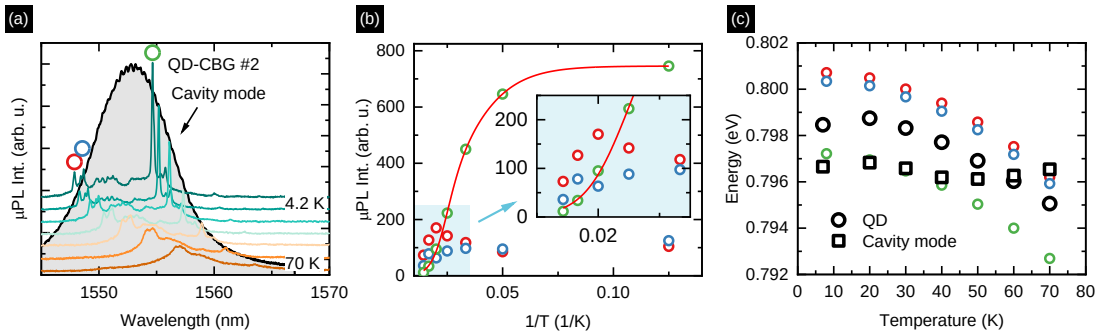

Supplementary Fig. S11. Analysis of the temperature-dependent μPL spectra for QD-CBG #2. **a**, Temperature-dependent μPL spectra for QD-CBG #2, overlapped with the cavity mode. **b**, Arrhenius plot for the integrated μPL intensity for three QD lines, indicated with the same symbols in panel (a). Inset: close-up of the marked region. **c**, μPL emission energy for the same QD lines. Black symbols stand for another QD-CBG device, with QD and cavity mode energies tracked up to $T = 70$ K. The mode crossing characteristic for the weak QD-cavity coupling regime is visible.

We record the temperature-dependent μPL signal for QD-CBG #2 in the temperature range of $T = 4.2\,\mathrm{K}$ to $70\,\mathrm{K}$ under the continuous-wave (cw) excitation and present the stacked spectra in Fig. S11a. Three emission lines, marked with rings, can be identified and their emission intensity and energy tracked as the temperature is increased. We plot also the mode profile for reference. Note the $\sim 2\,\mathrm{nm}$ redshift of the most intense line from the central wavelength of the cavity.

The μPL intensities change differently for lines with emission energy lower vs. higher compared to the mode profile. The short-wavelength lines, marked with red and blue rings, are tuned across the mode profile as the temperature raises. Their μPL intensity quench is greatly suppressed, in fact, the intensity of the line marked with a red circle has a maximum at $T = 50\,\mathrm{K}$. The behavior for the long-wavelength line, marked with a green ring, is opposite and its intensity quenches fast.

The temperature-dependent μPL intensity for the most intense line marked with the green ring is fitted with a standard formula assuming two activation processes [11]:

$$I(T) = \frac{I_0}{1 + B_1 \exp\left(-E_{\mathrm{a},1}/k_{\mathrm{B}}T\right) + B_2 \exp\left(-E_{\mathrm{a},2}/k_{\mathrm{B}}T\right)}, \tag{S18}$$

where I_0 is the μPL intensity for $T \to 0$, $E_{\mathrm{a},1}$ and $E_{\mathrm{a},2}$ are activation energies, and B_1 and B_2 are relative rates corresponding to the efficiency of involved processes. We achieve the activation energies of $E_{\mathrm{a},1} = (6.9 \pm 0.8)\,\mathrm{meV}$ and $E_{\mathrm{a},2} = (27.9 \pm 3.1)\,\mathrm{meV}$. We note that $E_{\mathrm{a},2}$ is similar to the activation energy $E_{\mathrm{Ref}} = (23.6 \pm 0.8)\,\mathrm{meV}$ found for a CX line from analogous QDs [7]. Accordingly to Ref. [12], this activation energy can be attributed to the charge transfer to higher orbital states, based on the band structure calculations within the 8-band $k \cdot p$ framework. Hence, another mechanism is responsible for the identification of $E_{\mathrm{a},1}$ energy which is absent in the case of high-energy lines (blue and red circles, see Supplementary Fig. S11b). This can potentially be associated with the enhancement of the QD emission rate when the overlap between the line and the mode energy is maximized.

In Supplementary Figure S11c we plot the temperature dependence of the emission energy for lines analyzed in Supplementary Fig. S11b and, additionally, for another investigated QD-CBG device, where the observation of the crossing of the temperature-tuned QD line and the cavity mode under high power off-resonant cw excitation was possible due to the QD energy being higher than the mode energy at $T = 4.2\,\mathrm{K}$. The temperature-induced evolution of cavity mode energy (black open squares) can be compared with the QD lines, evidencing a weaker temperature dependence, as expected for the cavity mode.

S-VII. QUANTUM OPTICS EXPERIMENTS

A. Off-resonant autocorrelation data for QD-CBG #2

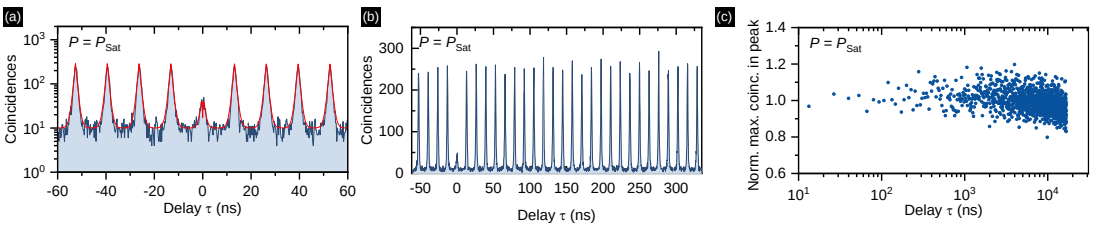

Supplementary Fig. S12. Analysis of the second-order autocorrelation function $g^{(2)}(\tau)$ of the photons emitted from QD-CBG #2 under pulsed off-resonant excitation for laser excitation power P corresponding to saturation of the CX line. **a**, **b**, The recorded histogram **c**, Normalized maximum number of coincidences for all 1260 registered peaks for positive delays of histogram shown in (b).

Supplementary Figure S12 shows the autocorrelation histogram recorded under pulsed off-resonant excitation for QD-CBG #2. We do not observe blinking there, as the normalized coincidences in consecutive peaks (maximum number of coincidences without fitting) in the $g^{(2)}(\tau)$ histogram is at a constant level (Supplementary Fig. S12c). We show data for all registered 1260 peaks, i. e. up to $\tau = 16.7\,\mu\mathrm{s}$ delay. Fluctuation in the data originates in the discretization of the $g^{(2)}(\tau)$ due to finite time binning in the experiment. The blinking would indicate the occupation of a meta-stable QD state [13], originating, e. g., in the emission wavelength fluctuations due to nearby defects [14] or trapped charges [15].

We fit the histograms with the function [16, 17]:

$$C(\tau) = B + A\left[\exp\left(-|\tau|/\tau_{\mathrm{dec}}\right) - \exp\left(-|\tau|/\tau_{\mathrm{cap}}\right)\right] + H\sum_{n\neq 0}\exp\left(-|\tau - n\tau_0|/\tau_{\mathrm{dec}}\right), \tag{S19}$$

where B is the level of background coincidences, A is a scaling parameter related to secondary photon emission, $n \neq 0$ is the peak number, τ_0 is the laser pulse period, and H the average height of the peaks at $\tau_n = n\tau_0$. The second-order correlation function $g^{(2)}(\tau)$ is then obtained by normalizing $C(\tau)$ with $(H+B)$.

The time-independent level of background coincidences B originates from the detector dark counts and uncorrelated photons contributing to the registered histograms. Our approach allows taking into account only coincidences caused by the QD signal. We define the purity as the ratio between the QD emission coincidences registered at τ_0 peak (area of this peak) to the average number of coincidences (peak area) registered at $\tau_{n\neq 0}$ peaks. Then, the $g^{(2)}(0)$ value is calculated by first subtracting the background contribution B, integrating the areas under the central peak and under the non-zero peaks, and dividing these two integrals, according to the formula:

$$g^{(2)}(0)_{\text{fit}} = \frac{\int_{-\tau_0/2}^{\tau_0/2} A\left[\exp\left(-|\tau|/\tau_{\text{dec}}\right) - \exp\left(-|\tau|/\tau_{\text{cap}}\right)\right] \mathrm{d}\tau}{\int_{-\tau_0/2}^{\tau_0/2} H \exp\left(-|\tau|/\tau_{\text{dec}}\right) \mathrm{d}\tau}. \tag{S20}$$

Supplementary Table. S5 summarizes the fit parameters for off-resonant autocorrelation histograms obtained for $0.5 \times P_{\text{sat}}$ and P_{sat} excitation power. The uncertainties are determined from the fit uncertainties and propagated in the case of $g^{(2)}(0)_{\text{fit}}$ which is calculated from the fit parameters.

Supplementary Table S5. Fitting parameters for off-resonant autocorrelation measurement.

	Off-resonant excitation power	
Fit parameter	$0.5 \times P_{\text{sat}}$	P_{sat}
Background contribution, B	14.4 ± 2.0	10.2 ± 0.7
Scaling of the center peak, A	54 ± 15	67 ± 19
Height of $\tau_{n\neq 0}$ peaks, H	187 ± 10	288 ± 3
Laser period, τ_0	(13.15 ± 0.01) ns	(13.14 ± 0.01) ns
Decay time, τ_{dec}	(678 ± 5) ps	(721 ± 10) ps
Recapture time, τ_{cap}	(544 ± 76) ps	(196 ± 98) ps
$g^{(2)}(0)_{\text{fit}}$, Eq. (S20)	0.05 ± 0.02	0.17 ± 0.03

B. Microphotoluminescence excitation spectroscopy of QD-CBG #2

The two-photon interference experiments were carried out under quasi-resonant excitation conditions. The exact excitation energy was determined based on the microphotoluminescence excitation (μPLE) experiment conducted with a pulsed tunable laser with 5 ps-long pulses and 80 MHz repetition rate. The excitation laser wavelength was varied in the range of 1470-1540 nm at constant average excitation power of 25 μW measured in front of the cryostat window. In the μPLE map, shown in Supplementary Fig. S13a, a clear maximum is visible at the wavelength 1484.2 nm, corresponding to 835.37 meV photon energy which was used for all experiments described in this section. The energy difference of 37.57 meV (see the map cross-section in Supplementary Fig. S13b) coincides reasonably well with the LO phonon energy of InP of 43.4 meV at low temperature [18]. Simultaneously, the measured energy difference is far above the calculated trion p-shell splitting of about ~ 20 meV [12] for QDs very similar in size and chemical composition (P admixture) to the ones investigated here. Therefore, we assume that the applied quasi-resonant excitation of the QD is LO-phonon-assisted.

The comparison of the time-resolved μPL time traces for the trion line in QD-CBG #2 for quasi- and off-resonant excitation, shown in Supplementary Fig. S13c, confirms the accelerated relaxation of the excited state by the reduced decay time under for the quasi-resonant excitation.

C. Quasi-resonant autocorrelation data for QD-CBG #2

The single-photon purity was verified in autocorrelation measurements taken at various excitation powers to identify the contribution of multi-photon emission and unsuppressed reflected laser light which lead to erroneous coincidences in HOM measurements. The lowest $g^{(2)}(0)$ value was found for the excitation power of 1.5 μW, and the corresponding autocorrelation data is shown in Fig. 4a of the main text. In this configuration, the autocorrelation histogram was measured directly through the HOM setup to make sure that no reflected laser obscures the HOM experiment. Increasing the excitation power is favored by

S-15

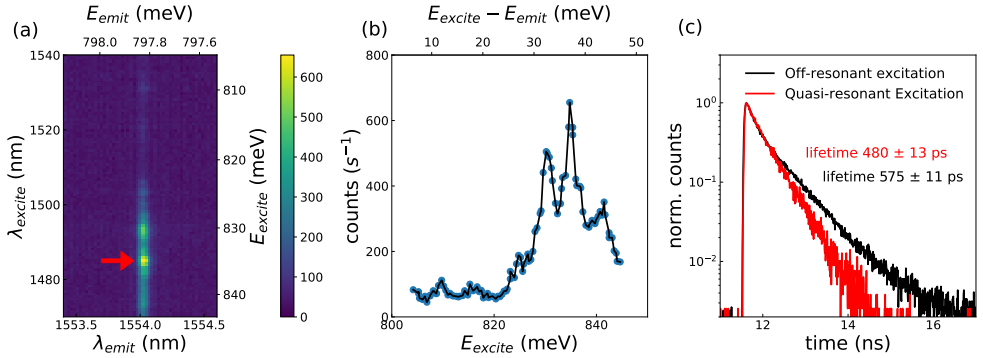

Supplementary Fig. S13. **a**, Microphotoluminescence excitation map of QD-CBG #2. **b**, Cross-section of the map taken at the center of the QD-CBG #2 emission line, revealing the quasi-resonant excitation energy of $\sim 0.835\,$eV used to excite the QD for the indistinguishability measurements. The energy difference corresponds to the detuning of $\sim 37\,$meV from the emission energy. **c**, Time-resolved µPL data for line in QD-CBG #2 for quasi- and off-resonant excitation.

increasing the signal-to-background ratio as long as the QD is in the linear response regime. On the other hand, increasing the excitation power once the QD emission intensity is saturated results mostly in the increase of the background counts due to the cavity being fed by other sources. They mostly originate in the low-energy tail of the wetting layer emission or radiative defects present in the sample.

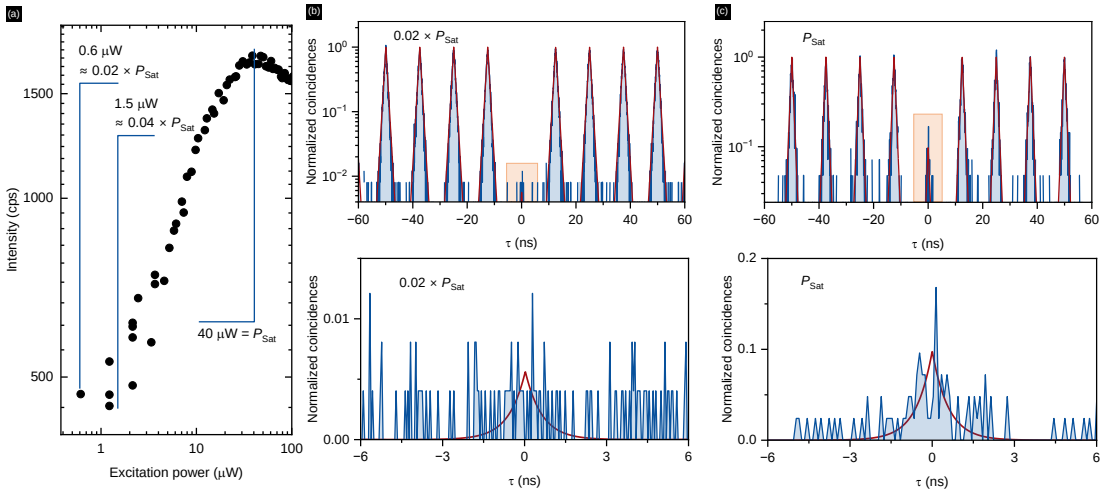

Supplementary Fig. S14. **a**, Excitation-power dependent µPL intensity of the line in QD-CBG #2 under quasi-resonant excitation with the powers chosen for HOM measurements marked. **b**, **c**, Autocorrelation histograms for QD-CBG #2 under (b) $P_{\mathrm{exc}} = 0.6\,\mu$W ($0.02 \times P_{\mathrm{sat}}$), (c) $P_{\mathrm{exc}} = 40\,\mu$W ($P_{\mathrm{sat}}$). Orange boxes mark the region that is zoomed in at the bottom.

The low power autocorrelation measurement taken using the HOM configuration leads to an integrated $g^{(2)}(0)_{\mathrm{raw}} = (3.2 \pm 0.6) \times 10^{-3}$ which confirms the suppression of the excitation laser in preparation for the HOM experiment.

To fit the autocorrelation histograms we modify Eq. (S19) used for fitting off-resonant data, as we do not observe background

counts ($B = 0$) and no carrier recapture so that the new formula reads

$$C(\tau) = c \cdot \left(g^{(2)}(0)_{\text{fit}} \exp(-|\tau|/\tau_{\text{dec}}) + \sum_{n \neq 0} \exp(-|\tau - n\tau_0|/\tau_{\text{dec}}) \right), \tag{S21}$$

where c is a global normalization factor.

The extracted fit parameters for the quasi-resonantly excited autocorrelation data shown in the main text and in Supplementary Figs. S14b-S14c are shown in Supplementary Tab. S6. Note that in real applications temporal filtering is not always possible which is why we state also the integrated value. For that, we integrate all coincidences in a window of ± 6 ns around each peak in the histogram. Then, we divide the sum of coincidences in the center window by the average of the sums in all side windows, as no blinking is present. The uncertainty is based on the variance of integrated side peak areas.

Supplementary Table S6. Fitting parameters for quasi-resonant autocorrelation measurement.

	Quasi-resonant excitation power		
Fit parameter	$P_{\text{exc}} = 0.6\,\mu\text{W}$ ($0.02 \times P_{\text{sat}}$), Fig. S14b	$P_{\text{exc}} = 1.5\,\mu\text{W}$ ($0.04 \times P_{\text{sat}}$), Fig. 4a	$P_{\text{exc}} = 40\,\mu\text{W}$ (P_{sat}), Fig. S14c
Decay time, τ_{dec}	(606 ± 3) ps	(584 ± 3) ps	(591 ± 7) ps
Laser period, τ_0	(12.49 ± 0.01) ns	(12.49 ± 0.01) ns	(12.49 ± 0.01) ns
$g^{(2)}(0)_{\text{fit}}$	$(5.6 \pm 5.0) \times 10^{-3}$	$(4.7 \pm 2.6) \times 10^{-3}$	$(9.81 \pm 1.94) \times 10^{-2}$
$g^{(2)}(0)_{\text{raw}}$	$(4.2 \pm 0.2) \times 10^{-3}$	$(3.2 \pm 0.6) \times 10^{-3}$	$(8.75 \pm 4.88) \times 10^{-2}$

D. Indistinguishability measurements and data analysis

Supplementary Fig. S15 presents the configuration of the experimental setup applied to record the HOM histograms. The 4 ns excitation delay is compensated on the detection side. A cross-polarization setup suppresses the reflected laser light and a 0.4 nm fiber bandpass spectrally filters the emission. The HOM setup consists of a 50:50 free-space beam splitter and a 50:50 fiber beam splitter in which the interference takes place. The fiber in-coupling can be translated for optimization of the temporal matching and the polarization is set in free space via waveplates and confirmed with a polarimeter.

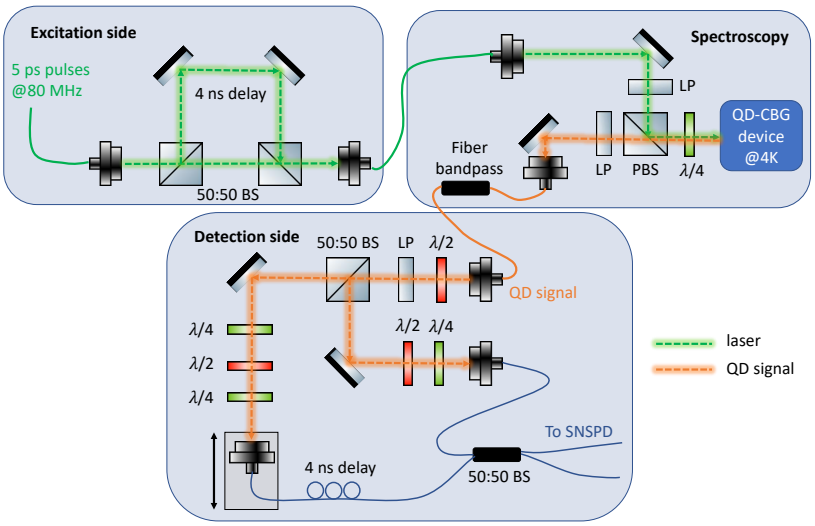

Supplementary Fig. S15. The HOM experimental setup. BS – beam splitter, $\lambda/2$, $\lambda/4$ – half and quarter wave-plate, SNSPD – superconducting nanowire single-photon detector.

The indistinguishability measurements were performed with a 4 ns delay. To do so, the train of laser pulses arriving every 12.5 ns was split on the excitation side into two pulses separated by a delay of 4 ns which was compensated on the detection side, to interfere subsequently emitted photons in a fiber beam splitter. The laser was tuned to excite the QD-CBG quasi-resonantly for three excitation powers, $P_{\mathrm{exc}} = 0.6\,\mu\mathrm{W}$ ($0.02 \times P_{\mathrm{sat}}$), $P_{\mathrm{exc}} = 1.5\,\mu\mathrm{W}$ ($0.04 \times P_{\mathrm{sat}}$), and $P_{\mathrm{exc}} = 40\,\mu\mathrm{W}$ (P_{sat}).

The obtained histograms are composed of a characteristic pattern of 5 peaks repeated every 12.5 ns corresponding to the 80 MHz repetition rate of the excitation laser. They are related to coincidences resulting from consecutive photons taking different paths in the imbalanced Mach-Zehnder interferometer (MZI). There are 5 possible final delay combinations leading to the observed pattern [19]. For the Poissonian statistics of the emission, the intensity ratio of the 5 non-central peaks is expected to be 1:4:6:4:1, whereas for the center peak (produced by coincidences originating in the pair of laser pulses separated by 4 ns), indistinguishable single photons produce the combination of coincidences 1:2:0:2:1 in contrast to 1:2:2:2:1 for completely distinguishable photons.

The figure of merit for the photon indistinguishability can be extracted from HOM measurements in different ways. Typically, the amount of coincidences in the case of expected indistinguishability is compared to the number of coincidences for expected maximum distinguishability, either at cross-polarized interference or from different laser pulses (photons that have not interfered). As the second approach with side peaks is more susceptible to blinking and imperfect setups, we determine the indistinguishability from the comparison of co- and cross-polarized HOM measurements and extract the visibility as the ratio of the central peak areas via

$$V = 1 - A_{\mathrm{Co}}/A_{\mathrm{Cross}}, \tag{S22}$$

while we still mention the values obtained from the side peak method for completeness at the end of this section. In order to extract also other physical quantities and to compensate for statistical fluctuations the data is fitted according to the model described below and the areas $A_{\mathrm{Co}} = A_3$ for the co-polarized case and $A_{\mathrm{Cross}} = A_3$ for the cross-polarized case are obtained.

To properly fit the entire HOM coincidence histograms one has to keep in mind that the areas of the ± 4 ns side peaks belonging to a laser pulse at the time delay $\tau = 0$ ns already overlap with the areas from the side peaks originating from the ± 8 ns laser excitation at $\tau = \pm 12.5$ ns (as they are present in the histogram at ± 4.5 ns), see Supplementary Fig. S16. Consequently, the individual contributions can be extracted by fitting the data by the sum of all contributions according to the formula. For the HOM histogram recorded for the co-polarized case, the formula reads

$$\begin{aligned} C_{\mathrm{HOM,Co}}(\tau,[\tau_1,T_2,\Delta t,\tau_0,\mathbf{A},\mathbf{B}]) = {} & A_3 \exp(-|\tau|/\tau_1)\left(1 - V_{\mathrm{PS}} \cdot e^{-|\tau|/T_2}\right) + \sum_{\mathrm{i}=\{1,2,4,5\}} A_i \exp(-|\tau+\Delta t_i|/\tau_1) \\ & + \sum_{n=-10,n\neq 0}^{10} \left[\sum_{\mathrm{i}=\{1,2,3,4,5\}} B_i \exp(-|\tau+\Delta t_i + n\cdot\tau_0|/\tau_1) \right], \end{aligned} \tag{S23}$$

and for the cross-polarized data

$$\begin{aligned} C_{\mathrm{HOM,Cross}}(\tau,[\tau_1,T_2,\Delta t,\tau_0,\mathbf{A},\mathbf{B}]) = {} & A_3 \exp(-|\tau|/\tau_1) + \sum_{\mathrm{i}=\{1,2,4,5\}} A_i \exp(-|\tau+\Delta t_i|/\tau_1) \\ & + \sum_{n=-10,n\neq 0}^{10} \left[\sum_{\mathrm{i}=\{1,2,3,4,5\}} B_i \exp(-|\tau+\Delta t_i + n\cdot\tau_0|/\tau_1) \right]. \end{aligned} \tag{S24}$$

These formulas for the normalized coincidences as a function of the detection time difference τ includes the 4 ns delay between two interfering photons $\Delta t_{1-5} = \{-8,-4,0,4,8\}$ ns, the 12.5 ns initial laser pulse delay τ_0, the photoluminescence decay time τ_1, the coherence time T_2, the post-selected visibility V_{PS}, the respective peak heights of the center 5-peak-structure A_{1-5}, and the averaged peak heights of all peaks at higher delays B_{1-5}. The two fits for co- and cross-polarized cases differ only by the existence of the volcano-shaped dip in the central peak of the co-polarized data, being the fingerprint of the two-photon interference. The post-selected visibility is the value one obtains also when comparing the center peak contribution of the co- and the cross-case at $\tau = 0$ as then

$$V_{\mathrm{PS}} = 1 - \frac{C_{\mathrm{HOM,Co}}(\tau=0)}{C_{\mathrm{HOM,Cross}}(\tau=0)} = 1 - \frac{A_3(1-V_{\mathrm{PS}})}{A_3}. \tag{S25}$$

The simulated histograms for our experimental parameters expected from this model are shown in Supplementary Fig. S16 top and bottom for perfectly indistinguishable and distinguishable photons, respectively.

While the fitted histogram for $0.04 \times P_{\mathrm{sat}}$ is presented in the article, Fig. 4b, the fitted histograms for $0.02 \times P_{\mathrm{sat}}$ and P_{sat} excitation powers are shown in Supplementary Fig. S17 and the extracted parameters in Supplementary Tab. S7. All fits were done on the unbinned raw data without correcting for finite $g^{(2)}(0)$, as the obtained $g^{(2)}(0)$ values are small. Additionally, the fits do not include corrections for the detector time response or subtracting a fixed background. The uncertainties are determined from the fit errors and propagated whenever a quantity was calculated from the fit parameters.

S-18

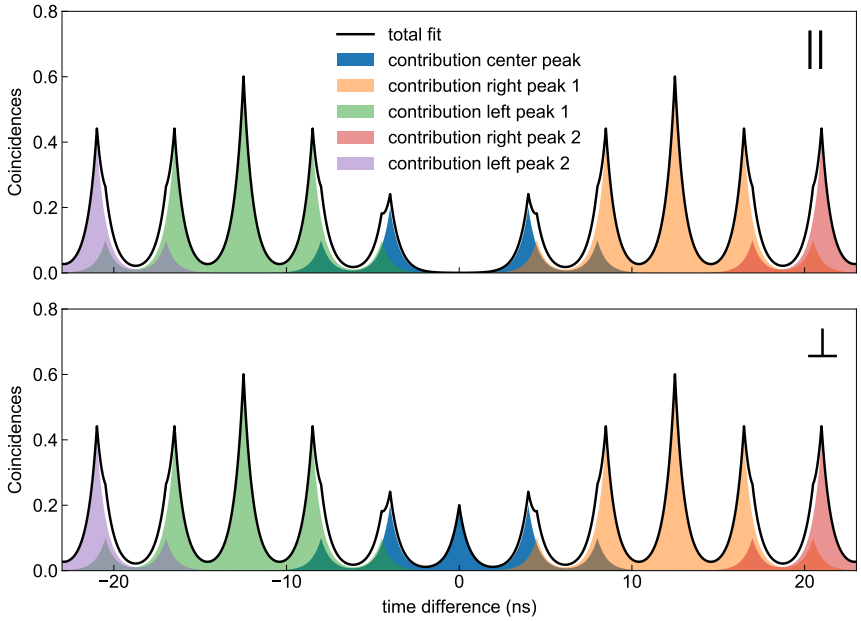

Supplementary Fig. S16. Expected HOM histograms of coincidences with individual peak contributions to the five peak patterns formed by 4 ns delay and laser repetition of $\tau_0 = 12.5$ ns, **a**, for perfectly indistinguishable photons, and **b**, for maximally distinguishable photons. The black lines represent the fits according to Eqs. (S23)–(S24) that include all contributions, plotted for $\tau_1 = 550$ ps lifetime.

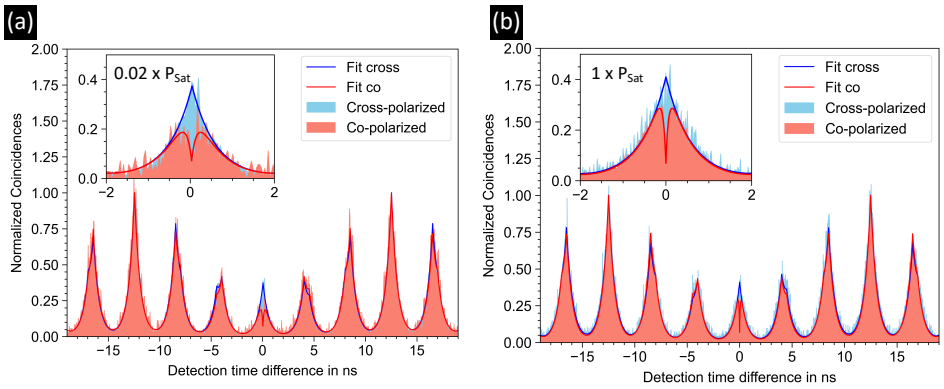

Supplementary Fig. S17. Comparison of HOM histograms taken at **a**, $0.02 \times P_{\text{sat}}$ and **b**, P_{sat} excitation power. HOM measurement recorded for $0.02 \times P_{\text{sat}}$ shows higher indistinguishability and longer coherence time than the one taken at P_{sat}, see Supplementary Tab. S7.

One can clearly see from the graph that the photon indistinguishability is reduced at higher power, as evidenced by the larger central peak area. That is confirmed also by the extracted visibilities of $(22.1 \pm 8.9)\,\%$, $(19.3 \pm 2.6)\,\%$ and $(11.3 \pm 2.3)\,\%$ for low to high power. That is partly due to a worse single-photon purity at P_{sat} (see Supplementary Fig. S14c) but mainly due to a reduced coherence, as indicated by the narrower central dip at higher excitation power. We find that the coherence time T_2 is reduced from (176 ± 9) ps over (103 ± 13) ps to (74 ± 6) ps with the increasing excitation power. The extracted post-selected values are $V_{\text{PS}} = (80 \pm 13)\,\%$, $(99 \pm 6)\,\%$ and $(84 \pm 3)\,\%$ without clear dependence on the excitation power within the determined

Supplementary Table S7. Extracted fitting parameters for recorded HOM histograms. MFR – mean fit residuals.

	Quasi-resonant excitation power		
Fit parameter	$0.02 \times P_{\text{sat}}$, shown in Fig. S17a	$0.04 \times P_{\text{sat}}$, shown in Fig. 4b	P_{sat}, shown in Fig. S17b
Co-pol areas **A**, **B**	$\begin{pmatrix}1.00\pm0.11\\2.08\pm0.11\\1.77\pm0.21\\2.14\pm0.11\\1.38\pm0.11\end{pmatrix}$, $\begin{pmatrix}1.00\pm0.06\\4.23\pm0.05\\6.66\pm0.04\\4.55\pm0.05\\1.27\pm0.06\end{pmatrix}$	$\begin{pmatrix}1.00\pm0.04\\1.84\pm0.04\\1.68\pm0.05\\1.95\pm0.04\\1.03\pm0.04\end{pmatrix}$, $\begin{pmatrix}1.00\pm0.02\\3.76\pm0.02\\5.69\pm0.02\\3.75\pm0.02\\1.03\pm0.02\end{pmatrix}$	$\begin{pmatrix}1.00\pm0.02\\1.96\pm0.02\\2.02\pm0.03\\1.92\pm0.02\\0.95\pm0.02\end{pmatrix}$, $\begin{pmatrix}1.00\pm0.01\\3.78\pm0.01\\5.68\pm0.01\\3.75\pm0.01\\0.98\pm0.01\end{pmatrix}$
Cross-pol area A_3,	2.28 ± 0.04	2.08 ± 0.04	2.27 ± 0.06
Lifetime, τ_1	(559 ± 4) ps	(553 ± 2) ps	(563 ± 7) ps
Coherence time, T_2	(176 ± 9) ps	(103 ± 13) ps	(74 ± 6) ps
V_{PS}	$(80\pm13)\,\%$	$(99\pm6)\,\%$	$(84\pm3)\,\%$
MFR, Co fit	0.0812	0.0286	0.0158
MFR, Cross fit	0.0280	0.0280	0.0526
TPI visibility, V	$(22.1\pm8.9)\,\%$	$(19.3\pm2.6)\,\%$	$(11.3\pm2.3)\,\%$

fit uncertainty and mainly limited by the detector timing resolution. The larger uncertainties for the fit parameters for the HOM histogram recorded at $0.02 \times P_{\text{sat}}$ are caused by the lower gathered statistics as indicated also by the larger mean fit residuals (MFR) for the fit of the co-polarized case (0.0812 vs. 0.0280). Note that for the same reason, the deviation from the expected peak ratios is larger in this case as well. The remaining deviations from the expected 5-peak-ratios (**A**, **B**) can also be caused by unequal transmissions in the two arms of the MZIs.

As mentioned at the beginning of this section, in addition to comparing the areas of the co- and cross-polarized central peak, the indistinguishability can also be extracted by comparing the areas of the central to the outer peaks for only the co-polarized data. This analysis of the low-power HOM histogram is presented in Supplementary Fig. S18. Evaluating the visibility from the extracted center A_3 and side peak areas A_2,A_4, and calculating the visibility as $V_{\text{side peaks}} = 1 - 2A_3/(A_2 + A_4)$ leads to $(15.9\pm9.9)\,\%$ for the low excitation power ($0.02 \times P_{\text{sat}}$), which agrees with the visibility result reported above obtained from the co-cross-comparison. The uncertainty is however larger, as the fitting relies on successfully separating the overlapping peak contributions.

Importantly, the obtained visibilities and the post-selected values compare favorably with the reports for GaAs-based QDs emitting at C-band [20–22]. For planar QDs, a visibility of $(14.4\pm1.5)\,\%$ has been reported under pulsed resonant excitation [21] while the raw visibility value of $(71\pm15)\,\%$ was obtained under two-photon-resonant cw excitation [20]. Values obtained under cw excitation can be related to the post-selected values determined from pulsed excitation. For QDs placed non-deterministically in CBGs, the only reported visibility so far is $(8.1\pm3.4)\,\%$ and the post-selected on the order of 60 % [22].

[1] U. M. Gür, S. Arslanagić, M. Mattes, and N. Gregersen, Open-geometry modal method based on transverse electric and transverse magnetic mode expansion for orthogonal curvilinear coordinates, Phys. Rev. E **103**, 033301 (2021).

[2] L. Novotny and B. Hecht, *Principles of Nano-Optics*, 2nd ed. (Cambridge University Press, 2012).

[3] A. V. Lavrinenko, J. Lægsgaard, and N. Gregersen, *Numerical Methods in Photonics* (CRC PR INC, 2014).

[4] L. Li, Formulation and comparison of two recursive matrix algorithms for modeling layered diffraction gratings, J. Opt. Soc. Amer. A **13**, 1024 (1996).

[5] C. A. Balanis, *Antenna Theory: Analysis and Design* (Wiley John + Sons, 2016).

[6] B. Yao, R. Su, Y. Wei, Z. Liu, T. Zhao, and J. Liu, Design for Hybrid Circular Bragg Gratings for a Highly Efficient Quantum-Dot Single-Photon Source, J. Korean Phys. Soc. **73**, 1502 (2018).

[7] P. Holewa, A. Sakanas, U. M. Gür, P. Mrowiński, A. Huck, B.-Y. Wang, A. Musiał, K. Yvind, N. Gregersen, M. Syperek, and E. Semenova, Bright Quantum Dot Single-Photon Emitters at Telecom Bands Heterogeneously Integrated on Si, ACS Photonics **9**, 2273 (2022).

[8] A. Sakanas, E. Semenova, L. Ottaviano, J. Mørk, and K. Yvind, Comparison of processing-induced deformations of InP bonded to Si determined by e-beam metrology: Direct vs. adhesive bonding, Microelectron. Eng. **214**, 93 (2019).

[9] B. Zhang, J. Zerubia, and J.-C. Olivo-Marin, Gaussian approximations of fluorescence microscope point-spread function models, Appl. Opt. **46**, 1819 (2007).

[10] J. Liu, M. I. Davanço, L. Sapienza, K. Konthasinghe, J. V. D. M. Cardoso, J. D. Song, A. Badolato, and K. Srinivasan, Cryogenic photoluminescence imaging system for nanoscale positioning of single quantum emitters, Rev. Sci. Instrum. **88**, 023116 (2017).

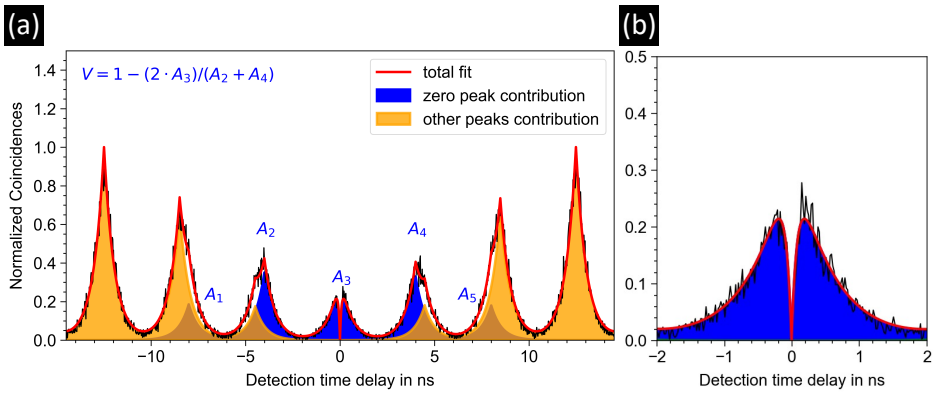

Supplementary Fig. S18. Data analysis of the low-power HOM histogram. **a**, Individual peak contributions extracted as part of the total fit according to Eq. (S23) for the lowest power HOM measurement ($0.02 \times P_{\mathrm{sat}}$). **b**, Close-up of the central peak.

[11] J. D. Lambkin, D. J. Dunstan, K. P. Homewood, L. K. Howard, and M. T. Emeny, Thermal quenching of the photoluminescence of InGaAs/GaAs and InGaAs/AlGaAs strained-layer quantum wells, Appl. Phys. Lett. **57**, 1986 (1990).
[12] P. Holewa, M. Gawełczyk, C. Ciostek, P. Wyborski, S. Kadkhodazadeh, E. Semenova, and M. Syperek, Optical and electronic properties of low-density InAs/InP quantum-dot-like structures designed for single-photon emitters at telecom wavelengths, Phys. Rev. B **101**, 195304 (2020).
[13] C. Santori, M. Pelton, G. Solomon, Y. Dale, and Y. Yamamoto, Triggered single photons from a quantum dot, Phys. Rev. Lett. **86**, 1502 (2001).
[14] M.-E. Pistol, P. Castrillo, D. Hessman, J. A. Prieto, and L. Samuelson, Random telegraph noise in photoluminescence from individual self-assembled quantum dots, Phys. Rev. B **59**, 10725 (1999).
[15] H. Robinson and B. Goldberg, Light-induced spectral diffusion in single self-assembled quantum dots, Phys. Rev. B **61**, R5086 (2000).
[16] P. A. Dalgarno, J. McFarlane, D. Brunner, R. W. Lambert, B. D. Gerardot, R. J. Warburton, K. Karrai, A. Badolato, and P. M. Petroff, Hole recapture limited single photon generation from a single n-type charge-tunable quantum dot, Appl. Phys. Lett. **92**, 193103 (2008).
[17] T. Miyazawa, K. Takemoto, Y. Nambu, S. Miki, T. Yamashita, H. Terai, M. Fujiwara, M. Sasaki, Y. Sakuma, M. Takatsu, T. Yamamoto, and Y. Arakawa, Single-photon emission at 1.5 µm from an InAs/InP quantum dot with highly suppressed multi-photon emission probabilities, Appl. Phys. Lett. **109**, 132106 (2016).
[18] G. Irmer, M. Wenzel, and J. Monecke, The temperature dependence of the LO(T) and TO(T) phonons in GaAs and InP, Phys. Status Solidi B **195**, 85 (1996).
[19] A. Thoma, P. Schnauber, M. Gschrey, M. Seifried, J. Wolters, J. H. Schulze, A. Strittmatter, S. Rodt, A. Carmele, A. Knorr, T. Heindel, and S. Reitzenstein, Exploring dephasing of a solid-state quantum emitter via time- and temperature-dependent Hong-Ou-Mandel experiments, Phys. Rev. Lett. **116**, 1 (2016).
[20] C. Nawrath, F. Olbrich, M. Paul, S. L. Portalupi, M. Jetter, and P. Michler, Coherence and indistinguishability of highly pure single photons from non-resonantly and resonantly excited telecom C-band quantum dots, Appl. Phys. Lett. **115**, 023103 (2019).
[21] C. Nawrath, H. Vural, J. Fischer, R. Schaber, S. L. Portalupi, M. Jetter, and P. Michler, Resonance fluorescence of single In(Ga)As quantum dots emitting in the telecom C-band, Appl. Phys. Lett. **118**, 244002 (2021).
[22] C. Nawrath, R. Joos, S. Kolatschek, S. Bauer, P. Pruy, F. Hornung, J. Fischer, J. Huang, P. Vijayan, R. Sittig, M. Jetter, S. L. Portalupi, and P. Michler, High emission rate from a Purcell-enhanced, triggered source of pure single photons in the telecom C-band, arXiv:2207.12898 [quant-ph] (2022).

APPENDIX B

List of publications and conference presentations

Publications

Publications included in the thesis

1. P. Holewa, M. Gawełczyk, C. Ciostek, P. Wyborski, S. Kadkhodazadeh, E. Semenova, M. Syperek, *Optical and electronic properties of low-density InAs/InP quantum dot-like structures devoted to single-photon emitters at telecom wavelengths*, **Physical Review B**, 101, 19 (2020).

2. P. Holewa, M. Gawełczyk, A. Maryński, P. Wyborski, J. P. Reithmaier, G. Sęk, M. Benyoucef, M. Syperek, *Optical and Electronic Properties of Symmetric InAs/(In,Al,Ga)As/InP Quantum Dots Formed by Ripening in Molecular Beam Epitaxy: A Potential System for Broad-Range Single-Photon Telecom Emitters*, **Physical Review Applied**, 14, 6 (2020).

3. P. Holewa, S. Kadkhodazadeh, M. Gawełczyk, P. Baluta, A. Musiał, V. G. Dubrovskii, M. Syperek, E. Semenova, *Droplet epitaxy symmetric InAs/InP quantum dots for quantum emission in the third telecom window: morphology, optical and electronic properties*, **Nanophotonics**, 11, 8 (2022).

4. P. Holewa, A. Sakanas, U. M. Gür, P. Mrowiński, A. Huck, B. Wang, A. Musiał, K. Yvind, N. Gregersen, M. Syperek, E. Semenova, *Bright Quantum Dot Single-Photon Emitters at Telecom Bands Heterogeneously Integrated with Si*, **ACS Photonics**, 9, 7 (2022).

Preprint included in the thesis

5. P. Holewa, E. Zięba-Ostój, D. Vajner, M. Wasiluk, B. Gaál, A. Sakanas, M. Burakowski, P. Mrowiński, B. Krajnik, M. Xiong, A. Huck, K. Yvind, N. Gregersen, A. Musiał, T. Heindel, M. Syperek, E. Semenova, *Scalable quantum photonic devices emitting indistinguishable photons in the telecom C-band*, arXiv:2304.02515 (2023).

Other publications

2023

6. P. Mrowiński, P. Holewa, A. Sakanas, G. Sęk, E. Semenova, M. Syperek, *Optimization of heterogeneously integrated InP-Si on-chip photonic components*, **Optics Express**, 31, 2 (2023).

2022

7. M. Syperek, R. Stühler, A. Consiglio, P. Holewa, P. Wyborski, Ł. Dusanowski, F. Reis, S. Höfling, R. Thomale, W. Hanke, R. Claessen, D. Di Sante, C. Schneider, *Observation*

of room temperature excitons in an atomically thin topological insulator, **Nature Communications**, 13, 1 (2022).

8. P. Holewa, A. Maryński, M. Gawełczyk, K. Ryczko, V. Liverini, M. Beck, J. Faist, G. Sęk, M. Syperek, *Inter-dash coupling within dense ensembles of quantum dashes: comparison of InAs/(In,Al,Ga)As/InP and InAs/(In,Al)As/InP systems*, **Physical Review Applied**, 17, 5 (2022).

2021

9. P. Holewa, J. Jasiński, A. Shikin, E. Lebedkina, A. Maryński, M. Syperek, E. Semenova, *Optical Properties of Site-Selectively Grown InAs/InP Quantum Dots with Predefined Positioning by Block Copolymer Lithography*, **Materials**, 14, 391 (2021).

2020

10. P. Holewa, M. Burakowski, A. Musiał, N. Srocka, D. Quandt, A. Strittmatter, S. Rodt, S. Reitzenstein, G. Sęk, *Thermal stability of emission from single InGaAs/GaAs quantum dots at the telecom O-band*, **Scientific Reports**, 10, 1 (2020).

11. S. Kreinberg, K. Laiho, F. Lohof, W. E. Hayenga, P. Holewa, C. Gies, M. Khajavikhan, S. Reitzenstein, *Thresholdless Transition to Coherent Emission at Telecom Wavelengths from Coaxial Nanolasers with Excitation Power Dependent Beta-Factors*, **Laser & Photonics Reviews**, 14, 12 (2020).

2019

12. A. Musiał, P. Holewa, P. Wyborski, M. Syperek, A. Kors, J. P. Reithmaier, G. Sęk, M. Benyoucef, *High-Purity Triggered Single-Photon Emission from Symmetric Single InAs/InP Quantum Dots in a Broad Range of the Third Telecommunication Window*, **Advanced Quantum Technologies**, 3, 2 (2019).

13. A. Shikin, E. Lebedkina, C. Ciostek, P. Holewa, S. Ndoni, K. Almdal, K. Yvind, M. Syperek, E. Semenova, *Synthesis and systematic optical investigation of selective area droplet epitaxy of InAs/InP quantum dots assisted by block copolymer lithography*, **Optical Materials Express**, 9, 4 (2019).

2018

14. N. Srocka, A. Musiał, P.-I. Schneider, P. Mrowiński, P. Holewa, S. Burger, D. Quandt, A. Strittmatter, S. Rodt, S. Reitzenstein, G. Sęk, *Enhanced photon-extraction efficiency from InGaAs/GaAs quantum dots in deterministic photonic structures at* $1.3\,\mu$m *fabricated by in-situ electron-beam lithography*, **AIP Advances**, 8, 8 (2018).

2017

15. Ł. Dusanowski, P. Holewa, A. Maryński, A. Musiał, T. Heuser, N. Srocka, D. Quandt, A. Strittmatter, S. Rodt, J. Misiewicz, S. Reitzenstein, G. Sęk, *Trigerred high-purity telecom-wavelength single-photon generation from p-shell-driven InGaAs/GaAs quantum dot*, **Optics Express**, 25, 25 (2017).

Conference proceedings

16. P. Holewa, A. Sakanas, U. M. Gür, P. Mrowiński, N. Gregersen, M. Syperek, E. Semenova, *Bright Quantum Dot Single-Photon Source at 1.55 µm Heterogeneously Integrated on Si*, **2021 Conference on Lasers and Electro-Optics (CLEO)**, 1-2 (2021).

17. P. Holewa, *Semiconductor quantum dot as a source of single photons for quantum telecommunication*, **15th Students' Science Conference proceedings**, Wrocław University of Technology Publishing House (2017).

Preprints under review

18. Y. Berdnikov, P. Holewa, S. Kadkhodazadeh, J. M. Śmigiel, A. Frąckowiak, A. Sakanas, K. Yvind, M. Syperek, E. Semenova, *Fine-tunable near-critical Stranski-Krastanov growth of InAs/InP quantum dots*, arXiv:2301.11008 (2023).

Presentations at international conferences

Contributed talks

1. P. Holewa *et al.*, *Deterministically fabricated Purcell-enhanced quantum dot-device emitting single indistinguishable photons in the telecom C-band*, **18th International Conference on Optics of Excitons in Confined Systems (OECS)**, Lecce, Italy, 06.2023.

2. P. Holewa *et al.*, *Droplet epitaxy symmetric InAs/InP quantum dots for quantum emission in the third telecom window: Morphology, optical and electronic properties*, **20th International Conference on Metalorganic Vapor Phase Epitaxy (ICMOVPE XX)**, Stuttgart/Fellbach, Germany, 07.2022.

3. P. Holewa *et al.*, *Optical properties of InAs/InP quantum dots emitting around 1.55 µm – Positioning of dots and deterministic fabrication of circular Bragg gratings*, **35thInternational Conference on the Physics of Semiconductors (ICPS 2022)**, Sydney, Australia, 06.2022.

4. P. Holewa *et al.*, *Positioning of InAs/InP quantum dots emitting at 1.55 µm and fabrication of circular Bragg gratings*, **50th International School & Conference on the Physics of Semiconductors "Jaszowiec 2022"**, Szczyrk, Poland, 06.2022.

5. P. Holewa *et al.*, *Fabrication and modeling of InP/Si waveguides integration of C-band single photon sources with the silicon platform*, **International workshop on telecom quantum dot non-classical light sources for quantum communication (QDotCom)**, Wrocław, Poland, 05.2022.

6. P. Holewa *et al.*, *Bright Quantum Dot Single-Photon Emitters at Telecom Bands Heterogeneously Integrated with Si*, **49th International School & Conference on the Physics of Semiconductors "Jaszowiec 2021"**, virtual environment, 09.2021.

7. P. Holewa *et al.*, *Bright Quantum Dot Single-Photon Source at 1.55 µm Heterogeneously Integrated on Si*, **CLEO – Laser Science to Photonic Applications**, virtual environment, 05.2021.

8. P. Holewa *et al.*, *Optical properties of selective area droplet epitaxy InAs/InP quantum dots assisted by block copolymer lithography*, **8th Workshop on Physics and Technology of Semiconductor Lasers**, Kraków, Poland, 10.2019.

9. P. Holewa *et al.*, *Semiconductor quantum dot as a source of single photons for quantum telecommunication*, **15th Students' Scientific Conference**, Jelenia Góra, Poland, 09.2017.

10. P. Holewa *et al.*, *Generation of single photons by InGaAs/GaAs quantum dots*, **6th Conference of the Students' Scientific Society "NanoIn"**, Szklarska Poręba, Poland, 05.2017.

11. P. Holewa *et al.*, *Observation of single-photon emission from a single InGaAs/GaAs quantum dot in the second telecommunications window*, **Conference of the University of Warsaw Students' Scientific Society "Nanorurki"**, Wrocław, Poland, 03.2017.

Posters

12. P. Holewa *et al.*, *Deterministic and scalable fabrication of hybrid circular Bragg gratings operating at C-band*, **8th international workshop on "Engineering of Quantum Emitter Properties"**, Stuttgart, Germany, 12.2022.

13. P. Holewa *et al.*, *Optical and electronic properties of low-density InAs/InP quantum dot-like structures devoted to single-photon emitters at telecom wavelengths*, **35th International Conference on the Physics of Semiconductors (ICPS)**, Sydney, Australia, 06.2022.

14. P. Holewa *et al.*, *Simulation and fabrication of heterogeneous InP/Si waveguides for coupling quantum dot emission at 1.55 µm into the silicon platform*, **50th International School & Conference on the Physics of Semiconductors "Jaszowiec 2022"**, Szczyrk, Poland, 06.2022.

15. P. Holewa *et al.*, *Towards Deterministic Fabrication of EDC Cavities with QDs*, **Conference on Fundamentals and Applications of Semiconductor Nanocavities**, Copenhagen, Denmark, 06.2022.

16. P. Holewa *et al.*, *Single-photon emission at elevated temperatures from InGaAs/GaAs quantum dots at the telecom O-band*, **17th International Conference on Optics of Excitons in Confined Systems (OECS)**, virtual environment, 08.2021.

17. P. Holewa *et al.*, *Epitaxy of Low Surface Density InAs/InP Quantum Dots for Single-Photon Source Applications at 1.55 µm*, **11th International Conference on Quantum Dots**, virtual environment, 12.2020.

18. P. Holewa *et al.*, *Optical properties of MOVPE grown InAs/InP quantum dots desired for single photon emitters in telecom bands*, **2nd Quantum Symposium (PicoQuant)**, Berlin, Germany, 06.2019.

19. P. Holewa *et al.*, *Multimodal distribution of low-density InAs/InP quantum dots emitting above* $1.5\,\mu$m, **Winter School of Physics**, University of Würzburg, Germany, 02.2019.

20. P. Holewa *et al.*, *Effect of temperature on deterministic quantum dot-mesas in the* $1.3\,\mu$m *range*, **1st PicoQuant Quantum Symposium**, Berlin, Germany, 05.2018.

21. P. Holewa *et al.*, *Temperature dependence of photoluminescence from deterministic quantum dot - micromesas emitting single photons at* $1.3\,\mu$m, **5th International Workshop on the Optical Properties of Nanostructures (OPON)**, Münster, Germany, 02.2018.

22. P. Holewa *et al.*, *High-Purity Single Photon Emission from InGaAs/GaAs Quantum Dots in the Telecommunication O-Band*, **International School & Conference on the Physics of Semiconductors "Jaszowiec 2017"**, Szczyrk, Poland, 06.2017.

Acronyms

µPL microphotoluminescence. 38, 39, 42, 55, 60, 62, 64–66, 72, 73, 75–78, 221

0D zero-dimensional. 5, 30, 32

1D one-dimensional. 30, 49, 50, 66

2D two-dimensional. 5, 7, 12, 16, 24–26, 31, 32, 52, 57, 66, 67, 77, 220, 222

3D three-dimensional. 5, 16, 23–25, 28, 31

AFM atomic force microscopy. 11, 19, 58, 59, 75, 221

AM alignment mark. 11, 61, 62, 66, 77

ATG Asaro-Tiller-Grinfel'd. 24

BCB benzocyclobutene. 60

c-QED cavity quantum electrodynamics. 49–51

CBG circular Bragg grating. 8–11, 49, 67, 72, 76, 77, 220

CI configuration interaction. 32, 33, 35, 36, 38, 221

CL cathodoluminescence. 11

cps counts per second. 67, 68

CSAR Chemical Semi Amplified Resist. 61, 62

cw continuous-wave. 62, 69, 76

CX charged exciton, or trion. 30, 33, 38, 39, 43, 65, 67, 72, 73, 77

DBR distributed Bragg reflector. 6, 8–10, 75, 76

DE droplet epitaxy. 7, 10, 12, 28, 29, 59, 71, 74, 75

DFT density functional theory. 22, 25

DI deionized. 60, 62

DOLP degree of linear polarization. 32, 65, 72, 73

DTU Technical University of Denmark. v, 55, 61, 62

EBL electron-beam lithography. 11, 61, 62, 66, 77, 78

EDX energy-dispersive x-ray spectroscopy. 75

EI exchange interaction. 29, 32, 33, 36–38, 64, 221

EM electron multiplication. 12

EMA effective mass approximation. 31, 32, 35

F-M Frank-van der Merwe. 23

FOV field of view. 11

FSS fine structure splitting. 7, 28, 29, 32, 36–38, 65, 72, 74, 75, 218

FWHM full width at half maximum. 8, 50

GI growth interruption. 26, 27, 57–59

GIXS grazing incidence X-ray scattering. 19

GR growth rate. 16–18, 20, 57

HBT Hanbury Brown and Twiss. 15, 44–48, 67, 221

HH-LH heavy-hole–light-hole states. 36, 37, 65, 72

HSQ hydrogen silsesquioxane. 61, 62

HVPE hydride vapor-phase epitaxy. 15

HWP half-wave plate. 64, 65, 221

ICP-RIE inductively coupled plasma-reactive ion etching. 61, 62

IR infrared. 4, 15

LDE local droplet etching. 29

LED light emitting diode. 15

LO longitudinal optical. 77

LP linear polarizer. 64, 65, 221

LPE liquid-phase epitaxy. 15

MBE molecular beam epitaxy. 15, 16, 73, 222

MBL metamorphic buffer layer. 6, 7

MC Monte Carlo. 22

MEM entropy maximization method. 72

MFC mass flow controller. 56

MOVPE metalorganic vapour-phase epitaxy. 15–20, 22, 55, 56, 58, 72, 74, 220–222

NA numerical aperture. 10, 75, 77

NIR near-infrared, $0.75 - 1.4$ µm. 11, 12, 66, 71, 77

OPO optical parametric oscillator. 64

PECVD plasma-enhanced chemical vapor deposition. 60, 62

PL photoluminescence. 10–12, 43, 44, 55, 59, 65, 66, 71–75, 222

PLE photoluminescence excitation. 43, 72, 73

QD quantum dot. 4–13, 15, 22–34, 36–39, 41–44, 49, 50, 52, 55–68, 71–78, 220–222

QDash quantum dash. 28, 73

QIP quantum information processing. 3, 4, 6, 7, 10, 22, 71, 74, 76

QW quantum well. 5, 30, 32, 36–38

RIE reactive ion etching. 61

S-K Stranski-Krastanow. 6, 7, 10, 12, 22–29, 43, 57, 59, 72, 74, 76, 220

SEM scanning electron microscopy. 11, 59

SM Supplemental Material. 12, 62, 65, 67, 77

SNR signal-to-noise ratio. 66

SNSPD superconducting nanowire single-photon detector. 47, 64, 67, 68, 221

SPS single-photon source. 3–6, 8, 26, 76

STEM scanning transmission electron microscopy. 57, 59, 75

STM scanning tunneling microscope. 19

TBP tertiarybutylphosphine, $(CH_3)_3CPH_2$. 55, 59

TMAl trimethylaluminium, $Al_2(CH_3)_6$. 55

TMGa trimethylgallium, $Ga(CH_3)_3$. 55

TMIn trimethylindium, $In(CH_3)_3$. 16, 55, 59

TRPL time-resolved photoluminescence. 55, 67, 72–75, 77

TTTR Time-Tagged Time-Resolved. 67

UV ultraviolet. 12, 15

V-W Volmer-Weber. 23, 28

WL wetting layer. 7, 16, 22–28, 31, 32, 43, 57, 59, 71–73, 220

WUST Wrocław University of Science and Technology. v, 77

X exciton. 8, 28, 33, 34, 36, 38, 39, 42, 43, 64, 65, 67, 72, 74, 75, 220, 221

X^+ positively-charged exciton. 30, 33, 34, 36, 38, 220

X^- negatively-charged exciton. 30, 33, 34, 36, 38, 220

XX biexciton. 8, 9, 28, 33–36, 39, 42, 43, 64, 65, 72, 74, 220, 221

List of symbols

$\langle \dots \rangle$	time averaging over a long period. 45
$\mathscr{A}$	antisymmetrizing operator. 35
a_i	activity. 18
C	exchange Coulomb integral. 33, 34, 37
c	speed of light in vacuum. 41, 54
D	direct Coulomb integral. 33, 34, 36, 220
$\mathbf{d}$	electric dipole. 39, 40, 52, 54
E_Y	Young's modulus. 24
E_A	activation energy. 20, 21, 43
$\boldsymbol{E}_\mathrm{vac}$	vacuum electric field. 51–53
$\boldsymbol{E}_0$	amplitude of the electric field. 39, 40, 53, 54
E	energy. 17, 30, 33, 34, 52
F_P	Purcell factor. 8–10, 49, 54, 77
$\mathscr{F}$	cavity finesse. 49, 50
$\lvert f \rangle$	final state. 39–41, 52
F	flow rate. 27, 57
f	oscillator strength. 39, 41
G	Gibbs free energy per mole. 17, 18
G	exciton photogeneration rate. 41, 42, 69
G'	Gibbs total free energy. 18
g_0	emitter-photon coupling parameter. 50–52
$g(\omega)$	photon density of states. 39, 51, 53, 54, 221
H	enthalpy. 17
$\mathscr{H}_{ex}$	exchange Hamiltonian. 37
$\mathscr{H}$	Hamiltonian. 31, 35
h_c	critical thickness of the wetting layer. 23–26, 57, 220
h_{eq}	equilibrium thickness of the wetting layer. 24–26, 57, 220
$\hbar$	reduced Planck constant. 30, 51, 52
I	light intensity. 41–47, 65, 221
$\lvert i \rangle$	initial state. 39–41, 52
i	photocurrent. 44
$J_{h,z}$	projection of the hole state spin on z-axis. 36
J_h	hole spin. 36, 37

k	reaction rate constant. 20
M	angular momentum. 36, 37, 40
M	transition matrix element. 35, 39, 40, 53, 54
m_0	electron rest mass. 31
m_e	electron effective mass. 29–31, 40
n	refractive index. 8, 41, 49, 54
P	pressure. 17, 18
P	purity of the single-photon emission. 3, 5, 6, 10, 44, 48, 55, 69, 75–77
p_i	partial pressure. 18, 21
Q	quality factor. 8, 9, 49–54
R	ideal gas constant. 18
R_g	maximum lateral size of islands. 27, 57, 58
$\mathbf{r}$	position. 31, 32, 34, 35, 39, 40
$S_{e,z}$	projection of the electron state spin on z-axis. 36
S_e	electron spin. 36, 37
S	entropy. 17
T	temperature. 17, 27, 41, 56, 57
T	transmission. 49
V_0	mode volume. 51, 52, 54
W_{2D}	elastic strain energy. 23, 24
x_i	mole fraction. 18
$\Delta(XX)$	biexciton binding energy. 8, 34–36, 38, 221
δ_0	bright-dark exciton states splitting, electron-hole exchange energy. 37, 38, 221
δ_1	bright exciton states splitting, also called FSS. 37, 38, 221
δ_2	dark exciton states splitting. 37, 38, 221
δ_Φ	correlation energy. 35, 36, 38, 221
ε	dielectric constant. 31, 34
ϵ_i	single-particle eigenenergy. 31
ϵ_0	layer mismatch. 6, 7, 24, 57
$\overline{\varepsilon}$	screened dielectric function. 33
ϵ_0	vacuum permittivity. 41
η_{Setup}	optical setup efficiency. 67, 68
η	photon extraction efficiency. 7–11, 55, 59, 67, 68, 72, 75–77
Γ	transition rate. 39–41, 53, 54, 69
γ	non-resonant photon decay rate. 50, 51
γ_1	substrate surface energy. 23
γ_2	epilayer surface energy. 23
γ_{12}	interface energy. 23
κ	photon decay rate. 50–52

λ_B	de Broglie wavelength. 29
μ	chemical potential. 18
$\boldsymbol{\mu}$	transition dipole moment. 39, 52
ν	Poisson's ratio. 24
Φ	Slater determinant. 35
ϕ_{nk}	bulk electron state. 32
$\pi_{\mathrm{x,y}}$	linear polarization of photons. 37, 38, 65, 221
Ψ_{exc}	exciton wavefunction. 35
ψ_i	single-particle eigenfunction. 31, 32, 34, 35
$\rho(E)$	density of states. 30, 39
ρ	island density. 27
$\sigma^{\pm}$	circular polarization of photons. 37, 38, 65, 221
σ	single-particle spin. 31, 33, 35, 40
τ_{cav}	cavity photon lifetime. 50, 52
τ_c	coherence time. 45, 46
τ	recombination time. 40–42, 53, 54
ζ	superstress. 25
$\Delta\omega$	spectral width of a cavity mode. 8, 49, 50
ω_m	mode angular frequency. 49, 50

List of Figures

List of Tables